Faculty of Applied Engineering
Research group of Applied
Electrochemistry & Catalysis
(ELCAT)

Towards a targeted optimization of electrocatalysts by combining electrosynthesis with *in-situ* electron paramagnetic resonance

This thesis is submitted in fulfilment of the requirements for the degree of
Doctor in Applied Engineering
(Doctor in de toegepaste ingenieurswetenschappen)

Sander Neukermans

Promotors:

Prof. dr. ing. Tom Breugelmans

Dr. ing. Jonas Hereijgers

Antwerp 2021

University of Antwerp
ELCAT | Applied Electrochemistry and Catalysis

University of Antwerp

Towards a targeted optimization of electrocatalysts by combining electrosynthesis with *in-situ* electron paramagnetic resonance

Sander Neukermans

Members of the Jury

Prof. dr. Thomas Altantzis	President of the jury University of Antwerp
Dr. H.Y. Vincent Ching	Secretary of the jury University of Antwerp
Prof. dr. ing. Tom Breugelmans	Promotor University of Antwerp
Dr. ing. Jonas Hereijgers	Promotor University of Antwerp
Prof. dr. Sabine Van Doorslaer	Jury member University of Antwerp
Prof. dr. ir. Annick Hubin	External jury member Vrije Universiteit Brussel
Prof. dr. Julie MacPherson	External jury member Warwick University
Prof. dr. Ward van der Stam	External jury member Utrecht University

Acknowledgements

After all these years, I am about to conclude one of the hardest tasks I have faced so far in my entire life. There were ups and downs. The euphoric moments when a setup worked like I imagined and the contrast with the periods when I found myself somewhat lost when it didn't. For me, this moment indicates the end of something, but it also gives me hope, that there is so much more to come. A journey like this would be very hard to face alone, therefore I want to thank some people on whom I could rely for so many different things during my PhD.

First of all I want to express my gratitude to Tom for giving me the opportunity to start my PhD here as the first non-native UA student in ELCAT. The faith you put in me, the guidance on the lows and the friendship are priceless. Thank you for reading and correcting my work. In the same breath, I also want to thank Jonas for giving independent and rational input when I needed it but sometimes didn't want to hear it.

I also want to thank all the colleagues at ELCAT (and previously ART). Our group has changed tremendously since I started, exploding in size, office space, lab space and lab equipment. Thanks colleagues for your indirect help and contribution to the team spirit of the group. To my office colleagues Oriol, Jonathan and Kristof for philosophizing about the important things in life. A special thanks to Lien and Thomas for their support both privately and professionally. Thanks Bart G., Danny and Bart V. for teaching me the basics in my first few months in the lab.

The support of the colleagues at BIMEF is very much appreciated. Vincent and Mo for always being able to fit my measurements in your schedules. For your help in the lab but also for brainstorming about conceptualization. Thank you Sabine for trusting these two guys with me from the very start.

I want to thank my friends and family for being there for me on moments that my mind needed to be diverted and for their unconditional love and patience.

Thank you mom, dad and my sister Elke for always supporting me in whatever decision I made during the course of my life. For giving me the possibility to go to university and to move to Ghent during that period. Thanks for being able to listen to my problems and stories about work, babies and family life.

Finally I want to thank Frederik, my husband, my friend, my everything. I know I sometimes had to pull the rope slightly more to my side to be able to combine our careers with building a family, but I think we manage it very well. You have supported me in everything and taught me to never regret a decision. No words can describe what I feel for you and what you mean to me.

Sander

Summary

The increasing renewable energy production and declining interest in fossil fuel generates opportunities for the electrification of industrial processes. This electrification can be reached through different routes. A chemical production process can be replaced by an electrochemical synthesis process with direct energy supply from a renewable source without inefficient energy conversions. The economic feasibility of such a process is then determined by the activation energy of the electrochemical reaction. Electrocatalysis investigates how this energy demand (overpotential) can be reduced and what the consequences are on the selectivity. Both these parameters depend on the used electrode material at which the reaction will take place through a specific reaction mechanism. Predictions about the catalytic activity of a material are not straightforward and their development mostly goes through trial and error. Knowledge about the reaction mechanism can help to improve and speed up this development.

The number of techniques that are available to study the reaction mechanism at the electrode are limited. The fact that in electrochemical reactions, electrons are transferred, often forming short-living radical intermediates, limits the possibilities for detection even more. Electron Paramagnetic Resonance (EPR) is probably the most relevant technique to gather information about the chemical nature and electronic structure of these radical intermediates. Despite the long history of the combination of electrochemistry with EPR, the use in electrocatalytic research remains underexploited up until today. The main reasons are: the availability of EPR infrastructure, the lack of specific knowledge to derive useful information from experiments and the scarcely available commercial cells and electrodes suitable for this application. This work focusses on the development and use of these cells and electrodes to map the limitations and diminish reservations about the combined techniques.

In the first part, several setups are designed taking into account the restrictions that apply for specific case studies. Improvements are proposed and their effects are assessed by two frequently-used testcases. First, the electrochemical behavior of the simplest design in a commercial flat cell is improved. Then, the possibility to reproducibly deposit catalytic materials on a conductive substrate is added. Afterwards, two setups are designed to fit in commercial EPR tubes which are suitable to electrolyze samples of electrochemical mediators that have to be frozen for low temperature EPR experiments. On the one hand, a wire electrode is proposed to possibly be frozen with the sample and on the other hand, a flat and chemically inert electrode is presented which has to be removed from the sample before freezing. Beside all the previously mentioned batch setups, a hydrodynamic channel electrode is designed with strategically positioned electrodes. This design allows for investigation of kinetics and mass transfer.

The second part focusses on the investigation of the electrochemical reaction mechanism of two relevant reactions: the aldol condensation of acetone to diacetone alcohol and the reduction of carbon-halogen bonds in aromatic compounds. Different setups from the first part are used and, in both cases, radical stabilization compounds are added to slow down radical decay. The influence of oxygen on the acetone reduction is examined and possible reaction mechanisms are postulated. The reduction of the carbon-halogen bonds is first electrochemically investigated for several compounds and electrode materials. Afterwards *in-situ* EPR electrolysis is used to assess the electrochemically derived reaction mechanism.

This work shows that combining electrochemistry with electron paramagnetic resonance is an appropriate combinatorial technique to gain information about radical intermediates of electrochemical reactions. It also attempts to take away reservations of scientists by offering setups for different purposes.

Samenvatting

De toenemende productie van hernieuwbare energie in combinatie met verminderde interesse in fossiele brandstoffen creëert opportuniteiten voor de elektrificatie van industriële processen. Deze elektrificatie kan op verschillende manieren uitgevoerd worden. Een chemisch productieproces kan vervangen worden door een elektrochemisch syntheseproces waarbij de nodige energie rechtstreeks afkomstig is van een hernieuwbare bron zonder dat inefficiënte energietransities moeten plaatsvinden. De economische haalbaarheid van dergelijk proces wordt dan vooral bepaald door de activatie-energie die nodig is om de reactie te laten doorgaan. Het domein van de elektrokatalyse onderzoekt hoe deze energie, gekwantificeerd door de overpotentiaal, kan verlaagd worden en welke invloed dit heeft op de selectiviteit. Beide parameters zijn afhankelijk van het gebruikte elektrodemateriaal waaraan de reactie zal plaatsvinden volgens een specifiek reactiemechanisme. Het voorspellen van de katalytische activiteit van een bepaald materiaal is niet eenvoudig en de ontwikkeling gebeurt meestal proefondervindelijk. Kennis over het reactiemechanisme kan helpen bij het versnellen en verbeteren van deze ontwikkeling.

Het aantal technieken waarmee het reactiemechanisme aan het elektrodeoppervlak kan bestudeerd worden, is beperkt. Aangezien elektrochemische reacties elektronen overdragen, worden vaak radicalaire tussenproducten gevormd. Elektron Paramagnetische Resonantie (EPR) is waarschijnlijk de meest relevante techniek om informatie te vergaren over de chemische aard en de elektronische structuur van deze tussenproducten. Ondanks de lange voorgeschiedenis van de combinatie van elektrochemie met EPR, blijft deze techniek tot op vandaag onderbenut in elektrokatalytisch onderzoek. De voornaamste redenen hiervoor zijn: het gebrek aan EPR-infrastructuur, de specifieke kennis om nuttige informatie uit metingen te halen en het gebrek aan commercieel verkrijgbare cellen en elektroden die geschikt zijn voor deze toepassing. Dit werk focust op het ontwikkelen en gebruiken van deze cellen en elektroden om de beperkingen van de gecombineerde techniek in kaart te brengen en zoveel mogelijk weg te werken.

In een eerste deel worden verschillende setups ontworpen met telkens een verbetering van verschillende aspecten om tegemoet te komen aan de vereisten van verschillende casestudy's. Het effect van deze verbeteringen wordt beoordeeld doormiddel van twee courante testcases. Eerst wordt het elektrochemische gedrag van het meest eenvoudige ontwerp in een commerciële *flat cell* verbeterd, waarna het mogelijk wordt om reproduceerbaar katalytische materialen te elektrodepositeren op het geleidende substraatoppervlak. Vervolgens worden twee opstellingen ontworpen op maat van commerciële EPR-buisjes met als doelstelling om op lage temperatuur metingen uit te voeren van elektrochemische mediatoren. De geometrie van de cel is hier ondergeschikt aan het feit dat de oplossing moet afgekoeld worden. Daarom wordt enerzijds een draadelektrode voorgesteld die lage temperaturen kan weerstaan. Anderzijds wordt een vlakke elektrode gebruikt die uit de oplossing moet verwijderd worden alvorens het staal te bevriezen. Naast al deze batchopstellingen wordt ook een hydrodynamische methode voorgesteld waarbij de oplossing door een kanaal stroomt waar de elektroden strategisch gepositioneerd zijn. Dit ontwerp laat toe om gecontroleerd de kinetiek en de massaoverdracht te bestuderen.

In het tweede deel wordt het elektrochemische reactiemechanisme van twee relevante reacties onderzocht, zijnde de aldolcondensatie van aceton naar diacetonalcohol en de reductie van koolstof-halogeen verbindingen. Verschillende opstellingen uit het eerste deel worden gebruikt en in beide gevallen worden stabilisatoren toegevoegd om het verval van de radicalen te vertragen. De invloed van zuurstof op de aceton-reductie wordt onderzocht en het reactiemechanisme voor de verschillende condities wordt gepostuleerd. De reductie van koolstof-halogeen verbinding wordt eerst elektrochemisch uitgevoerd op verschillende moleculen en elektrodematerialen om daarna na te gaan of het elektrochemisch afgeleide reactiemechanisme met EPR bevestigd kan worden.

Dit werk toont aan dat het combineren van elektrochemie met elektron paramagnetische resonantie nog steeds zeer relevante informatie kan opleveren en tracht de terughoudendheid van wetenschappers weg te nemen door verschillende opstellingen voor te stellen.

Table of contents

Nomenclature

ACN	Acetonitrile
BQ	1,4-Benzoquinone
CE	Counter Electrode
CPE	Constant Phase Element
CV	Cyclic Voltammetry
CW	Continuous Wave
DAA	Diacetone Alcohol
DFT	Density Functional Theory
DMF	Dimethylformamide
DMPO	5,5-dimethyl-2-hydroxyl-pyrrolin-1-yl
DMSO	Dimethylsulfoxide
EGB	Electrogenerated Base
EIS	Electrochemical Impedance Spectroscopy
EPR	Electron Paramagnetic Resonance
FE	Faradaic Efficiency
GC	Glassy Carbon
	As technique: Gas Chromatography
HPLC	High Performance Liquid Chromatography
ICP	Inductively Coupled Plasma
IPA	Isopropanol
IR	Infrared
ITO	Indium Tin Oxide

LSV	Linear Sweep Voltammetry
MS	Mass Spectrometry
MV	1,1’-dimethyl-4,4’-bipyridinium dichloride
NMR	Nuclear Magnetic Resonance
PBN	N-tert-butyl-α-phenylnitrone
PDA	Photo Diode Array
PEEK	Polyether Ether Ketone
POM	Polyoxymethylene
PP	Polypropylene
PTFE	Polytetrafluoroethylene
PVD	Physical Vapor Deposition
RDE	Rotating Disc Electrode
RDS	Rate-Determining Step
RE	Reference Electrode
SCE	Standard Calomel Electrode
SEM	Scanning Electron Microscopy
TBAP	Tetrabutylammonium Perchlorate
TBAB	Tetrabutylammonium Bromide
TBAFP	Tetrabutylammonium Hexafluorophosphate
UV-VIS	Ultraviolet-Visible
WE	Working Electrode

List of symbols

E	Half-cell potential [V]
E^0	Standard reduction potential [V]
R	Gas constant [8.3145 J mol^{-1} K^{-1}]
	Resistance [Ω]
	Reductant
T	Temperature [K]
n	Amount of substance [mol]
	Number of electrons exchanged per molecule of reagent
F	Faraday constant [96485 C mol^{-1}]
ν	Kinematic viscosity [cm^2 s^{-1}]
ν_i	Stoichiometric number of specie i
a_i	Activity of specie i
k	Reaction rate constant
A	Electrode surface area [m^2]
	Frequency factor in a rate expression
	Hyperfine coupling
E_a	Activation energy of a reaction
O	Oxidant
e	Electron
	Electron charge [1.6022 x 10^{-19} C]
v	Linear potential scan rate [V s^{-1}]
	Reaction rate [M s^{-1}]
$C_O(0,t)$	Oxidant concentration at the electrode surface [mol m^{-2}]

i_c	Cathodic current [A]
$C_R(0,t)$	Reductant concentration at the electrode surface [mol m^{-2}]
i_a	Anodic current [A]
$E^{0'}$	Formal half-cell potential [V]
G^{+}	Standard Gibbs free energy of activation [kJ mol^{-1}]
α	Electron transfer coefficient
κ	Kinetic indicator
C^*	Bulk concentration [M]
k^0	Standard rate constant [cm s^{-1}]
f	F/RT [V^{-1}]
j	Current density [A m^{-2}]
J	Flux of a specie [mol cm^{-2} s^{-1}]
D	Diffusion coefficient [m² s^{-1}]
z_i	Charge of a specie i
$v(x)$	Linear velocity of solution flow [cm s^{-1}]
R_s	Ohmic resistance of the solvent [Ω]
I	Current [A]
t	Time [s]
X_R	Conversion ratio to a reduced specie
Q	Charge [C]
	Quality factor of EPR resonator
ω	Width of a rectangular electrode [m]
	Angular frequency of rotation [s^{-1}]

	Angular frequency of a sinusoidal oscillation [s^{-1}]
x_e	Length of a rectangular electrode [m]
i_l	Limiting current [A]
h	Planck constant [6.626070040 x 10^{-34} m^2 kg s^{-1}]
	Half height of a channel [m]
d	Width of a channel [m]
V_F	Linear velocity of a fluid [m s^{-1}]
C_d	Capacitance of the electrochemical double layer [F]
i_p	Peak current [A]
ϕ	Local potential [V]
	Phase angle between two sinusoidal signals
j	Imaginary number
C	Capacitance [F]
Z	Impedance [Ω]
$\boldsymbol{S}$	Electron spin angular momentum
ħ	Reduced Planck constant [1.054571800 x 10^{-34}]
S	Spin quantum number
m_e	Mass of an electron [9.1093837015 x 10^{-28} g]
m_s	Electron spin angular momentum quantum number
μ	Magnetic dipole momentum
γ_e	Gyromagnetic ratio of an electron
μ_B	Bohr magneton [9.274009994 x 10^{-24} J T^{-1}]
g	g-factor
g_e	Electon g-factor [-2.002319304361]

v	Frequency in Planck's equation [s^{-1}]
γ_N	Gyromagnetic ratio of a nucleus
$\boldsymbol{l}$	Nuclear spin angular momentum
m_p	Mass of a proton [1.6726 x 10^{-24} g]
a	Hyperfine coupling constant
g_N	Nuclear g-factor
m_l	Nuclear spin angular momentum quantum number

Part I

Introduction

Chapter 1

General introduction

This chapter gives a general introduction and expresses the relevance of the field of electrochemistry in today's and future society. It denotes the challenges and suggests a fundamental strategy for improvement of catalyst materials.

1.1 Availability of renewable energy

The world and especially mankind is approaching a crossroad in their history. Our planet is experiencing significant and accelerated climate change caused by greenhouse gases emitted by human activities. It is vital that we reduce or even stop emitting these greenhouse gases if we want to prevent a mass extinction of species [1]. In 2019, global temperature increase reached 0.95°C compared to the pre-industrial era [2]. To counter these effects governments all over the world are trying to gradually transform their energy supply from fossil to renewable sources. The first significant step came with the Kyoto protocol in 1997 where 55 countries agreed to limit the amount of greenhouse gasses they could emit between 2008 and 2012 [3]. In the following period, from 2012 to 2020, countries failed to come to an agreement about further reduction so some countries prolonged the Kyoto protocol and set new goals for themselves in the Doha amendment [4]. In 2015, the Paris agreement stated the intention to keep the temperature change well under 2°C increase in the year 2100 and preferably below 1.5°C. Therefore the EU wanted to cut its emissions by 20 percent in 2020 and by 40 percent in 2030 compared to the levels of 1990 [5].

To be able to comply to these international agreements, governments look preferably to wind, solar, hydro, biomass and geothermal energy sources [6]. Others also include nuclear energy as an important contributor to the energy mix in the future because of low carbon emissions. This is a very controversial and debated topic up until today [7,8]. Whichever opinion one might have on solving the issue, it will always include previously named technologies with the inherent consequence to create electricity production on off-peak moments of energy demand. In other words, this way of energy production leads to an unavoidable mismatch between production time and consumption [9]. This mismatch leads to a lower efficiency of the renewable energy sources like wind farms which have to be temporarily shut down or other less sustainable backup is needed at times of peak consumption. In an ideal situation, the excess energy can be used for the production of chemicals in sustainable processes using these green energy sources at low cost.

It should be emphasized that electrolysis as a technique for the sustainable production of chemicals on an industrial scale will need continuous operation and that only the excess energy will not suffice. However, this strategy can make the process economical during the energy transition.

1.2 Role of the chemical industry

The Flemish chemical industry is one of the major energy consumers with a share of 37.8% of industrial energy consumption in 2017 [10]. Consequently it plays a significant role in finding solutions for lowering energy consumption. One of their cost-saving strategies is to increase the process efficiency which can be achieved through energy saving. Optimization of process parameters, like temperature, pressure and reagent concentration, is the obvious route to take but reaches its limits fairly fast. Installations can be adjusted in order to recirculate product streams or to recover thermal energy. An alternative strategy can be to reduce the intrinsic energy demand of a reaction by introducing a catalyst. These reaction-specific compounds promote reaction pathways that are energetically more favorable and will therefore require less energy provided by *i.e.* heating or compression. Over the years the focus shifted from homogeneous catalysts to heterogeneous ones with the clear advantage of excluding expensive phase separation procedures of the product stream [11]. The active catalyst is predominantly supported on a carrier material to reduce agglomeration and enlarge its active surface area. Three industrial examples are the (i) Haber-Bosch process, (ii) sulfuric and (iii) nitric acid production. In the Haber-Bosch process, ammonia is being produced from hydrogen and nitrogen gas. The catalytic material changed from iron-based to ruthenium-based ones over the years [12–14]. The production of sulfuric acid requires an alkaline doped vanadium catalyst for the oxidation of SO_2 to SO_3 but also combinations of other binary metal oxides have some catalytic activity [15]. Nitric acid is produced via the Ostwald process which uses a platinum-rhodium gauze catalyst for the conversion of ammonia with oxygen to nitric oxide and water [16].

Whilst providing clear advantages, regular heterogeneous catalysis depends on the inherent properties of the used materials to reach the activation energy of the reaction and further improvement (*i.e.* inhibition of side reactions) can be made by varying temperature and pressure or selecting another catalyst. A specific branch of heterogeneous catalysis can be found in electrochemistry, adding electrical energy as a variable for reaching the activation energy of a reaction. The two most relevant industrial electrochemical processes accounting for 90% of the energy used in industrial electrochemistry are the chlor alkali process and the refining of aluminum [17]. The chlor alkali process produces chlorine and sodium hydroxide from sodium chloride and water. Up to 55% of specialty chemicals manufactured, require one of the chlor alkali process products as a precursor. Examples are pesticides, rubbers, plastics, cosmetics, paints, disinfectants, lubricants, detergents, soaps, fuel additives and many more [18]. Aluminum ore, also known as bauxite, is used to produce aluminum oxide. Afterwards it is electrochemically refined to pure aluminum at a cathode while CO and CO_2 are formed at the anode. It was estimated in 1997 that at the time, 2.5% of total global anthropogenic CO_2 emissions were caused by aluminum refining [19]. Nevertheless, the discovery of these refining techniques made the metal, once as expensive as silver, drop significantly in price [20].

1.3 Electrochemical synthesis

The electrochemical production of compounds is called electrosynthesis. It is induced by a transfer of electrons requiring an amount of electrical energy to bridge the energy barrier between reagents and products. The electricity used, can be provided by green sources with the advantage that no inefficient energy conversion and no combustion of carbon-based compounds needs to take place. Electrosynthesis has some other advantages over classical chemical synthesis [21]:

- The energy of the electrons can be controlled through an applied potential with conditions typically being mild (room temperature and atmospheric pressure). In addition, the potential also determines the reaction selectivity and the reaction rate leading to a good atom economy and less waste.
- The use of renewable starting materials is possible.
- Reactions can be monitored during the experiment allowing modifications to be made *in operando*.
- No dangerous or polluting redox reactants have to be used in stoichiometric amounts since the electrons are inherently clean reactants and energy efficient for oxidation and reduction reactions, also leading to safer operating conditions.
- The catalyst, in this case the electrode, can be physically removed from the solution after the experiment.

All the advantages of electrosynthesis relate to at least 9 of the 12 principles of sustainable or green chemistry. This concept introduced in 1991 to decrease the impact of a production process on the environment by changing the strategy from containing pollution to preventing pollution [22]. Especially in the production of organic compounds through classical redox reactions, pollution is an important hurdle [23].

1.4 Organic electrosynthesis

Organic compounds are very useful for a wide range of applications like the manufacturing of polymers, dyes, agriculture, food additives and pharmaceuticals. Most of them are produced on a relatively small scale and the demand sometimes depends on a single final product [24]. Although being widely used in the electrochemical community, organic electrosynthesis is only recently being picked up by many chemists for several reasons. These reasons are mainly:

(i) the lack of goal indication in literature when performing electrolysis (to explain voltammetry, for laboratory synthesis or for commercial synthesis), (ii) the lack of experimental information about the cell, electrodes and conditions in publications and (iii) their demand for high conversion, yield and isolation of the pure product on a scale of interest [25]. As a result, there are only a few processes at pilot-plant scale or even industrial scale for the electrosynthesis of organic molecules [21].

Some examples of electrochemically produced organic compounds are; adiponitrile, methoxylated toluenes, p-anisaldehyde, m-hydroxybenzyl alcohol, 2,5-dimethoxy-2,5-dihydrfurfuryl-1-ethanol, salicylic aldehyde, succinic acid,…. A non-limiting list of commercial and pilot plant processes has been given by Santos and Sequeira in [17]. This list also shows that organic electrosynthesis is a field of great importance for present and future industrial production of chemicals.

One of the previously mentioned examples is the production of adiponitrile through the cathodic hydrodimerization of acrylonitrile (Figure 1.1). The total production of adiponitrile by electrolysis for instance surpassed 300 000 tons per year in 2001 [26]. Improvements have been made to the process, reducing the energy cost and suppressing side reactions even more. Despite these improvements, the route towards better efficiency went through trial and error of changing solution compositions, reactor design and electrode materials that inhibited hydrogen evolution whilst the reaction mechanism stayed unclear. Elucidating the different steps of the reaction pathway could help optimizing the process in a structured and targeted manner rather than trial and error. The case of adiponitrile production itself holds some inherent difficulties for mechanistic investigations to be successful;

- The high concentration of acrylonitrile hinders electrochemical kinetics determination and the rates of coupled chemical reactions. Electrolysis at lower concentrations (10 mM) leads to the two electron transfer towards propionitrile which is irrelevant for the desired hydrodimerization.

- Multiple pathways between the reactants and products (eleven in [27]) with several possible Rate-Determining Steps (RDS) are to be considered (at least 8 in [24]).
- No reaction intermediates have been detected by electrochemical or spectroelectrochemical techniques possibly confirming one of the postulated mechanisms.

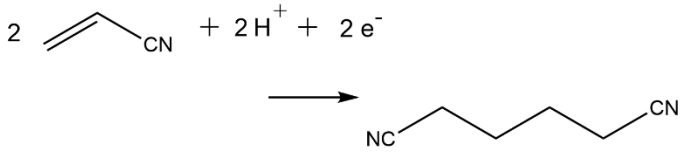

Figure 1.1: *Electrohydrodimerization of acrylonitrile.*

1.5 Mechanistic research

The previous section indicates the complexity of specific reactions and the importance of several variable parameters. These parameters for electrochemical reactions are for example: the choice of catalytic electrode material, the electrode potential, presence of oxygen, side reactions at the counter electrode, the used solvent and many other reaction conditions. They all have a potential influence on the reaction pathway towards products formed by electrolysis. Several analytical electrochemical techniques can be used to derive the influence of each parameter, and thus the probability of the hypothesized reaction pathway. This information can then later be used to adjust a process or to assess its economic viability.

The field of electrode reaction mechanism investigation has undergone tremendous changes since its conception with technical advances and digital control of instrumentation and modelling [28]. Electrochemical analysis techniques together with simulations can give mechanistic information about the electron transfer. The importance of the quality of experimental data should be emphasized in order to reach conclusions from simulations.

However, in more complex cases, for instance when organic structures are involved, one cannot determine the nature of intermediates (especially radicals) and conclusions are drawn only from the behavior of the total reaction system which essentially ends up in speculation.

1.6 Spectroelectrochemistry

The structural details of the species involved in a reaction are hard to describe with solely electrochemical analysis techniques and depend on the complexity of the system and the relative rates of reactions. There is a need for supplementary spectroscopic investigations to yield insight into the structure of intermediate species. *ex-situ* methods with spectroscopic characterization of the electrode reaction products far from the electrochemical cell where no electrode potential is applied could lead to misinterpretations of the situation at the electrode. *In-situ* spectroscopic electrochemical analysis techniques can help to study product species with a limited lifetime and contribute to the hypothesizing and subsequent confirmation of the reaction mechanism. Every spectroscopic technique can yield specific information about a specie; while infrared (IR) exploits vibrations and rotations of bonds to derive the presence of functional groups, UV-VIS radiation is absorbed by electronic transitions. Nuclear Magnetic Resonance (NMR) and Electron Paramagnetic Resonance (EPR) exploit respectively the nuclear spin and the electron spin of atoms in a molecule. Combinations of these spectroscopic techniques with *in-situ* generation of electrochemically activated species impose different requirements on the setup [29].

The time frame (Δt) of a method is an important aspect to identify the desired intermediate specie. For electronic absorption spectroscopy this Δt is < 10^{-15} s but for NMR spectroscopy it is in the seconds range [30]. EPR has the unique power to detect paramagnetic species, like radicals, while diamagnetic reactants or products do not directly interfere with the spectrum. Through the interactions with neighboring atoms the structure of a paramagnetic intermediate can be determined.

The combination of EPR with electrochemistry is very attractive as the removal or addition of one electron by electrochemical means yields paramagnetic intermediates when the reactant is diamagnetic and vice versa (It should be noted that the electron distribution in chemical species is often more complex). The paramagnetic specie can undergo a chemical follow-up reaction or a second electron transfer, making it no longer detectable by EPR and consequently requires another method for its detection. The electrochemical process is in essence a black box of which only the constitution of the feed and the product stream can be known in addition to the current or potential response. Electrochemical analysis techniques can give information about the kinetics, mass transfer, the general mechanism and the reversibility.

One would expect that for a thorough investigation of the electron transfer reaction mechanism, the dominant technique would be EPR as it is the only one that can detect radical intermediates directly. In reality other techniques are used because of their ease of application or their accessibility irrespective of the fact that these methods do not result in detailed structural information of the intermediate form (*i.e.* UV-VIS) [31]. This indicates the clear need to draw the attention of electrochemists towards the combined *in-situ* EPR-electrochemical technique by pointing out the advantages and taking away their reservations about the setup. The predominant hesitance, being the lack of commercially available cell and electrode designs and the specific restrictions imposed by EPR on the dimensions, should be removed. This can be accomplished by making setups designs and information on their construction readily available. In that way, scientists unfamiliar with the field can confidently select pre-engineered equipment for mechanistic research of their specific reaction systems. This thesis serves to fill the gap between physical chemists and electrochemists by proposing several setup designs, each with unique properties, leading to effective catalyst/reaction mechanism research.

Chapter 2

Scope and outline

This chapter highlights the goals and objectives of this work, followed by the strategy and outline of this thesis.

2.1 Objectives

The goal of this thesis is to explore the field of combined *in-situ* EPR spectroelectrochemistry and to provide suitable platforms to standardize investigation of electrochemical systems. Related to this, the thesis also aims to gather experimental data of relevant reaction systems. By combining these two tasks, the thesis demonstrates the importance of the combinatorial technique in providing new information to make targeted optimization of electrocatalysts possible. The setups will need to exploit the properties of the investigated case and formed paramagnetic species, complying to the limits that EPR imposes and the subsequent implications for electrochemical response and equipment.

2.2 Strategy

The strategy for reaching the objectives stated above consists of the construction of different setups for EPR spectroelectrochemistry. Commercial flat cells and EPR tubes will be used with custom-made electrodes and a standalone setup with electrodes housed in the cell walls will be designed. A detailed study of their construction will be performed by electrochemical means and subsequent *in-situ* EPR measurements detecting relatively stable radicals formed during electrolysis. These reactions provide advantages to check if a designed setup could be potentially useful for other relevant case studies.

An appropriate setup and reaction conditions will then be selected for two case studies after a thorough electrochemical screening of the system. The first reaction focusses on C-C bond formation by means of the electrochemical aldol condensation of acetone. The second reaction system is the reductive carbon-halogen bond breaking which is also relevant for C-C bond formation or can be used for the addition of functional groups to a molecule.

2.3 Outline

An overview of the content of this dissertation is given here. The general structure can be found schematically in figure 2.1.

Part I consist of the general introduction, scope, outline and, in the next chapter the electrochemical concepts and experimental techniques are explained. A retrospective of the field of *in-situ* EPR spectroelectrochemistry is given together with state-of-the-art.

In part II a detailed description is given for the construction of the different setups that have been designed for this thesis. Chapter 5 presents the general test cases used in this part with the construction of the simplest design currently used for EPR flat cell application. Adjustments have been made to this electrode in order to comply more to the requirement of semi-infinite linear diffusion. This resulted in thin planar electrode constructed with Physical Vapor Deposition (PVD) on a polypropylene substrate. In chapter 6, an Indium Tin Oxide (ITO) electrode has been constructed enabling the electrodeposition of complex and catalytic metallic nanoparticles. Two setups are specially made to fit in an EPR tube in chapter 7. The first one is based on the wire electrode from chapter 5. It is fixated in a polypropylene holder for reproducibility. The second setup is a thin glassy carbon rod electrode that can be moved and taken out of the tube during electrolysis. The sample can then be frozen for low temperature EPR investigations. Chapter 8 describes a channel flow cell with characterized hydrodynamic flow that can be used to derive both kinetic and mass transport parameters in conjunction with detection of radical intermediates.

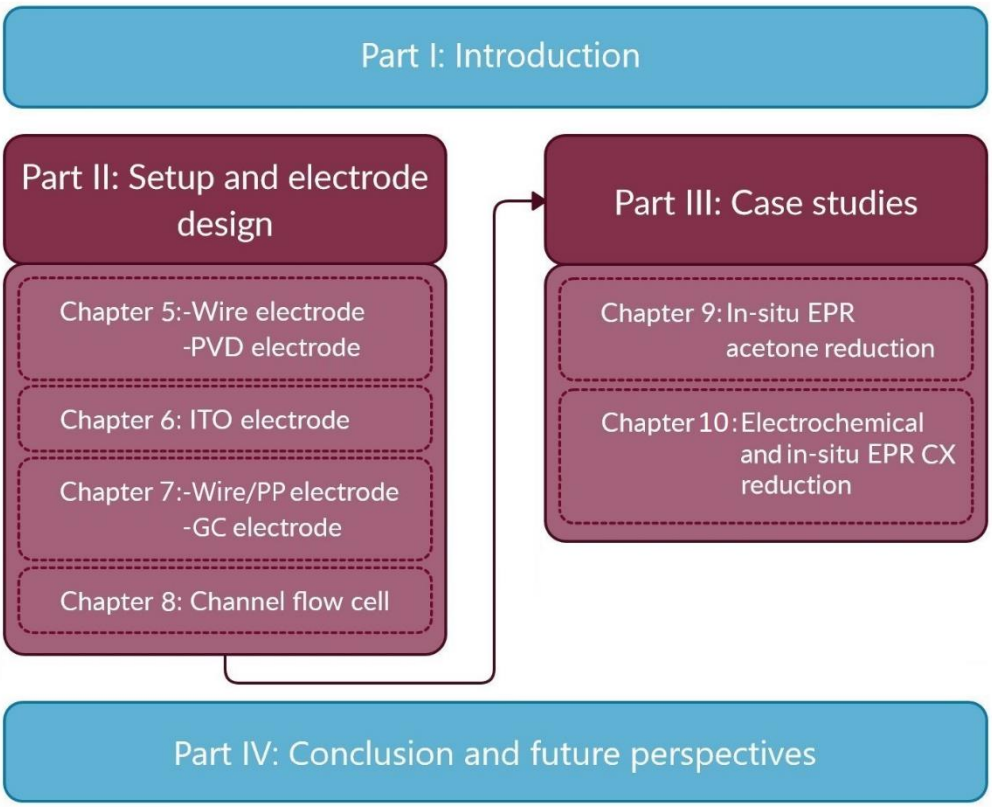

Figure 2.1: *Schematic outline of this thesis.*

In part III, setups from part II have been used for *in-situ* EPR-spectroelectrochemical investigation of some relevant case studies. In chapter 9, the wire electrode has been used for studying the aldol condensation of acetone by electrochemical reduction at different reaction conditions. Indirect detection with spin-trapping is discussed there.

In chapter 10 an electrochemical analysis has been performed of different cathode materials for the carbon-halogen (C-X) bond breaking of aromatic bromides directly attached to the aromatic ring. It serves to provide insight in the electrode reaction mechanism by electrochemical means. Subsequently, some of the cathode-compound systems are selected to be performed directly and indirectly *in-situ* in the EPR with the electrodes from chapter 4 and 5. The goal of this chapter is to couple the conclusions of the electrochemical assessment to those from the EPR measurement to get a complete image of the reaction mechanism supported by experimental proof.

To conclude this doctoral thesis, Part IV formulates the general conclusions of the experimental work in chapter 11. The most important aspects of creating an *in-situ* EPR-spectroelectrochemical setup are summed up and an overview is provided of possible adjustments to the existing setups. Some interesting case studies are listed for future research in the field of combined EPR and electrochemistry.

Chapter 3

Theoretical background

This chapter explains basic electrochemical concepts and their applications followed by a brief introduction of EPR fundamentals.

3.1 Electrochemical concepts

This section serves to acquaint the reader with the basic electrochemical principles and the techniques that are applied in this work. It is based on electrochemical handbooks [32,33] to which the reader is referred for more elaborated reading.

Applications of electrochemistry started off with the definition of the galvanic cell. Two electrodes are connected, allowing one half reaction to release electrons (oxidation) which flow through a connection cable to the other electrode where they are consumed by the other half reaction (reduction). In order to avoid side reactions, the half reactions are separated but electrically coupled. An electric current can only flow when there is a sufficient difference in standard reduction potential between the two half reactions. This difference will also determine the speed of the reaction, together with the concentration of reagents and other thermodynamic properties. In an electrolysis cell, a potentiostat is positioned between the electrodes which can impose a current that does not occur spontaneously. A reference electrode (RE) with stable potential is added to impose a well-controlled potential on the system. This concept is used throughout the thesis with variation of different parameters.

3.1.1 Kinetics and charge transfer

Electrode reactions are defined by the transfer of an electron from the electrode to a molecule or atom in the vicinity of this electrode or vice versa. This molecule should therefore move from the bulk of the solution to the vicinity of the electrode. Once it is close enough to the electrode and in the desired conditions, a charge transfer or electron transfer will occur. A generalized scheme is depicted in figure 3.1. After the charge transfer, possible follow-up reactions take place and subsequentially the product moves to the bulk of the solution. The follow-up reaction can be of chemical nature (protonation, dimerization, …), a second electron transfer or a surface reaction (adsorption, desorption, precipitation, …).

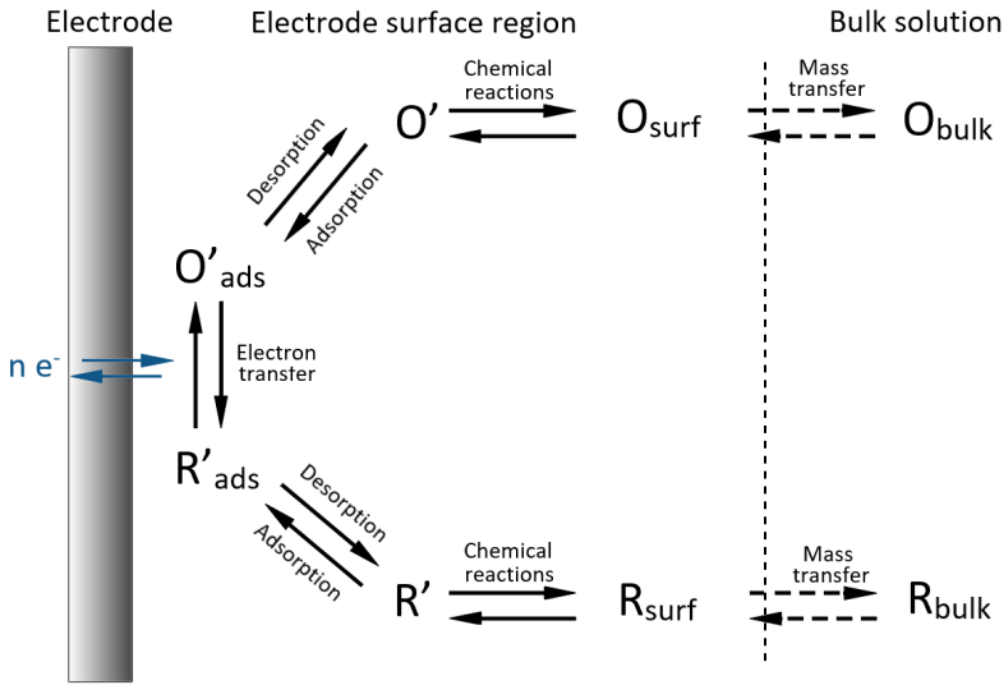

Figure 3.1: *Generalized electrode reaction steps for an electrochemical reaction where O is an oxidant and R is a reductant (adapted from* [33]*).*

Most systems contain a number of these steps which make up the total electrochemical reaction mechanism of a given system. The rate constant of the electrode reaction depends upon the electrode potential and that of the overall reaction on the most sluggish one or more reactions. These are called the Rate-Determining Steps (RDS). The faster reactions are held back by the slower one because the RDS only slowly creates or disposes the other reaction's reagents or products. The electrode subject to investigation is called the working electrode (WE) which is controlled by the potentiostat comparing its potential to that of the RE. The other half reaction occurs at the counter or auxiliary electrode (CE) specifically chosen to not influence the half reaction at the WE.

In order for the electron transfer to occur, there has to be a correspondence in the energies of the electron orbitals where the transfer will take place. For the electrode it is the energy of the conduction band. A transfer to a soluble specie happens when the energy level of the conduction band of the electrode is higher than that of the lowest unoccupied molecular orbital of the specie.

An oxidation on the other hand requires the energy level of the conduction band of the electrode to be lower than that of the highest occupied molecular orbital in the specie. The energy level of the electrode is variable through potential.

Every half reaction is associated with a specific standard redox potential (E^0) indicating to which extent a specie is prone to reduction or oxidation. The potential E of a half reaction at equilibrium can be related to the standard electrode potential through the Nernst equation:

$$E = E^0 - \frac{RT}{nF} \sum_i \nu_i \ln a_i \tag{3.1}$$

where R is the gas constant, T the temperature, n is the number of electrons exchanged for one reagent molecule, F is Faraday's constant, ν_i is the stoichiometric numbers and a_i is the activity. The Nernst equation can be applied when oxidized and reduced species are in equilibrium at the electrode implying a reversible reaction. The rate constant of a reaction is temperature dependent as first recognized by Arrhenius.

$$k = Ae^{E_a/RT} \tag{3.2}$$

This is a prediction of the rate constants at equilibrium (they are nonzero), just as kinetic equations describe. E_a is the activation energy corresponding to the peak when potential energies of a reaction are coupled to the reaction coordinate. A is a frequency factor. The maximum between the two minima (intersection of the 2 potential energy curves) is called the activated complex or transition state.

For a one step process at the electrode-solution interface as:

$$O + ne^- \rightleftarrows R \tag{3.3}$$

with O the oxidant, R the reductant and the rate constants of forward and backward reaction k_f and k_b. The rate of forward and backward reactions at the electrode surface are given by:

$$v_f = k_f C_O(0,t) = \frac{i_c}{nFA} \tag{3.4}$$

$$v_b = k_b C_R(0,t) = \frac{i_a}{nFA} \tag{3.5}$$

and the total rate and current by:

$$v_{net} = v_f - v_b = k_f C_O(0,t) - k_b C_R(0,t) = \frac{i}{nFA} \quad (3.6)$$

$$i = i_c - i_a = nFA\left[k_f C_O(0,t) - k_b C_R(0,t)\right] \quad (3.7)$$

Figure 3.2 shows the potential energy surfaces of reduction reaction 3.3 with $n = 1$. The reference potential being the formal potential $E^{0\prime}$ at which the cathodic and anodic activation energies equal ΔG_{0c}^{+} and ΔG_{0a}^{+}. When the potential is varied to another value E by ΔE, the energy of the electron in the electrode changes and the curve of $O + e^-$ moves a certain amount $-F\Delta E$ or $-F(E - E^{0\prime})$.

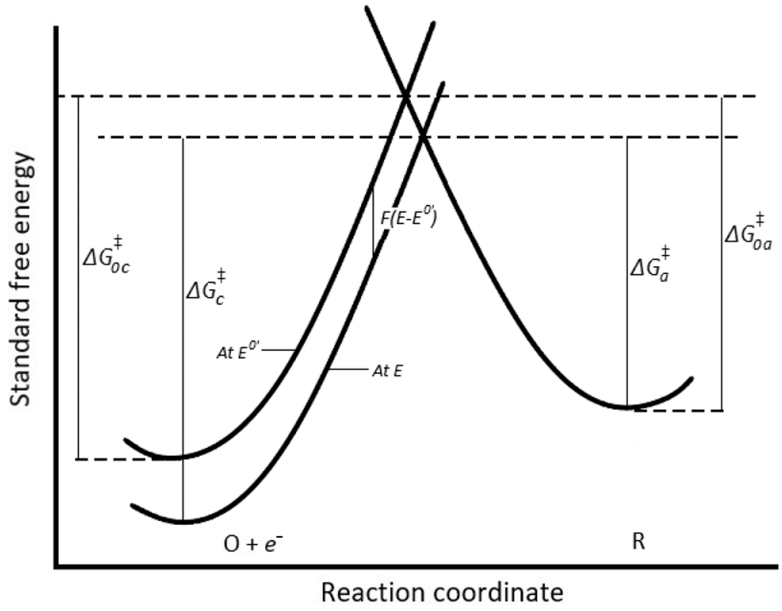

Figure 3.2: *Standard free energies for a reduction reaction with potential variation (redrawn from* [33]*).*

The energy barrier for oxidation will become ΔG_{a}^{+}, being a fraction of the total energy lower than at $E^{0\prime}$. This fraction is $1 - \alpha$, with α being the electron transfer coefficient. It ranges from zero to one, depending on the shape of the intersection of the potential energy curves resulting in:

$$\Delta G_{a}^{+} = \Delta G_{0a}^{+} - (1-\alpha)F(E - E^{0\prime}) \quad (3.8)$$

The cathodic barrier however, is higher at E than at $E^{0'}$:

$$\overset{+}{\Delta G_c} = \overset{+}{\Delta G_{0c}} + \alpha F(E - E^{0'}) \quad (3.9)$$

The introduction of these parameters in the Arrhenius equation consider the interface is at equilibrium with the solution with $C_O^* = C_R^*$, $E = E^{0'}$ and $k_f C_O^* = k_b C_R^*$ so $k_f = k_b$ results in:

$$k_f = k^0 e^{-\alpha f(E-E^{0'})} \quad (3.10)$$

$$k_b = k^0 e^{(1-\alpha) f(E-E^{0'})} \quad (3.11)$$

With k^0 being the standard rate constant ($A_f e^{-\overset{+}{\Delta G_c}/RT} = A_b e^{-\overset{+}{\Delta G_a}/RT} = k^0$) and $f = F/RT$.

If then 3.10 and 3.11 are put into 3.7;

$$i = FAk^0 \left[C_O(0,t) e^{-\alpha f(E-E^{0'})} - C_R(0,t) e^{(1-\alpha) f(E-E^{0'})} \right] \quad (3.12)$$

This relation is known as the Butler-Volmer equation and can be used for the treatment of almost any problem that requires the consideration of heterogeneous kinetics in combination with specific boundary conditions for each experiment. The transfer coefficient α is a measure for the symmetry of the energy barrier of a reaction.

3.1.2 Electrochemical double layer

Electrode reactions are heterogeneous and take place between the solid electrode and the reagent in the electrolyte. The interface between electrode and solution acts as a capacitor on which, depending on the potential, a determined charge will be present at the surface. The region around the electrode consequently has a different charge distribution than the bulk solution phase. When an electrode polarizes, the ions or dipoles in solution will organize themselves around the electrode in order to compensate the electrode charge. All those compensating species make up the electrochemical double layer.

The double layer can be described as an assembly of layers where the one closest to the electrode contains species that are specifically adsorbed. Ions that are solvated cannot approach the electrode as close and consequently, these species experience less potential than those that are specifically adsorbed.

3.1.3 Movement of species in solution

A molecule or reagent can only undergo a charge transfer if it is able to reach the electrode. In an experiment they will have to move from the bulk to the interfacial region. Depending on the nature of the reagent, it will be susceptible to different influences and driving forces for this movement. The first one is diffusion. It is governed by a difference in concentration and depends on the nature of the reagent. Solvated molecules will experience more resistance in their movement and will move at a lower velocity depending on their size and charge. Fick's first law (eq. 3.13) states that the flux by diffusion of a substance is proportional to the concentration gradient:

$$J_O(x,t) = -D_O \frac{\partial C_O(x,t)}{\partial x} \tag{3.13}$$

J_O is the flux of the oxidant with concentration C_O, at a certain position x and time t. D_O is a proportional factor between the flux and the concentration gradient and is called the diffusion coefficient. Fick's second law (eq. 3.14) predicts the concentration change due to diffusion over time:

$$\frac{\partial C_O(x,t)}{\partial t} = D_O \frac{\partial^2 C_O(x,t)}{\partial x^2} \tag{3.14}$$

The second one is migration. Charged species will move under the influence of an electric field towards the oppositely charged electrode. The flux is determined by the charge of the oxidant z_O, the potential gradient $\frac{\partial \phi(x)}{\partial x}$, the diffusion coefficient, the concentration and temperature T.

$$J_O(x) = -\frac{z_O F}{RT} D_O C_O \frac{\partial \phi(x)}{\partial x} \tag{3.15}$$

The last factor potentially influencing the flux of species in solution is convection with $v(x)$ the velocity of a volume element moving along the x-axis.

$$J_O(x) = C_O v(x) \tag{3.16}$$

Combining these three effects results in the Nernst-Planck equation for one-dimensional mass transfer:

$$J_O(x) = -D_O \frac{\partial C_O(x,t)}{\partial x} - \frac{z_O F}{RT} D_O C_O \frac{\partial \phi(x)}{\partial x} + C_O v(x) \qquad (3.17)$$

Applying this equation to electrochemical systems is not so straightforward when all three forms of mass transport are present in the experiment. Therefore, it is simplified by controlling the conditions of an experiment in a way that one or more of the previously named terms of the Nernst-Planck equation become neglectable or easily characterizable. Convection can be excluded by not agitating the solution or it can be taken into account when the flow of analyte to the electrode has a determined velocity profile. By adding an excess of inert supporting electrolyte, the influence of migration of charged analyte species on the total current will be nearly eliminated. In most cases, a salt is chosen with high conductance and mobility lowering the solution resistance and the uncompensated resistance (see section 3.1.4). Lastly, the diffusion itself mostly controls the mass-transport part of an electrochemical problem and will be focused upon in the next section dealing with the consequences of potential step experiments.

Boundary conditions of problems express concentrations of analyte and product as functions of t and x (one-dimensional). The initial condition for a reduction is: $C_O(x,0) = C_O^*$ and $C_R(x,0) = 0$. This means that only one form of the analyte is present in solution at the beginning of the experiment and its concentration at the electrode is equal to that of the bulk of the solution. Semi-infinite boundary conditions describe the concentrations at large distance from the electrode: $\lim_{x\to\infty} C_O(x,t) = C_O^*$ and $\lim_{x\to\infty} C_R(x,t) = 0$ at all t, assuming that the concentration at the cell walls reach a constant value (the initial concentration). Concentrations on the electrode surface when the potential is controlled: $C_O(0,t) = f(E)$ and $\frac{C_O(0,t)}{C_R(0,t)} = f(E)$ with $f(E)$ depending on the kinetics of the reaction when not diffusion controlled.

3.1.4 Cell resistance

All solvents have an inherent resistivity depending on their ability to split into ions that can transport charge through the solution. A supporting electrolyte is added to improve the conductivity of the solution as mentioned in the previous section. A suitable supporting electrolyte dissociates completely in solution to provide the necessary concentration of ions. The resistance of the solution that has to be accounted for in the cell potential depends on the distance between the working and the counter electrode. When a reference electrode is used and the potential is controlled, this resistance will be corrected by the potentiostat. The resistance between working and reference electrode is not accounted for by the potentiostat. Applying a potential to the working electrode will result in a lower effective applied potential if not accounted for in the software or in data processing.

$$E_{eff.\ appl.}\ (vs\ RE) = E_{demanded} - iR_s \tag{3.18}$$

This resistance is also dependent on the distance between the electrodes so positioning of the reference electrode close to the working electrode is critical but will never totally resolve this issue. To correct for this deviation, the resistance should be determined. Several methods are at hand but in this thesis, only Electrochemical Impedance Spectroscopy (EIS) was used which is briefly explained in section 3.2.4. The potential can then be partially compensated during the measurement (and the residual part corrected afterwards) or a post experiment correction can be done. This method is only accurate when the ohmic resistance does not change during the experiment.

3.2 Electrochemical techniques

There are several techniques utilizing the basic concepts explained in section 3.1 to derive intrinsic parameters of a reaction/electrode system. The ones mentioned here are those that have been used in this work. Depending on the frequency of use, some are explained more in detail. The potential was kept constant or was varied with time and current was recorded as function of time or potential.

3.2.1 Chronoamperometry

Considering the reaction in Eq. 3.3 at two different potentials; E_1 being a potential where the reaction does not occur and, E_2 a potential where the reaction does occur so fast that no oxidant can be in the vicinity of the electrode without being reduced. Performing a potential step experiment in an unstirred solution, varying the potential from E_1 to E_2 while recording the current over time will result in a concentration gradient depending on the time and the distance from the electrode surface. The layer where the concentration gradient arises is called the diffusion layer.

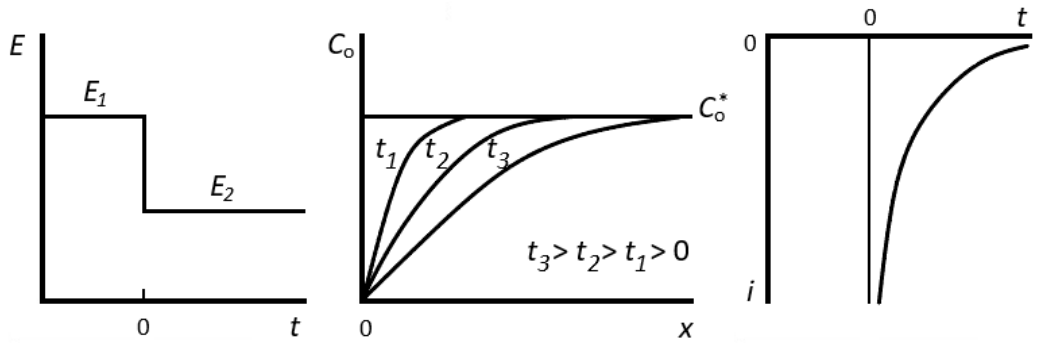

Figure 3.3: *Left: Step function of potential from E_1 to E_2 with the oxidant starting to be reduced from t = 0 at diffusion-limited rate. Middle: Concentration profiles at different times in the electrolysis. Right: current transient during the experiment (redrawn from* [33]*).*

The oxidant concentration in this layer varies from zero to the bulk concentration and expands over time. The current will consist of a capacitive current, due to the charging of the electrochemical double layer and a faradaic current due to the electron transfer. It will be very negative at first to reduce the oxidant at the electrode and approach a value closer to zero if the cell volume is considered large compared to the electrode surface area (figure 3.3). The current will thus be diffusion controlled and for a planar, uniformly accessible electrode it is called semi-infinite linear diffusion. The expression for the current is:

$$I = nFAD\left(\frac{\partial c}{\partial x}\right)_0 \tag{3.19}$$

With x being the distance from the electrode. Fick's second law of diffusion can be used to solve eq. 3.19 resulting in an expression for the diffusion-limited current for this specific electrode geometry:

$$I(t) = \frac{nFA\sqrt{D_O}C_O^*}{\sqrt{\pi t}} \tag{3.20}$$

which is known as the Cottrell equation. Longer timescale experiments will be influenced by vibrations that cause convective disruption of the diffusion layer.

In this thesis, when chronoamperometry is applied for electrolysis of a reagent, the solution is stirred when possible, to avoid the formation of a thick diffusion layer and consequential current drop. When the electrode surface over cell volume ratio is high enough, and kinetics are fast enough, the conversion of reagent can be maximized over a short period of time. Conversions X_R were determined by comparing t = 0 sample reagent concentrations (oxidant) with that of the products (reductant) at the end of the experiment by:

$$X_R = \frac{C_R(t)}{C_O(t=0)} \tag{3.21}$$

The total charge passed through the solution during the chronoamperometric experiment was used to calculate the theoretical amount of consumed reagent with Faraday's law:

$$n_{theoretical} = \frac{It}{zF} = \frac{Q}{zF} \tag{3.22}$$

With Q being the total charge passed and z the number of electrons passed per oxidant molecule. The Faradaic Efficiency (FE) was calculated by using $C_R(t)$ with eq. 3.22:

$$FE(\%) = \frac{n_R(t)}{n_{theoretical}} \tag{3.23}$$

3.2.2 Linear Scan Voltammetry

When performing Linear Scan Voltammetry (LSV), the potential is varied with time and current is recorded (figure 3.4). Starting at a potential where reaction 3.3 does not occur E_i and moving towards its E_{red}, first results in a reduction with the electrode reaction being the RDS. While the potential is changed, the electrode reaction will become faster, depleting the oxidant at the electrode surface and eventually mass transfer will become the RDS. At this point, the current will drop because the diffusion layer has formed. The technique is mostly used as a stationary one with the potential scan rate being in the range where the concentration of oxidant at the electrode will be the bulk concentration. The scan rate would be so slow that the timescale of the experiment would become undesirably long, therefore the technique is mostly combined with forced convection to supply of oxidant to the electrode in a controlled manner.

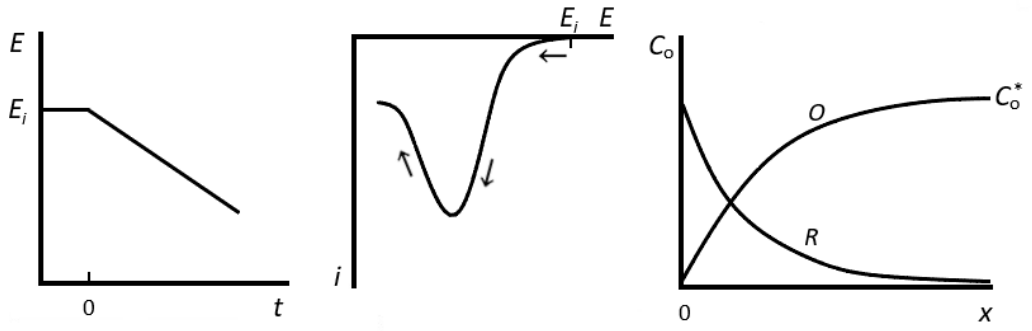

Figure 3.4: *Left: Linear potential sweep starting at E_i. Middle: resulting i-E curve. Right: Concentration profile of reductant (R) and oxidant (O) for potentials beyond the peak potential (redrawn from* [33]*).*

Several configurations are suitable to obtain a controlled flow pattern towards the working electrode. The most widely used hydrodynamic method is the Rotating Disc Electrode (RDE). It consists of a conductive rod embedded in the middle of a plastic insulator. In practice, the electrode body is cylindrical with only the intersection of the rod (disc) being exposed to the solution and the plastic surface around the disc being significantly larger than the disc. The electrode is rotated around the axis of the rod at an angular velocity of:

$$\omega = 2\pi f \tag{3.24}$$

Assuming there are no edge effects of the electrochemical cell, the spinning disc drags the fluid at the surface resulting in a centrifugal force, moving the solution in the boundary layer outward. As a consequence, solution will move perpendicular towards the surface of the electrode (figure 3.5). Imposing a potential in the limited current region where the surface concentration of oxidant goes to zero (mass transport controlled) results in a current transient which will not decay to zero (like in a chronoamperometric experiment without convection). The current will reach a constant value depending on the angular velocity which can be calculated with the Levich Equation:

$$i_{l,c} = 0.62nFAD_O^{3/2}\omega^{1/2}\nu^{-1/6}C_O^* \tag{3.25}$$

Where n is the number of electrons exchanged per molecule of oxidant and ν is the kinematic viscosity.

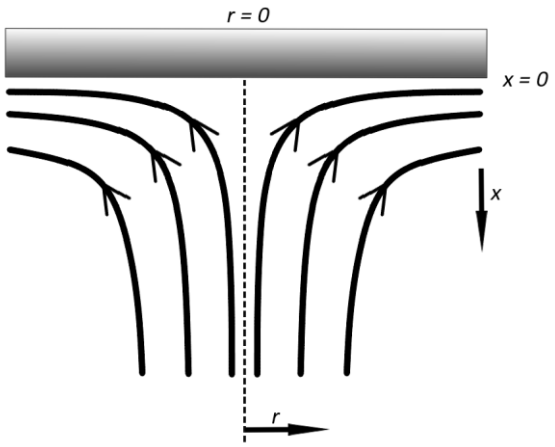

Figure 3.5: *Schematic flow pattern over a rotating disc electrode.*

Combining LSV with RDE over a potential range including regions of only mass transport limitation and only kinetic control results in current-potential curves like those shown in figure 3.6. The potential scan is done from right to left at different rotation speeds. At first, the current transients overlap, indicating that the current is kinetically controlled with the reaction rate being potential dependent.

Afterwards they diverge when mass transport and kinetics are similar in magnitude to result in a steady-state current which is totally mass-transport governed. As indicated in figure 3.6, these LSVs can be sampled at different potentials to study the process of interest. The current at E_1 obeys the Levich equation while at E_2 and E_3 a kinetic component should be added to calculate the total current:

$$\frac{1}{i} = \frac{1}{i_K} + \frac{1}{i_{l,c}} = \frac{1}{FAk_f(E)C_O^*} + \frac{1}{0.62nFAD_O^{3/2}\omega^{1/2}\nu^{-1/6}C_O^*} \quad (3.26)$$

This is the Koutecky-Levich equation with i_K the current in absence of mass-transport effects (surface concentration of oxidant equal to the bulk concentration) and $k_f(E)$ the potential dependent kinetic parameter. Practically $\frac{1}{i_K}$ is the intersection of the extrapolated data with the y-axis in a $\frac{1}{i}$ vs $\omega^{-1/2}$ plot.

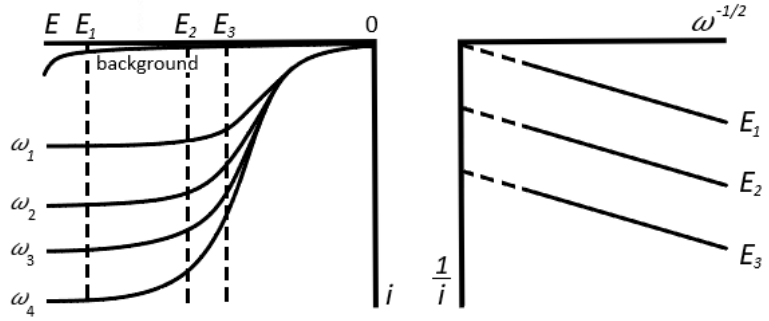

Figure 3.6: *Left: Current-potential curves of an LSV RDE experiment with different angular velocities. Right: Koutecky-Levich plots at different potentials.*

Other hydrodynamic methods consist mostly of tubular, wall-jet and channel electrodes. They impose different boundary conditions on the expression for the limiting current. A channel electrode consists of a rectangular channel with height $2h$, width d and length l.

If the working electrode is positioned at sufficient distance from the channel entrance and from the channel edge, Poiseuille flow will develop for determined flow speeds and following equation is valid to calculate the mass-transport limited current:

$$I_{l,c} = 0.925nFC_O^* \omega x_e^{2/3} D_O^{2/3} \left(\frac{V_F}{h^2 d}\right)^{1/3} \quad (3.27)$$

With ω and x_e respectively the width and length of the working electrode.

Besides the determination of $k_f(E)$ and D_O, α and the exchange current i_0 can be determined from the kinetically controlled section of the LSV by plotting the logarithm of the current vs the overpotential (η) of the investigated reaction in a Tafel plot (figure 3.7). The exchange current represents the cathodic or anodic current passed by the system at equilibrium potential ($\eta = 0$) and is often substituted by k^0 with:

$$i_0 = FAk^0C \quad (3.28)$$

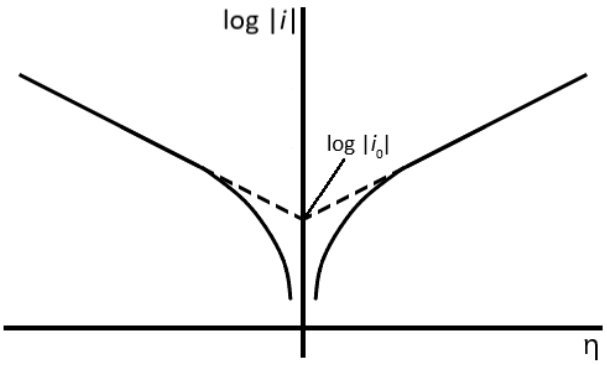

Figure 3.7: *Tafel plots for anodic and cathodic branches of reaction 3.3 with α = 0.5.*

In practice i_0 is determined by extrapolation of the linear regions to intercept with the y-axis. The electron transfer coefficient can be calculated from the slope of the anodic and cathodic linear regions for which the equation is derived from the Butler-Volmer equation:

$$slope_a = \frac{(1-\alpha)nF}{2.3RT} \qquad slope_c = \frac{-\alpha nF}{2.3RT} \quad (3.29)$$

3.2.3 Cyclic voltammetry

Cyclic Voltammetry (CV) is equivalent to the previously described LSV with the difference of it being a reversal technique. Where LSV stops at an end potential with the potential variation being one-way, the potential in a CV is reversed towards the initial potential resulting in the oxidation of the reduced product from the initial scan direction. Figure 3.8 shows the potential sweep and the resulting CV of such experiment. The form of the i-E curve of the reversed scan is similar (changed direction) to that of the initial one because the concentration of species at the electrode is reversed with mostly reductant present. This technique is often used for initial characterization of new systems at scan speeds that do not allow reaching equilibrium at the electrode.

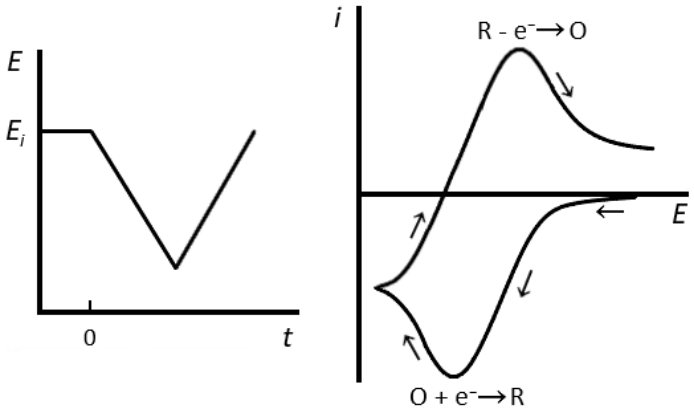

Figure 3.8: *Left: cyclic potential variation. Right: Cyclic voltammogram.*

The current is a sum of faradaic and capacitive currents with the latter not being neglectable. This capacitive current is proportional to the scan rate:

$$|i_c| = AC_d v \tag{3.30}$$

With C_d the capacitance of the double layer and v the scan rate. The peak current i_p is proportional to $v^{1/2}$ when it is controlled by linear diffusion.

Peak currents for reversible and irreversible systems at 25°C are given by eq. 3.31 and eq. 3.32 respectively:

$$i_p = (2.69 \times 10^5)\, n^{3/2} A D_O^{1/2} C_O^* v^{1/2} \quad (3.31)$$

$$i_p = (2.99 \times 10^5)\, \alpha^{1/2} A D_O^{1/2} C_O^* v^{1/2} \quad (3.32)$$

With the condition of semi-infinite linear diffusion and $n = 1$ for the irreversible case. The choice of v will have to be balanced with C_O^* to avoid deformation of the wave by i_c.

Beside the peak current, the peak potential (E_p) of the investigated process can be determined, giving information of the activation energy needed. The peak shape indicates the nature of the process occurring at the applied potential. The shape can be quantified as the difference between the peak potential and the potential at half height of the peak ($E_{p/2}$):

$$\left|E_p - E_{p/2}\right| = 2.20 \frac{RT}{nF} = \frac{56.5}{n} mV \quad (3.33)$$

$$\left|E_p - E_{p/2}\right| = \frac{1.857RT}{n\alpha F} = \frac{47.7}{n\alpha} mV \quad (3.34)$$

For reversible and irreversible systems respectively. Equation 3.34 and 3.35 will be used in chapter 10 for the determination of α as a measure for the reaction mechanism of carbon-halogen bond (C-X bond) breaking.

$$\frac{\partial E_p}{\partial \log v} = -1.151 \frac{RT}{n\alpha F} = \frac{29.6}{n\alpha} mV \quad (3.35)$$

3.2.4 Electrochemical Impedance Spectroscopy

Electrochemical impedance spectroscopy is a technique based on a small sinusoidal perturbation of the electrochemical system at a variable frequency. The concept is only briefly mentioned here for introductory purposes. The reader is referred to one of the reference works in the field for a more detailed reading on the subject [34].

Here, the perturbation of the system as a variation of potential is:

$$e = E \sin \omega t \tag{3.36}$$

The current response will then be:

$$i = I \sin\ (\omega t + \phi) \tag{3.37}$$

With ϕ being the phase angle between potential and current. An electrochemical system can be modelled by an equivalent electrical system to calculate the impedance of the electrochemical phenomena.

For a resistor, with impedance $Z_R = R$, the application of a sinusoidal voltage results in $i = \frac{E}{R} \sin\ \omega t$ by Ohm's law without any change in phase angle. For a pure capacitor with impedance $Z_C = \frac{1}{j\omega C}$:

$$i = \omega C E \cos\ (\omega t) \tag{3.38}$$

A non-ideal or leaky capacitor is called a Constant Phase Element (CPE) which has an impedance of $Z_{CPE} = \frac{1}{Y_0 (j\omega)^N}$. When $N = 1$, it behaves as a capacitor and when $N = 0$, it behaves as a pure resistor. This behavior is physically caused by surface roughness, distribution of reaction rates, varying thickness and conductivity or composition of an electrode surface layer, etc.. A circuit element used to describe semi-infinite linear diffusion is the Warburg element. It is actually a CPE with $N = 0.5$ resulting in a constant phase of 45° and impedance of $Z_W = \frac{1}{Y_0 \sqrt{j\omega}}$.

Combining these elements allows to fit experimental data with an equivalent circuit in a Nyquist plot as shown in figure 3.9. The imaginary impedance is plotted versus the real impedance with changing frequency. Fast processes will respond to high-frequency perturbations and slow ones to low-frequency perturbations. The first purely resistive intercept in the high frequency domain R_Ω can be attributed to the solvent resistance of the cell. At these high frequencies, the contribution of the capacitor goes to zero. With dropping frequency, it starts contributing to the impedance, resulting in a complex impedance and forming a semicircle.

The other intercept of the semicircle with the x-axis depends on the magnitude of the charge transfer resistance R_{ct}. The semicircle should usually be extrapolated to find this intercept because in this frequency region, the process is under mixed kinetic and mass transfer control. At lower frequencies, the impedance of C_d will grow so no current will flow through that branch and the impedance is defined by the other branch.

This technique will be used in chapter 6 to compare the resistance of different electrode materials and assess their potential for use in electrochemical EPR applications and to determine the uncompensated resistance of the setup in chapter 10.

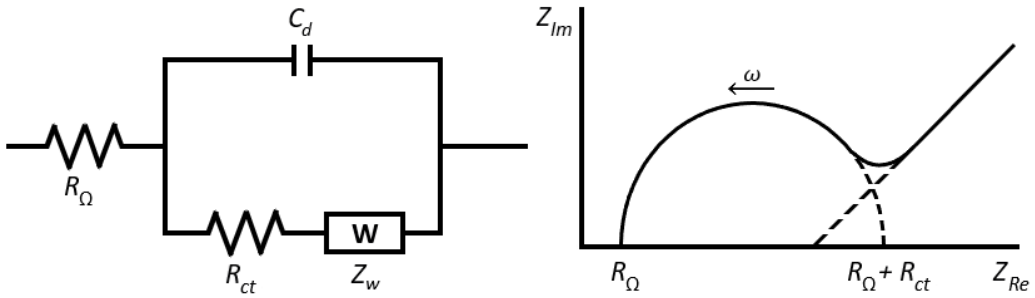

Figure 3.9: *Schematic Randles equivalent circuit of an electrochemical system (left), Nyquist plot of that system in the complex plain (right).*

3.3 Electron Paramagnetic Resonance

Electron Paramagnetic resonance (EPR) is a spectroscopic technique used to study species containing unpaired electrons. Although there are more compounds without unpaired electrons (diamagnetic) than with unpaired electrons (paramagnetic), they are usually of particular interest. Examples of these systems are: organic radicals in solution, organic radicals in solids, transition metal ions and complexes, photoexcited molecules and biological samples. The unpaired electron of the compound interacts with an applied magnetic field which is exploited to derive its structure. In this section, the basic principles of the technique will be discussed based on references [35–42]. The reader is referred to these references for a more profound explanation and more complex applications of the technique.

3.3.1 Principles

Electrons can be characterized by a mechanical angular momentum which is called 'spin'. It is a vector property characterized by a magnitude and an orientation in space. The spin vector $\boldsymbol{S}$ has a magnitude of:

$$|\boldsymbol{S}| = \hbar\sqrt{S(S+1)} \tag{3.39}$$

with S being the electron spin quantum number and $\hbar$ the reduced Planck constant $\hbar = h/2\pi$ as unit ($h = 6.626 \text{ x } 10^{-34}\, Js$). There are $2S+1$ projections allowed onto an axis, which is chosen in the z-direction, coinciding with the direction of an external applied magnetic field $\boldsymbol{B}$. The allowed orientations of the spin angular moment with the z-axis are given by m_s with $2S+1$ possible values and S being an integer or half integer between $+S$ and $-S$. For an electron, $S = 1/2$ so two spin states are possible; $m_s = +1/2$ the spin-up state and $m_s = -1/2$ the spin-down state. The magnitude of the spin vector of an electron will be: $|\boldsymbol{S}| = \sqrt{3/4}\,\hbar$. In an electron pair, each individual electron will have an opposite spin.

Figure 3.10: *Spinning electron with magnetic moment through its center.*

Considering that an electron with charge e and mass m_e (figure 3.10) which rotates with a spin angular momentum $\boldsymbol{S}$ will produce a circulating current, this current will generate a magnetic dipole momentum μ with:

$$\mu = g_e \gamma_e \boldsymbol{S}\hbar = g\mu_B \boldsymbol{S} \tag{3.40}$$

γ_e being the gyromagnetic ratio of the electron with $\gamma_e = -e/2m_e$, $e = 1.6022$ x 10^{-19} C the electron charge and $m_e = 9.1096$ x 10^{-28} g the mass of the electron. g_e is the electron g-factor with a value of -2.002319304361 for a free electron [39] . It is a correction factor for the magnetic moment of the quantum electron. In the absence of a magnetic field, an unpaired electron will switch between the two spin states as they have identical energy. Application of a magnetic field results in an energy difference between the energies of the spin states. The spin-down state will be the one with the lowest energy level. This is called the Zeeman effect and is schematically shown in figure 3.11. The energy difference is quantified by:

$$\Delta E = g\mu_B B_0 \tag{3.41}$$

with $\mu_B = \hbar e/2m_e$ the Bohr magneton, the unit for an electron's magnetic moment and ΔE is proportional to B_0, the applied magnetic field. The energy is supplied by electromagnetic radiation, quantified as the product of frequency v and h:

$$\Delta E = hv \tag{3.42}$$

When the resonance condition is met at a given ΔE and B_0, this energy quantum induces the transition from spin-down to spin-up state.

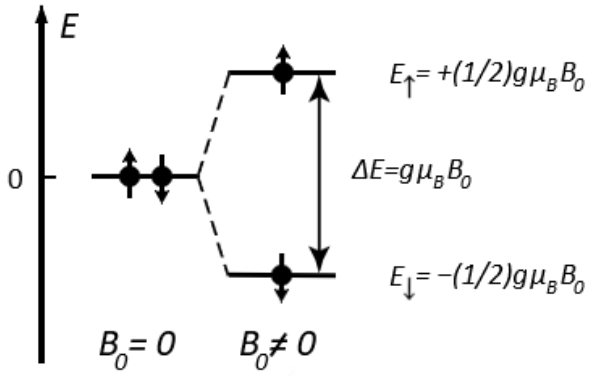

Figure 3.11: *Schematic representation of the electron Zeeman effect. At zero field the two spin states have the same energy. In the presence of a magnetic field, the spin states have different energy determined by the applied magnetic field (Redrawn from* [36]*).*

The field experienced by the electron in a molecule will differ from B_0 because of the influence of the chemical environment on the electron which gives a local effect on the field B_{local} resulting in the effectively applied field and because of spin-orbit coupling:

$$B_{eff} = B_0 + B_{local} \tag{3.43}$$

B_0 is easier to obtain than the local or effectively applied field so g_e is corrected with the effective g-factor characteristic for the unpaired electron in a specific molecule (as used in eq. 3.41). The g-factor is an important value for identification of paramagnetic species.

Besides the electron spin, nuclei can also have a magnetic spin ($\boldsymbol{I}$) complicating the spectrum and providing information about local interactions. There are $2I + 1$ possible states with I an integer between $-I$ and $+I$. The interaction of the nuclear spin with the applied field splits up the spectrum in multiple lines and is called the nuclear Zeeman splitting. The nuclear magnetic moment can be expressed as:

$$\mu_N = g_N \gamma_N \boldsymbol{I} \hbar \tag{3.44}$$

with g_N the effective nuclear g-factor, $\gamma_N = e/2m_p$ the nuclear gyromagnetic ratio and m_p the mass of a proton $m_p = 1.6726 \times 10^{-24}$ g [43].

The resulting interaction between the electron and nuclear magnetic moments is known as the hyperfine interaction. The electron spin energies will then become:

$$E = g_e \mu_B B_0 m_s - g_N \mu_N B_0 m_I + a m_s m_I \tag{3.45}$$

The first term is the electron Zeeman splitting, the second the nuclear Zeeman splitting and the third the hyperfine interaction. a is called the hyperfine coupling constant. This effect will create a deviation of the nuclear Zeeman energy levels which can be higher or lower. In Continuous Wave (CW) EPR, the transitions with the highest probability are those where the spin state of the electron changes but the nuclear spin state remains the same; $\Delta m_s = \pm 1$ and $\Delta m_I = 0$. Every nuclear spin state will then be represented by a separate transition.

In figure 3.12 (left), the unpaired electron interacts with a nucleus with $I = 1/2$ like ^{1}H. The hyperfine coupling constant is the separation between the two lines. If a ^{14}N nucleus with $I = 1$ would be interacting with an electron, the signal would split in three lines. The energy level of these states are:

$$E = m_s(-g_e \gamma_e \hbar B_0 + a m_I) \tag{3.46}$$

For two nuclei with $I = 1/2$ would become:

$$E = m_s(-g_e \gamma_e \hbar B_0 + a_1 m_{I1} + a_2 m_{I2}) \tag{3.47}$$

With a_1 and a_2 the coupling constants of the nuclei, m_{I1} and m_{I2} are their nuclear spin quantum numbers. The spectrum would show four lines of equal intensity being referred at as a 'doublet of doublets'. The nuclei can be considered equivalent when $a_1 = a_2$ which makes the energy levels of two transitions coincide resulting in a three line spectrum with the central one having a twofold intensity compared to the outer two lines as illustrated in figure 3.12. A number of n equivalent nuclei result in $2nI + 1$ equidistant lines in an EPR spectrum.

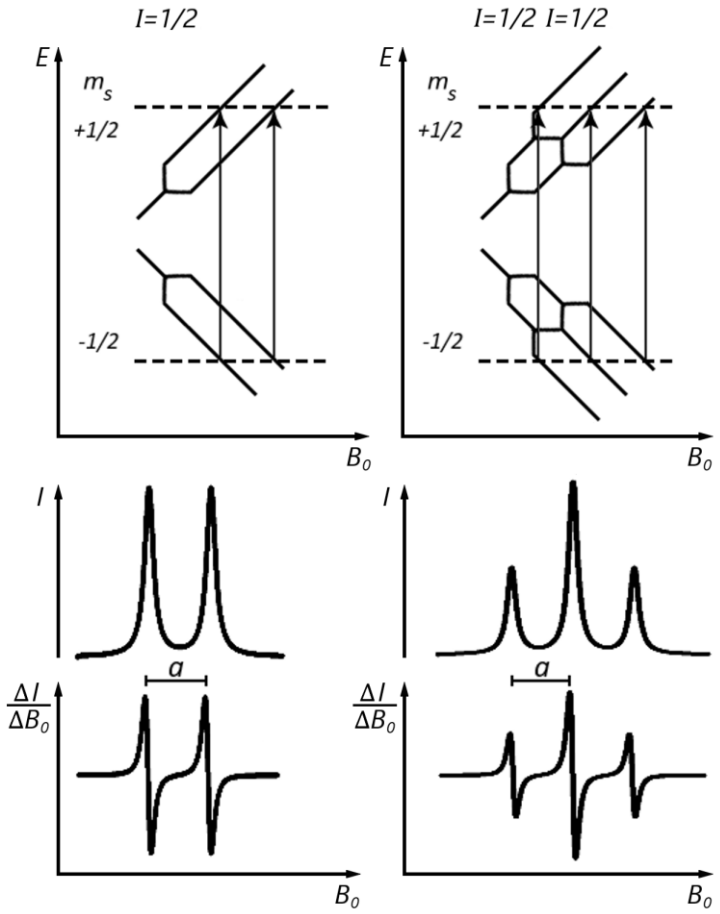

Figure 3.12: *Example of EPR spectra with signal splitting by hyperfine interaction between an unpaired electron and a nucleus with $I = 1/2$ (left) and 2 equivalent nuclei with $I = 1/2$ (right).*

Up until now, the g-factor and hyperfine coupling interactions have been isotropic scalar quantities. In reality they can be anisotropic tensors, mathematically represented by a 3 x 3 matrix. In a non-viscous solution the rapid tumbling of the molecules with multiple possible positions of the spin vector, averages the positions to one isotropic value. In systems where there is restricted movement such as viscous solutions, solids or crystals, the anisotropy can be observed which can provide more geometric information on the structure of the paramagnetic species but also greatly complicates the spectrum.

3.3.2 Spectrometer

CW EPR uses a continuous source of microwave radiation of a fixed frequency on the sample to induce spin transitions. The absorption is recorded while the magnetic field is varied. Figure 3.13 shows the components of a conventional X-band spectrometer schematically. The microwave source produces microwaves that travel through hollow rectangular waveguides. The intensity is reduced in an attenuator before entering a circulator which forces the microwaves downwards to the resonator or cavity. The iris at the entrance of the cavity regulates the amount of radiation reflected back out of the cavity. The reflected radiation goes back to the circulator where it is guided to the detector diode to measure its intensity. The radiation which the detector reflects, is sent back to the circulator where it is forced upward and is converted to heat. The circulator ensures that only reflected radiation from the cavity reaches the detector. Before the signal attenuator, part of the radiation is coupled to the reference arm. There it also passes an attenuator to control the power and a phase shifter to control the relative phase between the signal and reference arm.

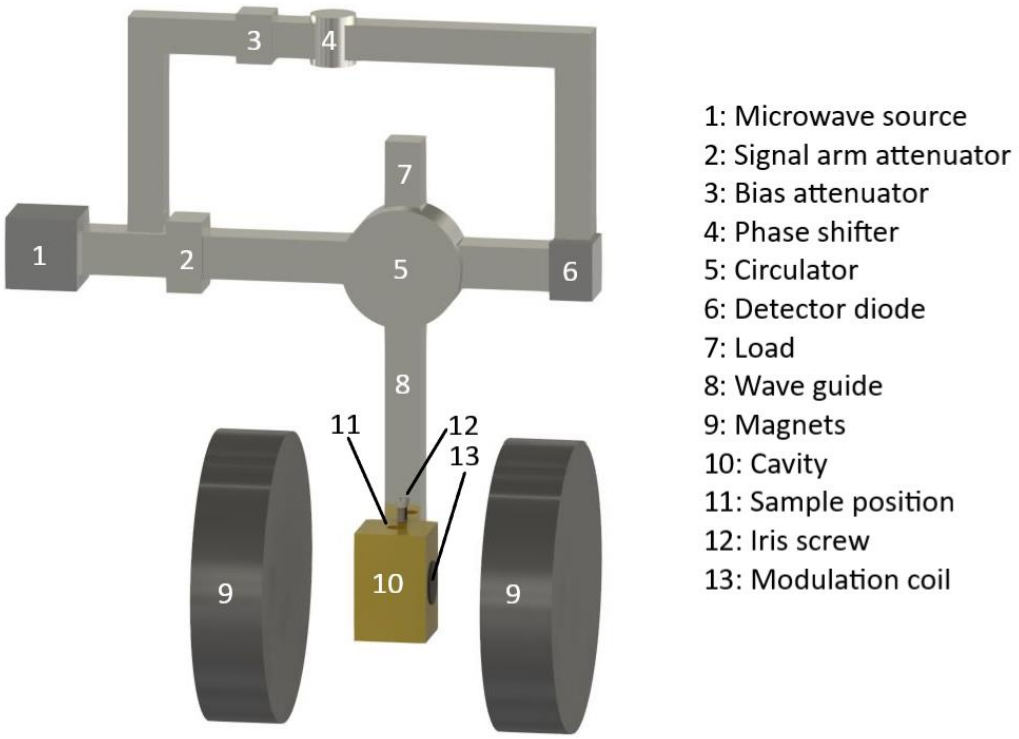

Figure 3.13: *Schematic drawing of an X-band spectrometer.*

The cavity has to be tuned with the iris in order to obtain a standing microwave at its resonance frequency such that all the microwaves are contained in the cavity and none are reflected back to the detector (figure 3.14). It also serves to enhance the microwave magnetic field at the sample to induce EPR transitions. The efficiency of a cavity in storing the microwave energy is presented by the Q-factor and is a measure for the cavity's sensitivity. It is defined as:

$$Q = \frac{2\pi(energy\ stored)}{energy\ dissipated} = \frac{v_{res}}{\Delta v} \tag{3.48}$$

The standing wave in the cavity has its magnetic component B_1 and electric component E_1 exactly out of phase; where the magnetic field is at its maximum, the electric field is at its minimum. These are spacially distributed in the cavity as shown in figure 3.15 for a rectangular TE_{102} cavity. To avoid non-resonant absorption of microwaves through the electric field component and corresponding degraded Q-factor, the sample is positioned in the magnetic field maximum. This is most important when using solvents with high dielectric constants, such as water, which strongly interact with E_1.

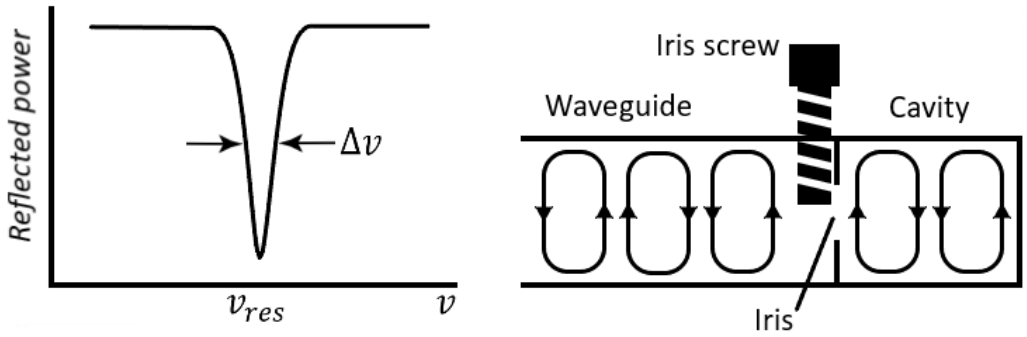

Figure 3.14: *The resonator Q-factor definition with v_{res} the resonance frequency of the cavity and Δv the bandwidth (left). Schematic visualization of the iris moving up and down to critically couple the cavity.*

The magnetic field is applied through two electromagnets which are water cooled. They are positioned left and right of the cavity and act as north and south pole. In addition to this main magnetic field, a modulation field is applied by coils mounted on the cavity.

The main field is slowly swept across a region of interest and the modulation field is applied with usually a frequency of 100 kHz. This results in an oscillating EPR signal with the change in amplitude of the oscillating signal being proportional to the change in amplitude of the absorption line between $B_0 - B_{mod}$ and $B_0 + B_{mod}$. This kind of detection gives a first-derivative-like line shape (figure 3.12 bottom). A consequence of the field-modulation detection is that the line shape and the signal amplitude depend on the magnitude of the modulation field. The signal amplitude is related to the square root of the microwave power at low power levels. The ratio of population of the different spin states is given by the Boltzmann factor $n_{spin\ up}/n_{spin\ down} = e^{-\Delta E/kT}$ with $k = 1.380662 \times 10^{-23}$ J K^{-1} the Boltzmann constant at equilibrium. Usage of higher power can lead to saturation of the spin system. Saturation happens when the populations of the electron Zeeman states become equal due to insufficient relaxation of excited spins. The signal will be weak and possibly lineshape distortions occur. Therefore measurements should be conducted in the region where the signal amplitude varies linearly with the square root of the microwave power.

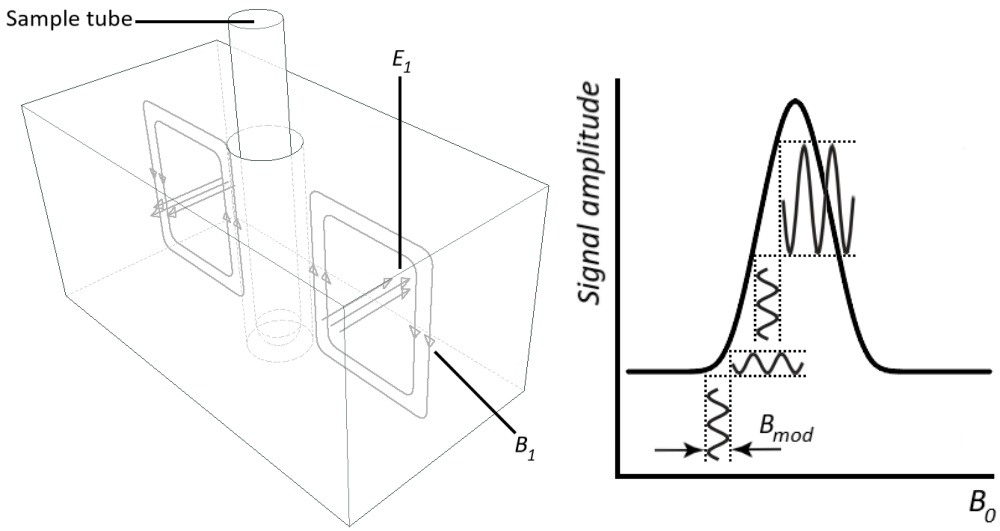

***Figure 3.15**: Magnetic and electric field orientation of the microwaves in a TE_{102} rectangular cavity (left). Absorption line with modulated signal on different positions on the line (right).*

Chapter 4

Retrospective of *In-situ* EPR spectroelectrochemistry and state-of-the-art

This chapter provides a historical overview of the advances in combined EPR spectroelectrochemistry from its first conception to the state-of-the-art.

Part of this chapter is in preparation to be published as: S. den Hartog, S. Neukermans, M. Samanipour, H.Y.V. Ching, S. Van Doorslaer, T. Breugelmans, A. Hubin, J. Ustarroz, Critical review of recent advances in EPR spectroelectrochemistry, *Electrochimica Acta*,(2021), to be submitted

4.1 Early stages and development

Combining electrochemical generation of radicals with EPR spectroscopy was first established by Ingram *et al*. in 1958 for *ex-situ* generated aromatic radicals which were measured at low temperature by taking aliquots and subsequent freezing [44]. Simultaneous Electrochemical and Electron Spin Resonance (SEESR), comprising of *in-situ* generation of paramagnetic species in solution, was first exploited around 1960 by Geske and Maki [45–47]. This simultaneous approach allowed for the detection of shorter-living radicals. In their first publication a two-electrode system was used. The working electrode was a Pt wire in a 3 mm outer diameter capillary which was positioned in the center of the cylindrical cavity. The counter electrode was separated from the working electrode compartment through two sintered glass disc to avoid counter electrode reaction radicals to be detected. A solution of $LiClO_4$ in acetonitrile (ACN) was electro-oxidized resulting in a four line spectrum linked to a radical species with a single chlorine nucleus ($I = 3/2$). In the two other publications, reduction of nitrobenzene in ACN and several semiquinones in ACN and dimethylsulfoxide (DMSO) was accomplished by using a Hg working electrode placed in the center of the resonator (figure 4.1 A) with Pt wire counter electrode (B) positioned below while the reference electrode sat in a reservoir on top (C). Ohmic resistance resulting from such positioning reached thousands of ohms which is undesirable.

In 1962, the Adams group published the use of an aqueous sample flat cell manipulated for electrochemical measurements (Figure 4.1) [48]. The commercially available WG-810-Q Suprasil Electrolytic Assembly of Wilmad is very similar to this setup indicating its continued importance [49]. Adams and co-workers were able to put a Hg pool electrode in the flat part measuring 0.5 mm in width for performing reductions (D) and made a Pt gauze electrode for oxidations (E).

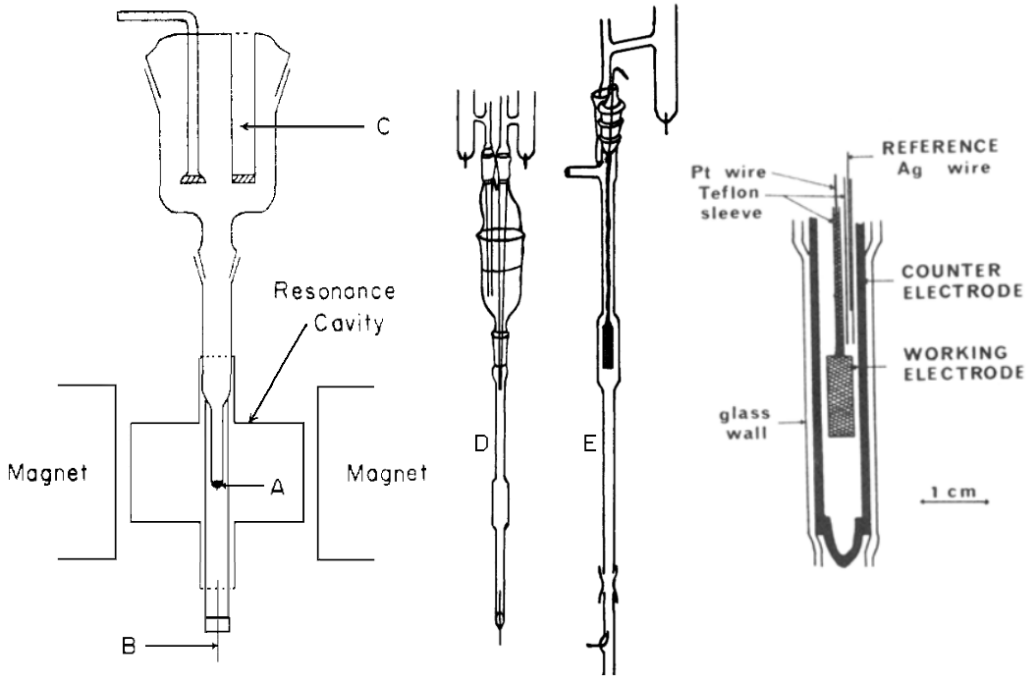

Figure 4.1: *Spectro-electrochemical tube cell used by Geske and Maki* [46] *(left), flat cell assembly used by the Adams group* [48] *(middle) and flat part zoom-in of electrode positioning by Goldberg and Bard* [50] *(right).*

The gauze provides a high surface area for radical production of sufficiently high concentration. The counter and reference electrodes were positioned in similar fashion as the setup of Geske and Maki. They studied radical cations of aromatic amines and diamides and radical anions of aromatic and aliphatic nitro compounds. Some of the drawbacks of the setup are; the irreproducible natural convection [51], the high electrical resistance and uneven polarization of the working electrode entailed by the small dimensions and large distances between electrodes and the fact that specific boundary conditions required for analytical voltammetry were not met.

The setup was adapted in 1971 by Goldberg and Bard [50] who positioned all three electrodes in the flat part of the cell (figure 4.1 right) solving most of the resistance issues inherently present in the use of narrow channels [52] and utilizing electrolyte flow. In order to fit in, the reference was a Ag wire pseudo reference passed through a Teflon tube with the edge of the Ag 3-5 mm above the end of the Teflon.

The tungsten rods as counter electrode were spaced out to the edge of the flat part with a U-shaped rod at the bottom of the cell. However, positioning of the counter electrode this way could result in the detection of undesired counter reaction radicals, complicating the spectrum [53,54]. Even when the counter electrode was placed in the bulk section of the flat cell these counter reaction radicals were able to diffuse into the flat part. They investigated reductions of anthraquinone, azobenzene and nitrobenzene and reductive dimerization rate constants of diethylfumarate, dimethylfumarate, cinnamonitrile and fumaronitrile in dimethylformamide (DMF) by rapid EPR data collection after the start of electrolysis to avoid influence of natural convection.

Experimental designs were constructed with at least one of the next aims considered; lowering detection limits for short-lived electrogenerated radicals, the investigation of reaction kinetics and mechanisms of radical decay. Focusing on one of these aims, can compromise the other aspects of the measurement leading to the need for a well-considered and rational setup design.

During the same period (60s and 70s) a number of groups worked on the Adams design focusing on these different aspects and consequences of adaptations to the design for specific reactions. Cauquis and co-workers started using a closed-loop flow system with a Pt grid or sheet electrode mostly for reactions with phenothiazine derivatives [55–59]. Dohrmann *et al*. employed a foil electrode and did current-interrupt experiments with estimation of the shortest radical lifetime possibly measurable with their setup being 10^{-5} s [60]. Kastening *et al*. divided the generating electrode in several independent strips with each of which having an individual power supply solving the uneven polarization of a lengthy electrode in a narrow channel [61]. Discussions exist between the leading researchers in the field of that time, stating that the estimations of Dohrmann and Kastening for the study of their kinetic processes, knowledge about the hydrodynamics of the setups should be obtained to solve the corresponding convective-diffusion equation [62,63].

One of the most sensitive cell designs for short-lived radical detection is the cell of Allendoerfer, Martinchek and Bruckenstein from 1975 [64]. They utilized a coaxial cylindrical cavity in TE_{011}-mode as illustrated in figure 4.2.1. A cylindric metallic conductor was positioned in a silica tube (C) along the axis of the cavity. The conductor (B) can be considered as a wall in the center of the cavity resulting in the microwave magnetic field line pattern as shown in figure 4.2.2. The conductor could also be used as an electrode for radical generation. They experienced heating of the conductor by the 100 kHz magnetic field modulation which distorted the magnetic field. The problem was circumvented by constructing it as a free standing finely wound, shallow-pitched helix (H), compressed against the sample tube wall.

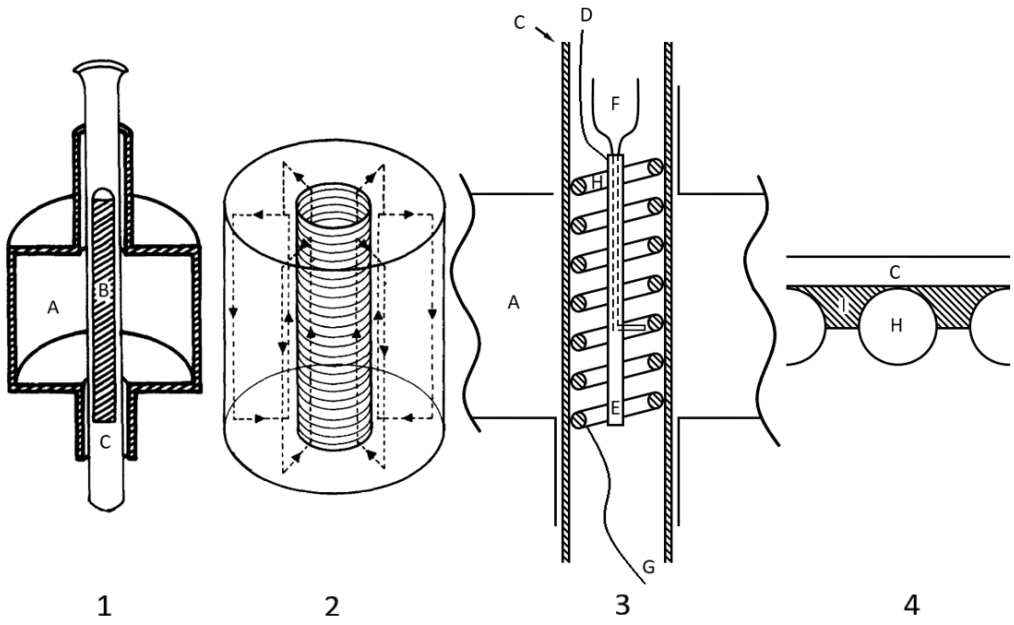

Figure 4.2: *(1) Schematic image of coaxial TE_{011} cavity: (A) standard TE_{011} cavity, (B) Central conductor, (C) Quartz tube. (2) Microwave magnetic field lines in the coaxial cavity. (3) Schematic drawing of the Allendoerfer cell in the cavity: (D) CE connection wire, (E) Pt CE, (F) Luggin capillary for the RE, (G) WE connection wire, (H) Au helical WE. (4) Interfacial diagram of the electrode surface: (I) Solution volume seen by the microwaves (modified from* [64]*).*

The only portion of the solution volume that is penetrated by the microwave is that between the wall and helix (I) so the CE and the Luggin capillary for the RE could be positioned inside the helix (E and F). This kind of geometry resulted in uniform current density over the surface of the working electrode as every point is equidistant to the CE. The Luggin capillary was positioned as close to the WE as possible. Their configuration had a solvent resistance of only 13 Ω when filled with 0.1M TBAP in DMF. This is extremely low when compared to 5-10 kΩ calculated by Goldberg and Bard [50] for the Adams flat cell setup. The small resistance also allows for undistorted CVs to be measured. The authors estimated that it only takes 30 seconds to electrolyze the entire EPR active volume and estimated that the shortest-lived radical measurable would have a lifetime of about 10^{-5} s which is similar to Dohrmann *et al*. Ohya-Nishiguchi *et al*. used it in several publications as a two-electrode configuration for the reduction of organic compounds which were then measured in EPR at low temperatures [65–67].

The Allendoerfer design was later adapted by Carroll allowing flow which contributed to even higher sensitivity by providing a constant supply of electroactive material to the electrode. He positioned a series of baffles preventing the solution from entering the central part in the helical WE which is not penetrated by the microwaves. The nitromethane radical anion was observed in aqueous solution with his cell with an estimated life-time of 10 ms [68].

In the following decades the flow aspect was exploited to facilitate combined research of electrode kinetics and decay reaction constants together with the identification of paramagnetic intermediates. The hydrodynamic flow had to be well-defined and calculable in order to know the distribution of radicals in time and space by solving the convective-diffusion equation. These calculations become much less complex when basic cell geometries were used and electrode surfaces are positioned in the surface of a cell wall. Albery *et al*. published the use of a cell with such geometry in 1974 [69]. The cell described and characterized was a tube electrode with part of the tube wall replaced by a Au ring with the same i.d. as the silica tube. The Au ring acted as a WE sitting just on the edge of the cavity. Side arms were connected to the main flow channel up and down stream to accommodate the RE and CE respectively [70].

They considered reactions of nitrogen containing aromatic radicals and the kinetics of their decay through a first- and second-order mechanism but also more complex mechanisms and transient signals were investigated [71–74]. The ring was replaced by a semi-annular ring coated with poly(nitrostyrene) and poly(vinylanthraquinone) positioned in the center of the sensitive part of the cavity (figure 4.3). They argued that the loss in sensitivity by placing the electrode in that location was partially avoided by using less electrode material and the fact that the radicals were now produced and measured at the same location [75].

Compton and Coles designed a cell with a different geometry, a channel flow cell, in 1983 [76]. The rectangular flow channel consisted of two demountable plates of synthetic silica. One had a flow channel whilst the cover plate housed a rectangular WE which was positioned in the sensitive part of the cavity (figure 4.3). A foil metal WE was utilized as thicker electrodes would diminish the sensitivity. The initial purpose was to do photo-electrochemical EPR by irradiating electrochemically produced species but the cell is also suitable for direct detection of the electrogenerated radicals. Two reservoirs were added to the entrance and end of the channel to equalize pressure over the width of the channel. The CE was located downstream and the RE upstream. The positioning of CE and RE lead to a high ohmic resistance. In another paper the effect on peak displacement of the resistance was calculated [77].

The tube and channel electrode have similar advantages for obtaining kinetic information in contrast to the Allendoerfer cell which has supreme sensitivity. Compton and Waller combined the better features of both cells to attain a higher electrode surface in the sensitive part of the cavity without compromising the well-characterized hydrodynamic flow. They used a coaxial cylindrical cavity like the Allendoerfer cell but incorporated the working electrode in the central conductor. It was separated from the rest of the conductor with Teflon pieces (figure 4.3). The advantageous positioning of the electrode in the center of the sensitive part and the narrow flow channel between the silica housing tube and the central conductor/electrode assembly results enabling large radical concentrations.

The flow pattern showed only small deviations compared to that of a channel electrode with the exception of rates lower than 10^{-3} cm³ s^{-1}. The setup needed to be supported by a current booster in order to overcome the high resistances entailed by the 100 µm flow channel and the positioning of the CE and RE outside of the cavity [78].

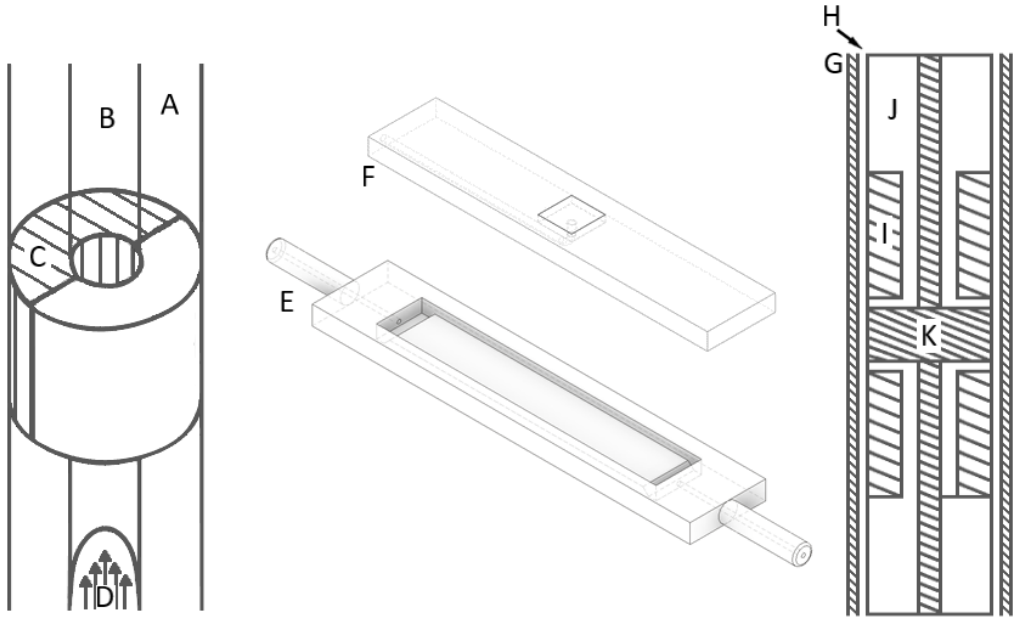

Figure 4.3: *Tubular in-situ flow cell in silica tube (A) with flow channel (B) and semi-annular Au electrode (C). The flow profile is indicated in (D)* [75] *(left). The Compton-Coles in-situ channel flow cell from* [76] *with on top the silica plate housing the WE (F) and below the flow channel (E) (middle). The Compton and Waller cell with (G) a silica tube, (H) the 100 µm flow channel, (I) the Cu central conductor, (J) Teflon insulators and (K) Hg-plated Cu WE (right).*

A considerably more complex cell geometry and consequently hydrodynamic flow pattern is that of a wall-jet electrode. Two tubes are concentrically positioned with the central one being the jet supplying the electrolyte to a planar WE (wall) positioned at small distance of this tube's outlet. The flow is perpendicular to the electrode and spreads out radially over its surface. After passing the electrode, the electrolyte flows through the annular gap between inner and outer tube to a waste container.

Such cell was proposed by Compton, Greaves and Waller in 1990 [79] and is depicted in figure 4.4. The cell complied to the hydrodynamic equations for its geometry when ACN with TBAP was used and Q-factors comparable to other flow cells were obtained. Aqueous solutions obliged them to reduce the cell volume because of a deteriorated Q-factor. Problems arose concerning reproducibility due to trapped bubbles and the varying location of the jet after dismantling and reassembling the cell with these smaller dimensions. The fact that the calculable flow pattern requirement was not met with these changed dimensions draws a parallel with a setup by Bond *et al*. published two years before [80].

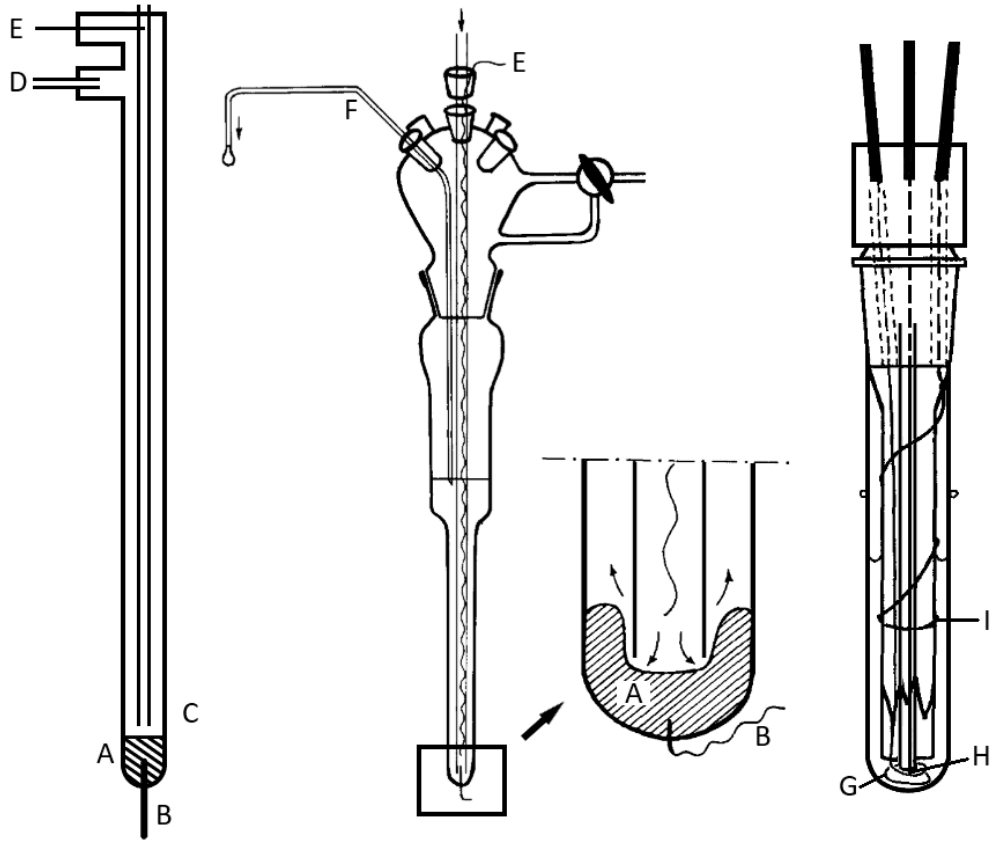

Figure 4.4: *Wall-jet electrode from* [79] *with (A) the Hg working electrode connected with (B) a Cu lead, (C) the inner 'jet' tube, (D) tubing to the CE and (E) a wire pseudo reference (left). Flow-cell of Bond et al. with (F) the stainless steel needle CE also serving as outlet (middle). The small volume cell of Bond et al. with (G) a Pt wire WE, (H) a Ag/AgCl coated Pt wire RE and (I) Pt wire CE (right).*

There the separation between the jet and Hg WE was minimized leading to a maximized electrode surface and a very thin solution layer ideal for exhaustive electrolysis losing the planarity of the electrode and the calculable flow pattern as a consequence.

Bond *et al*. described a small volume cylindrical cell of approximately 0.2 cm^3 in 1986 [81,82] utilizing a 4 mm outer diameter quartz EPR tube (figure 4.4, right). The earliest design had a small Pt rod working electrode with only the tip exposed and a Pt auxiliary electrode positioned at the entrance of the cavity. A Ag/AgCl reference electrode was separated from the sample solution by an asbestos plug and sat just adjacent to the working electrode for optimal potential control. It provided possibilities for the use of organic solvents like dichloromethane at temperatures as low as -75 °C. The second version consisted of two concentric tubes with the counter electrode wound around the outer tube and the inner tube being the AgCl coated Pt pseudo reference electrode.

In the space between the two tubes, a wire working electrode was led to the tip of the reference electrode where it was coiled in a way that every part of the working electrode was equidistant to the reference electrode. Omitting the real reference electrode with plug allowed for freezing of samples of ACN-based solutions to -143 °C without destruction of the cell so solid EPR spectra could be obtained. In an interesting publication Webster *et al*. compare this small volume cell with the Compton-Coles channel flow cell listing both advantages and disadvantages [83].

All of previously named setups suited special needs of the researchers in their search for sensitivity, kinetic information or intermediate identification. From here on, most of the setups are based on something that had already been done with the exception of adjustments related to their specific case studies, the used resonator or because technological progress in other areas which allowed for exchanging parts with newer/better alternatives. Some examples of adaptations for specific purposes are briefly listed here.

The publication of Hartl *et al*. from 2001 [84] reported an adaptation on the Allendoerfer cell which was also used by Ohya-Nishiguchi *et al*. at low temperatures by putting a Ag pseudo-reference on the inside of the WE helix. Wain *et al*. [85] published the use of a tube electrode in a cylindrical TE_{011}-cavity which entails a higher sensitivity than its rectangular counterpart. They also made a rather interesting microfluidic channel electrode in a two-stage photolithographic approach utilizing positive and negative photo resistive materials. Vapor deposition was used for fabrication of the electrodes. The rectangular duct was only 350 µm in height and the width was varied between 500 µm and 2000 µm. The electrodes were kept just outside of the cylindrical cavity [86]. A similar electrode fabrication method was used for variable temperature experiments which did not allow a flow-through approach. It was placed in an NMR tube serving as an outlet channel [87] and in [88] the tubular electrode was adjusted by using two coaxial tubes with the outer partly substituted for a gold tube electrode. Jouikov and Zeituny designed a four electrode cell capable of detecting radicals produced from a two-electron oxidized parent molecule that was reduced with one electron at a glassy carbon fiber WE. A Pt tube electrode was placed upstream of the WE to generate the oxidized molecule and a spiral Pt wire CE was put downstream [89].

4.2 State-of-the-art

This section lists the publications since 2010 which employ electrodes within the resonator or cavity to produce radicals and/or other paramagnetic species. Most are based on the cells in section 4.1 but some have been adapted for a specific application. It must be emphasized literature is scarce and that some publications fail to mention enough experimental details on the constructed or utilized setup for their experiments to be reproduced by other groups. This lack of information will be underlined for those publications suspected to have been performed *in-situ*.

Due to the specific nature of the combination of electrochemistry and EPR, it appeals to scientists acquainted with different subdivisions of the electrochemical science. Examples are; batteries, complexes, polymers, supercapacitors, organic radical, *etc.*. The largest body of literature being published for *in-situ* generated organic radicals and is listed in table 4.1. The nature of the radical and reagent is very diverse indicating that in the subdivisions given above, different variations on the setups are required. The majority of the listed publications utilizes a commercially available flat cell with wire or mesh working electrodes which are sometimes laminated. This approach is most straightforward as they are fairly simple to construct and position in the resonator. When tubes are used, the inner diameter is in the order of 1 mm to prevent the absorption of microwaves by the solvent. The two publications by Tamski *et al*. report the construction and use for quantitative measurements of their micro-electrochemical cell (1 mm inner diameter tube) in a loop-gap resonator [90,91].

Two publications are rather vague about the cell used [92,93]. The publication of the oxidation of β-cyclodextrin by ferrocene states the use of a Pt mesh WE which could be an indication of the use of a flat cell while the one about fluorinated/chlorinated 2,1,3-benzothia/selenadiazoles only mentions the use of a cylindrical cavity, the material of the working electrode and the solvent. The second does not even describe anything specific about the combined electrochemical experiments in the EPR, just the fact that they were indeed performed *in-situ*. Most of the publications do give enough experimental details like the counter electrode being preferably Pt wire and rods and the pseudo-references being Ag wires, AgCl coated Ag wires or real Ag/AgCl aqueous and Ag/Ag^+ non-aqueous reference electrodes presumably all positions outside of the flat part. Organic solvent are preferred over aqueous ones. The publication about the oxidation of phenazine-di-N-oxide uses the Allendoerfer cell also used by Hartl in 2001 with helically wound working electrode in a coaxial cavity for better sensitivity.

Table 4.1: *Publications with in-situ generated organic radicals (Microwave frequencies: X-band: ~9 GHz, Q-band: ~35 GHz, W-band: ~90 GHz).*

Nature	Cell	WE	CE	RE	Stabilisation	Solvent	Freq.	Ref.
Quinones, diimines, TMC, enzymes	Silica tube	Pt wire	Pt wire	Ag wire	None Temperature	DMF	W Q	[94]
(5-etoxycarbonylmethylidene-4-oxothiazolidine-2-ylidene)-N-phenylethanone	No info	No info	No info	No info	None	DMSO	X	[95]
Selenadiazoloquinolones	Flat cell	Pt mesh	Pt wire	Ag wire	Temperature	DMSO	X	[96]
Nitroquinolones	Flat cell	Pt mesh	Pt wire	Ag wire	Nitrosodurene	DMSO MeOH CD_3OD DMSO-d_6	X	[97]
Guanine oxidation through Ru (II) complex	Flat cell	Pt wire	Pt wire	Ag wire	PBN	H_2O	X	[98]
2,2-dinitroethene-1,1-diamine	Flat cell	Au mesh	Pt wire	Ag/AgCl wire	None	ACN DMF	X	[99]
Phenazine-di-N-oxide with IPA	Custom	Au and Pt helical wire	Pt rod	Ag wire	None	ACN	X	[100]
β-cyclodextrin with Ferrocene	'spectro-electrochemical quartz cell'	Pt mesh	No info	Ag/Ag^+	None	DMSO	X	[92]
Shikonin and isovalerylshikonin	Flat cell	Pt mesh	Pt	Ag/Ag^+	None	ACN	X	[101]
Methyl viologen	Custom LGR	Pt wire Ag wire	Pt wire Ag wire	Ag wire, AgCl wire	None	ACN H_2O	X	[90]

Table 4.1: *Continued.*

Nature	Cell	WE	CE	RE	Stabilisation	Solvent	Freq.	Ref.
Ketoconazole oxidation	Silica tube	Cu, Ag, Pt or graphite	Ag/AgCl wire	CE	None	H_2O	X	[102]
Benzoquinone	Custom LGR	Pt wire Ag wire	Pt wire Ag wire	Ag wire, AgCl wire	None	ACN	X	[91]
Oxidation of flavonolignan Silybin	Flat cell	Pt mesh	Pt wire	Ag wire	BMPO	ACN	X	[103]
Fluorinated/chlorinated 2,1,3-benzothia/selenadiazoles	'Electrochemical cell for EPR'	Pt	No info	No info	None	DMF	X	[93]
Sandmeyer reaction	Flat cell	Pt wire	Pt wire	None	PBN	DMF ACN MeOH	X	[104]
Tetrachloro-N-hydroxyl-phthalimide	Flat cell	Pt plate	Pt wire	Ag wire	None	ACN	X	[105]
Trithiatetrazocinyl Radical Anions	Flat cell	Au mesh	2 Pt wires	Ag/AgCl wire	None	CH_2Cl_2	X	[106]
Quinones, perylene-diimide, pyrene, flavin, tryptophan and tyrosine	Flat cell	Pt wire	Pt wire	Ag/AgCl Ref and Ag/Ag+ ref	None	ACN	X	[107]

Literature concerning oxidation or reduction of complexes can be found in table 4.2. All but one were performed in EPR tubes and four are performed in an Allendoerfer type of cell. The description can be found in [108]. The ones that use a Ag/Ag^{+} non-aqueous reference electrode presumably positioned between the helix and the central counter electrode through means of a Luggin capillary as the cell is in the range of 1 mm inner diameter. Inorganic species, like hydroxyl radicals or the sulphate radical anion, are usually too short lived for direct detection and thus need to be stabilized by a trapping agent [109]. A flat cell with liquid flow was used and electrodes were placed outside of the flat part making it a semi *in-situ* setup. The reason for this positioning probably originates from the choice of Boron Doped Diamond (BDD) as a WE. A flat cell and tube with Pt mesh WE, two Pt CE's and without RE were used at variable temperatures [110].

Other branches of electrochemistry also utilize the combined technique to study their systems dealing with similar restrictions. One being the field of battery research recently focusing on the improvement of the Li-based batteries to lighter systems or systems with higher specific energy. Monitoring of sulphur radicals in Li-S batteries has been performed in a silica flat cell of 0.8 mm in [111]. Li-O_2 batteries were investigated *in-situ* using two custom-made cells in [112]. One tubular and one flat cell were constructed with PTFE separators for evidencing the formation of singlet oxygen in the charging process. The singlet oxygen formed an adduct with 2,2,6,6-tetramethyl-4-piperidone which is said to be stable and selectively formed for singlet oxygen. The adduct formation was in competition with its decay to triplet oxygen. In a publication by Sathiya *et al*. [113], a cylindrical cell in polychlorotrifluoroethane of 5 mm inner diameter was proposed with Cu and Al current collectors for the investigation of $Li_2Ru_{0.75}Sn_{0.25}O_3$ as a positive electrode material through the signal of Ru^{5+} and paramagnetic oxygen species.

Table 4.2: *Publications with in-situ generated paramagnetic metal complexes.*

Nature	Cell	WE	CE	RE	Stabilisation	Solvent	Freq.	Ref.
$[Mo(CO)_4L]$ complexes	Silica tube	Pt	Pt	None	None	CH_2Cl_2	X	[114]
Ru(II) complex	Silica tube	Pt wire	Pt wire	Ag wire	Temperature	CH_2Cl_2	X	[115]
$Cr(bpy)_3$ complexes	Silica tube	Au helical wire	Pt wire	Ag wire	None	DMF	X	[108]
$[(dpp\text{-}bian)Re(CO)_3Br]$	Silica tube	Au helical wire	Pt wire	Ag/Ag^+	None	DMF ACN	X	[116]
$FcP(O)(OC_2H_5)_2$	Silica tube	Au helical wire	Pt wire	Ag/Ag^+	Temperature	DMF	X	[117]
Tris(2,2´-bipyridine)zinc(II) diperchlorate	Silica tube	Au helical wire	Pt wire	No info	None	DMF	X	[118]
Ni, Cu and Co with ligands: benzene-1,2-dithiolate or 3,6-dichlorobenzene- 1,2-dithiolate	Flat cell	Pt mesh	Pt wire	Ag wire	Temperature	DMF CH_2Cl_2	X	[119]

Apart from the battery research, surface properties of electrodes have been researched for conducting polymers on a Pt wire [120,121] and on ITO [122,123] in a flat cell and in a silica tube [124–126]. Deposition of Co from a complex [127], viologen modified particles silica particles [128] and protein or tempo modified surfaces [129] have been investigated with flat cell and Pt substrate electrodes for the first two and, ITO particles on Ti wire in a silica tube for the latter. Dissolution of Cu from a Cu/Ni catalyst during water oxidation has been proven with *in-situ* Raman and *in-situ* EPR. The carbon sheet with deposited catalyst material was placed in a flat cell with a Pt gauze counter electrode [130]. The group of Prof. Dryfe applied the technique for the characterization of supercapacitors proposing that the charge, stored in the double layer, is accepted by spin traps forming free radicals. The focus was on the intensity during the charging and discharging process. Two similar setups were used consisting of the investigated material pressed against a solid body with a Pt wire as current collector. The solid body was a Pt rod or a PTFE covered Pt rod which served as second current collector or counter electrode, respectively. When used as a current collector, a separate Pt counter electrode was placed above the sensitive part together with a reference electrode. In the other case, both electrodes were situated in the sensitive part with the reference electrode on top [131–133].

Part II

EPR-spectroelectrochemical setup construction

Chapter 5

Different electrodes for batch *in-situ* EPR measurements in a flat cell

In this chapter two electrodes for *in-situ* electrochemical EPR are constructed; a wire electrode and a metal-on-polymer physical vapor deposited (PVD) electrode. Both setups fit in a commercial flat cell and are ideal for an initial *in-situ* screening of the electrochemical system. They were experimentally validated to demonstrate the proof-of-concept. The PVD electrode exhibited improved electrochemical behavior whilst maintaining sensitivity in EPR application.

The wire electrode validation will be part of a publication: S. Neukermans, M. Samanipour, H.Y.V. Ching, J. Hereijgers, S. Van Doorslaer, T. Breugelmans, Re-evaluating the electrochemical self-condensation of acetone by *in-situ* EPR and DFT calculations, *Chemical Science*, (2021), to be submitted

The PVD electrode has been published in: D. Pauwels, H.Y.V. Ching, M. Samanipour, S. Neukermans, J. Hereijgers, S. Van Doorslaer, K. De Wael, T. Breugelmans, Identifying intermediates in the reductive intramolecular cyclisation of allyl 2-bromobenzyl ether by an improved electron paramagnetic resonance spectroelectrochemical electrode design combined with density functional theory calculations, *Electrochimica Acta*, 271 (2018) 10-18.

5.1 Introduction

Previous chapters show that combining electrochemistry and EPR imposes challenges on the setup. The selection of a reaction vessel for the first investigation of a reaction, coinciding with the requirements for EPR, depends on the nature of the radical that will be produced. Organic radicals that live long enough to be detected in the liquid phase are preferably generated in a commercial flat cell and TE_{102} rectangular cavity. The use of a flat cell ensures minimal absorption of the electromagnetic radiation by positioning the solution in the minimum of its electric field component. Drawback for these kind of cells is the poor electrochemical conditions they impose. The thin solution layer where the working electrode is located does not meet the semi-infinite linear diffusion boundary condition. This small volume makes potential control difficult, as one has to choose between a pseudo reference electrode close to the working electrode surface (in the flat part) or a real reference electrode in the bulk section of the cell, further away of the working electrode. The use of a flat cell also requires electrodes with a high length over diameter/width ratio, potentially resulting in a resistance contribution of the electrode itself or increasing the solution resistance, so special attention must be paid to electrode positioning. Every electrochemical reaction will therefore require specific adaptations to the electrode or the cell.

The first screening of an electrochemical system can be performed with a wire electrode as it is straightforward to construct. Different materials are commercially available as wires which are thin enough to fit in a flat cell [134]. Some are sold with a coating to conveniently prevent short circuits when electrodes are positioned closely together. The construction of such wire electrodes is covered in this chapter and the advantages and drawbacks are discussed. The second design focusses on improving the electrochemical behavior by changing the working electrode surface of the wire electrode by a physical vapor deposited (PVD) electrode suitable for *in-situ* measurements. The deposition of a metal coating requires specialized equipment with the possibility of depositing variable layer thicknesses [135].

The electrode should be an improvement compared to the wire electrode as the working electrode is single-use, a reproducible surface is provided, a flat surface will be obtained which is desirable for analytical electrochemistry and the surface area in the sensitive part of the resonator will be maximized. The cheap construction and the variety of material the PVD apparatus can deposit [136], provides a good basis for case studies considering that differences in electrochemical mechanisms can depend on the catalytic electrode material. Besides the PVD deposited material itself being potentially catalytic, it could also be used as a substrate for more advanced particle deposition, *i.e.* bimetallic or core-shell particles [137]. The choice of the substrate material is primordial to avoid participation of the substrate in the reaction and to isolate the catalyst properties without compromising conductivity or cavity tuning. Ultimately a 200 nm Ag layer was selected as working electrode material, deposited on a commercial polypropylene (PP) film.

Both electrodes are intended for use in the flat cell for liquid *in-situ* radical detection in an X-band EPR spectrometer. They were validated by performing two test cases in stagnant solution, first electrochemically and secondly *in-situ* EPR. The two reactions are the reduction of benzoquinone in an organic solvent and methyl viologen in aqueous solution.

5.2 Experimental

5.2.1 Chemicals

Electrochemical measurements were performed in acetonitrile (ACN, Chem-Lab, HPLC Grade) and MilliQ water (18.2 MΩ cm^{-1}) with respectively 0.1 M tetrabutyl ammoniumperchlorate (TBAP, Sigma-Aldrich, 99.0 %) and sodium sulphate (Acros Organics, 99.0%) as supporting electrolyte. Cyclohexa-2,5-dieen-1,4-dion also known as benzoquinone (BQ, Sigma-Aldrich, ≥99.5%) solutions were prepared in ACN and 1,1'-dimethyl-4,4'-bipyridinium dichloride; methyl viologen; (MV, Sigma-Aldrich, 98%) in water. All chemicals are used without any further purification.

5.2.2 Procedure

All electrochemical experiments in this chapter are conducted with a PAR VersaSTAT 3 potentiostat. The bulk experiments are done in a conventional undivided cell. Combined EPR-spectroelectrochemical measurements are executed in a Wilmad Supracil WG-810-A-Q. The setups were placed in a TE_{102} rectangular cavity in a Bruker E580 Elexsys spectrometer. The EPR spectra were recorded at X-band in continuous wave mode (CW) at ambient temperature with 100 kHz field modulation frequency. Microwave frequency, microwave power and field modulation amplitude are mentioned in captions. The setups were degassed by Ar purging prior to use.

5.2.3 Test cases

5.2.3.1 Benzoquinone

The two testcases that are used with all the setups described in part II of this thesis are selected given their properties in organic and aqueous environments. In organic solvents the behavior of BQ is investigated because the reduction provides a fairly stable radical which has a slightly different color than the parent molecule. The color change provides a visual check for connection exposure tests, indicating where reaction is occurring. BQ is a much studied and interesting case with known voltammetry [138,139] and EPR spectra [91,140–142]. A reason for this is that quinones in general are interesting for their use in dyes, oxidizing and reducing agents in lab scale and industrial synthesis and, for the fundamental understanding of organic redox chemistry [139,143,144].

Reduction in aqueous solutions yields different species depending on the availability of protons in the vicinity of the reduced species. This is illustrated in figure 5.1. Buffered solutions lead to a two-electron transfer yielding the hydroquinone after addition of two protons from the solvent. Unbuffered solutions result in the same species when the concentration of protons is relatively high compared to the concentration of BQ reduced. When this relative concentration is low, the reduced species cannot hydrogenate and will be stabilized by hydrogen bond formation with water molecules. The result will be a mix of the diprotonated, monoprotonated and the non-protonated form of the dianion.

Differences could also be observed in voltammetric behavior by comparing buffered and unbuffered solutions at similar pH. While the unbuffered solution shows near-perfect reversibility, the buffered one has a shifted oxidation potential resulting in semi-reversible behavior [139].

In an aprotic organic solvent the reduction of BQ is presented as two one electron transfers which are between 500 and 750 mV apart depending on the water concentration in the solution [139]. The first electron transfer yields the semiquinone radical anion and the second electron transfer yields the benzoquinone dianion. For the purpose of radical detection, only the first electron transfer is of interest.

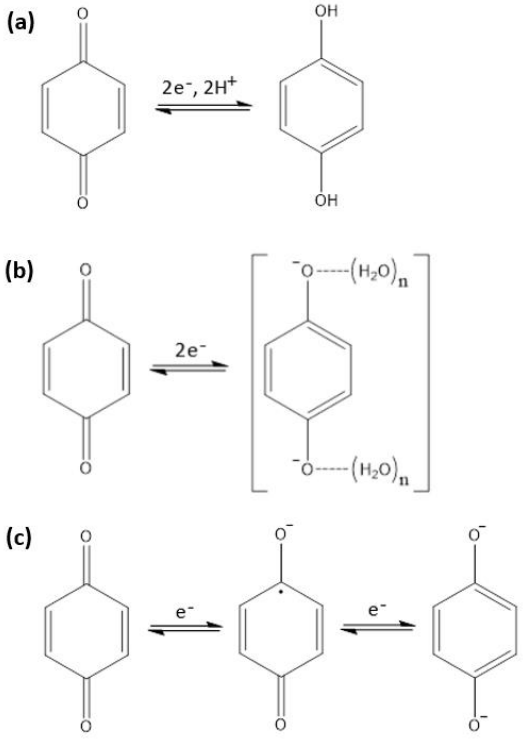

Figure 5.1: *BQ redox reactions in different media: (a) buffered water or unbuffered with [H⁺] > [BQ], (b) unbuffered water with [H⁺] < [BQ], (c) aprotic solvents (redrawn from reference* [139]*).*

5.2.3.2 Methyl viologen

MV was used to test the behavior of the EPR-spectroelectrochemical setups in aqueous solutions. It was commonly used as a non-selective herbicide before being banned for its neurotoxicity which is linked to its redox potential [145]. The general electron transfers are shown in figure 5.2 starting from the dication MV^{2+} which will be reduced to $MV^{\cdot+}$ (eq. 5.1). Like most dipyridyl radicals this results in an intensely colored radical in the blue-purple range. It has been identified as a good potentiometric indicator. For more specific information about this application the reader is referred to the work of Michaelis [146]. After the first reduction and at sufficient overpotential, the $MV^{\cdot+}$ can be reduced to the neutral MV^0 (eq. 5.2)

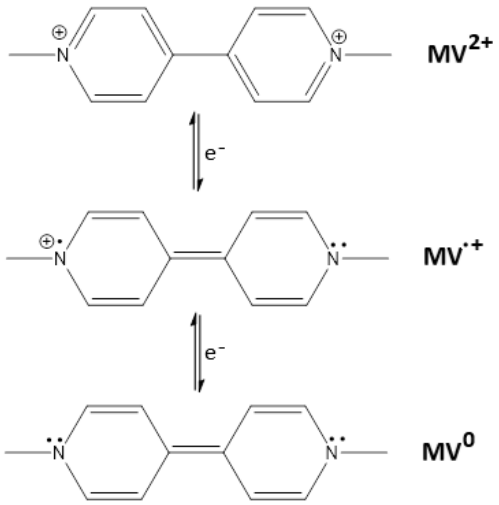

Figure 5.2: *Main oxidation states of the MV redox species (redrawn from reference* [147]*).*

Voltammetric behavior of the reduction seems independent of the electrodes that have been used. However, the back scan differs depending on the working electrode. Some materials promote the adsorption of the MV^0 species so that this desorption or stripping peak (eq. 5.4) convolutes with the oxidation to $MV^{\cdot+}$ (eq. 5.3). Those materials mostly exhibit a relatively flat surface without any roughness or surface structures allowing the formation of a structured MV^0 layer.

$$MV^{2+} + e^- \rightarrow MV^{\bullet+} \quad (5.1)$$

$$MV^{\bullet+} + e^- \rightarrow MV^0 \quad (5.2)$$

$$MV^0 \rightarrow MV^{\bullet+} + e^- \quad (5.3)$$

$$MV^0_{ads} \rightarrow MV^{\bullet+}_{aq} + e^- \quad (5.4)$$

When multiwalled carbon nanotubes are present at the surface, the MV^0 preferentially adsorbs on their surface, resulting in two subsequent oxidation waves without stripping peak. This strategy was suggested to prevent surface fouling by MV^0 in a publication of the Compton group [147]. O-terminated boron doped diamond electrodes were proposed to totally diminish the influence of this fouling on the voltammetric response [148]. $MV^{\cdot+}$ is the only form that is paramagnetic. Its EPR spectrum has been reported before and is, because of the abundance of protons and the extensive π-system, fairly complex [90].

None of the solutions of BQ and MV were deoxygenated before performing cyclic voltammetry in the second part of this thesis. The first reduction wave of BQ occurs at -0.497 V vs saturated calomel reference electrode (SCE) [149] whereas the onset for oxygen reduction is only reached at -0.75 V and the peak at -0.9 V vs SCE at GC electrode [150]. By adequately choosing the vertex potential of the CV, reduction of dissolved oxygen can be avoided. In the case of MV, which was solely investigated in aqueous environment, the solubility of oxygen is known to be low [151]. The oxygen reduction potential for several pathways of oxygen reduction in water is higher than 0 V vs SCE [152] and is known to have slow kinetics with low concentrations of protons or hydroxyls.

In the following chapters, references are made to the lifetime of the produced radicals in order to explain electrochemical and spectroscopic measurements. For BQ, the rate constants of decay reactions in aqueous media are given in [142] and are lower for higher pH (0.0256 s^{-1} for pH 3 and 0.0117 s^{-1} for pH 4). The decay of MV radical cation is mostly determined by the presence of oxygen. Decay rate constants vary from 5.7 x 10^8 M^{-1} s^{-1} for oxygen saturated to 5.9 x 10^8 M^{-1} s^{-1} for air saturated solutions. These were associated with half-life times smaller than 5 µs [153].

5.3 Results and discussion

Both the wire electrode and the PVD electrode are designed to fit in a commercial flat cell placed in a TE_{102} rectangular cavity. The position in the cavity was determined by rotating the setup, resulting in a minimal interaction with the electric field component of the incident microwaves.

The sensitive part of the cavity was determined by putting a strong pitch EPR sample and moving it in steps of 0.25 cm. This experiment indicated the ideal positioning of the flat cell and the maximal useful length of a working electrode placed in the flat section was around two centimeters (figure 5.3).

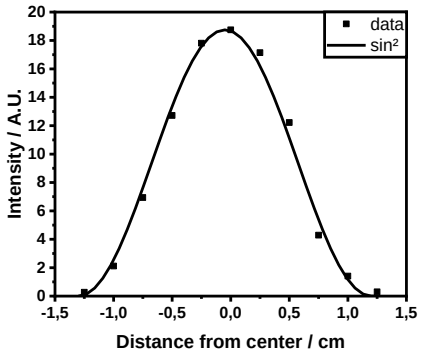

Figure 5.3: *Position variation of the strong pitch sample with related signal intensity and sin² fit.*

5.3.1 Wire electrode

The wire electrode was constructed with two polyfluoroalkane (PFA) insulated Ag wires. They were fixated in a glass tube with epoxy resin, one serving as working electrode and the other as pseudo reference electrode. Before fixating, the wires were aligned to make sure the working electrode reached the sensitive part of the cavity and the PFA insulation was partly stripped to expose the Ag to the solution.

The stripping was performed over a flame, such that the working electrode insulation started where the pseudo reference electrode exposed surface began. The pseudo reference wire was only stripped for 1 mm. A different option could be to position the exposed pseudo reference electrode closer to the tip of the working electrode consequentially increasing the risk of short circuiting when mispositioning the electrode assembly in the cell. The Pt wire counter electrode was put in the bulk section above the flat part to minimize the diffusion of counter electrode generated radicals to the sensitive part. This increases the cell resistance but it is inherent to the use of a flat cell. In this design, the counter electrode is spun around the glass tube holding the other electrodes and their connections to increase the surface area. The counter electrode helix has to be repositioned before every new measurement. This electrode is totally stripped of the PFA and fixated in a plastic cork on top. This cork also holds the glass tube and enables keeping the inside of the cell deoxygenated and to be filled in a glovebox. Figure 5.4 shows the different parts of the electrode and the positioning in the flat cell. The wires were polished by hanging the electrode assembly in a 1 µm Al_2O_3 suspension in a sonicator for 10 minutes before each measurement. In this manner, the electrodes can be cleaned and some reproducibility in surface roughness of the wire can be provided for electrolysis. However, reproducible and uniform catalyst electrodeposition is assumed to be difficult because of the indicated surface roughness and the geometrical shape of the electrode (ideally flat).

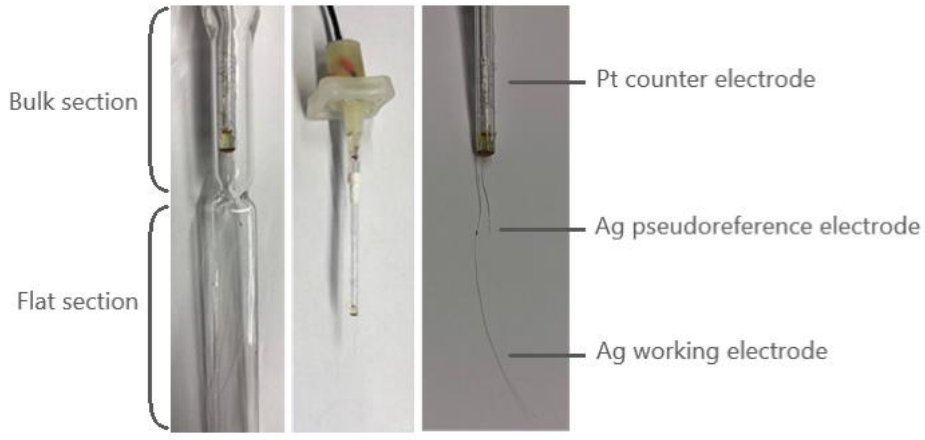

Figure 5.4: *Photographs of the wire electrode: in commercial flat cell (left), zoomed-out (middle) and zoomed-in (right).*

In order to reproducibly generate and detect the desired radicals, the electrochemical behavior of the electrode has to be comparable to the bulk experiments. This is mostly done by CV to identify the peaks which represent the different electron transfers. By applying the desired peak potential in a chronoamperometric experiment, the selected electron transfer should occur in a diffusion limited reaction in order to produce a maximum amount of radical for the used concentration without agitation. The positioning of the wire electrode is of great importance for the electrochemical behavior in the flat cell. By rotating the electrode assembly in the flat cell, the pseudo reference electrode can be brought in the vicinity of the working electrode (<1 mm) to improve potential control.

The confined space of the flat cell had an effect on the potential control, as the thin solution layer in the flat part was more resistive than a bulk solution resulting in a potential distribution over the length of the electrode. This was tested by applying a slow potential variation and observing the coloration of the area around the working electrode. Figure 5.5 shows coloration of the working electrode for both BQ and MV reduction. The area of the working electrode closest to the PFA insulation, showed formation of the colored radicals first. As scanning of the potential progressed, parts of the working electrode at larger distances of the PFA insulation gradually started to show radical formation too.

In bulk solutions with the same electrode the coloration of the working electrode was analogous on every part of the stripped wire. This showed that the resistance of the solution as such and the resistance of the wire were not the limiting factors but the dimensional restrictions imposed an extra resistance on the experiment. One must consider that less conductive metals and electrolytes will contribute to a bigger potential distribution over the wire electrode.

Voltammetry results on BQ displayed a stretched-out response in the flat cell in comparison to the bulk solution (figure 5.6 (left)). Reduction and oxidation peak were still definable so chronoamperometry could be performed to detect the product of the first electron transfer; the BQ radical anion.

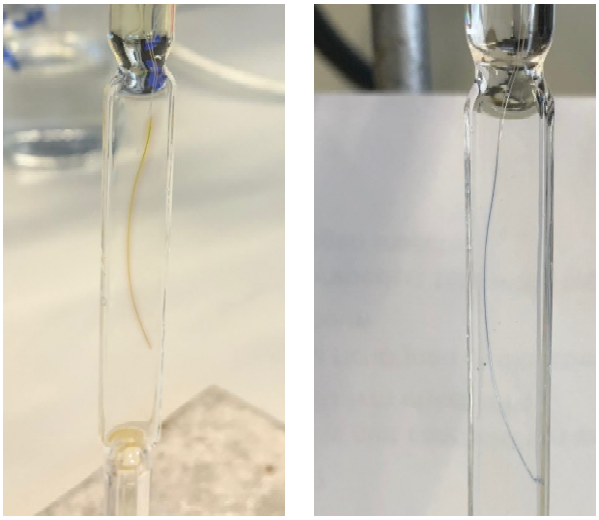

Figure 5.5: *Appearance of electrochemically generated BQ radical anion (left) and MV radical cation (right) in an EPR flat cell with a Ag wire working electrode (not deoxygenated).*

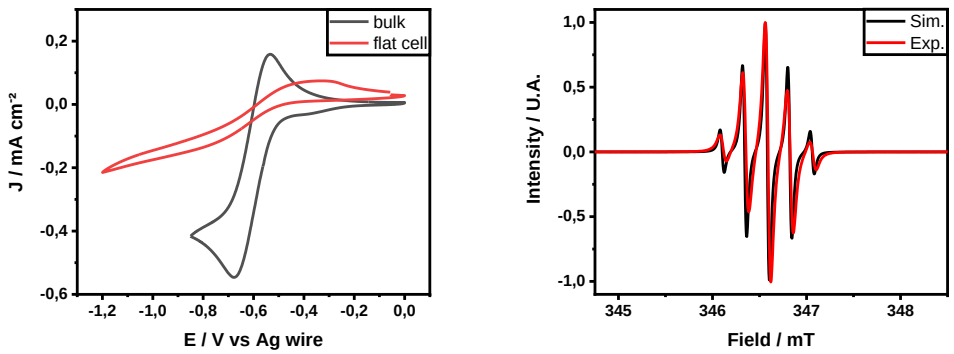

Figure 5.6: *CV of 5 mM BQ in ACN + 0.1 M TBAP on Ag wire electrode in bulk and flat cell (left) and the EPR spectrum at -0.8 V vs Ag wire with simulation (right) at 9.720 ± 0.001 GHz, 2 mW microwave power and 0.5 mT field modulation amplitude (not deoxygenated).*

Beside the potential control, the nature of the analyte and the formed product influenced the CV. A comparison between the voltammogram of BQ and MV (figure 5.6 (left) and figure 5.7 (left)) showed that with different solvent and analyte, the electrochemical behavior was totally different despite similar positioning in the flat cell. The reduction/oxidation peak spacing was much smaller for the latter and compared to the bulk, the deformation of the CV was minimal. The peak-to-peak separation of BQ CV was 138 mV in bulk and 417 mV in the flat cell whilst it was 84 mV and 184 mV for MV. One hypothesis was that the resistance of an aqueous solution is a factor smaller than that of acetonitrile together with the higher supporting electrolyte concentration making the peak spacing smaller and the potential control better.

When *in-situ* electrochemical EPR has to serve for other analytical purposes than radical identification, *i.e.* determination of kinetic parameters, the ohmic drop should be determined and compensated for. Properties of electrochemical cells can be modelled by using COMSOL Electrochemistry Module [154]. It can be used for the determination of resistive and capacitive effects of thin layers or surface films at the electrode-electrolyte interface like the electrodeposition of catalytic particles on a bulk electrode with different conductivity (chapter 6) or, to determine time-dependent concentration gradients for exhaustive electrolysis of thin solution layers (all flat cell experiments) [155].

The lower current density in the BQ reduction wave in the flat cell compared to bulk together with the relative drop in current density in the MV reduction being much smaller than in the BQ reduction supports this last hypothesis. In addition, the BQ reduction does not go into diffusion limitation like it does in the bulk. To fully describe the movement of these molecules in the used cell, equation 3.17 has to be used, taking into account the diffusion coefficient, the potential gradient in this geometry and neglecting the convection term. The diffusion coefficient for BQ in ACN reported in [156] is $3.11 \pm 0.01 \times 10^{-9}$ m^2 s^{-1} and for MV^{2+} in H_2O 6.56×10^{-10} m^2 s^{-1} reported in [157] (no error given). The potential gradient is not straightforward to determine in this cell geometry with field lines going from the anode in the bulk section to the cathode in the flat section.

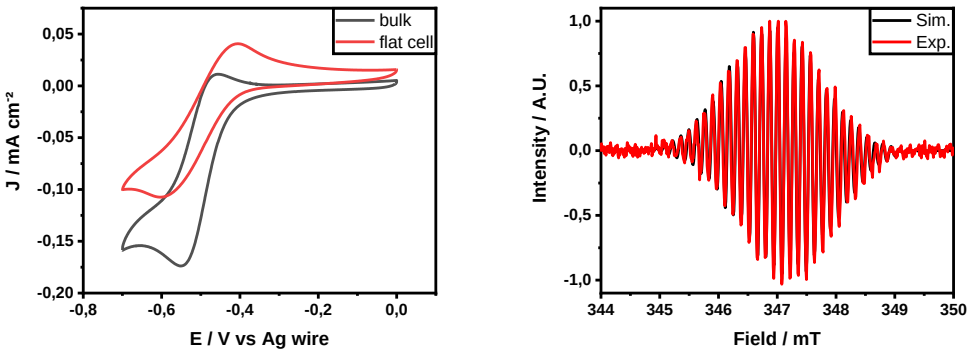

Figure 5.7: *CV of 1 mM MV in H_2O + 0.2 M Na_2SO_4 on Ag wire electrode in bulk and flat cell (left) and the EPR spectrum at -0.6 V vs Ag wire with simulation (right) at 9.720 ± 0.001 GHz, 2 mW microwave power and 0.5 mT field modulation amplitude (not deoxygenated).*

Both figures 5.6 and 5.7 show the EPR spectra of the $BQ^{\cdot -}$ and $MV^{\cdot +}$ respectively. The generation was done by applying -0.8 V for BQ reduction and -0.6 V for MV^{2+} reduction. The spectra were obtained by averaging 20 scans with 2 mW power of the incident microwaves. The spectra are in accordance to the literature that was stated in 5.2.3. The BQ signal presents four equivalent protons and has a good signal-to-noise ratio. The concentration used for this measurement is larger than that of the MV^{2+} reduction which results in a worse signal to noise ratio.

Nevertheless, the large amount of scans necessary to obtain a well-defined spectrum for both cases implies that the surface area of the working electrode in the sensitive part of the cavity is insufficient when shorter living radicals have to be investigated.

5.3.2 PVD electrode

In search for a substrate material, several options were considered. PP is resistant to most organic solvents and does not contain any detectable paramagnetic species. Polytetrafluoroethane (PTFE) would be one of the best chemically resistant polymers to use as a substrate in combination with being EPR silent and minimal microwave absorption [158].

However, the adhesion of the PVD sputtered layers to the PTFE is poor. The layers typically detach when inserting the electrode into the flat cell or when the cell wall is touched. The 30 µm PP was chosen to be rigid enough for insertion in the flat part whilst retaining enough solution volume on top to minimize solution resistance and edge effects.

PVD allows for several different metals or even carbon to be deposited. Thickness of the layer can be varied by changing the sputtering time and layers of different metals can be stacked on top of each other. Precious metals like Pt which have a lower conductivity when only a thin layer is deposited, can be put on top of a better conducting material like copper. Ideally the Pt surface totally covers the Cu to avoid exposure to the analyte. The experiments in this section are performed with a Ag-sputtered PVD layer. Silver has been chosen for its catalytic properties in several reactions, one of them being carbon-halogen bond breaking which is elaborated upon in chapter 10.

The geometrical shape of the sputtered electrode was obtained by utilization of a mask to shield part of the PP. The unmasked sputtered part consisted of a connection pad, the WE surface of 8 mm^2 which was positioned in the flat part of the flat cell and a lead of 0.3 mm wide to connect the pad to the WE surface. A Cu wire was connected to the pad and encapsulated by heat sealing PP over it to avoid contact with the solution and compressing the wire to the connection pad.

Caution was taken during the heat sealing because the substrate PP of the electrode melted more easily than the covering PP when directly exposed to a heat gun due to its limited thickness. The heat gun was set to 140 °C and the hot air stream was directed on the covering PP and subsequently pressed against the substrate to achieve proper sealing. Only a small amount of material is introduced in the active part of the cavity with the purpose of minimal disturbance of the cavity tuning and the EPR signal.

The PVD working electrode was combined with a PFA-coated Ag wire pseudo reference electrode which was placed in close proximity (<1 mm) to avoid uncompensated resistance as much as possible without causing a short circuit. The reference can be fixated at that distance to the working electrode by making a hole in the PP just beside the Ag surface and leading it through from the back

to improve reproducibility. A Pt rod auxiliary electrode sat in the bulk reservoir on top of the flat part as close as possible to the entry of the flat part. *In-situ* experiments were performed in the Wilmad Supracil WG-810-A-Q. The setup was placed in a TE_{102} rectangular cavity in a Bruker E580 Elexsys spectrometer as shown schematically in figure 5.8.

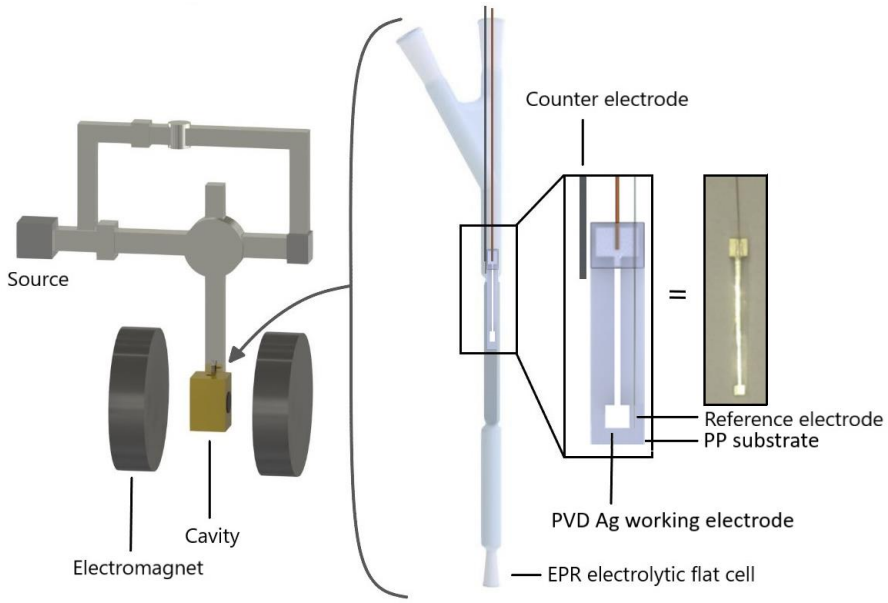

Figure 5.8: *Schematic drawing of the EPR-spectroelectrochemical setup (partly redrawn from* [159]*).*

The electrode was used for performing the two test cases mentioned in paragraph 5.2.3. Visual inspection showed that the total metal surface was electroactive meaning that the lead from the connection pad to the subjected surface also participated in the reaction, as shown in figure 5.9. The 22 mm x 0.3 mm lead had a significant contribution to the current. Due to the length of the Ag in the flat part and the potential being compared to the reference at the tip there was possibly a potential gradient present over the surface of the electrode. Overpotentials would be higher in the lead than at the tip potentially inducing undesired reactions.

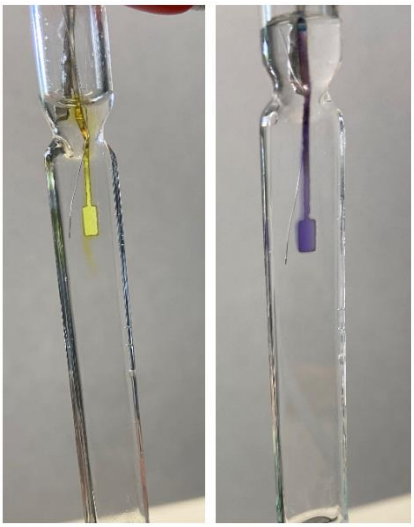

Figure 5.9: *Appearance of electrochemically generated BQ radical anion (left) and MV radical cation (right) in an EPR flat cell with a Ag PVD deposited working electrode (not deoxygenated).*

However, when performing electrolysis, the whole surface instantly produced the yellow and blue radical. When overpotentials would be too high, both systems could enter into a second electron transfer resulting in discoloration of that part of the surface (formation of MV^0 and BQ^{2-}). No such phenomenon has been observed with this electrode indicating that the Ag layer was thick enough to be sufficiently conductive, minimizing potential drop across the length of the Ag electrode. The connection pad and connection wire were also free from radical formation, thus the heat sealing technique resulted in a well-fitting PP coating.

The CVs of BQ in bulk and flat cell (figure 5.10) did not show many differences indicating that positioning of the electrode in the flat cell left enough space between the cell wall and the electrode and the reference was well-placed. The bulk measurement had a peak-to-peak separation of 118 mV.

The shape of the CV for the flat cell experiment was somewhat distorted in the sense that the peak was not only broadened but seemed to be topped-off, reaching a plateau and then falling back due to analyte depletion. Peak separation could therefore not be accurately determined for this measurement.

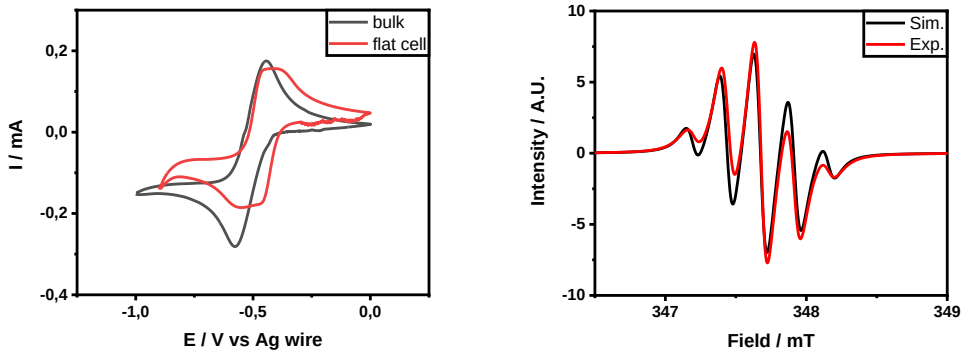

Figure 5.10: *CV of 5 mM BQ in ACN + 0.1 M TBAP on PVD electrode in bulk and flat cell at 50 mV s^{-1} (left) and the EPR spectrum at -0.5 V vs Ag wire at 5 mW microwave power with a field modulation amplitude of 0.1 mT and a frequency of 9.750 ± 0.001 GHz (right) (not deoxygenated).*

The potential difference between reaching the oxidation and reduction plateau was only 13.7 mV which could indicate that the actual peak was not reached as it was even less than that for the bulk experiment. Performing chronoamperometry on the peak potential in the EPR resulted in the spectrum shown in the same figure. The couplings were in accordance to the literature stated in section 5.2.3. The electrochemical behavior of MV^{2+} and the EPR signal are shown in figure 5.11. A shift in reduction peak potential occurred due to the use of the Ag pseudo reference electrode. Both curves showed a close-to-ideal response to the potential gradient. The peak separations for bulk and flat cell measurements were 60.8 mV and 34.5 mV respectively. This is similar to what was observed for BQ but here without the distorted peak shape. The fact that the peak separation in the flat cell was lower than expected might be due to the combination of exhaustive electrolysis (during several CV cycles) with the thin layer cell. This is counteracted by the fact that the ohmic resistance was not compensated for in the CVs. The intensity of the oxidation peak in the back scan in the flat cell was higher than in bulk. This could indicate a build-up of reduced species constrained in their movement.

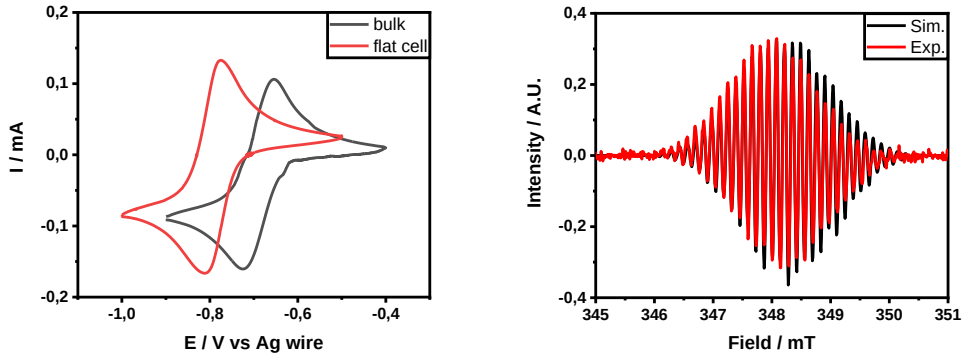

Figure 5.11: *CV of 5 mM MV in H_2O + 0.2 M Na_2SO_4 on PVD wire electrode in bulk and flat cell at 50 mV s^{-1} (left) and the EPR spectrum at -0.8 V vs Ag wire for 2.5 mM MV in H_2O + 0.2 M Na_2SO_4 at 2 mW microwave power with a field modulation amplitude of 0.1 mT and a frequency of 9.750 ± 0.001 GHz (right) (not deoxygenated).*

The CVs of the wire electrode, had better defined peaks with less separation than for the PVD electrode for the same cell geometry. The only difference being the electrode shape and surface area. Resistivity over the sputtered electrode and the lead was expected to be higher than for the wire due to the difference in cross-section area (6.0 x 10 µm² lead vs 4.4 x 10^3 µm² wire). The surface of the PVD electrode was flat and presumably more uniformly accessible than the wire which could explain the difference in behavior. The *in-situ* EPR electrolysis experiments were conducted on the peak potential. Acceptable signal-to-noise was obtained and parameters were in accordance to literature. Both electrode/reaction systems did only result in a signal of the reaction occurring at the working electrode and not of the species formed at the counter electrode.
The phenomenon which was mentioned in 4.4.1 ([50]) depends on the nature (paramagnetic or diamagnetic), the lifetime of the species and the ability to move from the bulk section to the flat section of the cell. Not observing the counter electrode product in the experiments indicates that at least one of these factors was favorable.

5.4 Conclusions

This chapter presented the design, construction and validation of two batch electrode designs fitted in a commercial EPR flat cell. The wire electrode is suitable to get an idea of the measurability of a certain radical in combined electrochemistry-EPR experiments. It is straightforward to make but has some limitations. The physical shape of the working electrode imposes non-ideal electrochemical behavior together with the effect of the confined space in which it has to be placed. The surface of a wire is not reproducibly polishable and therefore it does not allow for reproducible electrocatalyst deposition. The second batch electrode was constructed by exchanging the wire working electrode with a PP substrate deposited with a thin Ag layer by means of physical vapor deposition. The mask was used to provide the desired shape of the electrode with connection pad, connection lead and the subjected working electrode surface reaching the sensitive part of the cavity. This electrode is an improvement to the wire electrode due to its flat and reproducible surface. The general shape of the CVs in both solvents improved and the differences between bulk and flat cell were minimal. Peak potential determination from the CV was improved which is primordial for the *in-situ* generation of specific radicals. The design is cheap and versatile concerning the electrode material. The electrode can be deposited with several materials with the requirement of sufficient conductivity. It is ideal for cases where bulk electrode materials are necessary and can also serve as a substrate for more complex electrocatalyst deposition. The next chapter elaborates on this functionality by further improving the design.

Chapter 6

A versatile *in-situ* EPR approach for electrocatalyst research

This chapter presents the construction of a semiconductor based electrode enabling reproducible catalyst electrodeposition. This was assessed by deposition of Ag particles and a NiO layer together with scanning electron microscopy. The electrode displayed good spectroscopic sensitivity for simultaneous electrochemical electron spin resonance experiments.

This chapter has been published as: S. Neukermans, M. Samanipour, H.Y.V. Ching, J. Hereijgers, S. Van Doorslaer, A. Hubin, T. Breugelmans, A versatile *in-situ* EPR-spectroelectrochemical approach for electrocatalyst research, *ChemElectroChem,* 7 (2020) 4578-4586

6.1 Introduction

The previous chapter showed that *in-situ* EPR radical generation by electrochemical means is achievable with relatively simple electrode designs for batch measurements. Recent electrochemical research uses catalytic materials which are mostly nanostructured and require special deposition procedures (*i.e.* electrodeposition). To obtain uniform catalyst distribution and morphology, the surface of the substrate material should be flat and reproducible. On top of that, electrodeposition requires semi-infinite linear diffusion, sufficient surface conductivity and a homogeneous potential distribution over the working electrode. The wire electrode does not provide the required flat and reproducible surface. The PVD deposited electrode could be catalytic for certain reactions but showed acceptable voltametric behavior in bulk and flat cell.

One of the promising substrate materials possessing properties suitable for spectroscopic analysis techniques is Indium Tin Oxide (ITO) or other Transparent Conductive Oxides (TCO) like Aluminum Zinc Oxide (AZO). Multiple papers describe glass-supported ITO as a substrate because of its optical transparence and others deposited metallic particles on the surface [160–163]. It is being used in photovoltaic devices and thus has been already incorporated into EPR setups for electrically detected magnetic resonance [164]. However, the dimensions of commercial glass-supported electrodes do not allow their utilization in EPR flat cell applications.

The combination of *in-situ* UV-VIS/EPR spectroelectrochemistry was exploited by Neudeck and Dunsch in several publications using wire working electrodes [141], laminated Au and Pt meshes [165–167], LIGA electrodes [168] and laminated ITO-glass electrodes [169,170]. The latter focusing on the behavior of a polypyrrole layer on the surface and other hole-transporting organic substrates. Recently the use of mesoporous layers of ITO particles was reported for water oxidation and alcohol oxidation [171–173] and applied for the investigation of redox reactions in biomolecules. This electrode consisted of a Ti wire decorated with 50 nm ITO particles with the subsequent immobilization of proteins on the surface and was used in combination with an EPR tube [129].

In this chapter, the construction of a promising ITO-on-PET-based EPR-electrochemical setup fitting the commercial Wilmad flat cell for aqueous samples in a rectangular cavity in an X-band EPR spectrometer is demonstrated. The ITO working electrode has a flat surface allowing reproducible integration of (electro)deposited nano-scale catalysts. The construction is inexpensive and straightforward so experiments can easily be repeated multiple times. The setup is applicable in a broad range of reactions in both aqueous and non-aqueous environments and demonstrates reasonable electrochemical behavior in the EPR flat cell. Consequently, targeted *in-situ* radical generation is possible. It is optically transparent and very thin which is an improvement compared to the bulk metal electrodes because the material does not significantly interfere with the Q-factor of the resonator. The electrode surface area approaches the maximal available space in the flat cell producing the maximum radical concentration possible. As a proof of concept the electrodeposition of Ag nanoparticles and NiO layer was performed with consecutive *in-situ* use for the reduction of MV in aqueous solutions and BQ in ACN with detection of their radical intermediates demonstrating the sensitivity of the constructed electrode.

6.2 Experimental

6.2.1 Chemicals

Electrochemical measurements were performed in ACN (Chem-Lab, HPLC Grade) and MilliQ water (18.2 MΩ cm^{-1}) with respectively 0.1 M TBAP (Sigma-Aldrich, 99.0 %) and sodium sulphate (Acros Organics, 99.0%) as supporting electrolyte. BQ (Sigma-Aldrich, ≥99.5%) solutions were prepared in ACN and MV (Sigma-Aldich, 98%) in water. Depositions of Ag were performed using 1 mM $AgNO_3$ (Sigma-Aldrich, ≥ 99.0%) in ACN with 0.1 M $LiClO_4$ (Acros Organics, >99%). Ni depositions were performed in an aqueous solution with 0.01 M Ni $(SO_3NH_2)_2$ (Fluka, ≥ 99.0%), 0.227 mM $NiCl_2$ (Merck, ≥ 97.0%) and 0.025 M H_3BO_3 (Sigma-Aldrich 99.7%). Toluene was purchased from Merck (Uvasol for spectroscopy). All chemicals were used without any further purification.

6.2.2 Setup and procedure

All electrochemical experiments were conducted with a PAR VersaSTAT 3 potentiostat. The experiments performed in bulk and the depositions were recorded versus a saturated Ag/AgCl reference electrode with a Pt auxiliary electrode in a conventional undivided cell. The EPR spectra were recorded at X-band (frequencies specified in captions) in continuous wave mode at ambient temperature with a 0.1 mT field modulation amplitude and 100 kHz field modulation frequency, 5.12 ms time constant, sweep time of 10.49 s $scan^{-1}$ and a 0.2 mW and 0.8 mW microwave power for BQ and MV, respectively.

The Q-factors reported were determined by the built-in Q indicator of the Xepr programme. TEMPO (2,2,6,6-Tetramethyl-1-piperidinyloxy, Sigma-Aldrich, 98%) spin-count calibration was performed in the flat cell for concentrations ranging from 0.5 mM to 0.025 mM. at a power of 0,2 mW, sweep time of 10,49 s $scan^{-1}$ and with a time constant of 5.12 ms. The integral of the absorption curve was calculated considering that every molecule of TEMPO was EPR active. The same method and settings were used to determine the spin concentration of BQ and MV radicals generated on the custom ITO electrode.

Combined EPR-spectroelectrochemical measurements were performed in a Wilmad Supracil WG-810-A-Q quartz flat cell assembled as shown in figure 6.1. The setup was placed in a TE_{102} rectangular cavity in a Bruker E580 Elexsys spectrometer. Custom-made ITO working electrodes were made using ITO-on-PET microscope slides (8-10 Ω sq^{-1}, 200 µm thickness with a 700 nm ITO layer) obtained from SPI supplies and (60 Ω sq^{-1}, 178 µm thickness with a 100 nm ITO layer) from Sigma-Aldrich. This allowed it to fit inside the 500 µm thin gap of the quartz flat cell. The ITO layer of the SPI product had a homogeneous surface promoting reproducible electrodeposition of particles (figure 6.2A). This particular product was chosen because of its low resistivity (Bode and Nyquist plot of both in supp. info.) and high transmittance.

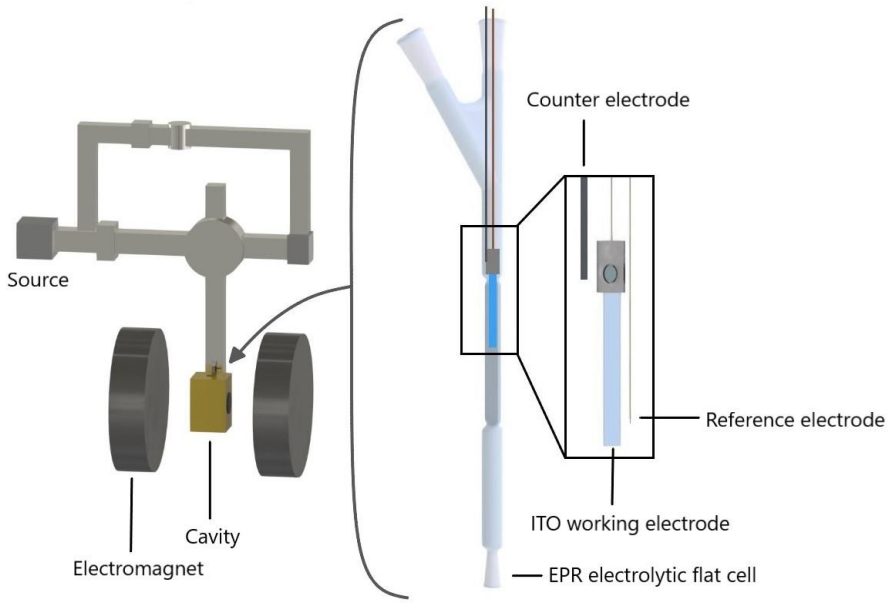

Figure 6.1: *Schematic drawing of the EPR-spectroelectrochemical setup.*

The increase in conductivity as function of the ITO layer thickness reaches a plateau as does transmittance at higher wavelengths [174,175]. Work of Do-Hyoung Kim *et al*. even suggests that electromagnetic wave shielding occurs with increasing film thickness [176]. The slides were cut to rectangles of 37.5 x 3.5 mm. The tip of the ITO working electrode was placed at the center of the flat part which coincided with the most sensitive section of the resonator. The junction with the connecting Cu wire was kept in the bulk section on top and was shielded by a PP encapsulation using a heat gun whilst being pressed against the semiconductor surface by carbon tape for maximum conductivity. The PP covered 10 mm of the ITO surface resulting in 0.96 cm^2 exposed working electrode surface area. A PFA coating covering a Ag wire with a diameter of 75 µm was used as pseudo reference electrode (stripped of the PFA at both ends) and positioned as close to the tip of the ITO electrode without causing a short circuit (<1 mm). The Pt auxiliary electrode was placed in the bulk section on top as close to the entry of the flat part as possible. The cell was filled with 1 ml solution submerging all electrodes while leaving the exposed Cu connection wire dry. This setup provided a cheap, straight-forward and versatile method for combined *in-situ* EPR and electrochemical measurements of electrodeposited catalytic materials.

6.3 Results and discussion

6.3.1 Electrodeposition

In order to do *in-situ* electrocatalyst research, a catalytic material should first be deposited on the ITO surface. It is possible to chemically synthesize particles and coat them on the surface of any material. Since the substrate is conductive, the catalytic material was electrodeposited directly on the ITO layer (figure 6.2A) after the electrode was assembled as mentioned in section 6.2. Deposition experiments were performed on the ITO obtained from SPI as the resistance of the Sigma-Aldrich product was too high ($2.25 \pm 0.23 \times 10^4$ Ω). Impedance values for the fitted Nyquist and Bode plots by R(RQ) and R(RQ)W circuits for the Sigma and SPI obtained ITO respectively, can be found in the supporting information. (Table S6.1). Every reference to ITO from hereon will be concerning the one from SPI unless stated otherwise.

Ag and Ni are active electrode materials for a number of reactions [177–182] and were therefore selected as catalyst material. Ag was deposited by reduction of Ag^+ from the solution with varying double pulse conditions. The nucleation potential was varied from -0.6 to -1 V vs Ag/AgCl for 1 to 2 s and the growth potential between -0.05 and -0.15 V vs Ag/AgCl for 50 to 150 s. The optimal parameters were found to be similar to what was published on a glassy carbon substrate resulting in the smallest and best distributed particles [183] namely 1.5 s at -0.8 V and 100 s at -0.15 V (figure 6.2B). The catalyst deposited onto the ITO layer did not show any discrimination between locations on the electrode in terms of particle size and morphology even though the surface resistance should theoretically vary from 62.9 to 94.3 Ω from connection to tip.

It was imperative to create the desired morphology at the tip of the electrode as it was positioned in the most sensitive part of the resonator. Deposition of a Ag layer by one pulse deposition at the nucleation potential was attempted for 5 min resulting in the formation and agglomeration of bigger clusters (figure 6.2C) giving the electrode a matt appearance (figure 6.3A). Ni was deposited by applying a potential of -1.3 V vs Ag/AgCl for 10 minutes and showed a tendency of depositing in 30 nm particles which clustered and formed a layer (figure 6.2D). As the layer was not electrodeposited under inert atmosphere, NiO should rapidly form. Total coverage of the ITO substrate was already visually evidenced by a shiny grey layer on the ITO semiconductor (figure 6.3B).

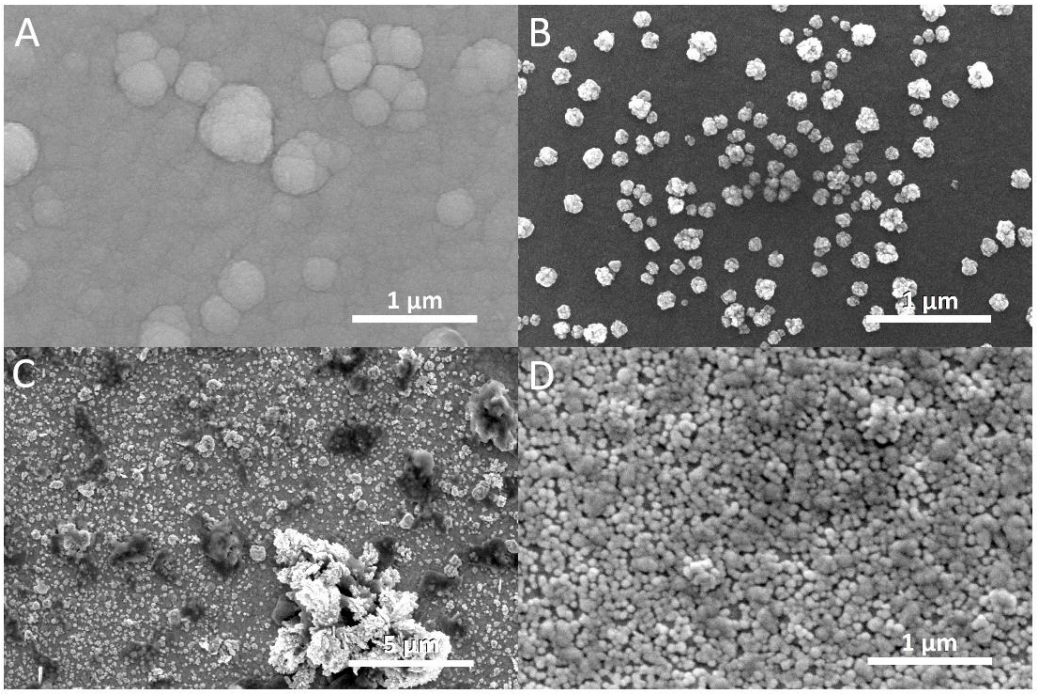

Figure 6.2: *Scanning electron microscopy images of bare ITO (A), Ag particles by double pulse deposition (B), Ag clusters by single pulse deposition (C) and NiO deposited on the ITO-on-PET (D).*

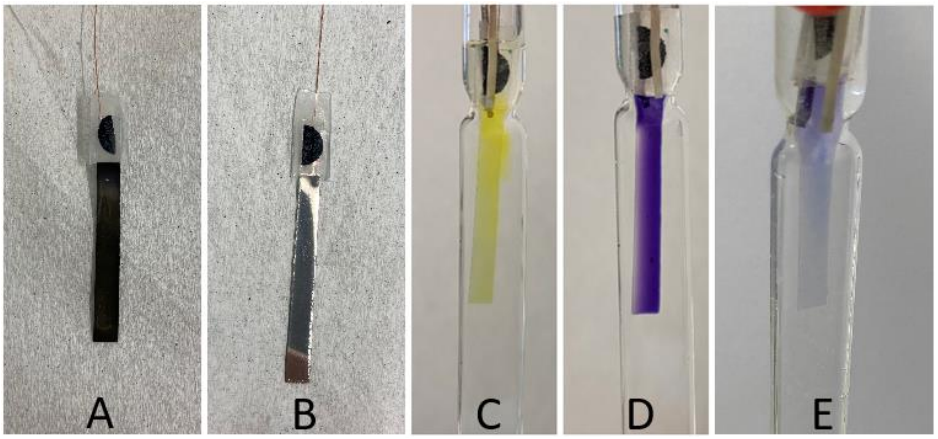

Figure 6.3: *Appearance of electrodeposited Ag/ITO (A) and NiO/ITO (B) on PET, electrochemically generated BQ radical anion (C) and MV radical cation (D) in an EPR flat cell on ITO (SPI Supplies) and (E) the MV radical anion generated on ITO-on-PET (Sigma-Aldrich).*

6.3.2 Electrochemical validation

The BQ radical anion could be observed visually through color change of the solution in the flat part from pale yellow to darker yellow and even orange in higher concentrations (figure 6.3C).

MV^{2+} reduction to the radical cation had a very distinct blue color (figure 6.3D). CVs of the bare ITO on PET, and the Ag- or Ni-deposited electrodes were done in an undivided setup and in the EPR flat cell. Figure 6.4 shows the response of the bare ITO electrode in both cases (BQ and MV). The splitting between oxidation and reduction peak of BQ was similar for both the bulk cell as the flat cell (0.6 V). The potential shift of 0.9 V between the cells was caused by the use of a pseudo reference electrode in the flat cell. The reduction reaction of BQ in the flat cell did not show a notable reagent depletion fallback after the reduction potential was reached. It should be noted that this reduction on a regular glassy carbon cathode displays normal reversibility [138].

MV was scanned to the second electron transfer in bulk and past the first in the flat cell. The peak splitting of the first wave was equivalent for both measurements (120 mV) and the currents were comparable. When the ITO acquired from Sigma-Aldrich was used, only reaction at the top section of the flat part was observed (figure 6.3E) indicating a too large potential gradient on the electrode surface to obtain the desired potentials in the center of the resonator.

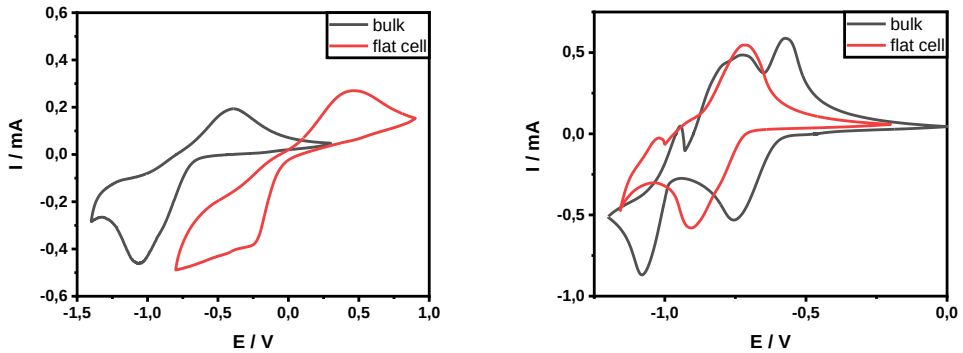

Figure 6.4: *CV of 5 mM BQ (left) and 5 mM MV (right) on bare ITO-on-PET electrode in bulk vs (sat.) Ag/AgCl and in EPR flat cell vs Ag wire at 25 mV* s^{-1} *(not deoxygenated).*

Hence, the resistance of the ITO layer should be preferably in the range of 8-10 Ω sq^{-1} (manufacturer's specification). Figure 6.5 presents the voltammetric data for the electrode with Ag particles deposited on ITO (Ag/ITO). The bulk experiment showed a bigger reduction current than that in the flat cell. This could be explained by the non-parallel positioning of the ITO surface to the flat cell wall, causing a smaller volume and thus less analyte to reach the surface of the electrode resulting in a lower current. Peak separation for both experiments was similar to that of the bare ITO electrode (0.6 V).

A difference exists between these CVs and the ones in figure 6.4 and can be found in the shape of the voltammogram. A more gradual current response for BQ can be seen between the peaks which could imply slower kinetics on this electrode or a contribution of the substrate material to the reaction.

The back scan for MV^{2+} reduction had, besides the oxidation peak of $MV^{\bullet+}$ radical cation, a clear oxidation peak at a lower potential. It was positioned at similar potentials as the oxidation of the neutral MV^0 in the bulk experiments but was much more pronounced even though the forward scan did not reach the second reduction peak. An explanation can be found in the adsorption of the neutral MV^0. As mentioned in chapter 5, some electrode materials promote the formation of an adsorbed MV^0 layer on the surface of which the oxidation peak in the back scan convolutes with its oxidation to $MV^{\bullet+}$ in solution (Equation 4.3 and 4.4).

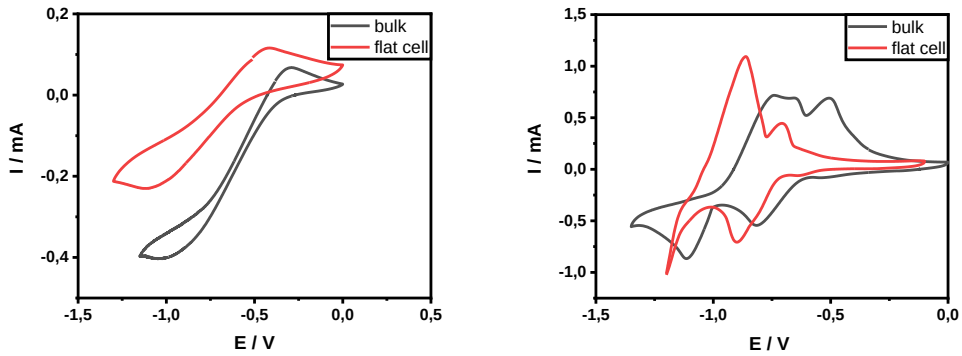

Figure 6.5: *CV of 5 mM BQ (left) and 5 mM MV (right) on Ag/ITO-on-PET electrode in bulk vs (sat.) Ag/AgCl and in EPR flat cell vs Ag wire at 25 mV* s^{-1} *(not deoxygenated).*

For BQ reduction the electrode with a NiO layer deposited on ITO (NiO/ITO) behaved similarly to the analogue Ag/ITO electrode (figure 6.6). There was a gradual separation of oxidation and reduction peaks in both bulk and flat cell with the latter showing less separation than any other BQ experiment (220 mV less).

The CV of MV in bulk is stretched out in both cells indicating that there is a background current with the peaks of MV superimposed. Hydrogen evolution onset potential could already be reached considering the steep increase in current. The CV vertex potential for the flat cell measurement was taken at -1.1 V. Scanning to more negatively potentials had the consequence of producing noisy current variations.

Presumably the thin ITO layer and its junction with the metallic particle deposits began to degrade at these negative potentials and associated current. This degradation could be the reduction of the ITO which we had suspected when scanning over a wider potential range with the bare ITO electrode.

The initially transparent surface produced a pinkish color on the surface, when scanning negatively, that faded in the back scan. This effect was undesirable because it may have influenced the electronic structure (conductivity) of the ITO and the transparence of the electrode by reducing the oxides in the semiconductor which may have led to inactive regions on the surface.

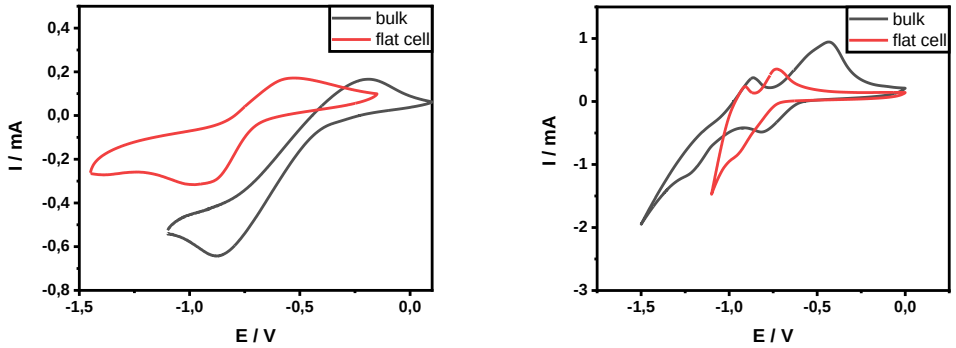

Figure 6.6: *CV of 5 mM BQ (left) and 5 mM MV (right) on NiO/ITO-on-PET electrode in bulk vs (sat.) Ag/AgCl and in EPR flat cell vs Ag wire at 25 mV* s^{-1} *(not deoxygenated).*

6.3.3 *In-situ* EPR-spectroelectrochemical validation

The Q-factor for the empty flat cell in the cavity was 2600 ± 100 which was in accordance with the specifications of the spectrometer for an empty cavity. Introduction of ACN + 0.1 M TBAP lead to a Q-factor of 700 ± 100, while H_2O + 0.2 M Na_2SO_4 reduced it even more to 300 ± 100. Introduction of a non-lossy solvent (toluene) lead to a Q-factor of 2000 ± 100. These Q-factors did not change when the ITO electrode was introduced into the electrolyte filled flat cell which was beneficial for the sensitivity.

In-situ electrolysis experiments were performed as described in section 6.2. The employed electrodes were bare ITO, Ag/ITO and the NiO/ITO. Half-height peak potentials of the corresponding CVs were applied. Figure 6.7 displays the spectra that were obtained for BQ and MV reductions. The EPR spectra were simulated using the EasySpin-5.1.11 module running in Matlab [184]. The following isotropic g and hyperfine values were used for the simulation of the spectra of the BQ radical anion: g_{BQ} = 2.0050 with A_H = 6.75 MHz (4), while for the MV radical cation g_{MV} = 2.0024, A_N = 11.85 MHz (2), A_H = 11.18 MHz (6), A_H = 4.4 MHz (4), A_H = 3.7 MHz (4). These are in accordance with the literature values [47,185].

The spectra showed that for the three electrodes that were utilized, the formed radicals for each reduction reaction were the same, indicating the formed radical was independent of the deposited electrocatalyst. This was as expected considering the mechanism of the reduction reaction being analogous on each of the catalytic materials and the substrate. The peak intensities differ depending on the electrode due to the different active surface area resulting from the electrodeposition. Comparison of the double integral of the acquired spectra with that of a TEMPO spin-counting calibration gave radical concentrations of approximately 83 µM BQ and 66 µM for MV reduction reactions (Tables S6.2, S6.3). When the concentration of BQ was increased, its reduction at the Ag/ITO electrode gave a broadened spectrum (figure 6.8). Using the same EPR parameters as above, the broadened spectrum can be simulated by simply increasing the Voigt linewidth from σ = 0.02 mT and γ = 0.034 mT, to σ = 0.144 mT and γ = 0.095 mT, where σ and γ are the Gaussian and Lorentzian components, respectively.

Broadening could be due to adsorption on the electrode surface and/or viscosity of the solution resulting in restricted mobility of the radicals. However, these phenomena were unlikely as broadening was not observed in the lower concentration experiments. A more probable reason for the spectral broadening is that a high concentration of the BQ radical anion is being generated, leading to dipolar interaction between the radicals. The high radical concentration may also result in the formation of aggregates which reduced the mobility of the radicals, further broadening the spectra.

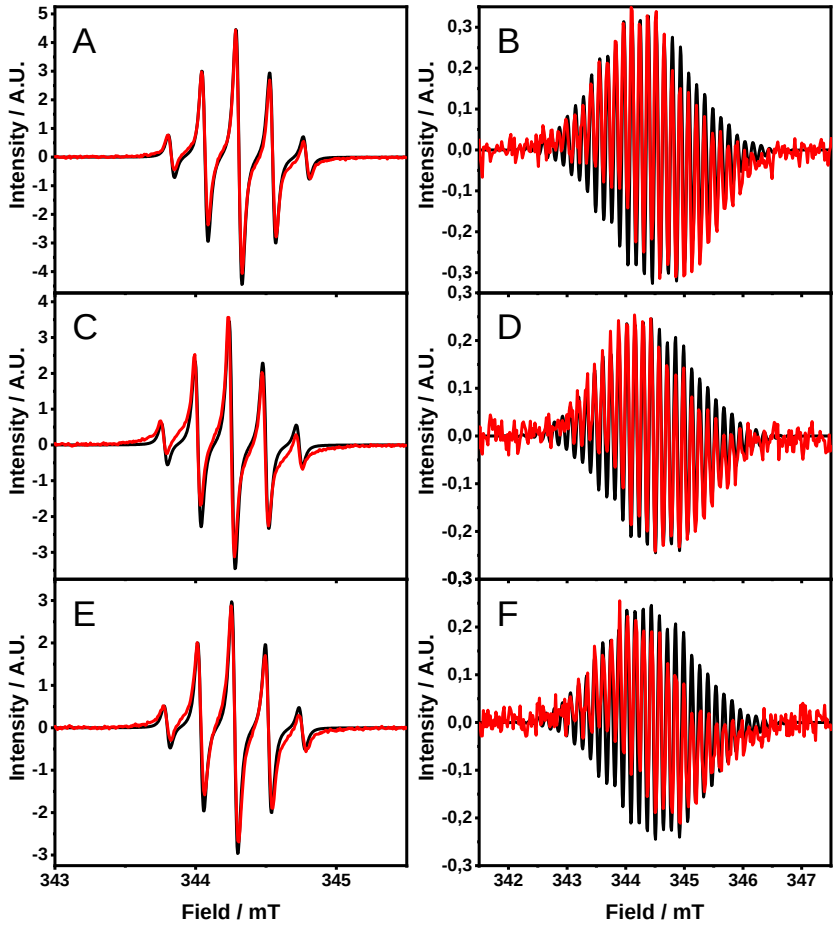

Figure 6.7: *. EPR spectra obtained from in-situ electrolyzing 0.5 mM BQ at 9.655 ± 0.001 GHz and 0.2 mW microwave power at -0.15 V (A), -0.75 V (C) and -0.75 V (E) vs Ag wire (left) and 5 mM MV at 9.661 ± 0.001 GHz and 0.8 mW microwave power at -0.8 V (B), -0.8 V (D) and -0.85 V (E) vs Ag wire (right) on bare ITO-on-PET (A,B) electrode, Ag/ITO-on-PET (B,C) and NiO/ITO-on-PET (E,F). The spectra are a mean of 10 scans over ~ 105 s. Red: experimental, black: simulation (not deoxygenated).*

The combination of favorable conditions for electrodeposition of catalytic material on the commercial ITO-on-PET substrate with generation of paramagnetic species or radicals in the sensitive part of the resonator on a high surface area electrode are critical for the detection of short living radicals (lifetime shorter than the timescale of 1 scan) in electrocatalytic research.

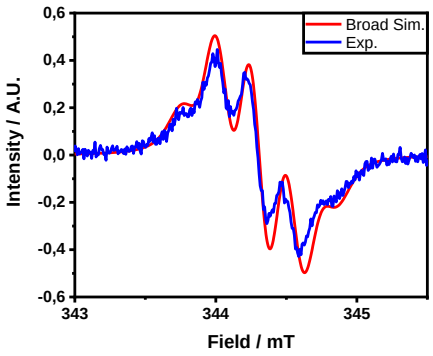

Figure 6.8: *EPR spectum obtained from in-situ electrolyzing 5 mM BQ at 9.661 ± 0.001 GHz and 0.2 mW on Ag/ITO-on-PET electrode with simulation of the broadened spectrum. The spectrum is the mean of 10 scans over ~ 105 s (not deoxygenated).*

6.4 Conclusions

Combining electrochemical catalyst research with *in-situ* EPR detection provides some challenges but also opportunities for the electrochemist. A working electrode material that is thin, inert, conductive and spectroscopically transparent can be found in an ITO layer deposited on PET as presented in this chapter. This commercially available substrate provided a reproducible surface area for electrocatalyst deposition and fitted in the flat part of the measuring cell, reaching the most sensitive part of the cavity. The electrode was thin and optically transparent and did not disturb the cavity tuning resulting in a good Q-factor. Both electrodeposited Ag nanoparticles and NiO layer were electrochemically and spectroscopically evaluated as electrodes for the BQ and MV reduction. Particles were evenly distributed across the total surface and could be tuned in size.

This setup shows the possibility of advanced electrocatalyst synthesis being tuned to fit the desired reaction pathway and final chemical products through *in-situ* monitoring. It can give an understanding of why an electrode material favors certain reaction pathways. The resistivity of the ITO layer was low enough to avoid a potential gradient from an order that would be detrimental for radical generation at the tip of the electrode. In general, the amount of radicals formed can be increased by raising the concentration of analyte or enlarging the active surface area. Especially the latter is of primordial importance for detecting short living radicals, as an increase in the bulk concentration is not always feasible or desirable. This setup maximally used the available space in terms of active surface area for commercial flat cells.

6.5 Supporting information

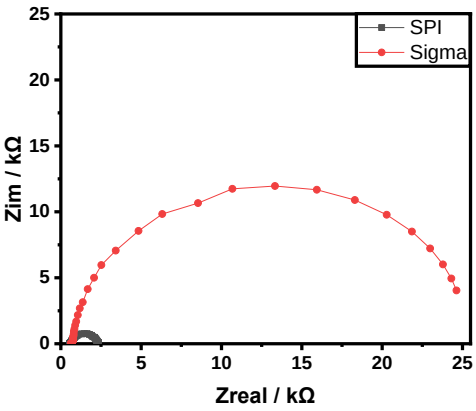

Figure S6.1: *Nyquist plot of the constructed electrodes in an undivided cell with 2.5 mM $K_4Fe(CN)_6$, 2.5 mM $K_3Fe(CN)_6$, 100 mM NaCl, 50 mM KCl and 20 mM phosphate buffer in water with pH adjusted to 7.15 by addition of NaOH. Frequency was varied between 105 Hz and 10^{-1} Hz at open circuit potential with 10 mV amplitude.*

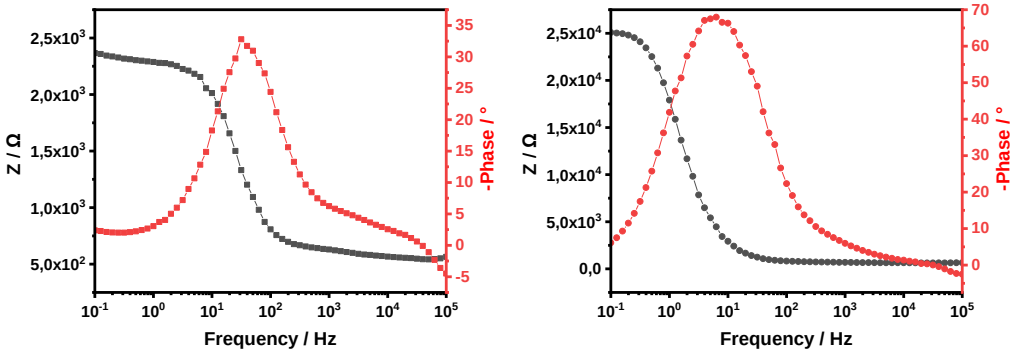

Figure S6.2: *Bode plot of the constructed electrode of SPI ITO (left) and Sigma ITO (right) in an undivided cell with 2.5 mM $K_4Fe(CN)_6$, 2.5 mM $K_3Fe(CN)_6$, 100 mM NaCl, 50 mM KCl and 20 mM phosphate buffer in water with pH adjusted to 7.15 by addition of NaOH. Frequency was varied between 105 Hz and 10^{-1} Hz at open circuit potential with 10 mV amplitude.*

Table S6.1: *Fitted parameters of the ITO purchased from SPI for a R(RQ)W equivalent circuit and of the ITO purchased from Sigma for a R(RQ) equivalent circuit. The χ^2 for the fits were between 0.004 and 0.026 for the SPI ITO and 0.009 and 0.014 for the Sigma ITO.*

	SPI ITO	**Sigma ITO**
Rs / Ω	$6.27 \pm 0.01 \times 10^{2}$	$7.87 \pm 0.54 \times 10^{2}$
Rct / Ω	$1.65 \pm 0.01 \times 10^{3}$	$2.25 \pm 0.23 \times 10^{4}$
CPE Y0 / F	$6.28 \pm 0.17 \times 10^{-6}$	$6.85 \pm 0.04 \times 10^{-6}$
CPE N	0.938 ± 0.001	0.961 ± 0.001
W Y0 / $s^{1/2}$ Ω^{-1}	$1.02 \pm 0.01 \times 10^{-2}$	/

Table S6.2: *Data TEMPO spin count calibration in flat cell.*

TEMPO concentration /mM	**Double integral / A.U.**
0.025	0.021 ± 0.005
0.050	0.041 ± 0.003
0.125	0.092 ± 0.015
0.250	0.181 ± 0.025
0.500	0.357 ± 0.024

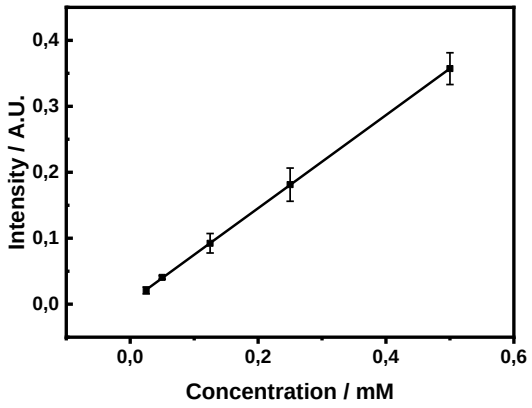

Figure S6.3: *TEMPO spin count calibration curve ($y = 0.7061x + 0.0043$).*

Table S6.3: *Spin count of experiments with spectra in figure 6.7.*

BQ double int. / A.U.	BQ spin concentration / mM	MV double int. / A.U.	MV spin concentration / mM	Electrode
(A) 0.076	0.101	(B) 0.062	0.082	ITO
(C) 0.060	0.078	(D) 0.048	0.062	Ag/ITO
(E) 0.054	0.071	(F) 0.042	0.053	Ni/ITO

Chapter 7

Small-volume electrochemical cells for low temperature EPR

This chapter presents the construction, design and validation of two electrode assemblies in a batch EPR tube. The first being a wire electrode design in a 3D-printed PP holder which is rigid and can be frozen with the sample. The second using an inert glassy carbon working electrode surface enabling reproducible voltammetric behavior. The latter can be used to perform exhaustive electrolysis and requires removal before samples are flash frozen for cryogenic EPR investigation.

This chapter is in preparation to be published as: S. Neukermans, V. H. Y. Ching, M. Samanipour, J. Hereijgers, S. Van Doorslaer, T. Breugelmans, Design and validation of small-volume electrochemical cells for cryogenic EPR, *ChemElectroChem*, 2021, to be submitted

7.1 Introduction

Chapter 5 and 6 focused on a commercial flat cell with custom-made electrodes for *in-situ* batch measurements. The cell geometry complicated the electrode design in order to obtain reasonably good electrochemical behavior. The flat cell is best suitable when using a lossy solvent like water and locates the solution in the electric field minimum of the resonator [35]. The more common EPR tube (in non-electrochemical EPR) can also be used for electrochemical measurements. Preferably, in combination with non-lossy solvents and a suitable cavity [186]. All of the previously constructed and described working electrodes could be placed in a tube when designed thin enough. The focus of this chapter is to design an electrode that will ultimately serve to investigate metal-centered complexes as electrochemical mediators for different follow-up reactions. The study of these complexes is beyond the timeframe of this work.

Despite the fact that voltammetric studies of transition-metal complexes are regularly performed with GC discs [187–189], cryogenic EPR investigation of these electrochemically-generated mediators is preferably done with metal wires [115]. Presumably, the choice of electrode material is affected by the fact that samples have to be flash frozen to slow down the paramagnetic relaxations in these complexes in order to obtain an absorption spectrum. GC discs are usually embedded in a solid polymer or resin which could make it susceptible to breaking or disconnecting from the connection point when frozen. Long wires can circumvent this problem by avoiding exposure of any other material than the wire to the frozen solution.

Here, two electrode designs are proposed for this type of electrochemical reactions and subsequent EPR detection. The first one is an EPR tube-adapted version of the wire electrode from chapter 5. The second one is based on a glassy carbon disc working electrode which is considered to have high chemical stability and promote a non-catalytic outer-sphere electron transfer for some reactions [190]. Both designs are first electrochemically validated for the reduction of BQ and MV in a batch configuration. The design showing the most desirable response, was subsequently used for electrolysis with sample freezing for cryogenic EPR detection.

7.2 Experimental

Electrochemical measurements were performed in ACN (Chem-Lab, HPLC Grade) and MilliQ water (18.2 MΩ cm^{-1}) with respectively 0.1 M TBAP (Sigma-Aldrich, 99.0 %) and sodium sulphate (Acros Organics, 99.0%) as supporting electrolyte. BQ (Sigma-Aldrich, ≥99.5%) solutions were prepared in ACN and MV (Sigma-Aldrich, 98%) in water. All chemicals are used without any further purification.

Electrochemical experiments were conducted with a PAR VersaSTAT 3 potentiostat. The experiments performed in bulk were done in a conventional undivided cell. Samples for EPR were frozen in liquid nitrogen as fast as possible without stopping the electrolysis. X-band continuous wave EPR measurements were performed on a Bruker ElexSys E580 spectrometer (microwave frequency 9.731 ± 0.001 GHz) equipped with a liquid-helium cryostat (Oxford Inc). The low temperature CW-EPR measurements were performed at 50 K using a field modulation amplitude of 0.5 mT, a field modulation frequency of 100 KHz, microwave power of 1.5 mW and a time constant of 40.96 s.

7.3 Results and discussion

An important consequence of EPR detection of metal-centered complexes is the significant cooling required to slow down their paramagnetic relaxation times. Reproduction and different reaction conditions impose extreme stress on the electrode when they have to be frozen with liquid nitrogen and thawed for reuse after. The choice of electrode needs to be weighed off between removal just before freezing or the use of a rigid and simple design that can be frozen with the sample.

7.3.1 Wire electrode

A wire electrode design is most suitable to be frozen with the sample, as no connections need to be made in the tube itself. The proposed design held the three wire electrodes in a 3D-printed polypropylene body (figure 7.1). The PP was printed in a triangular bar shape leaving enough space between the cell wall of the EPR tube and the PP for the solution. Three small channels (± 0.2 mm) were created in the PP for the wires to fit through. The metallic wires were provided with a PFA insulation similar to chapter 5. The Pt counter electrode was put through one of the channels ending in a volume created from a portion of the bar having a flattened corner and was stripped from PFA over 15 mm.

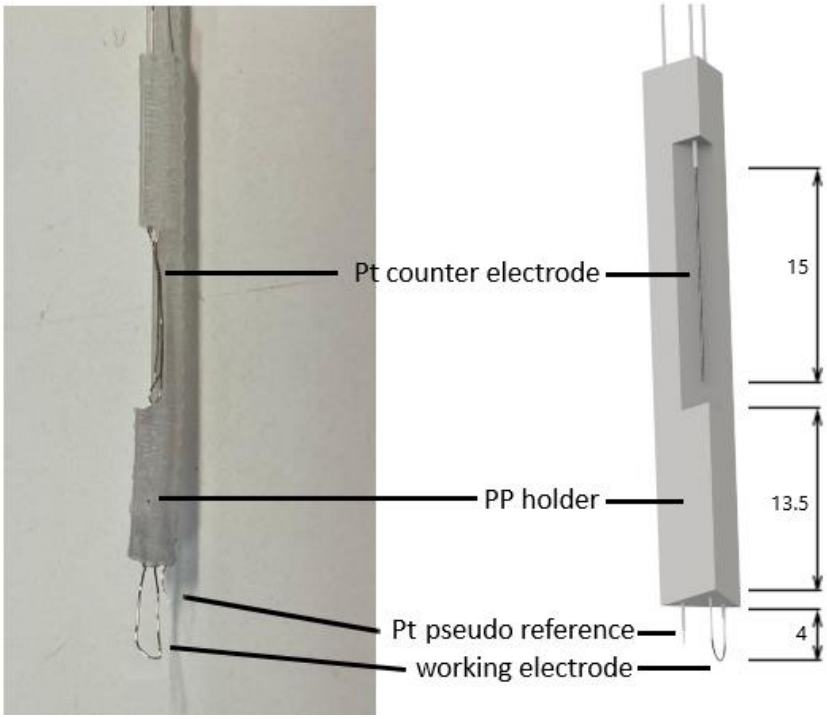

Figure 7.1: *Photograph (left) and digital image (right) of the 3D-printed polypropylene design with three Pt electrodes. Numbers indicated are dimensions in mm.*

The reference and working electrode were led to the bottom of the PP holder to a volume created between the bottom of the EPR tube and the PP holder. The Pt reference electrode was stripped from PFA over 1 mm. The working electrode was bent back to the PP and fixated therein. These electrode positions were chosen, attempting to equalize the distances between working and reference electrode to obtain similar potential control over the total length of the working electrode. Bending the electrode back up doubles the electrode surface area which is desirable in exhaustive electrolysis experiments. The counter electrode positioning, in the spatially separate volume, prevented the diffusion of radicals produced at the working electrode, diffusing to the counter electrode. If the subjected reaction is reversible, this radical could be electrolyzed to the parent specie when reaching the counter electrode. In the case of BQ, the diffusion coefficient is 3.11 ± 0.01 x 10^{-9} m^2 s^{-1} [156] in acetonitrile. The approximated distance that a specie is able to travel in one direction through means of diffusion can be calculated by Einstein's diffusion theory $x = \sqrt{2Dt}$ [191]. For this electrode x is 13.5 mm so t will be ± 8.14 h. The time-scale of electrolysis experiments for such small sample volumes (in the range of 100 -200 µl) is in the order of minutes so this phenomenon can be excluded with the used dimensions.

The electrochemical behavior of this electrode was, like in the previous chapters, investigated with the BQ and MV reduction reactions. The working electrode material was chosen to be a carbon-based wire. It was a Galvorn Carbon Nanotube (CNT) yarn of 130 µm diameter purchased at Dexmat [192]. The material was chosen for its rigidness, corrosion resistance and similar resistivity to metal wires (1.00 x 10^{-7} Ωm vs 1.06 x 10^{-7} Ωm for Pt and 1.56 x 10^{-8} Ωm for Ag [193]).

The bulk CVs can be found in figure 7.2. Both measurements showed a relatively large capacitive current at 150 mV s^{-1}. This can be assignable to the surface structure that is actually a yarn which differs significantly from a smooth wire. The yarn is built up out of several interlocked bundles of wires [192]. The peak separation for the BQ reduction was 272 mV and peaks were clearly distinguishable from the CV to perform electrolysis. The separation for MV reduction was 81 mV and between the reversible couple around 0.6/0.7 V.

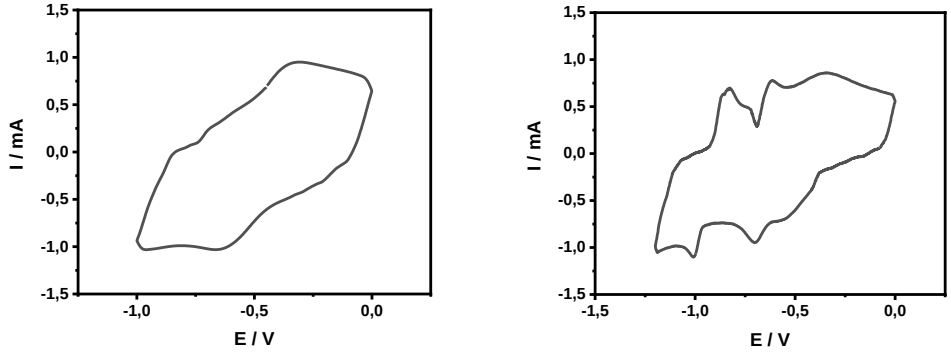

Figure 7.2: *CV of 5 mM BQ (left) and 10 mM MV (right) on CNT wire fixated in PP holder in bulk vs Pt wire at 150 mV s^{-1} (not deoxygenated).*

Both reduction and oxidation processes are sharper than for the BQ CV, probably because of the difference in concentration. A particular feature could be observed in both CVs. The peaks attributed to BQ reduction could also be observed in the MV CV. The BQ reduction in ACN was done at different scan speeds to check the nature of the process resulting in the reduction peak. A diffusion controlled peak should exhibit a linear relationship of the peak current with the square root of the scan speed. This was the case for the reduction peak at ± -0.6 V (Figure S7.1). The relation was: $I_p = -0.023\sqrt{v} + 0.0904$ with $R^2 = 0.9978$.

Both blanc measurements (in both solvents) did not show the peaks at similar potentials, indicating that the processes are analyte related (Figure S7.2). These two measurements contradict each other so no conclusions can be drawn. Nevertheless, CVs of figure S7.2 did show that the CNT electrode itself is not very suitable as an inert substrate for electrochemical reactions. At several potentials, peaks can be observed which could influence the reaction mechanisms, formed products, kinetics, etc. The CNT can be replaced by a metal wire similarly to chapter 5 with different/more ideal cell geometry when using a tube. This design will therefore not be pursued for combined electrochemical EPR measurements.

7.3.2 Glassy carbon disc electrode

The second design for the reduction of metal-centered complexes is based on a glassy carbon electrode which should be removed before freezing. When frozen, the GC rod could break or the fitting between plastic holder and GC could be interrupted exposing the electrode connection to the solution. GC has the advantage of being relatively chemically inert and exhibits slow kinetics. It was also used for electrochemical characterization by the group that synthesized the metal-centered complex for which the electrodes in this chapter were designed [194].

The outer diameter of the used X-band tube was 4 mm and the inner diameter 3 mm. The GC electrode was purchased from ALS and had a diameter of 1.6 mm (GC surface) with a total diameter of 3 mm (embedded in PEEK). The PEEK body was sanded to approximately 2 mm over its whole length. A PFA insulated Pt wire was led to the tip of the GC electrode with the PFA stripped from the tip as a pseudo reference electrode. The same type of wire was used as counter electrode and wound around the PEEK body of the electrode. The insulated wire had a diameter of 200 µm and kept the lead of the reference electrode in place, 127 µm without insulation. The assembled electrode measured 2.6 mm on the widest point, leaving 0.4 mm solution between the counter electrode and the tube wall.

The GC electrode was connected through a brass rod which was hollow at the end connection and fitted tightly around the electrode connection. The Pt wires were led out of the tube and fixated with tape at the top. Figure 7.3 shows the assembled electrode in an EPR tube. The solution needed to be brought into the tube before putting the electrode in place. Due to the surface tension of the solution and the small distance between the electrode and the tube, bubbles readily form, blocking the surface of the working and the reference electrode. As a result, the assembly had to be flicked several times for them to be removed.

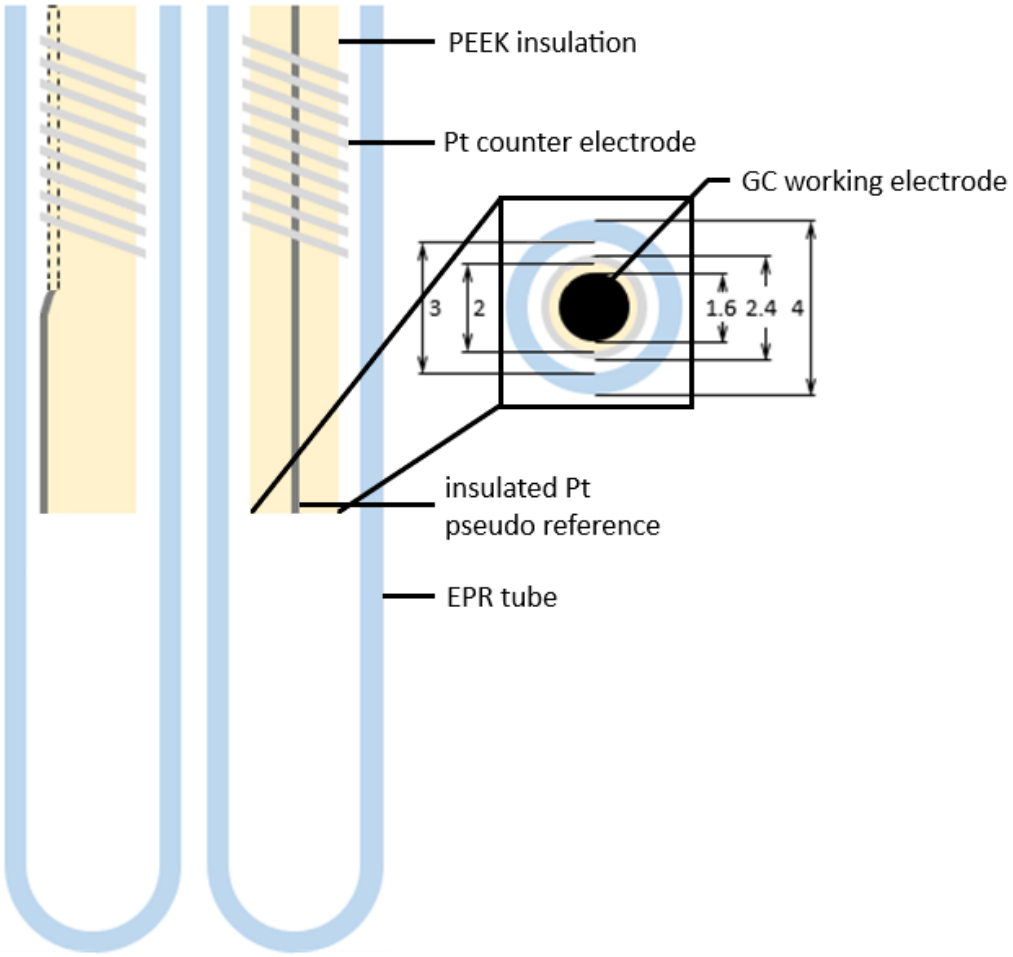

Figure 7.3: *Two side views of the GC electrode in an EPR tube and zoom of the electrode surface (not to scale). Numbers indicated are dimensions in mm.*

Sample volumes were approximately 100 µl, filling the tube for 14.14 mm. The electrode surface over electrolyte volume ratio was 0.02 which is rather small for exhaustive electrolysis. Adding the electrode 1 mm from the bottom of the tube resulted in an immersion depth of 23.65 mm without accounting for the counter electrode volume. The Pt counter electrode with a circumference of 0.399 mm only needed 1 revolution around the PEEK to excess the WE surface area. It was taken into account that some parts were compressed against the PEEK body and that, in worst case 25% of the surface was not or badly accessible.

A minimum of 6 revolutions of the counter electrode was used, which resulted in a surface area of 11.28 mm² and a ratio of 5.6 counter electrode surface over working electrode surface. The excess surface was added to compensate the solution resistance which increased with every revolution as revolutions are spaced-out fitting it tighter around the PEEK body.

Positioning the electrode in the tube sometimes resulted in movement of the counter electrode. Even with several revolutions, the drag between the counter electrode and the tube was strong enough and moved it away from the working and reference electrode. This could be due to varying inner diameter of the EPR tube (no tolerances given in specifications), outer diameter of the PEEK around the working electrode (uneven sanding) or the reference and counter electrode wires being stacked on top of each other. Several attempts were needed to properly assemble the cell. After the initial testing, we chose to use thin wall EPR tubes (3.2 mm inner diameter) with less variation in wall thickness (±0.013 mm). In this way, the bubble removal and assembly was significantly improved.

Visual inspection for electroreduction of BQ solutions performed in the EPR tube indicated that the BQ radical anion has a lifetime long enough to spread through the solution, turning it darker yellow (figure 7.4). The reduction of MV^{2+} to MV radical cation only resulted in a blue solution layer at the surface of the GC electrode. It is again an indication of its shorter lifetime and will increase the importance of the solution volume over WE surface area ratio to achieve a detectable concentration of radicals.

The CVs for the test cases in bulk and EPR tube are shown in figure 7.5. Both tube experiments were similar to their bulk analogues. Most differences in the CVs can be attributed to the cell geometry since that is the only variable. Compared to the setups from previous chapters, the Pt wire reference electrode is fixated in the cell assembly making measurements more reproducible. Literature for glassy carbon on benzoquinone in acetonitrile [149], where quasi-reversible behavior ($E_{pa} - E_{pc}$ = 87 mV) was observed, indicates that the peak-to-peak distance here was rather high with respectively 360 mV and 512 mV in bulk and in EPR tube.

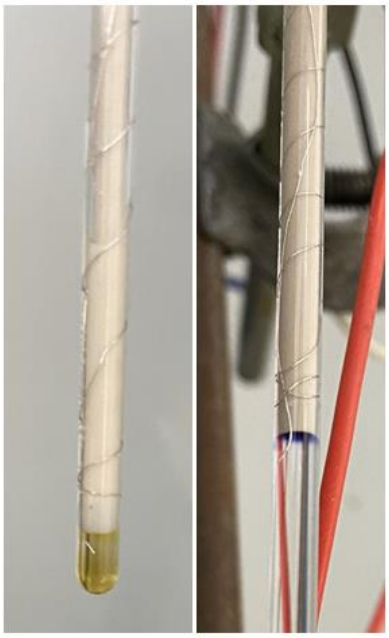

Figure 7.4: *Appearance of the electrode/EPR tube assembly with BQ radical anion (left) and MV radical cation generation (right).*

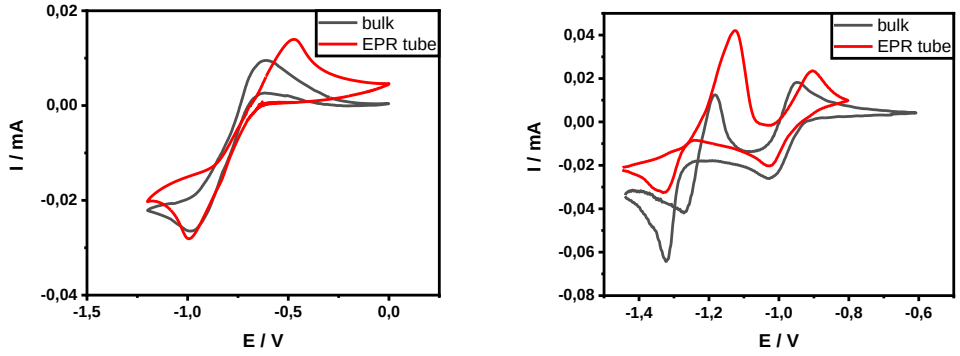

Figure 7.5: *CV of 5 mM BQ (left) and 5 mM MV (right) on GC in bulk and in EPR tube vs Ag wire at 50 mV* s^{-1} *(not deoxygenated).*

This leads to the conclusion that the relative positioning of the three electrodes with the counter electrode being wound around the PEEK of the working electrode seems far from ideal for analytical electrochemical measurements. The peaks in bulk were also less sharp than in the tube and the forward scan first goes into oxidation before the reduction wave starts. The oxidation wave in the back scan of the tube experiment was significantly bigger than for the bulk experiment which could indicate restriction of diffusion by the tube dimensions so more reduced species were still in the vicinity of the electrode.

The MV CV in bulk had a peak separation for the first one-electron transfer of 76 mV in bulk and 121 mV in EPR tube. The value in bulk was similar to literature [147] (80 mV, not exactly stated). The relative positioning of the electrodes was analogous to the BQ reduction but here, the shape of the voltammogram was not very different from literature. Possible explanations for this discrepancy can be found in the previously stated difference in charge between the two analyte molecules (chapter 5) or it could have originated from the resistance of the electrolyte, which is significantly higher in acetonitrile compared to water. Both of the oxidation peaks of MV for the tube experiment were shifted to higher potentials compared to bulk ones, this is also presumed to be due to increased resistance, more than due to the oxidation of the adsorbed MV^0 like in equation 5.4. Electrochemically, the electrode design behavior to potential variation was satisfactory to continue to EPR detection of the formed radicals in chronoamperometric experiments.

To obtain the EPR spectrum, the electrolysis was performed at peak potential with the electrode positioned at around 1 mm from the bottom of the tube. While the electrolysis was running, the tube was slowly moving downward so the solution first located at the counter electrode moved to the working electrode. This convection firstly helped refreshing the solution and ensured that the reduced species from the working electrode were not able to diffuse to the counter electrode to be reoxidized.

Secondly, it increased the total current passed to the solution by supplying analyte to the electrode, increasing the amount of radicals formed. Lowering the tube was done slowly (± 0.5 mm s^{-1}). The movement was established by using an electrical motor with an adjustable resistor for power control and gears to transfer the movement to a custom EPR tube holder. The counter electrode started to be increasingly exposed to the atmosphere and the tube was then 'dropped' in liquid nitrogen during electrolysis to flash freeze the formed radicals. This 'dropping' was done by increasing the speed of the downward movement, still gently sliding the tube in the liquid nitrogen to prevent it from breaking.

The electrolysis of BQ at peak potential and subsequent freezing resulted in the EPR signal presented in figure 7.6. The simulated parameters together with the ones from literature can be found in Table 7.1. The parameters match well with the two references with only the g_y deviating. Both of the references used a solvent different from ours and only state or the g-tensor or the hyperfine tensor. Electrolysis of MV was performed similarly. However, the shorter lifetime of the radical required faster freezing of the sample in order to keep the radical from decaying. The aqueous solution of MV expanded and broke the thin-walled EPR tube.

The detection of MV radical cation at low temperature was not pursued to avoid breaking more tubes which are roughly 5 times more expensive than the thicker walled ones and are more prone to breaking. The purpose of this setup was to measure oxidation states of electrolyzed metal-centered complexes. These experiments are done in acetonitrile and the molecules with in their subjected oxidation stated are expected to have a longer lifetime than the MV radical cation reducing the need for fast freezing and consequently tube breaking is less of an issue.

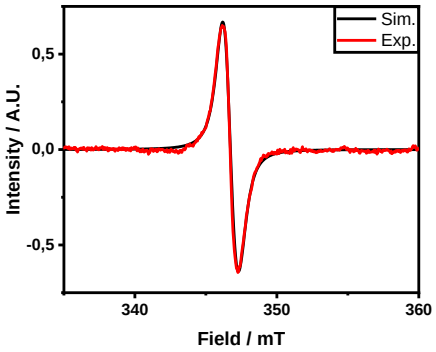

Figure 7.6: *EPR Spectrum and simulation for BQ radical anion in ACN at 50 K after electrolysis of 5mM BQ at -1 V vs Ag wire on GC electrode.*

Table 7.1: *EPR parameters for BQ radical anion compared to literature values (A in mT).*

	g_x	g_y	g_z	A_x	A_Y	A_z
Simulation	2.0065	2.0063	2.0023	-0.35	-0.059	-0.31
Literature	2.00645[a]	2.00526[a]	2.00229[a]	-0.350[b]	-0.059[b]	-0.310[b]

[a] from ref [195] with error 0.5 x 10^{-4} in frozen isopropyl alcohol
[b] from ref [196] with error ± 0.007 mT at 123 K in deuterated propan-2-ol

7.4 Conclusions

Two setups were designed to perform exhaustive electrolysis in an EPR tube with the possibility of subsequent sample freezing. Both were very different and approach the freezing problem from another angle. The first design was chosen for its rigidness to enable sample freezing with the electrode in the tube and the electrolysis still running. This design; the wire electrode design, housed three wire electrodes in a 3D-pinted PP holder and was equipped with a carbon nanotube yarn for the electrochemically screening of the reduction of benzoquinone in acetonitrile and methyl viologen in water. The electrochemical measurements showed a rather large capacitive contribution to the current, indicating a large surface area due to the structure of the CNT surface. Some peaks were unassignable in the methyl viologen CV and the blanc measurements showed non-ideal electrochemical behavior. For these reasons, the design was not used for EPR measurements but it can nevertheless be used when metal wires are chosen as working electrode material. Chapter 5 showed the advantages and shortcomings in that regard for flat cell applications.

The second strategy was to remove the electrode after electrolysis so an electrode material could be chosen that is known to behave favorably. The design consisted of a commercial inert glassy carbon electrode. The reference and counter electrode had fixed positions, increasing reproducibility. The electrode assembly was used for the two testcases with only small differences between experiments in bulk and in the EPR tube. During exhaustive electrolysis, the EPR tube was lowered automatically while the electrode remained in place. This ensured that while the solution in the tube moved towards a liquid nitrogen container under the setup, there was no risk of freezing the electrode which could break under low temperature conditions. The technique worked for long living radicals in an organic solvent but caution is advised when using aqueous solutions in the EPR tube because it is prone to breakage due to sudden expansion of the fluid upon flash freezing. The setup will be later used for the detection of paramagnetic form(s) of metal-centered complexes which are expected to have a sufficiently long lifetimes and are soluble in acetonitrile.

7.5 Supporting information

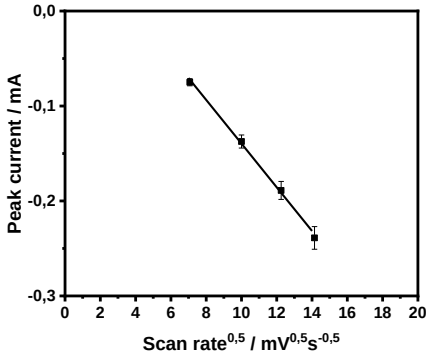

Figure S7.1: *Peak current vs square root of scan rate for 5 mM of BQ in ACN + 0.1 M TBAP on the CNT electrode vs Pt wire at 50, 100, 150 and 200 mV s^{-1}.*

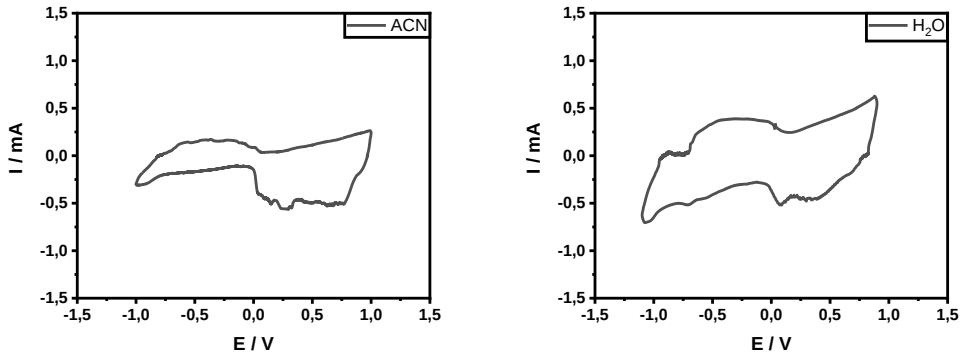

Figure S7.2: *Blank CVs of the CNT electrode in ACN + 0.1M TBAP (left) and H_2O + 0.2 M Na_2SO_4 (right) vs Pt wire at 100 mV s^{-1}.*

Chapter 8

An *in-situ* electrochemical-EPR channel flow cell: construction and validation

This chapter presents the construction, design and validation of a flow cell to perform *in-situ* electrochemical EPR experiments which combines conditions to determine kinetic properties and simultaneously detecting intermediates.

This chapter has been published as: S. Neukermans, J. Hereijgers, H.Y.V. Ching, M. Samanipour, S. Van Doorslaer, A. Hubin, T. Breugelmans, A continuous *in-situ* EPR-electrochemical reactor as a rapid in-depth mechanistic screening tool for electrocatalysis, *Electrochemistry Communications*, 97 (2018) 42-45

8.1 Introduction

From an electrochemical perspective, the commonly used flat cell setups like the ones mentioned in chapter 5 and 6 have some drawbacks: i) the cell surfaces are sometimes irreproducible, ii) the shape of the surface and the small cell size compared to the electrode surface area prevent semi-infinite linear diffusion, and iii) the potential control is done by a pseudo reference electrode [94,159], which needs to be well-positioned for data collection to be reliable, i.e. adjacent to the working electrode and in a stable environment. Often in static setups the pseudo reference and the working electrode are positioned in the flat section of the cell where radicals are generated using chronoamperometric techniques. However, the potential of the pseudo reference electrode can fluctuate during the experiment, as reactants are consumed and products are generated that subsequently diffuse from the electrode surface. These shifts in potential cannot be detected before or after the experiment using a known redox couple.

The use of hydrodynamic characterized flow for electrolyte supply, as mentioned in chapter 3, helps to exclude some of the drawbacks encountered in batch or flat cell setups [76]. For the latter, Compton *et al.* reported a rectangular set-up where the reference and counter electrode were positioned at larger distances from the working electrode combined with the use of a current booster [78] and calculated the effect on peak displacement [77].

This chapter describes an *in-situ* flow cell utilizing channel electrodes made out of polyoxymethylene (POM) with the advantages of being modular, facilitating flow electrochemistry, allowing good potential control and the use of POM as a sealing agent. We have evaluated this platform using CV and LSV on BQ in water, and chronoamperometry coupled to CW EPR at X-band on BQ in ACN and MV in water.

8.2 Experimental

8.2.1 Chemicals

ACN (≥99.9%) was purchased from Chem-Lab. BQ (≥99.5%), MV (98%) and TBAP (99.0%) were purchased from Sigma-Aldrich. Sodium sulphate (99.0%) was supplied by Acros Organics. All chemicals were used without further purification. Aqueous solutions were prepared with Milli-Q water (18.2 MΩ cm^{-1}). All solutions were purged with nitrogen before being pumped through the setup.

8.2.2 Setup

The constructed cell was made out of two pieces of POM (Eriks Baudoin) of which one contained a small channel with a width of 6 mm and a height of 0.4 mm. The electrodes were embedded in the second part by heat treatment. The working electrode was a silver foil (99.9985%) from Alfa Aesar, the counter electrode was a platinum sheet (99.95%) from Goodfellow and the pseudo reference electrode was a platinum wire (99.99%) from Science Products. The reference was located <1 mm upstream of the 4 by 5 mm working electrode and the counter electrode was positioned 3.3 cm downstream of the working electrode and measured 4 by 25 mm (Figure 8.1). It could be further observed that between the work and counter electrode, the use of POM is minimized. From here on, this part will be called 'the window'. This part was positioned in the sensitive part of the resonator. Tubing connections were made with Teflon rings which are held in place with PEEK spacers. The channel itself has a reservoir at the inlet, followed by a narrow channel of 35 × 2 × 0.4 mm which then resulted in the wider channel where the electrodes were positioned.

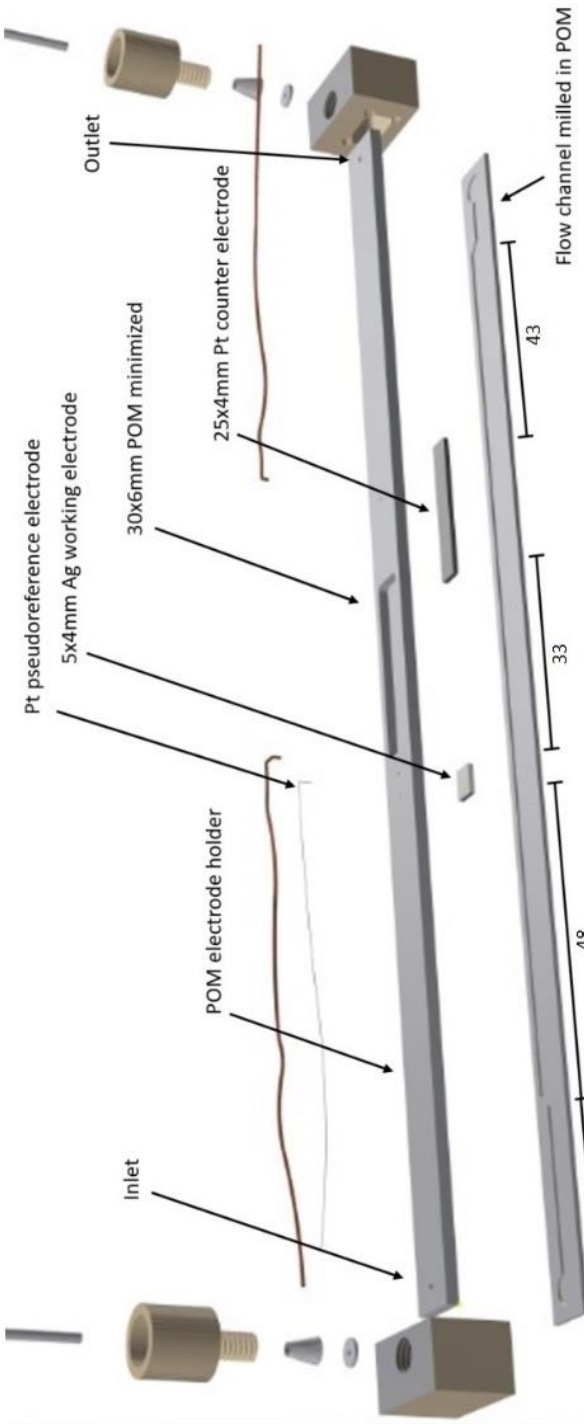

***Figure 8.1**: Exploded drawing of the in-situ EPR channel electrode.*

8.2.3 Electrochemistry

Electrochemical measurements were performed using an Autolab PGSTAT302N potentiostat without any need for a current booster. Potentials applied in the experiments were derived from CV cathodic peaks. Electrodes were subsequently polished with 1 µm and 0.3 µm Al_2O_3 powder from Streurs.

8.2.4 EPR spectroscopy

The cell was positioned in a TE_{102} cavity in an X-band Bruker E580 Elexsys spectrometer in CW mode with the working electrode positioned under the sensitive part of the resonator and the counter electrode above.

8.3 Results & discussion

8.3.1 Cell design

By adapting a previously reported modular design [76], our channel flow cell enabled the easy replacement and adjustment of electrode materials and improved reproducibility of the results. Our channel configuration with the inlet to the working electrode being 40 mm, ensured a Poiseuille flow profile [197] with respect to the flow rates used in this chapter. It allowed the determination of kinetics and mass transfer parameters. Potential control was achieved by positioning the pseudo reference electrode <1 mm upstream from the working electrode in an environment where it was not affected by concentration changes or products that formed at the counter electrode. In this setup the potential of pseudo reference only shifted 20 mV over 3 working hours.

POM was used to build the channel flow cell because this cheap material is rigid, easy to handle, can be milled, sealed by melting and is resistant to most solvents. It also did not give an EPR signal in the organic radical region. However, solid pieces of POM made the cavity harder to tune, reducing the sensitivity.

Therefore, we have introduced the window in our design which reduced the POM wall thickness to 0.8 mm inside the sensitive part of the resonator. This resulted in good tune-ability of the resonator, implying that POM is suitable for use in EPR applications. The window also provided a visual detection of the formation of colored radicals and products, when not positioned in the resonator. By sealing the setup with the same material, the use of potentially reactive sealing agents was avoided. The POM elements were easy to reproduce and precious metal components could be recovered for reuse. To the best of our knowledge this is the first *in-situ* EPR-electrochemical setup constructed with POM.

8.3.2 Electrochemical characterization

The two electron reduction of BQ in unbuffered water [139] was used to characterize the electrochemical properties of the cell. For more mechanistic information the reader is referred to the literature [140–142]. During the electrochemical characterization, multiple Ag working electrodes were used in order to see the influence of the replacement of electrodes. This did not result in any changes on the measurements.

The initial design had a distance of 6 cm between the WE and CE to ensure that none of the electrodes could interfere with the microwaves in the cavity. Figure 8.2 shows a photograph of that configuration with the inlet and outlet PTFE tubing together with the solution reservoirs. Preliminary *ex-situ* electrochemical testing through CV of BQ solution in water showed a cut-off in current when the peak potential and associated peak current should be reached (figure 8.3). The distance between the electrodes and the channel dimensions of 0.4 mm by 6 mm made the potentiostat reach its compliance voltage because of the high cell resistance. The electrodes were then positioned at 3.3 cm as indicated in figure 8.1 which was still more than sufficient to keep both electrodes out of the sensitive part of the resonator, as evidenced in chapter 5 (figure 5.3).

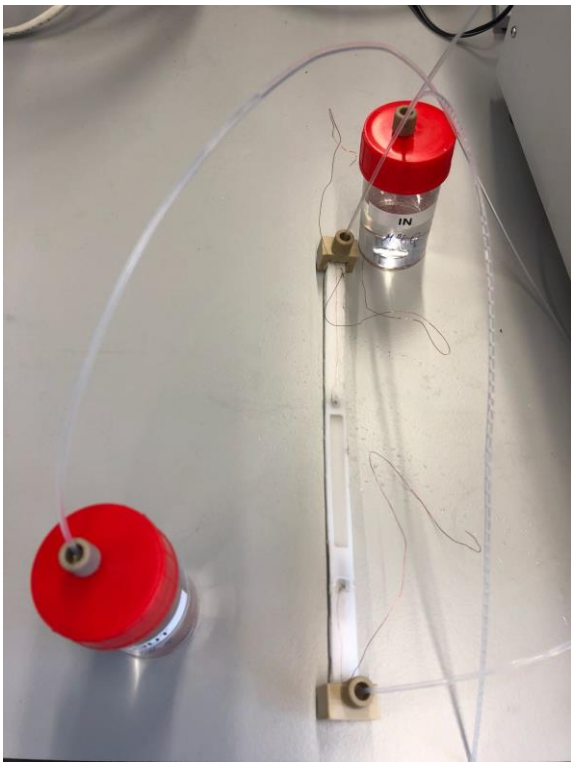

Figure 8.2: *Photograph of the reservoir connected POM channel flow cell with 6 cm distance between WE and CE*.

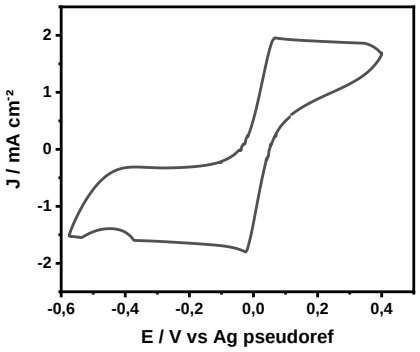

Figure 8.3: *CV of 5mM BQ in water with 0.2 M Na_2SO_4 at pH 4.5 recorded at 50 mV s^{-1} at 0.007847 ml s^{-1} in the channel electrode WE and CE positioned at 6 cm (not deoxygenated).*

To validate the configuration with smaller distance between the WE and CE, it should fulfil the boundary conditions of a channel flow cell electrode. The diffusion coefficient of BQ was calculated by applying the equation 3.27 for channel electrodes.

The same order of magnitude and linearity (figure 8.4 A) was observed with our setup, hence fulfilling the necessary conditions of a channel electrode, as was expected. One of the LSV measurements in the channel electrode can be found in figure 8.4 B. The diffusion coefficient was determined to be $8.75 \pm 0.41 \times 10^{-10}$ $m^2\ s^{-1}$ which was very similar to the value obtained from RDE measurements in (figure 8.4 C) governed by equation 3.25 ($8.46 \pm 0.17 \times 10^{-10}$ $m^2\ s^{-1}$). Both values were within the literature range for BQ and hydroquinone (7.3 to 12.6 × 10^{-10} $m^2\ s^{-1}$) [198–200].

Other than the expected increase in current, the CVs recorded with and without flow display some differences (figure 8.4 D). The static CV was distorted in the sense that the oxidation peak had a more negative potential than the reduction peak. This effect could be caused by a local change in pH or a changing environment of the pseudo reference electrode. In flow, the reduction peak was broader and bigger than the oxidation peak. This was most likely caused by the convection of recently reduced species away from the electrode in the microchannel reactor, hindering reversible oxidation afterwards. It needs to be stressed that the usage of CV had the purpose of determining the potential that should be applied for radical generation.

8.3.3 Spectrometric characterization

The one electron reductions of BQ in ACN [139] and of MV in water [90] are used to assess the performance of the channel flow cell inside the resonator for *in-situ* generation and EPR detection of radicals. The applied potentials for radical generation are derived from the *in-situ* CVs (figure. 8.5).

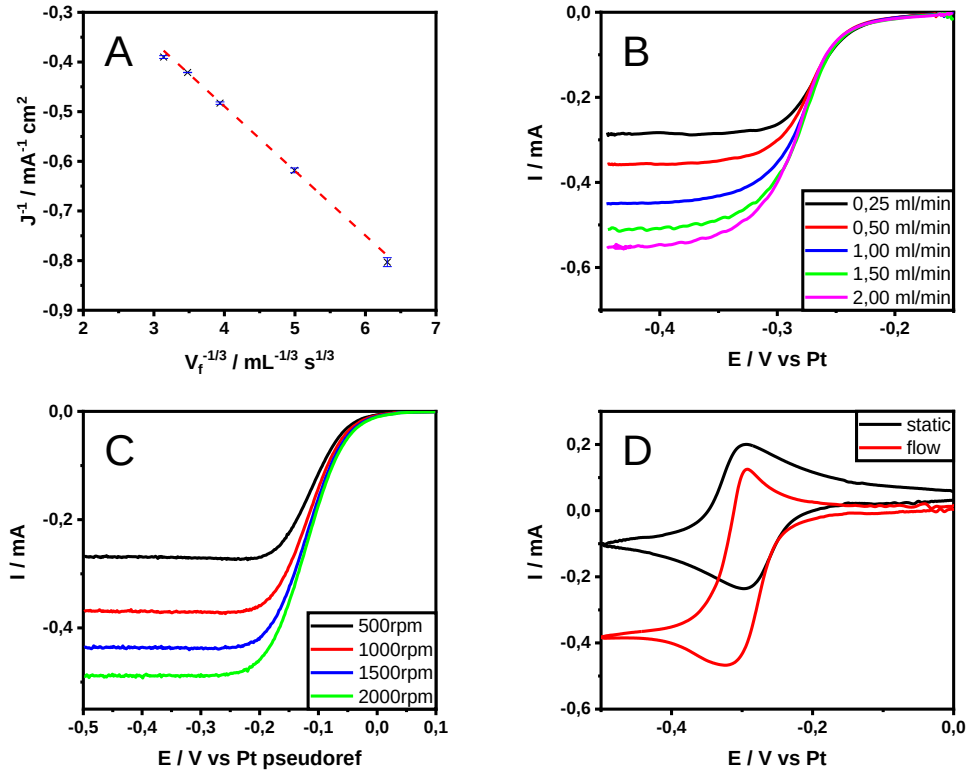

***Figure 8.4**: (A) Linearity of LSV data compared to Eq. 3.27. (B) LSV in the channel electrode recorded at 10 mV s^{-1}. (C) LSV with RDE in bulk at 10 mV s^{-1} (D) CV at 0.007847 ml s^{-1} and 50 mV s^{-1}. The solution consisted of 5 mM BQ in water with 0.2 M Na_2SO_4 at pH 4.5 (not deoxygenated).*

The obtained spectra from the chronoamperometric EPR measurements were in accordance to literature [79,90]. $BQ^{\bullet-}$ showed a very clear spectrum after one scan which indicated that the lifetime of this radical is sufficient to reach the sensitive part of the cell in resonator before decaying. On the other hand, $MV^{\bullet+}$ showed a noisier spectrum even after 35 scans which is consistent with the relatively shorter lifetime of the radical. In *ex-situ* CV experiments at a flow rate of 0.00416 ml min^{-1} the blue color of $MV^{\bullet+}$ did not "migrate" to the most sensitive part of the window. This suggests that a substantial amount of the generated $MV^{\bullet+}$ had already decayed before arriving at the center of the window, which coincides with the center of the resonator where its sensitivity is maximized.

It should be noted that water is not an ideal solvent because its polarity makes it susceptible for electromagnetic radiation. The use of higher flow rates and higher microwave power only resulted in small improvements to the signal. In previous static measurements shown in chapter 5, a period of time was needed for $MV^{\bullet+}$ to accumulate before it could be detected. Accumulation was not possible in a flow cell, at a certain time the concentration gradient of $MV^{\bullet+}$ along the channel will reach steady-state. The decay of the $MV^{\bullet+}$ was almost not visible in the CV in figure 8.5 because of the experimental timescale of such experiments. Chronoamperometry at more negative potentials (−1.1 V vs the Pt pseudo-reference), did not give an EPR signal in *in-situ*, nor blue coloration in *ex-situ* measurements. This was consistent with the CV of MV where at a second reduction wave $MV^{\bullet+}$ undergoes a second electron transfer to give neutral and diamagnetic MV^0 (Figure 8.6). During CVs of 50–100 mV s^{-1} with a flowing solution 0.00083 ml s^{-1} to 0.00417 ml s^{-1}, coloration at the first reduction wave, followed by decolorization at the second reduction wave, confirmed the two-step reduction process. This precise control over the potential highlights the stability of the pseudo reference electrode potential arising from this channel flow cell design. Furthermore, the EPR spectra in figure 8.5 and 8.6 clearly show that this design is suitable for the electrochemical generation and detection of radicals.

Redox couples of BQ in both water and ACN showed the same peak shape indicating that the solvent does not cause this shape change compared to bulk experiments. The redox couple of MV did not show any distortions due to the dimensions or the electrode configuration of the cell. This may be due to the positive charges of the MV species which allows migration or better kinetics of the reaction. The first oxidation peak in the back scan of figure 8.6 between -0.8 V and -0.7 V showed similarities to the adsorption phenomenon explained in chapter 5. The peak was a composition of two peaks where one is the oxidation of the adsorbed diamagnetic MV^0 and the other the oxidation of the MV^0 in solution.

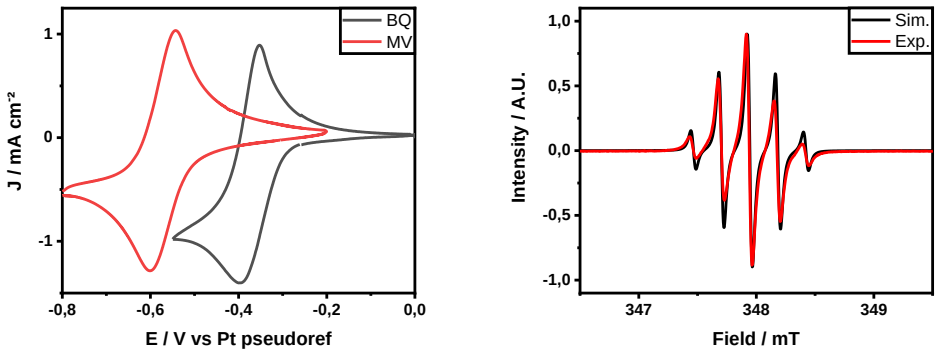

Figure 8.5: *CV of 5 mM BQ in acetonitrile with 0.1 M TBAP with a flow speed of 0.00333 ml s^{-1} and 50 mV s^{-1} and of 5 mM MV in H_2O + 0.2 M Na_2SO_4 with a flow speed of 0.00167 ml s^{-1} and 100 mV s^{-1} (left). EPR spectrum of electroreduction of the BQ solution at −0.5 V and flow speed of 0.00167 ml s^{-1} at 0.15 mW microwave power and 9.763 ± 0.001 GHz microwave frequency (right) (not deoxygenated).*

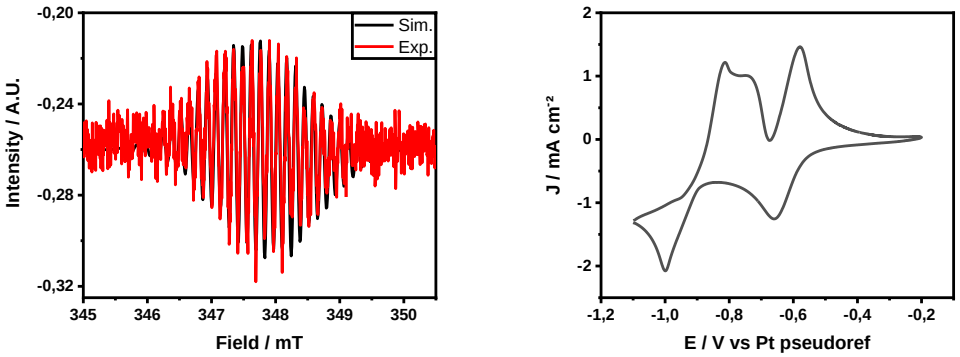

Figure 8.6: *EPR spectrum of electroreduction of the methyl viologen at −0.8 V and flow speed of 0.00667 ml s^{-1} at 1.00 mW microwave power and 9.746 ± 0.001 GHz microwave frequency (left). CV of 5 mM MV in H_2O + 0.2 M Na_2SO_4 with a flow speed of 0.00167 ml s^{-1} and 100 mV s^{-1} (right) (not deoxygenated).*

8.4 Conclusions

In this chapter, a new modular electrochemical EPR flow cell was designed, featuring (i) the use of POM as a material suitable for the setups combining electrochemistry and EPR, (ii) an increased modularity and surface reproducibility in order to have rapid change of material, (iii) an enhanced potential control by reducing electrode distances and optimizing the position of the pseudo reference electrode, and (iv) a well-defined hydrodynamic flow pattern by the chosen dimensions of the channel. The flow cell was validated in both aqueous and organic media using the test cases. This experimental platform allows thorough research of new electrocatalysts by determination of electrochemical properties with radical intermediate detection.

Part III

Case studies

Chapter 9

Re-evaluating the electrochemical self-condensation of acetone by *in-situ* EPR.

This chapter investigates the self-condensation of acetone towards diacetone alcohol. Several reaction conditions can lead to this product, both chemically and electrochemically. The mechanism for the electroreduction of acetone was investigated here, using a combination of electrochemistry and *in-situ* spin trap Electron Paramagnetic Resonance. The hypothesized mechanisms from literature are compared with our experimental data, and the presence of O_2 is shown to activate acetone at lower overpotentials through the oxygen reduction reaction.

This chapter is in preparation to be published in: S. Neukermans, M. Samanipour, H.Y.V. Ching, J. Hereijgers, S. Van Doorslaer, T. Breugelmans, Re-evaluating the electrochemical self-condensation of acetone by *in-situ* EPR and DFT calculations, *Chemical Science*, (2021), to be submitted

9.1 Introduction

Acetone is a broadly used chemical solvent and reagent which can serve as a feedstock for higher C-products through C-C bond formation, for instance via self-condensation [201–204]. The initial product formed during the self-condensation of acetone is 4-hydroxy-4-methyl-pentan-2-one also known as diacetone alcohol (DAA) [205]. Dehydration of DAA results in the formation of mesityl oxide [206], a precursor to methyl isobutyl ketone which has a great number of industrial applications [207]. Conventionally, ketones can be chemically condensated with aldehydes by using homogeneous catalysts like H_2SO_4 and alkali metal bases [208,209]. Both of these options have downsides on the industrial scale because of the homogeneous nature and the harsh reaction conditions, requiring catalyst separation and corrosion-protective measures for the reactor. Therefore, several studies focused on the performance of heterogeneous catalysts for these transformations, by using fixed-bed reactors employing bases like $Ba(OH)_2$ and $Ca(OH)_2$ and various metal oxides with strong basic sites like MgO, BaO, SrO, La_2O_3, ZrO_2, etc. [210–218].

Electrosynthesis combines the benefits of heterogeneous catalysis with mild reaction conditions and usually high selectivity due to the precise control over the electrode potential. Reports on the electrochemically induced condensation of aldehydes and ketones are abundant in aqueous solutions [219–224], organic solvents [225], such as DMF [226–228], DMSO, ACN [226], as well as ionic liquids [229]. Inherently, the selection of the solvent affects the reaction pathway and the formed products. Aqueous studies are mostly performed in the presence of sulfuric acid on a Pt electrode promoting the formation of 2-propanol at milder overpotentials and propane at higher overpotentials (close to the hydrogen evolution reaction). In other solvents, the reduction leads to combinatory products of the reagents like pinacols, diones or β-hydroxy ketones.

The electrosynthetic reduction of pure acetone with only a supporting electrolyte present has received much less attention, while it offers the benefit of keeping the extra solvent-component out of the subsequent separation process.

In previous studies of our group, this system has been investigated in batch and flow configurations [230,231]. Selectivity up to 90% was achieved for DAA at Pt cathodes in an undivided batch cell and up to 97% in an divided batch cell. Lower yields were observed with increasing water concentration and when Au and GC were used as cathodes compared to Pt. Flow experiments showed that while Pt and GC had similar yields per time unit, the GC electrode showed a fourfold increase in faradaic efficiency.

Mechanistically, the acid-catalyzed pathway is initiated by enolization of the reagent (figure S9.1) while during the base-catalyzed mechanism an enolate anion is formed, followed by an nucleophilic addition to the reagent (figure S9.2). Electrochemically, the reduction of pure acetone with only a supporting electrolyte present in solution is still unclear. To the best of our knowledge, three mechanisms for the electrosynthetic aldol condensation of aldehydes or ketones have been postulated in literature for organic solvents.

In the mechanism proposed by Shono *et al.* [232], an electrochemically generated base (EGB) is formed at the electrode which then deprotonates an aldehyde molecule to yield an anion. The anion reacts with a second aldehyde molecule to give the aldol addition product. The study of Shono *et al.* comprised of a small number of aliphatic aldehydes which were self- or cross-condensed, yielding dimethylformamide. If this mechanism was applied to acetone reduction, the most obvious EGB would be the acetone radical anion ($[CH_3C(O)CH_3]^{\bullet -}$, figure S9.3) but it could also be an *in-situ* formed derivative. The global mechanism towards DAA can be found in figure S9.4.

In contrast, Kumar *et al.* [233] proposed that an electrogenerated aldehyde radical anion undergoes homolytic C-H bond splitting to give an enolate anion and a hydrogen free radical (figure S9.5). This enolate anion couples with another electrogenerated aldehyde radical anion and loses an electron to give the alkoxide of an aldol product. This specie loses another electron and couples with the previously generated hydrogen free radical to give the aldol product. The study of Kumar et al. comprised of a small number of benzaldehydes which were also self- or cross-condensed in a DMF/H_2O mixture. If this mechanism was applied to acetone reduction, once again $[CH_3C(O)CH_3]^{\bullet -}$ is an important intermediate.

Tsai [234] proposed a mechanism for the self-condensation of acetone in water where a paired electrolysis occurs in an undivided cell with *in-situ* generated OH^- and H^+ catalyzing the reaction, in the same way the reaction can occur classically without electrolysis [235]. However, he proposed that without water, the reaction at the cathode would be similar to that shown in figure S9.3. At the anode, he states the formation of a carbocation. This mechanism conflicts with our observations between undivided and divided experiments showing higher selectivity for the latter [230,231].

In this chapter, the solvent-free electrochemical self-condensation of acetone to DAA was studied. Due to the radical nature of some intermediates in current literature, the reaction was studied by using *in-situ* spin-trapping electron paramagnetic resonance spectroelectrochemistry. The trapped radicals were identified and the effect of dissolved O_2 has been investigated. Radicals have been spin-trapped and EPR spectra have been simulated. In conclusion, a detailed reaction mechanism is proposed considering the experimental findings.

9.2 Experimental

Combined EPR-spectroelectrochemical measurements were performed in a Wilmad Supracil WG-810-A-Q quartz flat cell. A PFA insulated Pt wire was used as working electrode (WE). The PFA was stripped off for the section that was placed in flat part. A leak free reference electrode (RE)(W3 69-00) was used (Harvard Apparatus) which is equivalent to a Ag/AgCl 3 M KCl reference. The RE was positioned at the entrance of the flat part to ensure optimal potential control. The Pt rod counter electrode (CE) was put in the reservoir on top of the flat part. The tip was also put as close to the entrance of the flat part to reduce the cell potential. Solutions and the cell assembly were prepared in a glovebox for all measurements. An N_2 atmosphere (Air Liquide, 99.999 %) was provided for the measurements without O_2.

The setup was then placed in a TE_{102} rectangular cavity in a Bruker E580 Elexsys spectrometer. The EPR spectra were recorded at X-band (9.664 ± 0.001 GHz) in continuous wave mode at ambient temperature with 3.317 mW microwave power, 0.1 mT field modulation amplitude and 100 kHz field modulation frequency. All electrochemical experiments were conducted with a PAR VersaSTAT 3 potentiostat. The experiments performed in bulk were recorded versus a saturated Ag/AgCl reference electrode in a conventional undivided cell. The EPR spectra were simulated using the EasySpin-5.1.11 module running in Matlab [184].

Electrochemical measurements were performed in dry acetone stored in a glovebox (Acros Organics, 99.8%, Extra dry, Acroseal) with 0.1 M tetrabutylammonium perchlorate (TBAP, Sigma-Aldrich, 99.0 %). 10 mM 5,5-dimethyl-1-pyrroline-N-oxide (DMPO, TCI, >97.0 %) was added to the solutions as a radical trapping agent.

9.3 Results

9.3.1 Electrochemistry

Bulk CVs of acetone were performed on a Pt wire electrode with and without O_2 present (figure 9.1). The presence of O_2 gave rise to a first irreversible reduction peak around -1.35 V vs Ag/AgCl. This is known to be the reduction of O_2 with the exact species formed depending on the solvent and impurities (see discussion). More negatively the solvent, here acetone, starts to reduce at the electrode.

The current increase with onset around -1.8 V cannot be caused by impurities due to its magnitude. Experiments in the flat cell show similar behavior except for a shape distortion probably due to the space limitations of the flat cell. The test cases in chapter 5 also exhibit these distortions in organic solutions. Nevertheless, with a stable RE and the right choice of electrolysis potential, the two phenomena could be isolated for radical determination in the EPR. The chosen potentials were -1.6 V and -2.1 V as the first isolates the O_2 reduction reaction when O_2 is present and at -2.1 V the direct acetone electroreduction occurs.

In previous work from our group the reduction at -1.6 V in presence of O_2 resulted in substantial yields of the product DAA comparable to those at -2.1 V for both circumstances [236]. This is an indication of an altered reaction mechanism for acetone reduction towards DAA when O_2 is present.

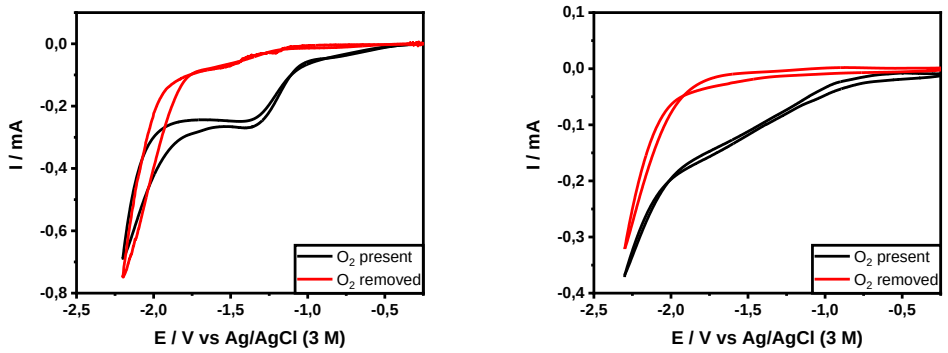

Figure 9.1: *CV acetone + 0.1 M TBAP on Pt wire electrode in bulk (left) and flat cell (right) with O_2 or N_2 atmosphere at 50 mV s^{-1}.*

9.3.2 *In-situ* spin trap EPR spectroelectrochemistry

In order to determine radical intermediates that are generated in the electrochemical reactions, *in-situ* spin trap EPR spectroelectrochemistry was performed under 4 different conditions (i.e. -1.6V, -2.1V, O_2 present environment and O_2 free environment). Spin traps react with short-living radicals and convert them to more stable, EPR-detectable radical species. Experiments were performed with 10 mM DMPO spin trap and the results are shown in figure 9.2. No signal was observed when the electrolysis was performed at -1.6 V in the absence of O_2. When the electrolysis was performed at -2.1 V in the absence of O_2 a typical signal for a DMPO-trapped radical adduct (DMPO-R1) was observed. When the electrolysis was performed in the presence of O_2 at -1.6 V or -2.1 V the R1 signal was observed combined with a second DMPO-trapped radical adduct signal (DMPO-R2). Simulations of the separated and combined DMPO-R1 and DMPO-R2 signals are also shown in figure 9.2. The isotropic *g*-values (g_{iso}) and hyperfine coupling values (A_{iso}) used for the simulations are given in Table 9.1.

The EPR parameters of DMPO-R1 are similar to those found in the literature (table 1) for DMPO-trapped $^{\bullet}C(CH_3)_2OH$ (the protonated product of $[CH_3C(O)CH_3]^{\bullet-}$) and $^{\bullet}CH_2C(O)CH_2C(O)OH$ (structurally similar to the acetonyl radical ($^{\bullet}CH_2C(O)CH_3$), where a H-atom has been abstracted from acetone). The EPR parameters of DMPO-R2 are consistent with those found in the literature (table 9.1) for DMPO-trapped alkoxyl radicals such as $^{\bullet}OCH(CH_3)_2$ and $^{\bullet}OC(CH_3)_3$.

Table 9.1: *Simulated EPR parameters for the two trapped radicals and for similar/possible structures from literature (A in mT).*

trapped radical	g_{iso}	$A_{iso\ N}$	$A_{iso\ H\alpha}$	$A_{iso\ H\gamma}$	Solvent	Ref.
R1	2.0056	1.46	2.14	-	Acetone	this work
R2	2.0057	1.30	0.78	0.16	Acetone	this work
$^{\bullet}OCH(CH_3)_2$	-	1.343	0.782	0.179	7:1 ACN/IPA	[237]
	2.0061	1.28-1.30	0.6-0.7	0.2	Benzene	[238]
$^{\bullet}OC(CH_3)_3$	2.0061	1.31	0.8	0.2	Benzene	[238]
	-	1.311	0.79	0.197	Benzene	[239]
$^{\bullet}C(CH_3)_2OH$	2.0053	1.60	2.41	-	H_2O pH 7.8	[240]
	-	1.58	2.39	-	H_2O pH 11	[241]
	2.00537	1.579	2.436	-	IPA	[242]
	-	1.458	2.391	-	Benzene	[239]
$^{\bullet}CH_2C(O)CH_2C(O)OH$	2.0060	1.424	2.384	-	H_2O	[243]
$^{\bullet}OO^-$	-	1.31	0.91	-	Acetone	[244]
	-	1.275	1.019	0.13	Acetone	[245]
$^{\bullet}OOH$	2.0060	1.31	1.08	-	Acetone	[246]

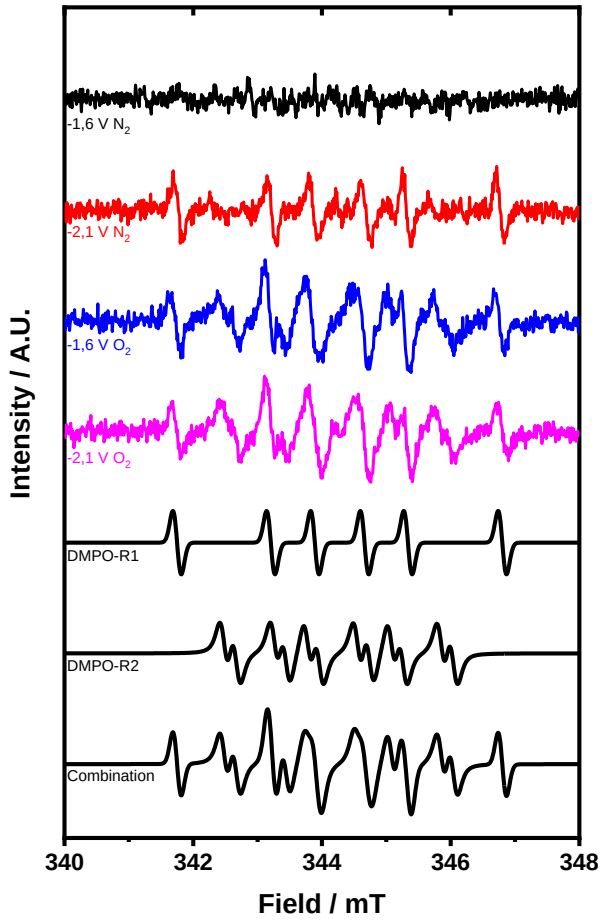

Figure 9.2: *EPR spectra of in-situ generated DMPO-trapped radicals through cathodic reduction of acetone with 0.1 M TBAP and 10 mM of DMPO at -1.6 V and -2.1 V vs Ag/AgCl (3 M) under N_2 and O_2 atmosphere. EPR settings stated in experimental section.*

9.4 Discussion

The detection of DMPO-R1 at -2.1 V vs Ag/AgCl during *in-situ* EPR-spectroelectrochemical experiments of acetone in the absence of O_2 with supporting electrolyte and DMPO suggests that radical R1 is a desorbed specie, unlike the species found in the acetone adsorption on platinum pathways in acidic aqueous media [220,222,224]. First considering R1 as $^{\bullet}C(CH_3)_2OH$; DMPO-trapping of this carbon-centered radical as opposed to the oxygen-centered radical $^{\bullet}OCH(CH_3)_2$ is consistent with the electronic structure of $[CH_3C(O)CH_3]^{\bullet-}$. DFT calculations show that the spin density is mostly localized on the carbonyl carbon atom while the negative charge density mostly localized on the O-atom (figure 9.3), which has also been previously described [247].

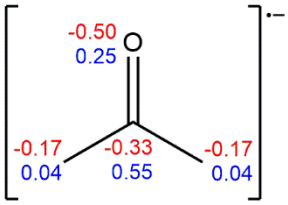

Figure 9.3: *structure of the acetone radical anion show the Loewdin charge (red) and spin (blue) densities on selected atoms.*

The negatively charged O-atom is protonated in the final DMPO-trapped adduct, but it is not possible to determine whether this occurs before or after the spin-trapping reaction. If the protonation step is assumed to be occurring before the spin-trapping reaction, then the presence of DMPO-R1 can be considered as evidence for $[CH_3C(O)CH_3]^{\bullet-}$, acting as an EGB within the mechanism proposed by Shono *et al.* [232]. After the EGB is formed, the mechanism essentially follows the classical base-catalyzed pathway. For homogenous acetone self-condensation, a strong base such as an alkali metal hydroxide (pK_a in H_2O is 14.00) is required [235]. However, the pK_a of $^{\bullet}C(CH_3)_2OH$ is only around 12 [248], meaning $[CH_3C(O)CH_3]^{\bullet-}$ is ~100 times less basic than an alkali metal hydroxide, making it seem unlikely that $[CH_3C(O)CH_3]^{\bullet-}$ can catalyze the self-condensation to the degree of efficacy that has been observed.

An alternative route (figure 9.4) could be that $[CH_3C(O)CH_3]^{\bullet-}$ first abstracts a H-atom to form isopropoxide ($^{-}OCH(CH_3)_2$), which then acts as a strong base (pK_a of isopropanol is 17.10 [249]) to initiate the base-catalyzed pathway. The reaction mixture contains mostly acetone; 13.5 M acetone, 0.1 M of supporting electrolyte and, 3.3 mM residual water with the pK_as in water being 19.16 for acetone and 14 for water. The abstracted H-atom can originate from water or from another acetone molecule which becomes $^{\bullet}CH_2C(O)CH_3$. Considering these pK_as as an indication for the molecules intrinsic tendency to release a proton and their respective concentrations, the concentration of protons originating from the residual water is 5 times higher than that from acetone. Furthermore, it has been shown that $[CH_3C(O)CH_3]^{\bullet-}$ is adsorbed on a Pt electrode in aqueous media [224,250]. Therefore, it is most likely that $[CH_3C(O)CH_3]^{\bullet-}$ first becomes isopropoxide before leaving the surface along with the formation of $^{\bullet}CH_2C(O)CH_3$ which goes into the bulk. The assignment of R1 as $^{\bullet}CH_2C(O)CH_3$ would support this mechanism, and the results of the spin-trapping experiments in the presence of O_2 makes this assignment appear more likely, although two different DMPO spin-trapped adducts having indistinguishable isotropic EPR parameters is not impossible.

Radical termination between $^{\bullet}CH_2C(O)CH_3$ and another molecule of adsorbed $[CH_3C(O)CH_3]^{\bullet-}$ yields a deprotonated DAA which also feeds into the base-catalyzed pathway. The concentration difference between the DMPO and acetone (10 mM vs ±13.5 M) influences the relative rate of the reaction between $[CH_3C(O)CH_3]^{\bullet-}$ and either of them. The reaction with acetone will be favored due to this excess. Assuming that $[CH_3C(O)CH_3]^{\bullet-}$ is consumed almost quantitatively after its formation, the probability of the R1 being $^{\bullet}CH_2C(O)CH_3$ increases significantly.

When the *in-situ* EPR spectroelectrochemistry experiment was performed at -1.6 V vs Ag/AgCl, no spin-trapped species were detected, consistent with the lack of product formation during electrosynthesis at this potential. In contrast, when O_2 was introduced to the experiment, signals for DMPO-R1 and DMPO-R2 were observed. The presence of R1 at a potential where the reduction of acetone to $[CH_3C(O)CH_3]^{\bullet-}$ is not expected, supports the assignment of R1 as $^{\bullet}CH_2C(O)CH_3$.

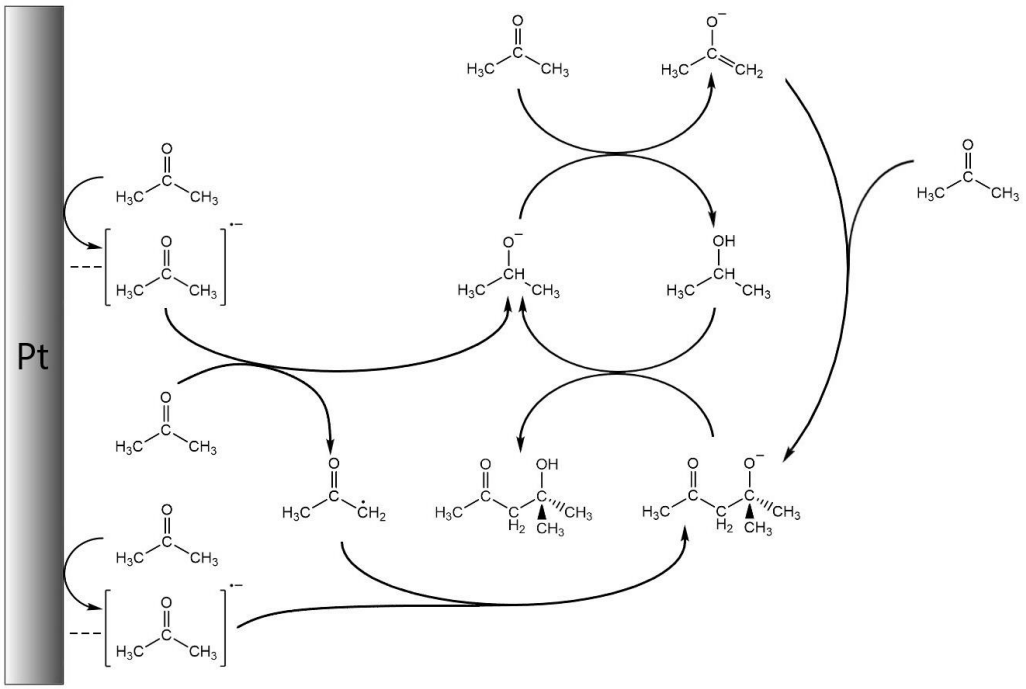

Figure 9.4: *Proposed route for the direct reduction of acetone at Pt electrode towards DAA.*

An obvious candidate to abstract a H-atom from acetone to give $^{\bullet}CH_2C(O)CH_3$ is $O_2^{\bullet-}$ from the one electron reduction of O_2 ($E_{1/2}$ = -0.88 vs SCE) at Hg in anhydrous acetone [251]. However, $O_2^{\bullet-}$ has been shown to be relatively stable in anhydrous acetone [251,252]. Indeed chemically or photochemically generated $O_2^{\bullet-}$ is stable enough in acetone to be readily spin-trapped by DMPO [244–246]. Since no DMPO-OO or DMPO-OOH adducts were observed in the *in-situ* EPR-spectroelectrochemical experiments, it is unlikely that a significant amount of desorbed $O_2^{\bullet-}$ was generated, suggesting that other intermediates of the O_2 reduction reaction are responsible for the formation of $^{\bullet}CH_2C(O)CH_3$ in solution. Noel *et al.* [253] reported that electroreduction of O_2 in aprotic polar solvents at a Pt surface can produce desorbed $^{\bullet}OH$ with an overall reaction of:

$$O_2 + 2H^+ + 3e^- \rightarrow {}^{\bullet}OH + OH^-$$

The irreversibility of the CV suggests that this may also be occurring in acetone. Previous studies [254,255] have shown that $^{\bullet}OH$ can abstract a H-atom from acetone to give H_2O and $^{\bullet}CH_2C(O)CH_3$, and it is most likely to also be the case

here since acetone is both the substrate and solvent (figure 9.5). The protons necessary for the electron transfer at the surface can be provided by acetone or residual water with water being produced in the first follow-up reaction so it will be continually available. Since $[CH_3C(O)CH_3]^{\bullet-}$ is not present to terminate with $^{\bullet}CH_2C(O)CH_3$ to give deprotonated DAA , unlike the O_2-free experiments at -2.1 V vs Ag/AgCl. $^{\bullet}CH_2C(O)CH_3$ instead propagates with acetone to give DAA and the DAA alkoxyl radical ($^{\bullet}OC(CH_3)_2CH_2C(O)CH_3$) as an intermediate. The detection of DMPO-R2, a secondary or tertiary alkoxyl radical adduct, is consistent with this pathway. However, the DMPO-OH adduct was not detected in the spin-trapping experiments. This is probably due to the large excess of acetone compared to DMPO in the solution meaning most of the formed $^{\bullet}OH$ reacted with acetone (±13.5 M) and not with DMPO (10 mM). Furthermore, OH^- is also generated at the Pt surface in the mechanism which can also initiate the classical base catalyzed pathway in the bulk. The fact that the parameters of R1 were the same for the experiments with and without O_2 confirms the hypothesis that $^{\bullet}CH_2C(O)CH_3$ is also the trapped intermediate in the O_2-free experiments.

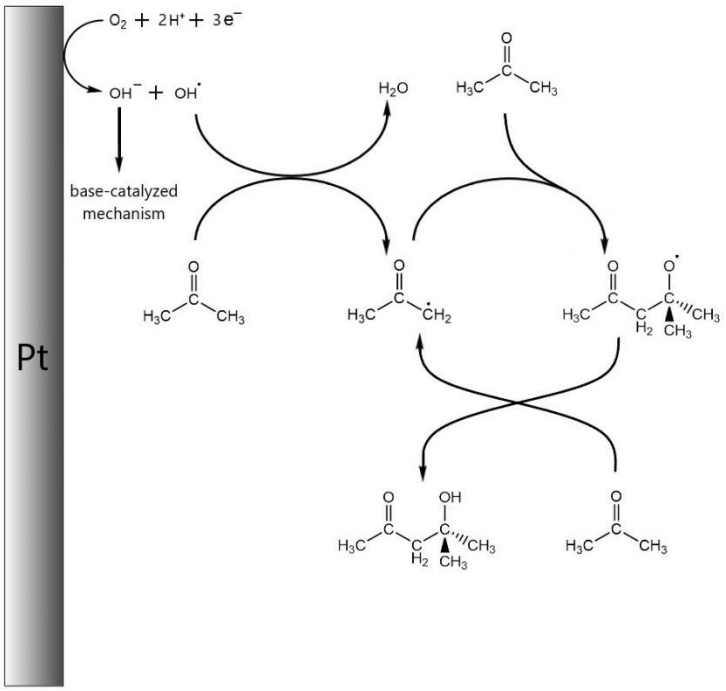

Figure 9.5: *Proposed route for the oxygen-mediated reduction of acetone at Pt electrode towards DAA.*

9.5 Conclusions

The reaction mechanisms for the electroreduction of acetone from literature have been assessed by performing *in-situ* EPR in the presence of a spin-trapping agent. Electrochemical measurements have indicated that DAA was the main product for solutions with and without the presence of O_2. The EPR results indicate that the direct acetone reduction at the electrode proceeds through the acetone radical anion which was proposed in literature to be an adsorbed species. At the electrode, it can react with the excess solvent molecules in its vicinity to form the acetonyl radical and isopropoxide. Both intermediates have a pathway towards DAA; the acetonyl radical through a termination with the acetone radical anion formed at the electrode and the isopropoxide through the base-catalyzed pathway (isopropoxide as EGB).

The presence of O_2 resulted in a significant reduction of the overpotential at which the radical intermediates in the acetone reduction are formed. It can be considered as an electrochemical mediator for the reaction towards DAA. The mechanism of oxygen reduction on Pt in aprotic polar solvents was suggested to produce hydroxide anions and hydroxyl radicals considering that the superoxide radical anion nor the hydroperoxyl radical were spin-trapped. Also here, both formed species have a route towards DAA; the hydroxide anion through the base-catalyzed mechanism and the hydroxyl radical through reaction with acetone to form the acetonyl radical. The subsequent reaction with acetone will then yield a DAA alkoxyl radical which disproportionates with acetone to DAA and the acetonyl radical.

9.6 Supporting information

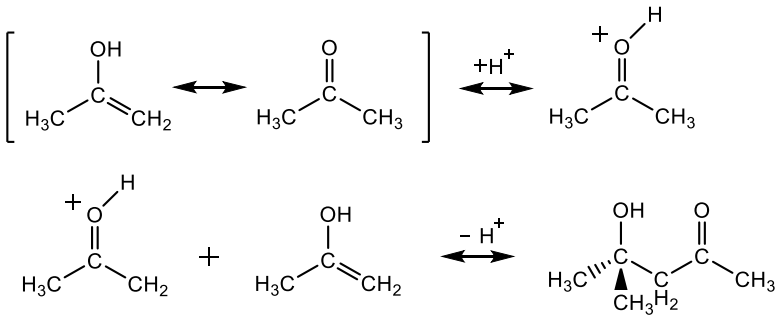

Figure S9.1: *Homogeneous acid-catalyzed self-condensation of acetone* [235].

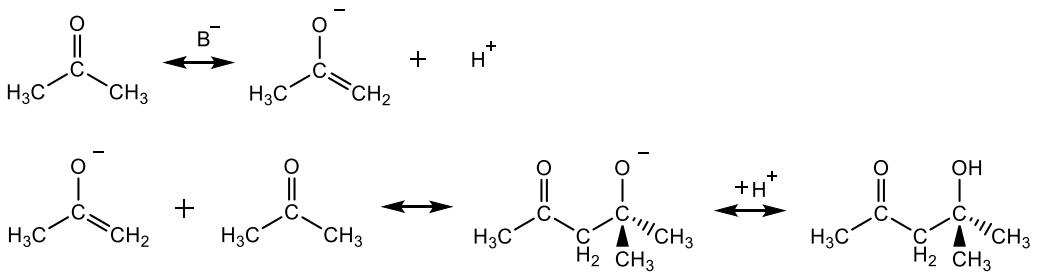

Figure S9.2: *Homogeneous base-catalyzed self-condensation of acetone* [235].

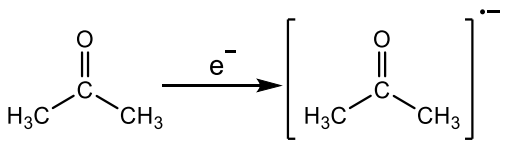

Figure S9.3: *Electrode reduction of acetone towards the radical anion* $[CH_3C(O)CH_3]^{\bullet -}$ [247].

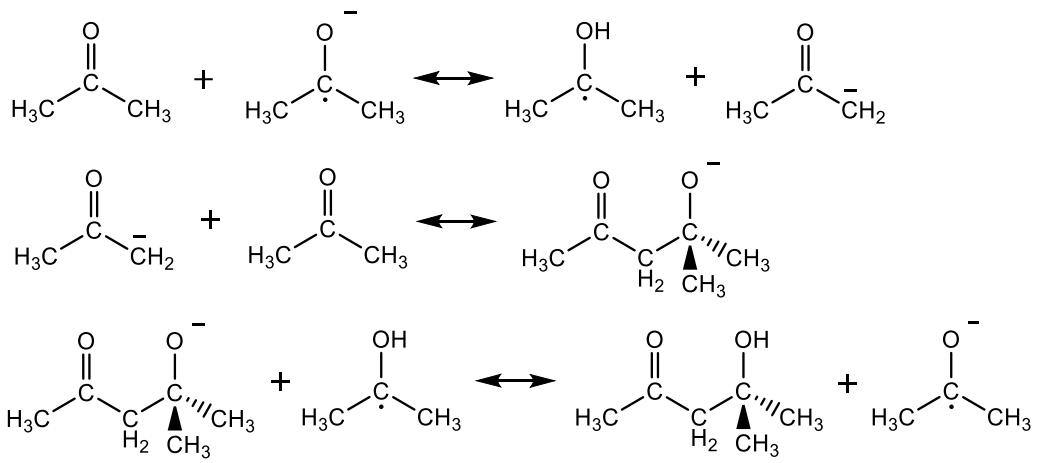

Figure S9.4: *Electrochemically-induced aldolcondensation mechanism proposed by Shono et al. applied for acetone* [232].

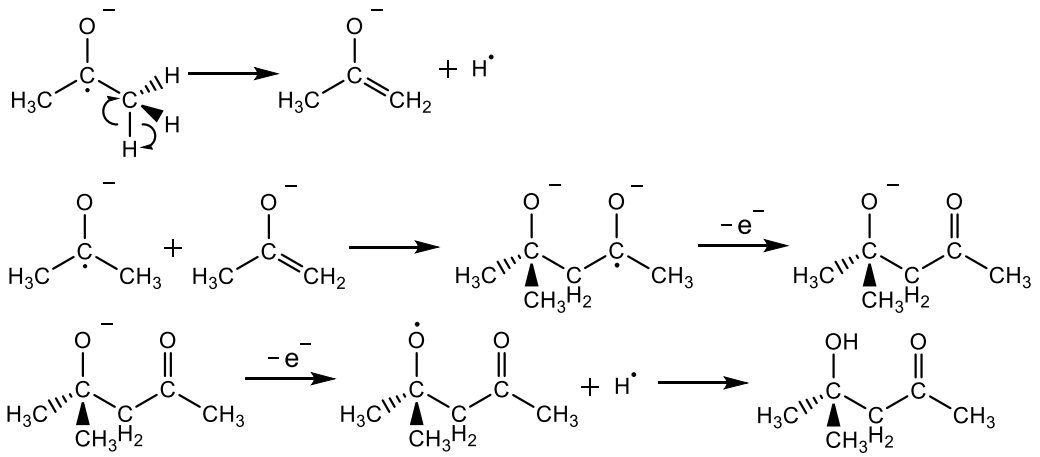

Figure S9.5: *Electrochemically-induced aldolcondensation mechanism proposed by Kumar et al. applied for acetone* [233].

Chapter 10

Electrochemical and *in-situ* EPR investigation of the carbon-halogen reduction of organic compounds

This chapter investigates the electrochemical reaction mechanism of several metal cathodes for carbon-halogen bond breaking of aromatic compounds with different configurations. A selection of cathodes and halogenated aromatic compounds have been tested with *in-situ* EPR in search for confirmation of the proposed reaction pathways.

The electrochemical part of this chapter has been published as: S. Neukermans, F. Vorobjov, T. Kenis, R. De Wolf, J. Hereijgers, T. Breugelmans, Electrochemical reduction of halogenated aromatic compounds at metal cathodes in acetonitrile, *Electrochimica Acta,* 332 (2020) 135484

The spectroelectrochemical part of this chapter in under preparation to be published as: S. Neukermans, M. Samanipour, H.Y.V. Ching, J. Hereijgers, S. Van Doorslaer, T. Breugelmans, Intermediate identification for the carbon-halogen bond electroreduction with Electron Paramagnetic Resonance, *Electrochimica Acta*,(2021), to be submitted

10.1 Introduction

Selective addition/removal of electrons to/from organic molecules by electrochemical means provides a tool for the activation and tuning of functional groups [256]. One of the functional groups that can be used for tuning of molecules is the organic halide. The electrochemical reductive cleavage of carbon-halogen bonds (C-X) received a lot of attention from the electrochemical society during the last decades. The interest in this process is caused by the possibilities it offers in synthesis [257–259], reduction of organic pollution [260–262] and the investigation of the dissociative electron transfer (DET) [261]. The biggest downside for the reduction of organic bromides is the substantial overpotential that has to be overcome to activate the molecule. Studies have been performed using homogeneous metal complex electrocatalysts like Ni(salen) and Co(salen) for activation or cyclisation of organic halides [187,262].

In heterogeneous electrocatalysis, Ag exhibits an extraordinary catalytic activity that has been investigated in several publications [263–265]. Studies of other cathode materials were conducted to investigate certain case-studies of C-X-compounds [190,266,267]. A substantial amount of research has been carried out to map the reaction mechanism at catalytic and non-catalytic electrodes, by i.e. the group of Gennaro [190,261,264,267] and our group, mostly for electrodeposited catalysts [137,159,178,183,268–270]. The first step in the reaction mechanism consists of the electron transfer (ET) from the electrode to the organic halide. The Savéant group proposed the formation of an intermediate radical anion at a mercury cathode because subsequent reactions were inhibited when the scan rate was significantly increased [271]. This mechanism is also considered at other electrodes such as GC and is known as a stepwise mechanism. The radical anion formed in equation 10.1 subsequently undergoes a cleavage of the C-X bond with formation of the bromide anion and an organic radical (Eq. 10.2).

For bromides and chlorides, this organic radical has a lower reduction potential than the parent molecule and is therefore reduced almost instantaneously afterwards (Eq. 10.4) which makes this a stepwise two electron transfer. For some iodides this mechanism is observed as two separate reduction waves [272].

$$RX + e^- \leftrightarrow RX^{\bullet -} \quad (10.1)$$

$$RX^{\bullet -} \rightarrow R^{\bullet} + X^- \quad (10.2)$$

$$RX + e^- \rightarrow R^{\bullet} + X^- \quad (10.3)$$

$$R^{\bullet} + e^- \leftrightarrow R^- \quad (10.4)$$

Ag exhibits, depending on the investigated halide, a tendency towards a concerted mechanism (Eq. 10.3) and the subsequent reduction of the formed organic radical yielding an organic anion (Eq. 10.4) [178,261,273]. It has been shown that different parameters have an influence on the reaction; the surface morphology of the electrode [274], the nature of the halide [268], the molecular structure of the organic halide [273], the solvent [190,272], the nature and concentration of the supporting electrolyte [275] and adsorption/desorption phenomena [274,276]. The organic radical could react with the radical anion intermediate to yield an anion and the initial reagent (Eq. 10.5) or with another radical to form a dimer (Eq. 10.6). The produced anions from Eq. 10.4 and Eq. 10.5 can enter into a reaction to bind with a proton from the solvent/residual water to the corresponding aromatic compound (Eq. 10.7).

$$R^{\bullet} + RX^{\bullet -} \leftrightarrow R^- + RX \quad (10.5)$$

$$R^{\bullet} + R^{\bullet} \rightarrow RR \quad (10.6)$$

$$R^- + H^+ \rightarrow RH \quad (10.7)$$

By sweeping the potential further negative, depending on the molecular structure of the halide and the electrochemical window of the solvent, one can produce the radical anion of this hydrogenated dehalogenated compound (Eq. 10.8).

$$RH + e^- \leftrightarrow RH^{\bullet -} \quad (10.8)$$

The aromatic radical could exchange a hydrogen with the solvent with formation of a solvent radical (Eq. 10.9) which can then be reduced at either the electrode itself (Eq. 10.10) or by the radical anion (Eq. 10.11) [277].

$$R^\bullet + SH \rightarrow RH + S^\bullet \quad (10.9)$$

$$S^\bullet + e^- \leftrightarrow S^- \quad (10.10)$$

$$S^\bullet + RX^{\bullet -} \leftrightarrow S^- + RX \quad (10.11)$$

In this chapter, first the DET mechanism is investigated electrochemically at varying cathode materials for one class of bromides. These aromatic bromides have the halogen directly bound on the aromatic ring. The main difference between the investigated compounds is the number of aromatic rings, their configuration and the position of the bromide on the ring (figure 10.1). Bromine was chosen as a halogen for having intermediate overpotentials so reduction waves are present in the electrochemical window of acetonitrile as a solvent, in contrast to analogous chlorides. The cathode materials were selected for their proven catalytic activity or because they are considered inert in previous publications.

Secondly, after the electrochemical mechanistic screening, the most promising cathode-compound combinations were performed with direct *in-situ* EPR detection. The difference in mechanism essentially comes down to the lifetime of the intermediate radical anion $RX^{\bullet -}$ species (Eq.10.1-10.3). The publications of Wang et al. and Huang et al. [265,278] report on the mechanism of C-X reduction with more than only electrochemical techniques. They used *in-situ* SERS combined with DFT to identify intermediate states. For the reduction of benzyl chloride they concluded that the parent species were weakly adsorbed on the surface of a Ag electrode and the benzyl intermediate was strongly bound to the surface. The technique is however limited to surface bound species and to SERS-active electrode materials.

In this chapter, experiments were performed using the wire electrode from chapter 5 and the ITO electrode from chapter 6 to detect intermediate radicals of these reductions to couple the electrochemical measurements to the experimental proof of an EPR spectrum. Through these measurements, the reaction mechanism can unambiguously be differentiated between the concerted and stepwise mechanism by detecting the $RX^{\bullet -}$ species.

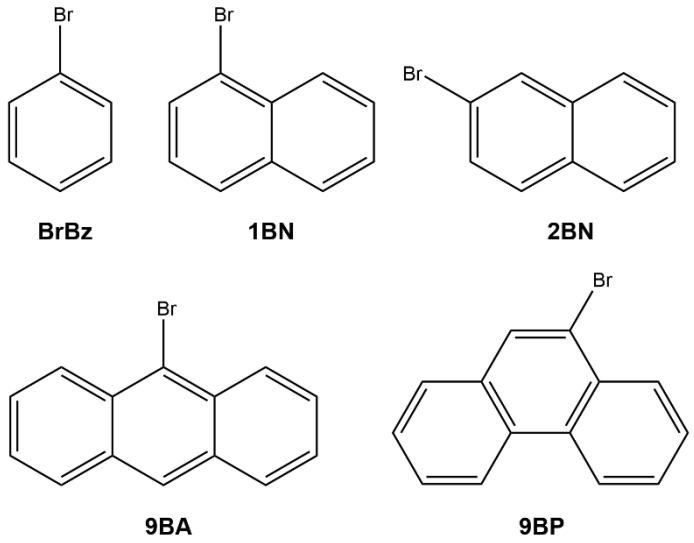

Figure 10.1: *Molecular structure of the aromatic bromides investigated.*

10.2 Experimental

10.2.1 Pretreatment of electrodes

11 multicrystaline cathode materials were screened in this work: GC, Ag, Au, Pd, Cu, Ti, Pt, Ni, Zn, Mg, Mn. To exclude morphology influence of the cathode surface, all bulk metal electrodes were polished with 1 and 0,3 µm alumina powder suspensions (Streurs), followed by rinsing them in an ultrasonic bath, first with MilliQ water (18.2 MΩ cm^{-1}) and then with ACN (Chem-Lab, HPLC Gradient Grade). As some electrode materials are sensitive for oxidation to air the electrodes were only rinsed with ACN that was deoxygenated by Ar bubbling and then transported to the pre-deoxygenated cell.

10.2.2 Chemicals

Electrochemical reductions of bromobenzene (BrBz, 99.5%), 1-bromonaphthalene (1BN, 97%), 2-bromonaphthalene (2BN, 99.0%), 9-bromoanthracene (9BA, 94%) and 9-bromophenanthrene (9BP, 96%) were performed in ACN and 0.1 M TBAP (99.0%) by means of CV.These chemicals were used as received and were all purchased at Sigma-Aldrich. Spectroelectrochemical measurements were performed in ACN, DMF (Biosolve, HPLC grade) and DMSO (Acros Organics, >99.8%). TBAP, tetrabutylammonium bromide (TBAB, Acros Organics, >99%) and tetramethylammonium hexafluorophosphate (TMAFP, TCI, >98.0%) were used as supporting electrolyte. N-tert-Butyl-α-phenylnitrone (PBN,Sigma-Aldrich, for ESR spectroscopy) was added as a radical trapping agent. Toluene (Uvasol for spectroscopy) was purchased from Merck.

10.2.3 Electrochemical characterization

Reductions were carried out with an Autolab PGSTAT 302 N using a Pt rod counter electrode and saturated Ag/AgCl reference electrode. The reference electrode was separated from the organic medium by a salt bridge, preventing the influence of chlorides and water on the reaction at the working electrode. An undivided cell was used. All solutions were purged with Ar for several minutes before measurement and the atmosphere above the solution was purged continuously with Ar during the measurement to avoid the influence of oxygen. The jacketed cell was thermostated at 25 °C with an LKB Bromma 2219 Multitemp II thermostatic circulator. Before all measurements the ohmic drop of the electrochemical system was determined to be 85 Ω (average) with electrochemical impedance spectroscopy and reduced to 60% of this value. Higher compensation percentages gave, identical with literature [279,280] rise to oscillation and were therefore not performed. CV experiments were recorded with a steptime of 0.0097656 s – 0.048828 s (depending on the scanspeed) and 0.1 s for CA experiments. The current range for both experiments was 1 mA and the bandwidth was set to the ‘high stability’ option corresponding to 12.5 kHz.

10.2.4 Bulk electrolysis

Chronoamperometric experiments were conducted in a 5 mL cell with analogous electrode configuration and setup as above. The geometrical surface area of the Ag and GC electrodes were 0.2 cm^2. Because of the constant stream of Ar and the longer timescale of these experiments the Ar was first bubbled through a reservoir of ACN to saturate the gas phase and prevent evaporation in the reaction vessel. Identification of the reaction products was carried out by gas chromatography coupled with mass spectrometry detection (GC/MS) using a RXI-1 ms (Restek) capillary column (30 m, 0.32 mm i.d. and 0.25 µm film thickness). Samples of the BrBz reduction were injected with a split ratio of 20. Other samples were injected splitless. Spectra were recorded at 70 eV and compared to the NIST/EPA/NIH library. Retention times were compared to calibration standards (Acros Organics, Sigma Aldrich).

The quantitative analysis of the reaction products was performed by high performance liquid chromatography (HPLC) using a reversed-phase C18 column (Triart C18, YMC) and a Photo Diode Array (PDA) detector. Wavelengths were set to 210 nm for BrBz, 270 nm for 1BN and 2BN and 254 nm for 9BA and 9BP, as at these wavelengths the best sensitivity was obtained. Calibration standards were prepared from analytical grade products (Acros Organics, Sigma Aldrich).

10.2.5 *In-situ* EPR detection

Combined EPR-spectroelectrochemical measurements were performed with Wilmad Supracil WG-810-A-Q quartz flat cell in a TE_{102} rectangular cavity of the Bruker E580 Elexsys spectrometer. The EPR spectra were recorded at X-band (≈9.7 GHz) in CW mode at ambient temperature with 2 mW microwave power, 0.1 mT field modulation amplitude (unless mentioned differently in caption) and 100 kHz field modulation frequency. The ITO (SPI Supplies) and wire working electrodes were used for all *in-situ* experiments. Depositions on ITO were performed as stated in chapter 6. A leak free reference electrode (W3 69-00) was used (Harvard Apparatus) which is equivalent to a Ag/AgCl 3 M KCl reference. The RE was positioned at the entrance of the flat part to ensure optimal potential control. The Pt rod counter electrode CE was put in the reservoir on top of the flat part. The tip was also put as close to the entrance of the flat part to reduce the cell potential.

10.3 Results and discussion

10.3.1 Electrochemical screening

To help determining the mechanism at different electrodes, one can calculate the approximated electron transfer coefficient (α) from the reduction peak in the CV. Specifically for C-X reduction, literature states that when α is found to be significantly smaller than 0.5, the transfer coefficient indicates a concerted mechanism. If a stepwise mechanism is considered, either the ET or the subsequent cleavage reaction can possibly be rate-determining. When the electron transfer coefficient is significantly bigger than 0.5, this parameter is called the apparent transfer coefficient and the cleavage reaction is rate-determining. The ET is rate-determining in the stepwise mechanism when the transfer coefficient is only moderately smaller than 0.5. Between these two extremes, there is a range where the process is under mixed control. The rate constant of a concerted reaction can be slower than that of a stepwise, indicating that the catalysis and overpotential are not solely dependent on the kinetics of the ET [273]. In the case of a concerted mechanism, the ET is considered very sluggish as it has to happen simultaneously to the bond cleavage. Transfer coefficients derived from the CVs are used as an indication for the mechanism and are calculated from the shift of the peak potential when the scan speed is varied (Eq. 3.35) [281] or from the potential difference between the peak and the potential at half height of the peak (Eq. 3.34) ($E_{p/2}$) [33]. Calculations using these two equations can sometimes lead to deviating values for α and in extreme cases to a different mechanism. This error is more profound when adsorption phenomena influence the shape of the peaks as is the case with bromide on Ag cathodes in ACN in a defined potential range [282]. Equation 3.35 does not account for peak shape changes and should therefore be better for mechanistic considerations [283]. It must be stressed out that the values for α calculated in this chapter do not equal the electron transfer coefficient as stated in fundamental electrochemical theory because of the complex mechanism with limiting factors different from the electron transfer. They are however calculated from the same equations and can give an indication of the overall mechanism as mentioned above.

For the sake of clarity, the mean result of the two equations used, will be called 'the kinetic indicator' (κ), similar to what is reported in literature [273].

10.3.1.1 Bromobenzene

Most bulk electrodes that were tested for BrBz did not show any reduction peak which implies that the reduction potential of this molecule is outside the electrochemical window of the solvent for these electrodes. This was the case for Au, Pd, Ti, Pt, Ni, Mn and Mg. Measurements were conducted in threefold. The Mg and Mn electrodes did not seem to be active for any of the investigated compounds even when utilized in a deoxygenated environment. In a previous study of our group concerning the reduction of 2-allylbromobenzylether both showed activity in the potential range where Au, Ni and GC presented a reductive cleavage of the bond [178]. Possibly this is due to the moderating effect of the substituent on the bond strength and the convenience of the follow up reaction.

Pt had a small oxidation wave in the back scan in both blank and BrBz measurements and was seen for all organic bromides throughout the experiments. The electrodes that are active for this system were Ag, Cu, GC and Zn (figure 10.2). Ag had the most remarkable catalytic activity showing the lowest overpotential which was approximately 0.9 V lower than that of the GC electrode. Cu and Zn both had a lower overpotential than GC with respectively 0.664 V and 0.271 V difference. A linear correlation was obtained between the square root of the scan rate and the peak current indicating that the peak was under diffusion control as expected [33]. This was the case for all combinations of halides and cathodes investigated in this chapter.

Table 10.1: *Voltammetric data of active electrodes for the reduction of 3mM BrBz in acetonitrile + 0.1 M TBAP at 50 mV s^{-1} (E_p and J_p) and derived parameters for scan speeds between 50 mV s^{-1} and 500 mV s^{-1}.*

	${E_p}^a$	${J_p}^b$	$E_p - E_p^{(GC)}$	$\partial E_p/\partial log v$	${\alpha_1}^c$	$E_p - E_{p/2}$	${\alpha_2}^d$	κ
Ag	-1.775	0.87	0.936	-0.166	0.18±0.03	0.198	0.25±0.04	0.21
Cu	-2.047	0.93	0.664	-0.071	0.41±0.05	0.111	0.43±0.05	0.42
GC	-2.711	0.47	0	-0.122	0.24±0.03	0.103	0.46±0.01	0.35
Zn	-2.440	1.09	0.271	-0.051	0.58±0.04	0.104	0.49±0.05	0.53

[a]V vs Ag/AgCl. [b]mA/cm² [c]Calculated from eq. 3.35. [d]Calculated from eq. 3.34.

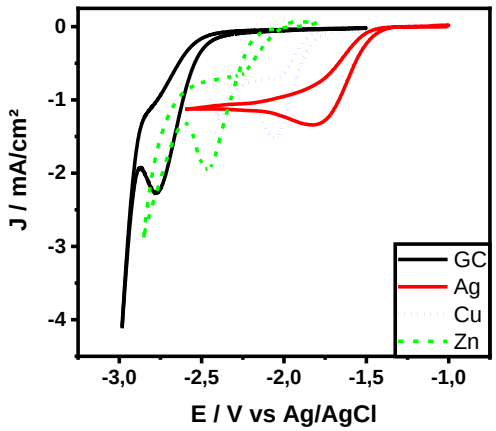

Figure 10.2: *Cyclic voltammetry at 50 mV s^{-1} of Ag, Cu, GC and Zn in ACN + 0.1 M TBAP and 3 mM BrBz.*

Kinetic indicators (also table 10.1) of 0.35 and 0.21 indicated that respectively GC and more profoundly Ag have a tendency to follow the concerted reaction mechanism. Cu and Zn on the other hand were in the region where the reaction in under mixed control and respectively the first reaction was more ET-controlled in contrast to the other which was more controlled by the chemical follow-up reaction. These data show the complexity of the electrocatalysis because the overpotential was not always a measure for the reaction mechanism as the overpotential of GC was significantly bigger than that of Cu but the kinetic indicator was smaller. This is especially important when the cleavage is used as an initiating reaction for polymerization or functionalization and moreover when the electrode plays a catalytic role one of those follow-up reactions.

10.3.1.2 1-Bromonapthalene

More cathode materials exhibited catalytic activity for 1BN than for BrBz (table 10.2 and figure 10.3). Overpotentials were generally lower. The metals can be divided into three groups of which Ag was by far the most catalytic with an E_p of -1.50 V.

GC, Cu and Au had intermediate reduction potentials around -2.03 V and Ni, Pd and Zn only achieved reduction about -2.31 V. The peak potential gap between the inert GC and Ag was almost halved compared to BrBz and it should be noted that only Ag showed an improvement in E_p compared to the inert GC electrode.

In terms of mechanism, only the kinetic indicator of Ag, indicate a concerted pathway. Those for Cu, Ni and GC were very close to 0.5 and indicated that the ET and the chemical reaction rates were in the same order of magnitude. Zn, Au and Pd had kinetic indicators which were significantly higher than 0.5 wherefore the chemical reaction rate was rate-determining.

Comparing catalysis between BrBz and 1BN implies that the influence of steric hindrance of the bulkier aromatic halide when approaching the electrode had a less-pronounced effect than other factors that might influence the reduction potential. These other factors are potentially: (i) Changed bonding strength of the C-X bond, (ii) more resonance structures which promote the radical anion intermediate formation and (iii) its lifetime.

Table 10.2: *Voltammetric data of active electrodes for the reduction of 3 mM 1BN in acetonitrile + 0.1 M TBAP at 50 mV s^{-1} (E_p and J_p) and derived parameters for scan speeds between 50 mV s^{-1} and 500 mV s^{-1}.*

	$E_p{}^a$	$J_p{}^b$	$E_p - E_p^{(GC)}$	$\partial E_p/\partial log v$	$\alpha_1{}^c$	$E_p - E_{p/2}$	$\alpha_2{}^d$	κ
Ag	-1.500	1.08	0.508	-0.085	0.35±0.02	0.128	0.37±0.01	0.36
Cu	-2.033	0.73	-0.025	-0.059	0.50±0.03	0.098	0.49±0.04	0.49
GC	-2.008	1.10	0	-0.070	0.42±0.02	0.084	0.57±0.01	0.50
Zn	-2.333	0.63	-0.325	-0.050	0.59±0.02	0.077	0.62±0.02	0.60
Au	-2.064	0.52	-0.056	-0.057	0.52±0.03	0.075	0.66±0.04	0.59
Pd	-2.317	0.74	-0.309	-0.042	0.72±0.05	0.087	0.55±0.03	0.63
Ni	-2.266	0.98	-0.258	-0.068	0.44±0.04	0.098	0.49±0.05	0.46

[a]V vs Ag/AgCl. [b]mA/cm² [c]Calculated from eq. 3.35. [d]Calculated from eq. 3.34.

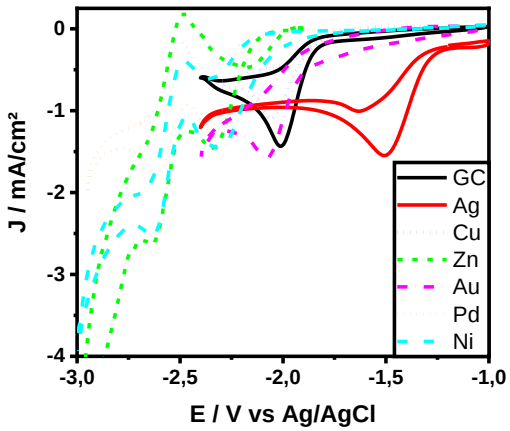

Figure 10.3: *Cyclic voltammetry at 50 mV s^{-1} of Ag, Cu, GC, Zn, Au, Pd and Ni in ACN + 0.1 M TBAP and 3 mM 1BN.*

The subsequent reversible reduction and oxidation of the hydrogenated dehalogenated aromatic compound (naphthalene) to its derived radical anion located at -2.56 V is depicted in figure 10.3 for Ni, Pd and Zn. This wave should have the similar reduction potentials for all cathodic materials as it is considered an outer-sphere reaction with no or little influence of the cathode material on the reaction. It was not specifically recorded for all electrodes because the scope was the halide reduction itself.

10.3.1.3 2-Bromonaphthalene

The influence of the position of the bromide atom on the reduction potential varies with the used electrode material. Pd experienced the least from this position change resulting in difference of only 22 mV for the reduction peak potential. Ag, GC and Au had reduced catalytic activity with respectively 110, 99 and 208 mV downward shift in potential (table 10.3). Cu and Zn were positively influenced and achieve lower overpotentials than for 1BN. The gap between the inert and catalytic electrode did not change significantly with respect to 1BN. A change in steric hindrance, strength of the C-X bond and the adsorption on the electrode surface could affect the overpotential in both directions.

Analogous to 1BN, the DET mechanism for Ag is of a concerted nature, indicated by the kinetic indicator. Cu was located in the mixed control region with Pd, Au, Zn and GC respectively tended more to a stepwise mechanism controlled by the chemical follow-up reaction. Nickel did not catalyze the reaction in the potential region up to -3 V which shows that the small change in position can lead to extensive shifts depending on the cathode material.

Table 10.3: *Voltammetric data of active electrodes for the reduction of 3 mM 2BN in acetonitrile + 0.1 M TBAP at 50 mV s^{-1} (E_p and J_p) and derived parameters for scan speeds between 50 mV s^{-1} and 500 mV s^{-1}.*

	$E_p{}^a$	$J_p{}^b$	$E_p - E_p^{(GC)}$	$\partial E_p/\partial log v$	$\alpha_1{}^c$	$E_p - E_{p/2}$	$\alpha_2{}^d$	κ
Ag	-1.610	1.03	0.497	-0.082	0.36±0.04	0.147	0.32±0.02	0.34
Cu	-1.903	0.49	0.204	-0.053	0.56±0.04	0.106	0.45±0.03	0.50
GC	-2.107	1.25	0	-0.046	0.64±0.03	0.093	0.51±0.02	0.58
Zn	-2.250	1.31	-0.143	-0.050	0.59±0.03	0.088	0.54±0.02	0.57
Au	-2.272	0.44	-0.167	-0.052	0.57±0.05	0.087	0.55±0.07	0.56
Pd	-2.294	0.42	-0.187	-0.054	0.55±0.06	0.089	0.54±0.05	0.54

[a]V vs Ag/AgCl. [b]mA/cm² [c]Calculated from eq. 3.35. [d]Calculated from eq. 3.34.

In figure 10.4, the onset for the reduction of the formed naphthalene can be seen. It was located around the same potential as the one in 10.3.1.2 which was quite logical considering the same molecule was formed. It also strengthens the hypothesis that in ACN these reduction products tend to hydrogenate rather than dimerize as is also the case in DMF [284]. As the vertex potential of the CV was located in the reduction wave of the reduction of the dehalogenated aromatic compound to its radical anion (Eq. 10.8) on Au, Pd and Zn, it did not go into the mass transport limiting region resulting in the absence of the $RH^{\bullet-}$ oxidation in the backscan.

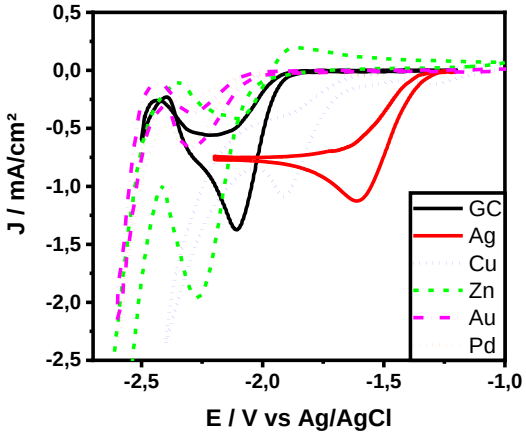

Figure 10.4: *Cyclic voltammetry at 50 mV s^{-1} of Ag, Cu, GC, Zn, Au, and Pd in ACN + 0.1 M TBAP and 3 mM 2BN.*

10.3.1.4 9-Bromophenanthrene

There was a general downward tendency of the reduction potential by increasing the aromaticity of the halide. Ag was also here the best choice with a relatively high peak current density (0.98 mA cm^{-2}) and the lowest overpotential (-1.45 V) as can be seen in figure 10.5. Cu only surpassed the GC electrode by 59 mV. Ni was not active for 2BN but it was for 1BN and 9BP.

Current densities of Cu, Au and especially Pd were on the low side. Pd only reaches 0.13 mA cm^{-2} and the peak presented as a shoulder when higher scan rates were applied. The addition of an extra ring which in the case of 9BP could be seen as a combination of the 1BN and 2BN positioning of the bromide compared to either of the surrounding rings. The behavior on Cu and Au, with GC as a reference point, was an averaging in potential of the effect of these two positions. The gap between Ag and GC diminished even more compared to the smaller aromatics. The kinetic indicators were mostly just over 0.5 (table 10.4), even for Ag, which supports the hypotheses that the energy barrier for the formation of the radical anion is going down, favoring the stepwise mechanism. Zn has an α_{mean} of 0.62 indicating that the rate constant of the cleavage reaction is getting smaller compared to the ET.

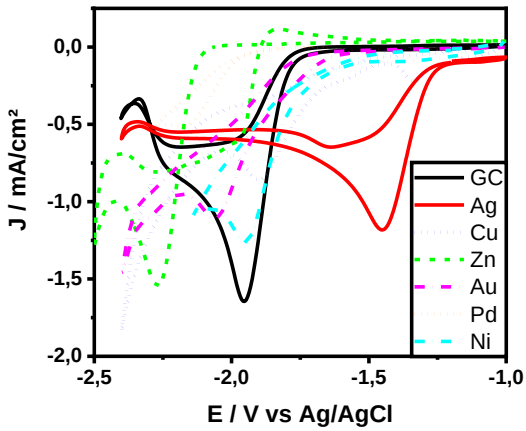

Figure 10.5: *Cyclic voltammetry at 50 mV s^{-1} of Ag, Cu, GC, Zn, Au, Pd an Ni in ACN + 0.1 M TBAP and 3 mM 9BP.*

Table 10.4: *Voltammetric data of active electrodes for the reduction of 3 mM 9BP in acetonitrile + 0.1 M TBAP at 50 mV s^{-1} (E_p and J_p) and derived parameters for scan speeds between 50 mV s^{-1} and 500 mV s^{-1}.*

	$E_p{}^a$	$J_p{}^b$	$E_p - E_p^{(GC)}$	$\partial E_p/\partial log v$	$\alpha_1{}^c$	$E_p - E_{p/2}$	$\alpha_2{}^d$	κ
Ag	-1.449	-0.98	0.401	0.056	0.53±0.02	0.090	0.53±0.01	0.53
Cu	-1.891	-0.35	0.059	0.053	0.55±0.02	0.091	0.53±0.01	0.54
GC	-1.950	-1.19	0	0.053	0.56±0.02	0.084	0.57±0.02	0.57
Zn	-2.264	-1.27	-0.314	0.051	0.59±0.05	0.073	0.66±0.09	0.62
Au	-2.050	-0.27	-0.100	0.059	0.50±0.04	0.081	0.59±0.05	0.55
Pd	-2.145	-0.13	-0.195	0.068	0.44±0.03	0.078	0.62±0.07	0.53
Ni	-1.945	-0.59	0.005	0.062	0.48±0.04	0.070	0.68±0.03	0.58

[a]V vs Ag/AgCl. [b]mA/cm² [c]Calculated from eq. 3.35. [d]Calculated from eq. 3.34.

10.3.1.5 9-Bromoanthracene

Most of the investigated cathode materials were active for the reduction of 9BA. Ti only starts reducing the halide at high overpotentials (figure 10.6). The peaks for Zn and Ti diminished slowly after the CV with the lowest scan rate was recorded. For most cathodes, there were two interesting consecutive processes visible in the CV. At lower overpotentials the DET reaction to strip the halogen and at higher overpotential the reduction (and oxidation in the back scan) of anthracene to its radical anion after a proton was taken from the solvent or residual water. For Ti it was questionable to assume that the reduction peak can be due to the reductive cleavage of the halide. If so, anthracene should be formed and at that potential reduced to its radical anion leading to an oxidation peak because the potential of the reversible couple seemed mostly independent of the used cathode material.

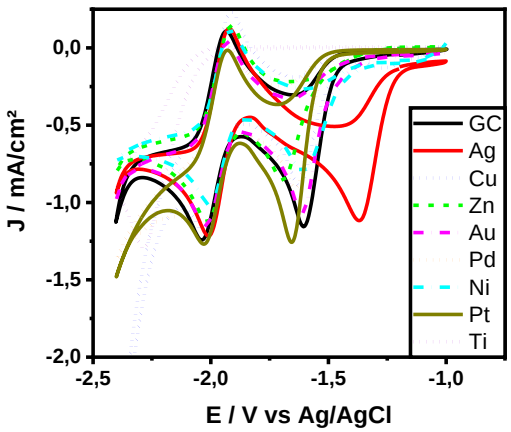

Figure 10.6: *Cyclic voltammetry at 50 mV s^{-1} of Ag, Cu, GC, Zn, Au, Pd, Ni, Pt and Ti in ACN + 0.1 M TBAP (0.1 M) and 3 mM 9BA.*

Ag remained the best electrode material with a peak potential of -1.366 V. $E_p^{(Ag)} - E_p^{(GC)}$ was the lowest (0.235 V) that has been observed in this chapter. The C-X reduction peak of all metal electrodes but Ag were positioned very close to each other. These two last observations indicated that the ability of the C-Br bond to adsorb on the Ag electrode had the largest contribution to the catalytic activity, as proposed by Huang et al. for benzyl chloride [265].

The reduction on GC is always considered as an outer sphere reaction and the similarity in E_p and α indicate that this reasoning could be generalized for all active electrodes except Ag and Ti. Kinetic indicators were well over 0.5 for all the electrodes (table 10.5) indicating that 9BA yielded the most stable radical anion.

Voltammograms of the deoxygenated electrolyte solutions can be found in the supporting information (figure S10.1) together with those for every metal on the different bromides (figure S10.2-S10.8).

Table 10.5: *Voltammetric data of active electrodes for the reduction of 3 mM 9BA in acetonitrile + 0.1 M TBAP at 50 mV s^{-1} (E_p and J_p) and derived parameters for scan speeds between 50 mV s^{-1} and 500 mV s^{-1}.*

	$E_p{}^a$	$J_p{}^b$	$E_p - E_p^{(GC)}$	$\partial E_p/\partial log v$	$\alpha_1{}^c$	$E_p - E_{p/2}$	$\alpha_2{}^d$	κ
Ag	-1.366	-0.89	0.235	0.061	0.48±0.08	0.081	0.59±0.02	0.54
Cu	-1.625	-0.46	-0.024	0.048	0.62±0.03	0.075	0.64±0.04	0.63
GC	-1.601	-0.87	0	0.053	0.56±0.06	0.067	0.71±0.04	0.64
Zn	-1.696	-0.55	-0.097	/	/	/	/	/
Au	-1.613	-0.75	-0.012	0.061	0.49±0.07	0.077	0.62±0.09	0.55
Pd	-1.637	-0.63	-0.036	0.043	0.69±0.03	0.071	0.67±0.03	0.68
Ni	-1.603	-0.52	-0.002	0.049	0.61±0.04	0.090	0.53±0.03	0.57
Pt	-1.654	-0.96	-0.053	0.057	0.52±0.05	0.068	0.70±0.06	0.61
Ti	-2.277	-0.56	-0.676	/	/	/	/	/

[a]V vs Ag/AgCl. [b]mA/cm² [c]Calculated from eq. 3.35. [d]Calculated from eq. 3.34.

10.3.1.6 Summary of the electrochemical screening

The $E_p - E_p^{(GC)}$ parameter ranged from 0.936 to 0.235 V for Ag. It decreased together with the absolute peak potential indicating that the catalytic role of the cathode material diminished with increasing aromaticity. If Ti and Ag were not taken into consideration, reduction peaks for all metals were found within a 100 mV interval for 9-Bromoanthracene. A visual representation of the reduction peak potentials for all bromides is shown in figure 10.7. Cu and Zn had similar behavior with E_p sequence BrBz < 1BN < 2BN = 9BP < 9BA.

For Ag and GC the order of E_ps was BrBz < 2BN < 1BN < 9BP < 9BA. In general, the overpotential tended to drop with more aromaticity and aligned rings were preferred over angled ones. Au, GC and Ag favor the reduction when the bromide was positioned adjacent to the ring junction whereas Cu, Zn and Pd favored the other configuration in bromonaphthalenes.

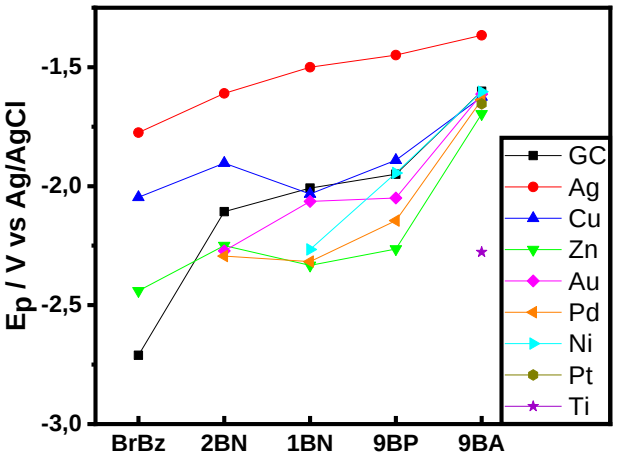

Figure 10.7: *Peak potentials for all combinations in this chapter at 50 mV s^{-1}.*

The reduction potentials of investigated bromides were outside of the potential range where bromide anions adsorb onto Ag cathodes and could possibly influence the peak shape/reaction [282]. Additionally there was no indication in the voltametric response that adsorption was taking place which would split the peak in two waves as the adsorbed bromide anions would at some point compromise the electron transfer to its halide parent molecule. Therefore, the use of equation 3.34 was assumed to be justified in this case.

The kinetic indicators were dependent on both cathode material and aromatic halide. Reduction of BrBz proceeded through a concerted mechanism on Ag, GC and Cu. For 1BN, 2BN this was the case only for the Ag electrode. In all other cases the stepwise pathway was more favorable. For 9-Bromoanthracene the calculated kinetic indicators were well over 0.5 indicating that the cleavage reaction becomes predominant.

For aromatics with bromides directly bound to the ring, the difference between Ag and inert cathodes (GC) diminished completely in terms of E_p and α. The high energy level of a carbon-chlorine σ*-orbital favors the formation of an energetically favorable intermediate, the radical anion, through the stepwise mechanism [283]. Our bromide analogues were able to receive the incoming electron in the σ*-orbital of the carbon-bromine bond which makes the concerted pathway a possibility in combination with some cathodes.

10.3.2 Electrolysis

Electrolysis was performed for all the molecules from section 10.3.1 on Ag and GC electrodes at 50 mV overpotential compared to the potential of the reduction peak taken from the 50 mV s^{-1} CV for 1 h. The GC/MS chromatograms were analyzed for the reagent, dehalogenated hydrogenated compound, dimers and other possible side products. Dimers were considered because of previous publications mentioning their formation for iodides [285,286], bromides which are not directly bound to an aromatic carbon [287] and dibromides with substituents on the aromatic ring [288]. The mass fragment chromatograms for BrBz, 1BN and 2BN reduction on Ag can be found in the supplementary information (figures S10.9-S10.11) and did not indicate any other products than the dehalogenated hydrogenated compounds. The m/z chromatogram for 76 and 154 for BrBz reduction were added as these should be the most intense ones for biphenyl. A system peak was observed at 1.08 min., benzene peak at 1.38 min. and bromobenzene peak at 3.97 min. For both these bromonaphthalene reductions, the supporting electrolyte was responsible for the peak on 4.98 min and naphthalene on 4.75 min. 1BN and 2BN exited the column at respectively 6.82 and 6.78 min. The m/z chromatogram for 126 and 254 for 1BN and 2BN reduction are most important for determination of 1,1'-binaphthalene, 1,2'-binaphthalene and 2,2'-binaphthalene. No dimer formation was observed for the reduction of previously named bromides, which is similar to the conclusions reported in [277]. The obtained mass spectra for the formed aromatics can be found in figures S10.12-S10.14. The HPLC conversions and Faradaic Efficiencies (FE) can be found in table 10.6. The conversion rates were lowest for 2BN and 9BA and significantly higher for BrBz.

The efficiencies for aromatic products range from 42 to 80% for Ag cathode and 12 to 72% for GC. One should be aware that the FE depends on numerous factors as i.e. the stability of the aromatic radical/anion, their local concentration profile, the nature of the solvent and the reaction constants of Equations 10.5, 10.6, 10.9, 10.10 and 10.11. In conclusion, the electrolysis only resulted in low to intermediate yields of dehalogenated hydrogenated aromatic compounds and the faradaic efficiencies seem to have little value due to the possible occurrence of side reactions.

Table 10.6: *Conversion rates and faradaic efficiencies for the reduction of the aromatic bromides at Ag and GC cathode after 1 h electrolysis.*

	BrBz		1BN		2BN		9BA		9BP	
	conv.	FE	conv.	FE	conv.	FE	conv.	FE	conv.	FE
Ag	41%	80%	29%	42%	7%	64%	4%	64%	14%	45%
GC	12%	72%	47%	64%	1%	12%	1%	22%	11%	42%

10.3.3 *In-situ* EPR C-X reduction

According to the data in the previous section, BrBz reduction proceeds mostly through a concerted pathway, except on Zn. The reduction of 1BN and 2BN have a concerted mechanism on Ag and a stepwise mechanism on the other electrode materials. Theoretically, the only radical intermediate species that can be formed are the bromonaphthalene radical anion ($RX^{\bullet -}$) and a deprotonated naphthalene radical ($R^{\bullet}$) for the stepwise pathway. The latter should be the only species formed under concerted conditions. A side reaction (HAT) with the solvent could occur, forming a deprotonated acetonitrile radical ($S^{\bullet}$). Poor potential control could result in the formation of a naphthalene radical anion ($RH^{\bullet -}$). 9BA and 9BP reduction always proceed through a stepwise pathway possibly forming all of the previously named radical species ($RX^{\bullet -}$, $R^{\bullet}$, $S^{\bullet}$ and $RH^{\bullet -}$).The bare ITO, Ag/ITO and NiO/ITO electrodes were used for the reduction of 9BA in the flat cell. The CVs can be found in figure 10.8. The reduction peaks were easily identifiable and differ 47, 111 and 88 mV from the ones in section 10.3.1.5, with bare ITO compared to GC.

The reductions were subsequently performed at peak potential, one bubbled with Ar and one prepared in a glovebox. Presumably the oxygen and water content of the Ar bubbled sample was higher than for the sample prepared in the glovebox. Extra features could be seen in between 344.5 mT and 345 mT attributable to the difference in preparation (figure 10.9). The hyperfine couplings in the main spectrum were much larger in literature for the delocalized electron on the naphthalene radical anion ($RH^{\bullet -}$) than in the experimental spectra; 0.538 mT, 0.266 mT and 0.153 mT for the three different proton positions (9,1 and 2 respectively) [289]. This indicates that the spectrum might be caused by another species formed through a side reaction. A CV was done on Ag/ITO with 1BN present in the solution. This resulted in noisy current variations with the solution turning orange/brown and a deposit forming on the bottom of the used cylindrical flask (figure S10.15).

Several possible explanations could be hypothesized for this behavior; (i) the PET substrate was susceptible to 1BN attack and contaminants were released in the solution, (ii) the ITO layer adhesion to the substrate was influenced resulting in a deposit of the detached ITO and the Ag particles or (iii) the Ag particles detached from the ITO. Inductively Coupled Plasma Mass Spectrometry (ICP/MS) was performed on a deposit sample to check for presence of the metals in the second and third hypothesis stated above. No significant amount of In, Sn or Ag was detected and thus, no conclusions could be drawn from the deposit analysis.

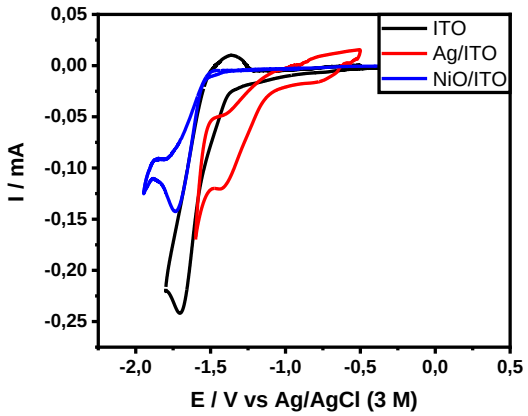

Figure 10.8: *CVs of 0.5 mM 9BA in ACN + 0.1 M TBAP on bare ITO, Ag/ITO and NiO/ITO at 50 mV s^{-1} in the flat cell (left), in Ar atmosphere.*

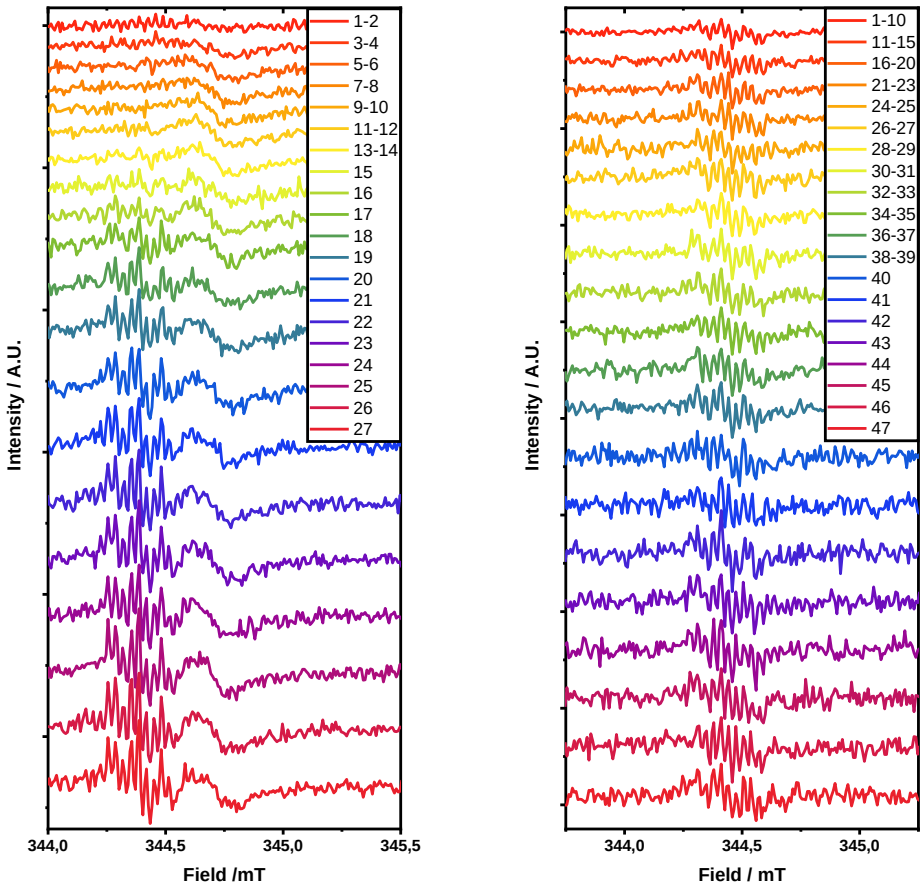

Figure 10.9: *Time dependent in-situ EPR spectra of 1 mM 9BA in ACN + 0.1 M TBAP on Ag/ITO in flat cell at -1,5 V vs Ag/AgCl (3 M) at 9.660 ± 0.001 GHz, 1mW microwave power and Ar bubbled (left), 9.662 ± 0.001 GHz, 2mW microwave power and 0.1 mT field modulation amplitude, prepared in N_2 atmosphere in a glovebox (right).*

The remaining reductions were pursued with wire electrodes because the pure metallic form of the WE did not result in any problems in the bulk experiments from section 10.3.2. The 9BA reduction was repeated with a Ag, Au and Cu wire electrode prepared in a glovebox resulting in a similar signal as the one on

Ag/ITO (figure S10.15) without difference between cathode materials used. This was expected from the α calculations as they indicated that only the stepwise mechanism could occur on all cathode materials and consequentially the same reaction intermediates should be detected. The CVs of Ag, Au and Cu wire WEs for 1BN reduction are shown in figure 10.10 as an indication of the increased difficulty of determination of the peak potentials. The peaks were shifted compared to the potentials in section 10.3.1.2 and were less pronounced. Overpotentials of the onset were in the same order Au > Cu > Ag.

2BN reduction was performed, similarly to 9BA, with a glovebox prepared sample and an Ar bubbled one. No difference in spectrum could be observed between the two samples nor between the three cathode materials. 1BN solutions were only prepared by Ar bubbling. The EPR spectra of 1BN and 2BN reductions (figure 10.10 right and 10.11 left) did not show many features. The expectation of observing a naphthalene radical or bromonaphthalene radical anion would result in an EPR spectrum with extensional splitting for both reductions. Considering a delocalized electron on a naphthalene radical anion ($RH^{\bullet -}$) with two times 4 equivalent hydrogens resulting in 25 lines and hyperfine couplings of 0.490 mT and 0.183 mT [290], the naphthalene radical ($R^{\bullet}$) and bromonaphthalene radical anion ($RX^{\bullet -}$) would have less symmetry, giving rise to the more peak splitting. For the latter, the splitting should be more extensive due to the nuclear spin of the bromide (5/2).

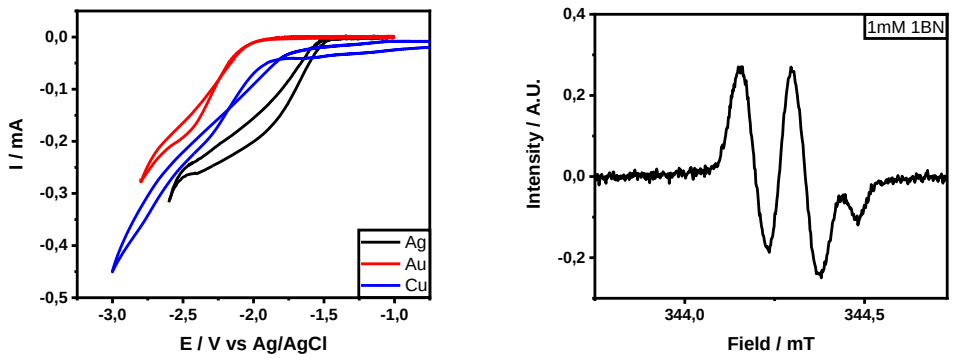

Figure 10.10: *CV on Ag, Au and Cu wire WE (left) and In-situ EPR spectra on Ag wire WE with 1 mM 1BN in ACN + 0.1 M TBAP (right) at -1.75 V vs Ag/AgCl (3 M) and 9.659 ± 0.001 GHz, in Ar atmosphere.*

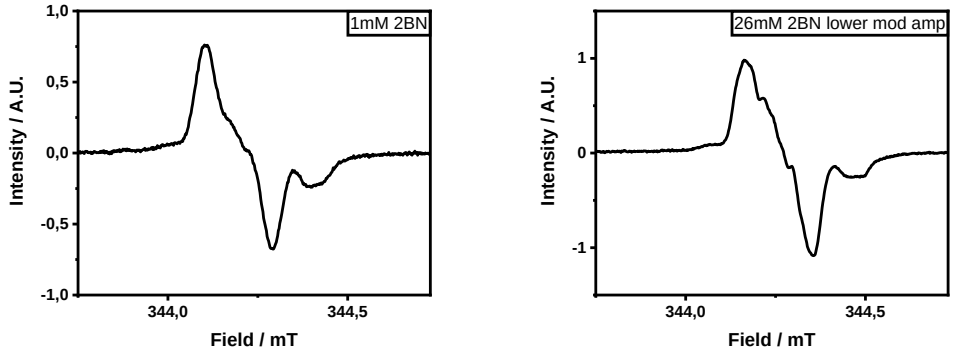

Figure 10.11: *In-situ EPR spectra on Ag wire electrode with 1mM 2BN (mod. amp. 0.1 mT and 0.4 mW microwave power at 9.656 ± 0.001 GHz) (left) and 26 mM 2BN (mod. amp. 0.05 mT) (right) in ACN + 0.1 M TBAP at 9.660 ± 0.001 GHz, both at -1.85 V vs Ag/AgCl (3 M) in Ar atmosphere.*

There was a significant difference in shape for 1BN and 2BN reductions. The 1BN radical product had a clear splitting in 2 peaks and a smaller feature around 344.5 mT while the 2BN product only had one with separation between positive and negative part plus the extra feature around 344.5 mT. The modulation amplitude and concentration of 2BN was adjusted from 0.1 mT to 0.05 mT and from 1 mM to 26 mM to obtain the spectrum in figure 10.11 (right). The spacing of the peak in figure 10.11 revealed a symmetric shoulder. These spectra could originate from a structure stabilizing a radical or electron. It could be a resonance effect or stacking effect. The latter being a stack of naphthalene molecules accommodating the transferred electron. The system would have so many protons that energy levels splitting would not be discernible. It would not explain the different spectra for the two reductions as the naphthalene stack would be the same. Possibly the naphthalenes stack without taking up a proton or bromonaphthalenes are included expressing the difference in bromide position.

The composition of the solutions was changed to see which parameters contributed to the formation of the structure resulting in the EPR signal in figure 10.10 and 10.11. The reductions were first done in DMF and DMSO with TBAP as a supporting electrolyte in bulk (figure S10.16) to assess if the solvent variation had an influence on the electrochemical behavior. DMSO showed some instability in the region of the second electron transfer where in ACN the $RH^{\bullet -}$ is

formed. Experiments in EPR were performed at the peak potentials of the first reaction which excluded the phenomenon encountered in the DMSO CVs. No signal was detected for analogous settings to the spectrum from figure 10.10. Varying the supporting electrolyte anion from perchlorate to bromide or hexafluorophosphate did also not result in any detectable signal. The presence of the perchlorate together with the ACN whilst performing these reductions seems crucial for forming the stabilizing structure of which the spectra are shown in figure 10.10 and 10.11.

Additionally, the reductions of 9BA, 1BN and 2BN were performed in the presence of PBN as a spin-trapping agent with the averaged spectra shown in figure 10.12 and 10.13. They will be simulated and compared to DFT data to identify the radical species formed through the reduction. Capturing the radicals in the adduct prevented the stabilizing structure from forming or the electron/radical from being associated with it. Experiments with a lower concentration of PBN and higher concentration of halogenated compound could be performed to check for the signal after the spin-trap is exhausted. The signal from direct electrolysis of 9BA can be observed (figure 10.13) with addition of one or more other trapped species that still need to be determined.

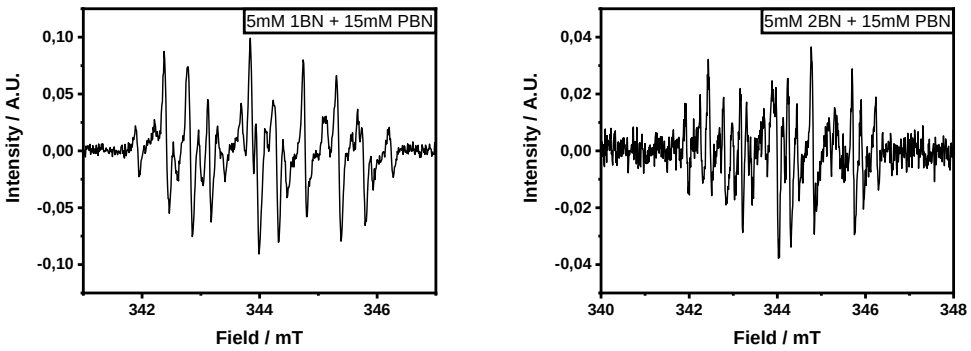

Figure 10.12: *Averaged in-situ EPR spectra of 300 scans on Ag wire electrode with 5 mM 1BN at -1.75 V vs Ag/AgCl (3 M)(left) and 5 mM 2BN at -1.85 V vs Ag/AgCl (3 M) (right) in ACN + 0.1 M TBAP with 15 mM PBN at 9.659 ± 0.001 GHz, 2 mW microwave power and 0.1 mT field modulation amplitude, both in Ar atmosphere.*

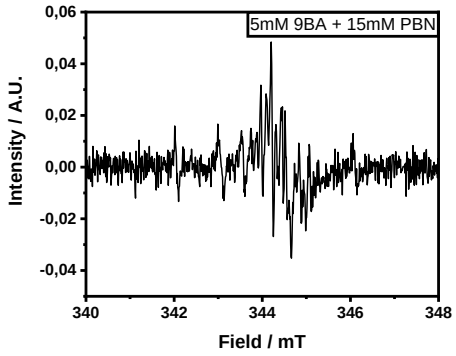

Figure 10.13: *Averaged in-situ EPR spectra of 300 scans on Ag wire electrode with 5 mM 9BA in ACN + 0.1 M TBAP ans 15 mM of PBN at -1.5 V vs Ag/AgCl (3 M), 9.659 ± 0.001 GHz, 2 mW microwave power and 0.1 mT field modulation amplitude, both in Ar atmosphere.*

10.4 Conclusions

A thorough and systematic electrochemical screening was performed for cathode materials which possibly eligible for the reduction of aromatic halides *in-situ* EPR. CV experiments were performed in ACN + 0.1 M TBAP to map the reduction peak potential and kinetic indicators were calculated for mechanistic purposes. The DET mechanism showed a tendency to the concerted pathway when smaller aromatics were investigated. For bigger aromatics the radical anion was more stabilized by the π-system leading to a more favorable reaction pathway; the stepwise mechanism. For Ag the turning point from concerted to stepwise was only observed when three aromatic rings were present in the halide. Ag exhibited the largest potential shift compared to GC for every bromide. The higher the aromaticity, the more cathodes showed activity for reduction. Mn and Mg did not react with any of the tested compounds. Ti only showed a reduction wave for 9-bromoanthracene at very negative potential. Other cathodes had intermediate reactivity which changed position among each other on the activity scale depending the number and configuration of aromatic rings and, on the position of the bromide.

The GC/MS chromatograms per mass indicated formation of the corresponding aromatic compound out of the bromide without any other product being qualitatively determined. The carbon-halogen bond breaking was the performed *in-situ* EPR in search for intermediates possibly confirming the proposed electrochemical mechanisms. The ITO electrode from chapter 6 served its purpose well for 9BA reduction but showed instability when being employed for 1BN reduction. Different cathode materials (wires) did not result in changed EPR spectra with direct detection. The spectra of the 1BN and 2BN reductions were rather peculiar. The small couplings and lack of peaks evoque hypotheses about supramolecular structures stabilizing radicals/electrons. These spectra were unique for the combination of ACN with TBAP and did not occur in DMF or DMSO as a solvent and with TBAB or $TMAF_6P$ as a supporting electrolyte. Depending on the results coming from the simulations of PBN adduct spectra, 1BN and 2BN reduction could still be classified as stepwise or concerted with the spin-trap experiments for Cu and Au cathodes as future work.

10.5 Supporting information

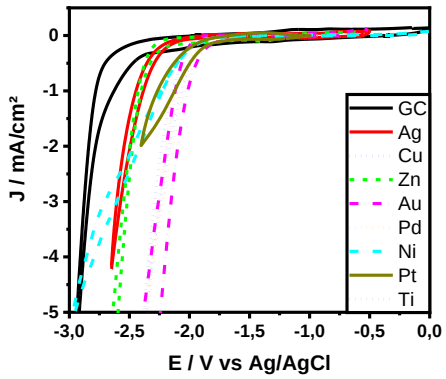

Figure S10.1: *CV of all active cathodes in a blank solution of Ar-bubbled ACN + 0.1 M TBAP in Ar atmosphere.*

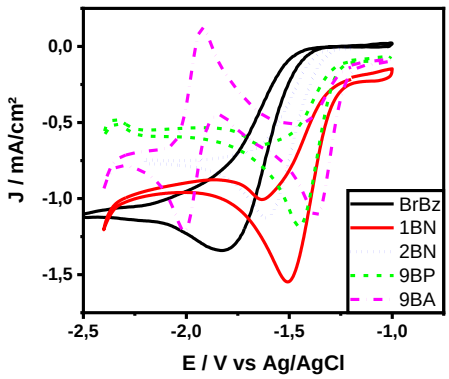

Figure S10.2: *Cyclic voltammetry at 50 mV s^{-1} of BrBz, 1BN, 2BN, 9BA, 9BP on Ag cathode in ACN + TBAP (0.1 M) in Ar atmosphere.*

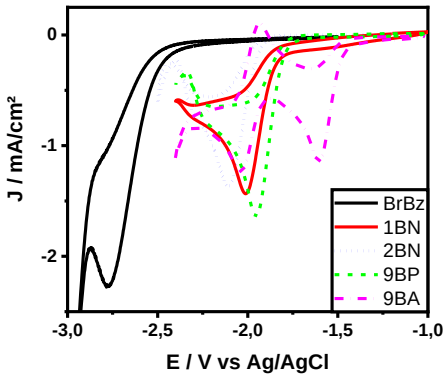

Figure S10.3: *Cyclic voltammetry at 50 mV s^{-1} of BrBz, 1BN, 2BN, 9BA, 9BP on GC cathode in ACN + TBAP (0.1 M) in Ar atmosphere.*

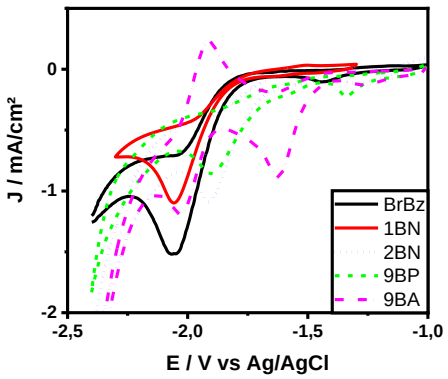

Figure S10.4: *Cyclic voltammetry at 50 mV s^{-1} of BrBz, 1BN, 2BN, 9BA, 9BP on Cu cathode in ACN + TBAP (0.1 M) in Ar atmosphere.*

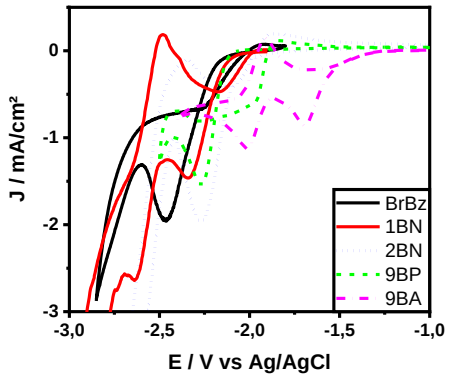

Figure S10.5: *Cyclic voltammetry at 50 mV s^{-1} of BrBz, 1BN, 2BN, 9BA, 9BP on Zn cathode in ACN + TBAP (0.1 M) in Ar atmosphere.*

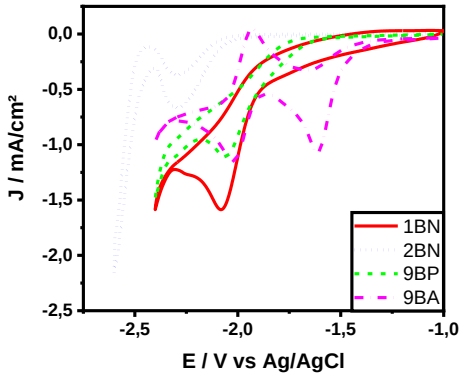

Figure S10.6: *Cyclic voltammetry at 50 mV s^{-1} of 1BN, 2BN, 9BA, 9BP on Au cathode in ACN + TBAP (0.1 M) in Ar atmosphere.*

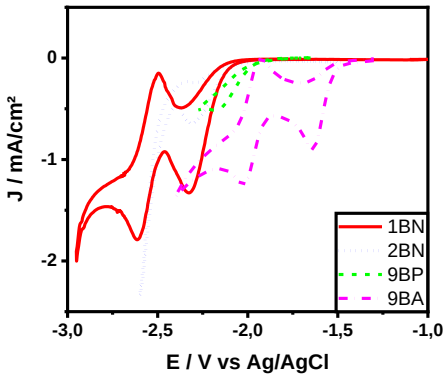

***Figure S10.7**: Cyclic voltammetry at 50 mV s-1 of 1BN, 2BN, 9BA, 9BP on Pd cathode in ACN + TBAP (0.1 M) in Ar atmosphere.*

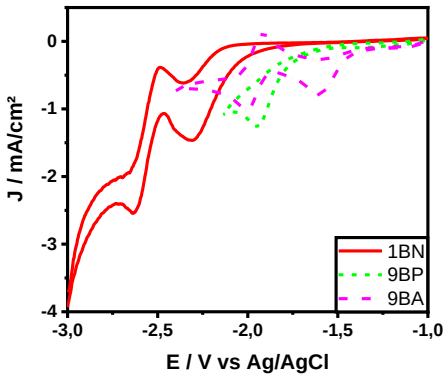

***Figure S10.8:** Cyclic voltammetry at 50 mV s^{-1} of 1BN, 9BA, 9BP on Ni cathode in ACN + TBAP (0.1 M) in Ar atmosphere.*

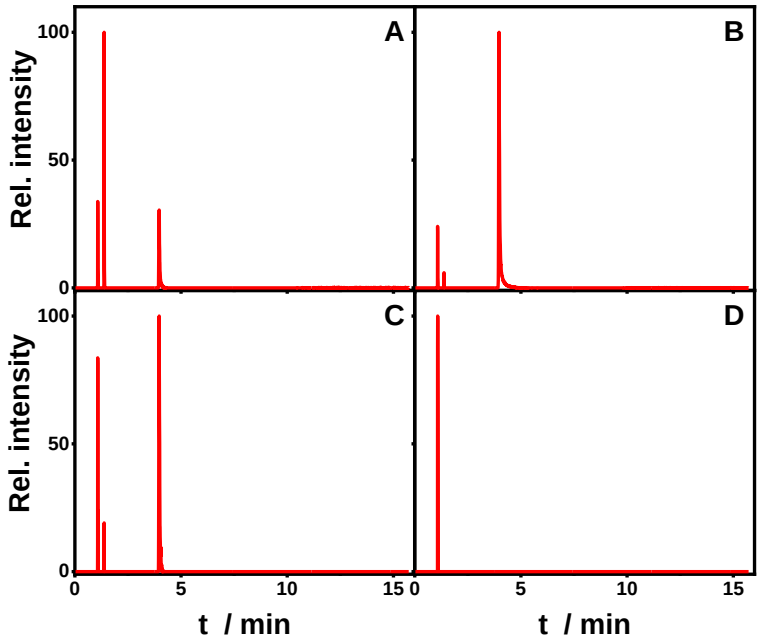

***Figure S10.9**: Chromatograms filtered on m/z 78 (A), 77 (B), 76 (C) and 154 (D) for the reduction of BrBz on Ag cathode in Ar atmosphere.*

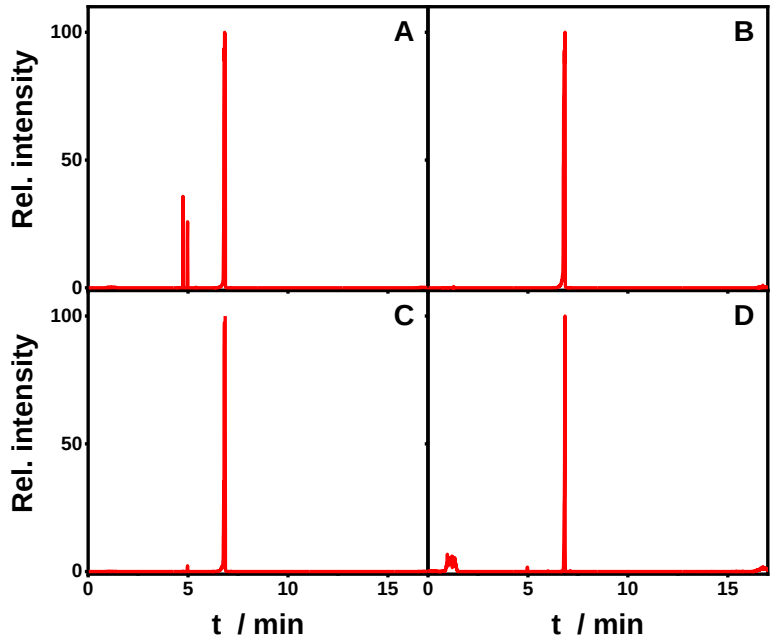

Figure S10.10: *Chromatograms filtered on m/z 128 (A), 206 (B), 126 (C) and 254 (D) for the reduction of 1BN on Ag cathode in Ar atmosphere.*

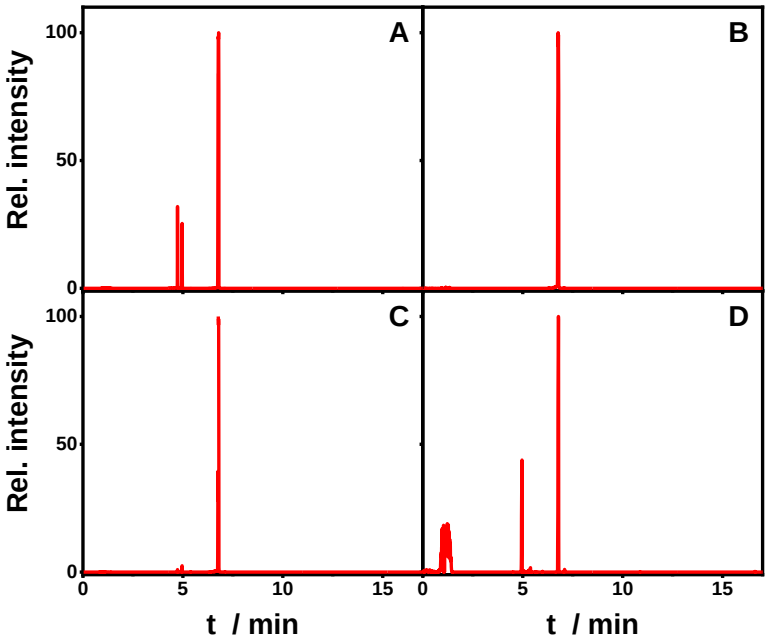

Figure S10.11: *Chromatograms filtered on m/z 128 (A), 206 (B), 126 (C) and 254 (D) for the reduction of 2BN on Ag cathode in Ar atmosphere.*

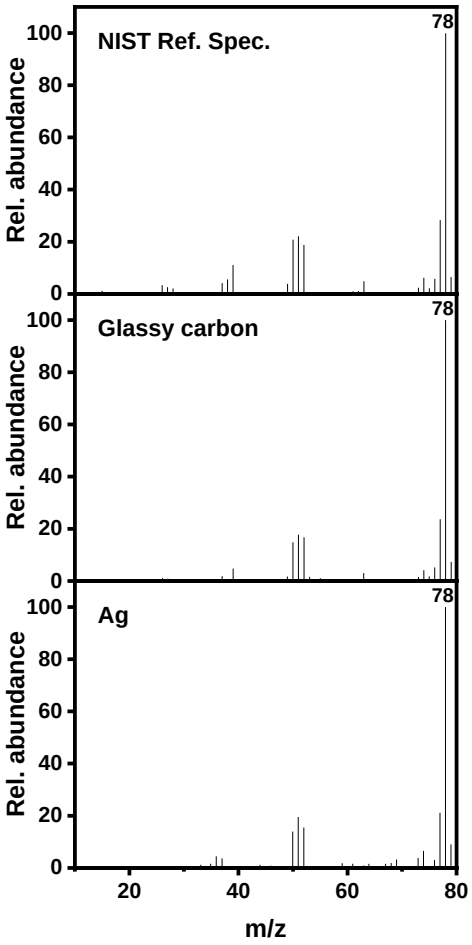

Figure S10.12: *Mass spectrum from GC-MS measurement after electrolysis of BrBz, in Ar atmosphere.*

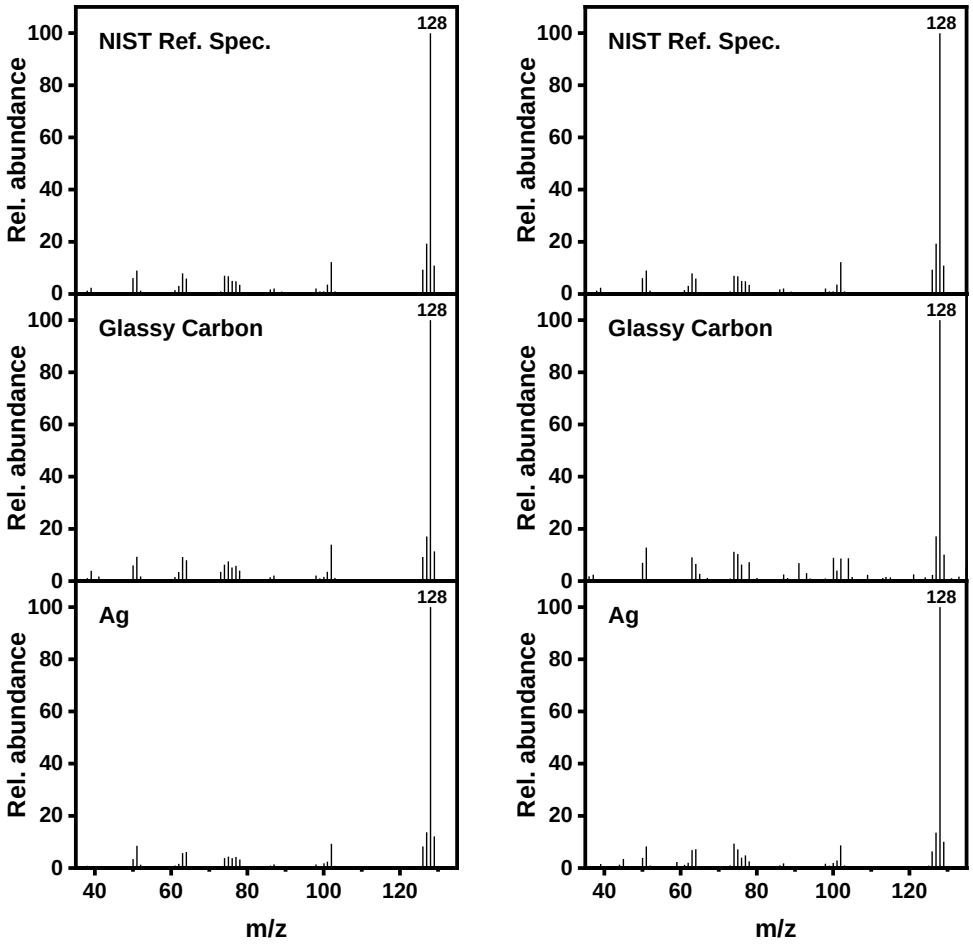

Figure S10.13: *Mass spectra of naphthalene from GC-MS measurement after electrolysis of 1BN (left) and 2BN (right), both in Ar atmosphere.*

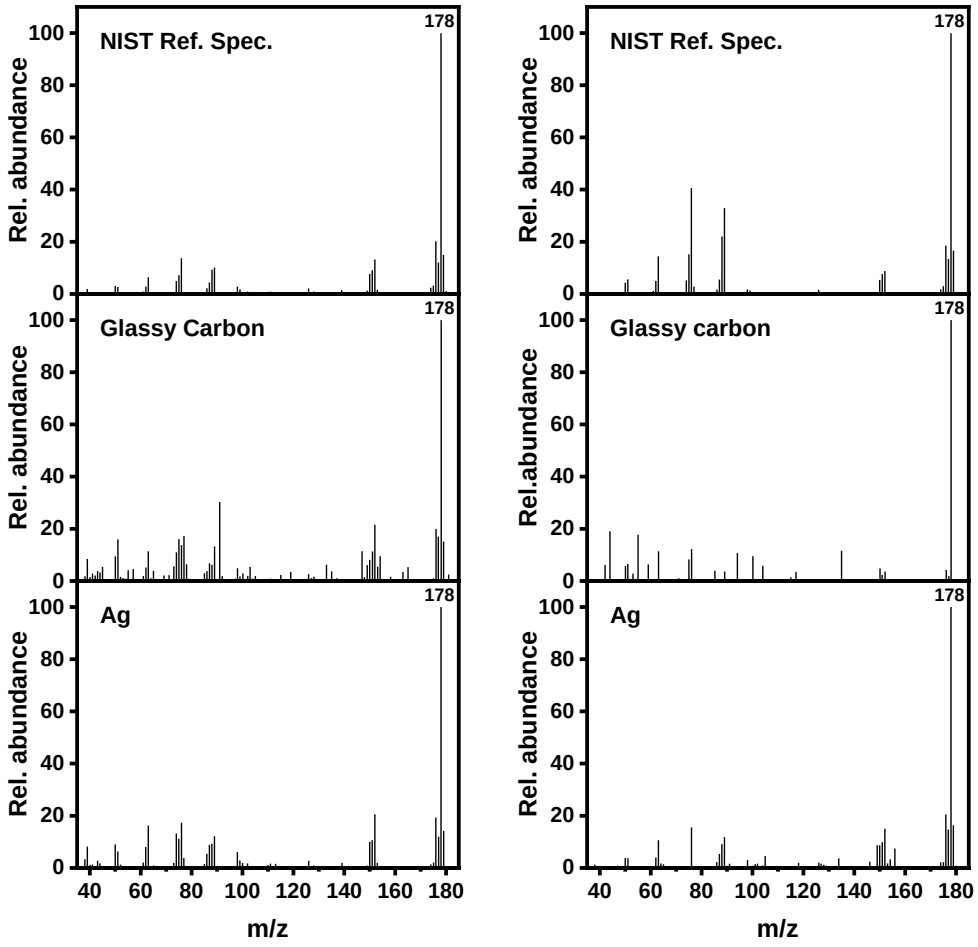

Figure S10.14: *Mass spectra of phenanthrene from GC-MS measurement after electrolysis of 9BP (left) and of anthracene after electrolysis of 9BA (right), both in Ar atmosphere.*

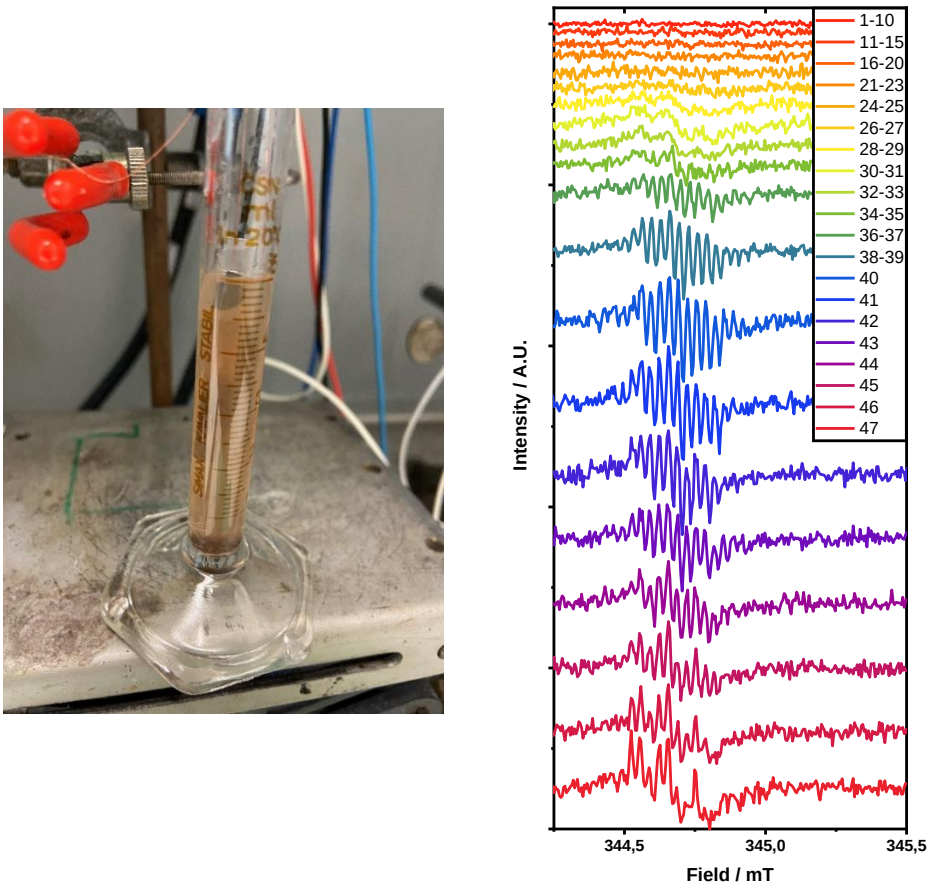

Figure S10.15: *Photograph of deposit formation during 1BN electroreduction (left). Time dependent in-situ EPR spectra of 10 mM 9BA in ACN + 0.1 M TBAP on Ag wire in flat cell at -1,5 V vs Ag/AgCl (3 M) at 9.667 ± 0.001 GHz, 2mW microwave power and 0.1 mT field modulation amplitude prepared in glovebox (N_2 atmosphere)(right).*

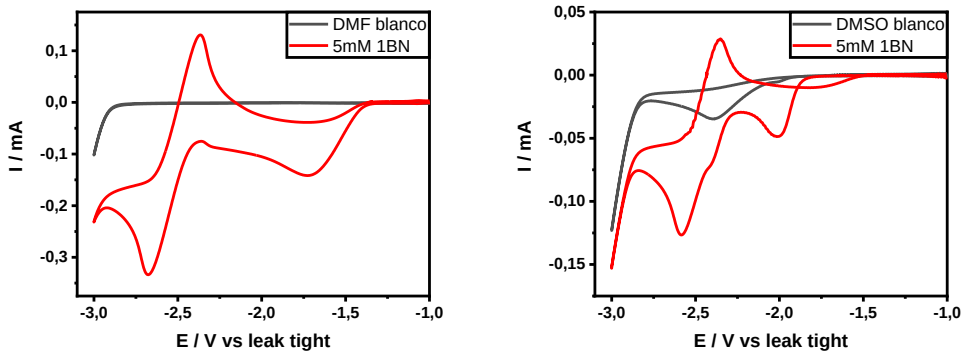

Figure S10.16: *CV of 5 mM 1BN and blanc in DMF (left) and DMSO (right) in bulk on a Ag disc electrode at 50 mV s^{-1}, in Ar atmosphere.*

Part IV

Conclusions

Chapter 11

Conclusions and future perspectives

The final chapter concludes this doctoral dissertation. Conclusions of both the setups part and the case studies part are summarized and perspectives for future research are presented.

11.1 Conclusions

This thesis shows the strength and versatility of combining two very relevant and complementary techniques. Firstly, electrochemistry, enabling the formation of specific products by means of a heterogeneous electron transfer to a molecule in solution at their unique reduction potential. Secondly, Electron Paramagnetic Resonance with its power to identify intermediate products, where generally used detection techniques only succeed in analysis of products. This technique can be used for unraveling information about reaction pathways involving compounds with unpaired electrons and their close environment. Although both very powerful, combining these techniques seems all but straightforward and one should be educated in chemistry, physics and electrochemistry in order to set up meaningful experiments in avoidance of naïve interpretations.

Several v keep in mind when performing successful combinatorial experiments are listed below. They form the conclusion of the setup design part of the thesis (part II). The setup itself must comply to some requirements to be considered for use *in operando* EPR measurements. Fulfilling these requirements as much as possible is necessary to maximize the success rate. Materials introduced should:

- have high chemical resistance to the used solvents and analyte. This was illustrated by the use of the promising ITO electrode for carbon-halogen bond reduction in chapter 10, resulting in detachment of the catalyst layer for 1BN whilst being perfectly suitable for 9BA reduction. Similarly, the dissolution of the PET supporting the ITO in acetone solution was anticipated (chapter 9), therefore the wire electrode design was employed instead.

- not contain any radical species possibly influencing the spectrum. If present, a blank can be subtracted for every measurement as there could be a concentration gradient of paramagnetic centers in the used material. If the g-factor of that center falls out of the subjected region of the magnetic field, the presence of this center is of minor importance.

- not or only minimally absorb electromagnetic waves in the microwave region. Tuning of the cavity can become impossible at high absorption. Minimizing the volume of absorbing material serves as a possible solution if a specific material is required (illustrated in chapter 8).

Electrochemical determination of peak potentials in cyclic voltammetric experiments indicates the specific working potential for the phenomenon of interest to occur. The design should consider:

- reasonable electrochemical behavior. It was shown in Part II that every setup has a unique electrochemical response due to the electrode and cell geometry. As long as electrochemical phenomena can be distinguished in the CV, desired radicals can be isolated.

- the electrode surface needs to be reproducible in order to obtain similar electrochemical behavior and signal intensity.

- a careful selection and positioning of the reference electrode. Stability over the course of the experiment is required favoring real reference electrodes over pseudo reference electrodes. To minimize uncompensated resistance, the reference electrode should be positioned as close as possible to the working electrode favoring the pseudo reference electrode which can be small enough to be placed in the flat part whilst a real reference electrode can only sit in the bulk section on top for batch measurements. The use of a less conductive working electrode material with a reference electrode outside of the flat part can result in poor potential control in the sensitive region of the resonator. In chapter 5 and 9 a different choice was made in this respect. Acetone reduction required a real reference electrode to avoid direct reduction of acetone isolating the oxygen reduction reaction whereas the test cases did not have this issue.

- the counter electrode positioning. Similarly to the reference electrode, putting a rod in the bulk section for batch measurements brings about a higher cell voltage yet avoiding counter electrode radical generation in the sensitive cavity part. In all batch experiments, the choice was made to exclude the counter electrode from the sensitive part, requiring a potentiostat with sufficient compliance voltage. The flow cell in chapter 8 therefore required a change in interelectrode distance.

Electrodeposition and investigation of a chosen catalyst on the electrode surface generally requires:

- a flat and reproducible surface.
- a substrate that does not participate in the electron transfer or has an effect that can be separated of that of the electrocatalyst, yet being conductive enough to reach the applied potential at the reaction site.
- preferably cheap and replaceable or reusable.

Finally, the reaction itself can impose some requirements due to the lifetime of the radical. The radical concentration should be sufficiently high to reach the detection limit. This can be reached by:

- having a large active surface area in the sensitive part in combination with a high analyte concentration.

- slowing down decay reactions by lowering the temperature can be an option but will also affect electrode kinetics. In extreme cases flash freezing can be attempted, stopping the electrolysis potentially preserving the radicals.

- adding a spin trap if its reaction constant with the desired radical is sufficiently high.

- introducing hydrodynamic flow to avoid dipolar couplings as was discussed in chapter 6. Averaging of scans then enhances the signal even though no high concentration of radical analyte is present.

The acquired information from part II was then used for the investigation of two case studies in part III. Firstly, the intermediates of direct and indirect acetone electroreduction were identified by combining a wire electrode and real reference electrode with the use of DMPO as a spin trap (chapter 9). The results indicated that different radical species were formed depending on the presence of oxygen in solution. Two mechanisms were proposed considering these experimental findings, bearing in mind the literature concerning electrochemical self-condensation of acetone and oxygen reduction reaction in organic solvents.

Secondly, the C-X reduction of aromatic bromides was investigated electrochemically by analyzing the kinetic indicator which is known to give an indication of the dissociative electron transfer mechanism. These mechanisms have not yet been fully evidenced in literature by spectroscopic determination of intermediates. Therefore, the electrochemical data was complemented *in-situ* EPR electrochemistry with direct and indirect detection in the presence of the PBN spin trap. Analysis and simulation of the obtained data will help identify the intermediate species in order to unravel this reaction mechanism.

Overall, this thesis has shown that the combinatorial technique of *in-situ* electrochemical EPR still has a lot of potential. It provides novel setups for several types of reaction systems that should be considered by anyone attempting to combine electrocatalysis with EPR. We hope that it can convince scientists to take the leap and that it will help them to advance in their electrocatalysis research.

11.2 Future perspectives

After identifying the pitfalls and opportunities of the different setups and their application in some of the shown cases in this thesis, a multitude of cases can be investigated by *in-situ* electrochemical EPR spectroscopy utilizing the most suitable setup. The C-X spin-trapped spectra will be analyzed in the future to provide the necessary information to postulate an evidence-based mechanism. Some setups can still be improved, making handling of samples more user

friendly or providing other advantages. One example is the glassy carbon electrode from chapter 7. The electrode positions can be fixated and a Pt cylinder can be incorporate as a counter electrode in the PEEK holding the glassy carbon working electrode (figure 11.1).

Figure 11.1: *Optimized GC electrode for standard EPR tube.*

This will enable the use of EPR tube with a thicker wall which is cheaper and more rigid. Bubble formation due to surface tension will be minimized. The pseudo reference electrode should be positioned in the same plane as the working electrode. Polishing will then also result in a new reference electrode surface.

Preliminary testing has been performed to incorporate the ITO from chapter 6 into the flow cell from chapter 8. It will allow positioning of the electrocatalyst electrode in the center of the cavity. Some issues still need to be resolved like the fixation and connection of the electrode material in the POM housing. The challenge will be to prevent leakages and to minimize the dead volume created by compressing the electrode material against the POM.

The ITO electrode can be adjusted for use in an EPR tube and proteins can be fixated to the surface to investigate their redox behavior as exemplified by the Roessler group [129]. Our approach simplifies the process as they deposit and anneal the ITO particles on a Ti wire themselves, taking several days.

List of figures

List of tables

Bibliography

[1] A.E. Cahill, M.E. Aiello-Lammens, M. Caitlin Fisher-Reid, X. Hua, C.J. Karanewsky, H.Y. Ryu, G.C. Sbeglia, F. Spagnolo, J.B. Waldron, O. Warsi, J.J. Wiens, How does climate change cause extinction?, Proc. R. Soc. B Biol. Sci. 280 (2013). https://doi.org/10.1098/rspb.2012.1890.

[2] NOAA National Centers for Environmental Information, State of the Climate: Global Climate Report for Annual 2019, (2020). https://www.ncdc.noaa.gov/sotc/global/201913 (accessed March 26, 2020).

[3] United Nations, Kyoto protocol to the United Nations Framework Convention on Climate Change, 1998.

[4] United Nations, Doha amendment to the Kyoto Protocol, 2012.

[5] United Nations, Paris Agreement to the United Nations Framework Convention on Climate Change, 2015.

[6] Federatie van Belgische elektriciteits- en Gasbedrijven, Jaarverslag, 2018.

[7] A. Verbruggen, Y. Yurchenko, Positioning nuclear power in the low-carbon electricity transition, Sustain. 9 (2017) 1–14. https://doi.org/10.3390/su9010163.

[8] H.H. Rogner, World outlook for nuclear power, Energy Strateg. Rev. 1 (2013) 291–295. https://doi.org/10.1016/j.esr.2012.12.001.

[9] VREG, Toekomst nettarieven – capaciteitstarief, (2020). https://www.vreg.be/nl/toekomst-nettarieven-capaciteitstarief (accessed December 2, 2020).

[10] J. Kaat, T. Neven, N. Renders, P. Vingerhoets, M. Pelgrims, Energiebalans Vlaanderen 1990-2017, 2017.

[11] R. Agrawal, Separations: Perspective of a process developer/designer, AIChE J. 47 (2001) 967–971. https://doi.org/10.1002/aic.690470503.

[12] F. Haber, Thermodynamik technischer Gasreaktionen: Sieben Vorlesungen (German Edition), 1st editio, 1905.

[13] C. Bosch, Process of producing ammonia, 1911. https://doi.org/10.1145/178951.178972.

[14] F. Rosowski, A. Hornung, O. Hinrichsen, D. Herein, M. Muhler, G. Ertl, Ruthenium catalysts for ammonia synthesis at high pressures: Preparation, characterization, and power-law kinetics, Appl. Catal. A Gen. 151 (1997) 443–460. https://doi.org/10.1016/S0926-860X(96)00304-3.

[15] J. Loskyll, K. Stöwe, W.F. Maier, Search for new catalysts for the oxidation of SO2, ACS Comb. Sci. 15 (2013) 464–474. https://doi.org/10.1021/co400023j.

[16] W. Ostwald, Improvements in and relating to the Manufacture of Nitric Acid and Oxides of Nitrogen, GB190208300A, 1902.

[17] C.A.C. Sequeira, D.M.F. Santos, Electrochemical routes for industrial synthesis, J. Braz. Chem. Soc. 20 (2009) 387–406. https://doi.org/10.1590/S0103-50532009000300002.

[18] G.G. Botte, Electrochemical manufacturing in the chemical industry, Electrochem. Soc. Interface. 23 (2014) 49–55. https://doi.org/10.1149/2.F04143if.

[19] A. Steinfeld, High-temperature solar thermochemistry for CO2 mitigation in the extractive metallurgical industry, Energy. 22 (1997) 311–316. https://doi.org/10.1016/S0360-5442(96)00103-X.

[20] American Chemical Society, Hall Process: Production and Commercialization of Aluminum., Natl. Hist. Chem. Landmarks. (n.d.). http://www.acs.org/content/acs/en/education/whatischemistry/landmarks/aluminumprocess.html (accessed December 1, 2020).

[21] B.A. Frontana-Uribe, R.D. Little, J.G. Ibanez, A. Palma, R. Vasquez-Medrano, Organic electrosynthesis: A promising green methodology in organic chemistry, Green Chem. 12 (2010) 2099–2119. https://doi.org/10.1039/c0gc00382d.

[22] P.T. Anastas, M.M. Kirchhoff, Origins, current status, and future challenges of green chemistry, Acc. Chem. Res. 35 (2002) 686–694. https://doi.org/10.1021/ar010065m.

[23] E. Steckhan, T. Arns, W.R. Heineman, G. Hilt, D. Hoormann, J. Jörissen, L. Kröner, B. Lewall, H. Pütter, Environmental protection and economization of resources by electroorganic and electroenzymatic syntheses, Chemosphere. 43 (2001) 63–73. https://doi.org/10.1016/S0045-6535(00)00325-8.

[24] J.J. Leddy, Industrial electrochemistry, 1989. https://doi.org/10.1179/bcj.1983.18.2.70.

[25] D. Pletcher, Organic electrosynthesis – A road to greater application. A mini review, Electrochem. Commun. 88 (2018) 1–4. https://doi.org/10.1016/j.elecom.2018.01.006.

[26] H. Lund, O. Hammerich, eds., Organic electrochemistry, 4th editio, Marcel Dekker, Inc., New York, 2001.

[27] F. Beck, Cathodic Dimerization, Angew. Chemie Int. Ed. English. 11 (1972) 760–781. https://doi.org/10.1002/anie.197207601.

[28] B. Speiser, Methods to Investigate Mechanisms of Electroorganic Reactions, 2007. https://doi.org/10.1002/9783527610426.bard080001.

[29] M. Li, N.S. Marinkovic, In situ infrared spectroelectrochemistry: Principles and applications, Infrared Spectrosc. Theory, Dev. Appl. (2014) 307–331.

[30] W. Kaim, A. Klein, eds., Spectroelectrochemistry, 2008.

[31] L. Dunsch, Recent Advances in in-situ multi-spectroelectrochemistry, J. Solid State Electrochem. 15 (2011) 1631–1646. https://doi.org/10.1007/s10008-011-1453-1.

[32] C. Brett, A. Brett, Electrochemistry: principles, methods, and applications, Springer. (1993) 427. https://doi.org/10.1002/anie.199419892.

[33] A.J. Bard, L.R. Faulkner, E. Swain, C. Robey, Fundamentals and Applications, n.d.

[34] M.E.. Orazem, B. Tribollet, Electrochemical Impedance Spectroscopy, John Wiley & Sons, Inc., Hoboken, New Jersey, 2008.

[35] W.R. Hagen, Biomolecular EPR spectroscopy, 2008. https://doi.org/10.1201/9781420059588.

[36] M. Brustolon, G. Giamello, Electron Paramagnetic Resonance: A Practitioner's toolkit, Wiley, 2009.

[37] G.R. Eaton, S.S. Eaton, D.P. Barr, R.T. Weber, Quantitative EPR, Springer, 2010.

[38] V. Chechik, E. Carter, D. Murphy, Electron Paramagnetic Resonance,

2016.

[39] J.D. Wadhawan, R.G. Compton, EPR Spectroscopy in Electrochemistry, in: E.D. Calvo (Ed.), Encycl. Electrochem., 2004: pp. 170–220. https://doi.org/10.1002/chin.200350274.

[40] R.G. Compton, A.M. Waller, ESR Spectroscopy of Electrode Processes, in: R.J. GALE (Ed.), Spectroelectrochemistry, Theory Pract., Plenum Press, New York, 1988: pp. 349–396.

[41] F. Gerson, W. Huber, Electron Spin Resonance Spectroscopy of Organic Radicals, Wiley-VHC, Weinheim, 2003.

[42] D. Goldfarb, S. Stoll, eds., EPR Spectroscopy: Fundamentals and methods, Wiley, 2018.

[43] NIST, 2018 CODATA Value: proton mass, NIST Ref. Constants, Units, Uncertainty. (2019).

[44] D.E.G. Austen, P.H. Given, D.J.E. Ingram, M.E. Peover, Electron resonance study of the radicals produced by controlled potential electrolysis of aromatic substances, Nature. 182 (1958) 1784–1786. https://doi.org/10.1038/1821784a0.

[45] A.H. Maki, D.H. Geske, Detection of electrolytically generated transient free radicals by electron spin resonance [3], J. Chem. Phys. 30 (1959) 1356–1357. https://doi.org/10.1063/1.1730187.

[46] D.H. Geske, A.H. Maki, Electrochemical Generation of Free Radicals and Their Study by Electron Spin Resonance Spectroscopy; the Nitrobenzene Anion Radical, J. Am. Chem. Soc. 82 (1960) 2671–2676. https://doi.org/10.1021/ja01496a004.

[47] E.W. Stone, A.H. Maki, Electron spin resonance of semiquinones in aprotic solvents, J. Chem. Phys. 36 (1962) 1944–1945. https://doi.org/10.1063/1.1701296.

[48] L.H. Piette, P. Ludwig, R.N. Adams, Electron Paramagnetic Resonance and Electrochemistry: Studies of Electrochemically Generated Radical Ions in Aqueous Solution, Anal. Chem. 34 (1962) 916–921. https://doi.org/10.1021/ac60188a013.

[49] Wilmad Labglass, SPScienceware, WG-810-Q Suprasil Electrolytic Assembly - Varian, Radiopan, (n.d.). https://www.wilmad-labglass.com/Products/WG-810-Q/ (accessed November 20, 2020).

[50] I.B. Goldberg, A.J. Bard, Simultaneous Electrochemical-Electron, 76 (1971) 3281–3290.

[51] R.N. Adams, Application of Electron Paramagnetic Resonance techniques in Electrochemistry, J. Electroanal. Chem. 8 (1964) 151–162.

[52] I.B. Goldberg, A.J. Bard, S.W. Feldberg, Resistive Effects in Thin Electrochemical Cells: Digital Simulations of Electrochemistry in Electron Spin Resonance Cells, J. Phys. Chem. 76 (1972) 2550–2559.

[53] I.B. Goldberg, A.J. Bard, Simultaneous Electrochemical-Electron Spin Resonance Measurements. II. Kinetic Measurements Using Constant Current Pulse, J. Phys. Chem. 3 (1974) 290–294. https://doi.org/10.1021/j100596a021.

[54] I.B. Goldberg, D. Boyd, R. Hirasawa, A.J. Bard, Simultaneous Electrochemical-Electron Spin Resonance Measurements. III. Determination of Rate Constants for Second-Order Radical Anion Dimerization, J. Phys. Chem. 78 (1974) 295–299.

[55] J.P. Billon, G. Cauquis, J. Combrisson, A. Li, Mise en évidence par résonance magnétique du radical libre obtenu par oxydation électrochimique de la phénothiozine., Bull. Soc. Chim. Fr. (1960) 2062.

[56] C. Barry, G. Cauquis, M. Maurey, Propriétés électrochimiques en millieu organique de quelques hétérocycles isologues du diphénylènedioxide., Bull. Soc. Chim. Fr. 8 (1966) 2510–2516.

[57] G. Cauquis, M. Geniés, Oxydation électrochimique de quelques pentaphénulpyrroles en milieu organique. Radicaux cations correspondants., Bull. Soc. Chim. Fr. 9 (1967) 3220–3227.

[58] G. Cauquis, M. Genies, H. Lemaire, A. Rassat, J.P. Ravet, Electrochemical oxidation of nitrosobenzene and derivatives in organic medium. Electron spin resonance of the cation-radicals, J. Chem. Phys. 47 (1967) 4642–4644. https://doi.org/10.1063/1.1701676.

[59] G. Cauquis, J.P. Billon, J. Raisson, Etude d'une famille de bases de Lawis: Les arylamino-9 anthracènes. I. Oxidation électrochimique au sein de l'acétonitrile, Bull. Soc. Chim. Fr. 1 (1967) 199–207.

[60] J.K.. Dohrmann, K.J. Vetter, Anwendungsgrenzen der ESR-Spektroskopie in der electrochemischen kinetik, Electroanal. Chem. Interfacial Electrochem. 20 (1969) 23–32.

[61] B. Kastening, B. Gostisa-Mihelcic, J. Divisek, ESR Investigations of Short-lived Intermediates in Electrochemical Reactions, Faraday Discuss. Chem. Soc. 56 (1973) 341–352.

[62] A.R. Despić, I. Epelboin, H. Gerischer, M. Keddam, S. Bruckenstein, W.J. Albery, A.J. Bard, J.K. Dohrmann, E.J. Casey, C.L. Gardner, B. Kastening, M. Fleischmann, R.E.W. Jansson, R.D. Rieke, General discussion, Faraday Discuss. Chem. Soc. 56 (1973) 367–378. https://doi.org/10.1039/DC9735600367.

[63] R.G. Compton, A.M. Waller, ESR Spectroscopy of Electrode Processes, Spectroelectrochemistry. (1988) 349–398. https://doi.org/10.1007/978-1-4613-0985-7_7.

[64] R.D. Allendoerfer, G.A. Martinchek, S. Bruckenstein, Simultaneous Electrochemical-Electron Spin Resonance Measurements with a Coaxial Microwave Cavity, Anal. Chem. 47 (1975) 890–894.

[65] F. Gerson, H. Ohya-nishiguchi, C. Wydler, Indirect Determination of the Half-Wave Reduction Potentials of Benzene and (2,2)Paracyclophane, Angew. Chemie - Int. Ed. 15 (1976) 552–553.

[66] F. Gerson, R. Gleiter, H. Ohya-Nishiguchu, Isomerization of the radical anions of 6a-Thiathiophthenes, Helv. Chim. Acta. 60 (1977) 1220–1225.

[67] H. Ohya-Nishiguchi, Both Oxidation and Reduction of Aromatic Hydrocarbons by an Electrolysis Cell Designed for Low-temperature ESR Studies, Bull. Chem. Soc. Jpn. 52 (1979) 2064–2068. https://doi.org/10.1246/bcsj.52.2064.

[68] J.B. Carroll, Ph. D thesis, State University of New York at Buffalo, 1983.

[69] W.J. Albery, B.A. Coles, A.M. Couper, K.M. Garnett, Electrochemical electron spin resonance using a tube electrode, J. Chem. Soc. Chem. Commun. (1974) 198–199. https://doi.org/10.1039/C39740000198.

[70] W.J. Albery, B.A. Coles, A.M. Couper, The tube electrode and E.S.R, J. Electroanal. Chem. 65 (1975) 901–909.

[71] W.J. Albery, A.T. Chadwick, B.A. Coles, N.A. Hampson, The tube electrode and E.S.R.: Second order kinetics, J. Electroanal. Chem. 75 (1977) 229–239.

[72] W.J. Albery, R.G. Compton, A.T. Chadwick, B.A. Coles, J.A. Lenkait, Tube electrode and electron spin resonance. First-order kinetics, J. Chem. Soc.

Faraday Trans. 1 Phys. Chem. Condens. Phases. 76 (1980) 1391–1401. https://doi.org/10.1039/F19807601391.

[73] W.J. Albery, R.G. Compton, I.S. Kerr, The anodic oxidation of 1,4-diaminobenzene: an Electron Spin Resonance and Electrochamical Study, J. Chem. Soc. Perkin Trans. 2 (1981) 825–829.

[74] W.J. Albery, R.G. Compton, Tube electrode and electron spin resonance transient signals, J. Chem. Soc. Faraday Trans. 1 Phys. Chem. Condens. Phases. 78 (1982) 1561–1567. https://doi.org/10.1039/F19827801561.

[75] W.J. Albery, R.G. Compton, C.C. Jones, A novel electrode for electrochemical ESR and its application to modified electrodes, J. Am. Chem. Soc. 106 (1984) 1980–1984.

[76] B.A. Coles, R.G. Compton, Photoelectrochemical ESR, J. Electroanal. Chem. Interfacial Electrochem. 144 (1983) 87–98. https://doi.org/10.1016/S0022-0728(83)80146-6.

[77] B.A. Coles, R.G. Compton, R.A. Spackman, A finite-element method for determining ohmic distortion of current-voltage curves at hydrodynamic electrodes, Electroanalysis. 5 (1993) 41–46. https://doi.org/10.1002/elan.1140050108.

[78] R.G. Compton, A.M. Waller, An improved cell for in-situ electrochemical ESR, J. Electroanal. Chem. 195 (1985) 289–297. https://doi.org/10.1016/0022-0728(85)80049-8.

[79] R.G. Compton, C.R. Greaves, A.M. Waller, A wall-jet electrode for in-situ electrochemical ESR, J. Electroanal. Chem. 277 (1990) 83–92. https://doi.org/10.1016/0022-0728(90)85092-J.

[80] R.N. Bagchi, A.M. Bond, F. Schulz, A newly designed variable temperature stationary and flow-through cell for in situ ESR-electrochemical experiments in solvents having either low or high dielectric constants, J. Electroanal. Chem. 252 (1988) 259–267. https://doi.org/10.1016/0022-0728(88)80215-8.

[81] R.N. Bagchi, A.M. Bond, R. Colton, Simultaneous in-situ electron spin resonance and voltammetric studies in high resistance solvents at low temperatures using a newly designed small volume electrolysis cell, J. Electroanal. Chem. 199 (1986) 297–309. https://doi.org/10.1016/0022-0728(86)80005-5.

[82] D.A. Fiedler, M. Koppenol, A.M. Bond, An ESR-Electrochemical Cell Which Can Be Used in High and Low Dielectric Solvents Over Wide Ranges of Temperature and Time Domain, J. Electrochem. Soc. 142 (1995) 862–867.

[83] R.D. Webster, A.M. Bond, B.A. Coles, R.G. Compton, ESR-electrochemical cells: A comparative study, J. Electroanal. Chem. 404 (1996) 303–308. https://doi.org/10.1016/0022-0728(95)04363-2.

[84] F. Hartl, R.P. Groenestein, T. Mahabiersing, Air-Tight Three-Electrode Design of Coaxial Electrochemical-EPR Cell for Redox Studies at Low Temperatures, Collect. Czechoslov. Chem. Commun. 66 (2001) 52–66. https://doi.org/10.1135/cccc20010052.

[85] A.J. Wain, M. Thompson, O. V Klymenko, R.G. Compton, An improved configuration for simultaneous electrochemical ESR studies: a tubular electrode in a cylindrical cavity, Phys. Chem. Chem. Phys. 6 (2004) 4018–4027. https://doi.org/10.1039/b405219f.

[86] A.J. Wain, R.G. Compton, R. Le Roux, S. Matthews, K. Yunus, A.C. Fisher, A microfluidic channel flow cell for electrochemical ESR, J. Phys. Chem. B. 110 (2006) 26040–26044. https://doi.org/10.1021/jp064903b.

[87] A.J. Wain, R.G. Compton, R. Le Roux, S. Matthews, A.C. Fisher, Microfluidic channel flow cell for simultaneous cryoelectrochemical electron spin resonance, Anal. Chem. 79 (2007) 1865–1873. https://doi.org/10.1021/ac061910n.

[88] A.J. Wain, R.G. Compton, Hydrodynamic cryoelectrochemical ESR: The reduction of ortho-bromonitrobenzene in acetonitrile, J. Electroanal. Chem. 587 (2006) 203–212. https://doi.org/10.1016/j.jelechem.2005.11.009.

[89] J. Zeitouny, V. Jouikov, Reversed redox generation of silyl radicals in a four-electrode flow-through EPR spectroelectrochemical cell., Phys. Chem. Chem. Phys. 11 (2009) 7161–7170. https://doi.org/10.1039/b905072h.

[90] M.A. Tamski, J. V. Macpherson, P.R. Unwin, M.E. Newton, Electrochemical electron paramagnetic resonance utilizing loop gap resonators and micro-electrochemical cells, Phys. Chem. Chem. Phys. 17 (2015) 23438–23447. https://doi.org/10.1039/C5CP04259C.

[91] M.A. Tamski, M.W. Dale, B.G. Breeze, J. V. Macpherson, P.R. Unwin, M.E.

Newton, Quantitative measurements in electrochemical electron paramagnetic resonance, Electrochim. Acta. 213 (2016) 802–810. https://doi.org/10.1016/j.electacta.2016.07.114.

[92] L.S. Hernández-Muñoz, C. Frontana, F.J. González, Covalent modification of carbon surfaces with cyclodextrins by mediated oxidation of β-cyclodextrin monoanions, Electrochim. Acta. 138 (2014) 22–29. https://doi.org/10.1016/j.electacta.2014.06.077.

[93] Y. Makarov, A. V Zibarev, Electrochemical reduction , radical anions , and dehalogenation of fluorinated / chlorinated 2 , 1 , 3-benzothia / selenadiazoles, (2017) 166–180.

[94] P.R. Murray, D. Collison, S. Daff, N. Austin, R. Edge, B.W. Flynn, L. Jack, F. Leroux, E.J.L. McInnes, A.F. Murray, D. Sells, T. Stevenson, J. Wolowska, L.J. Yellowlees, An in situ electrochemical cell for Q- and W-band EPR spectroscopy, J. Magn. Reson. 213 (2011) 206–209. https://doi.org/10.1016/j.jmr.2011.09.041.

[95] I. Cekić-Lasković, R. Marković, D.M. Minić, E. Volanschi, Electrochemical reduction of (5-etoxycarbonylmethylidene-4-oxothiazolidine- 2-ylidene)-N-phenylethanone in aprotic medium: A spectroelectrochemical approach, J. Electroanal. Chem. 651 (2011) 50–60. https://doi.org/10.1016/j.jelechem.2010.11.001.

[96] A. Staško, K. Lušpai, Z. Barbieriková, J. Rimarčík, A. Vagánek, V. Lukeš, M. Bella, V. Milata, M. Zalibera, P. Rapta, V. Brezová, Stable radical trianions from reversibly formed sigma-dimers of selenadiazoloquinolones studied by in situ EPR/UV-vis spectroelectrochemistry and quantum chemical calculations, J. Phys. Chem. A. 116 (2012) 9919–9927. https://doi.org/10.1021/jp307270b.

[97] K. Luspai, Z. Barbieriková, M. Malcek, L. Bucinsky, A. Stasko, M. Bella, V. Milata, P. Rapta, V. Brezová, Cathodic and Photocatalytic Reduction of Nitroquinolones Investigated by In Situ EPR/UV-Vis Spectroelectrochemistry and EPR spectroscopy, Curr. Org. Chem. 17 (2013) 2427–2439. https://doi.org/10.2174/13852728113179990056.

[98] C. Ribaut, G. Bordeau, P. Perio, K. Reybier, V. Sartor, O. Reynes, P.L. Fabre, N. Chouini-Lalanne, EPR spectroelectrochemical investigation of guanine radical formation and environment effects, J. Phys. Chem. B. 118 (2014) 2360–2365. https://doi.org/10.1021/jp500952q.

[99] L. Šimková, E. Dmitrieva, J. Klíma, L. Dunsch, J. Ludvík, (Spectro) Electrochemical investigation of reduction mechanism of a new energetic molecule 2,2-dinitroethene-1,1-diamine (FOX-7) in aprotic solvents, J. Solid State Electrochem. 19 (2014) 103–112. https://doi.org/10.1007/s10008-014-2663-0.

[100] S.I. Kulakovskaya, A. V. Kulikov, L.N. Sviridova, E. V. Stenina, Electrochemical and electron paramagnetic resonance study of the mechanism of oxidation of phenazine-di-n-oxide in the presence of isopropyl alcohol at glassy carbon and single-walled carbon nanotube electrodes, Electrochim. Acta. 146 (2014) 798–808. https://doi.org/10.1016/j.electacta.2014.08.039.

[101] G. Armendáriz-Vidales, C. Frontana, Insights into dissociative electron transfer in esterified shikonin semiquinones by in situ ESR/UV-Vis spectroelectrochemistry, Phys. Chem. Chem. Phys. 17 (2015) 29299–29304. https://doi.org/10.1039/C5CP04306A.

[102] M.A. Morsy, A.N.M. Kawde, Electron paramagnetic resonance monitoring for on-demand electrochemically-generated radicals, Electrochim. Acta. 160 (2015) 22–27. https://doi.org/10.1016/j.electacta.2015.02.014.

[103] R. Sokolová, J. Tarábek, B. Papoušková, J. Kocábová, J. Fiedler, J. Vacek, P. Marhol, E. Vavříková, V. Křen, Oxidation of the Flavonolignan Silybin. in situ EPR Evidence of the Spin-Trapped Silybin Radical, Electrochim. Acta. 205 (2016) 118–123. https://doi.org/10.1016/j.electacta.2016.04.107.

[104] Q. Liu, B. Sun, Z. Liu, Y. Kao, B.W. Dong, S. Da Jiang, F. Li, G. Liu, Y. Yang, F. Mo, A general electrochemical strategy for the Sandmeyer reaction, Chem. Sci. 9 (2018) 8731–8737. https://doi.org/10.1039/c8sc03346c.

[105] M.A. Buckingham, W. Cunningham, S.D. Bull, A. Buchard, A. Folli, D.M. Murphy, F. Marken, Electrochemically Driven C−H Hydrogen Abstraction Processes with the Tetrachloro-Phthalimido-N-Oxyl (Cl4PINO) Catalyst, Electroanalysis. 30 (2018) 1698–1705. https://doi.org/10.1002/elan.201800147.

[106] X. Yu, T.L. Roemmele, R.T. Boeré, Synthesis, Electronic Structures, and Electrochemistry of 3-Triarylphosphoraniminato-1,3,5-trithia-2,4,6,8-tetrazocines: Detection of Trithiatetrazocinyl Radical Anions, ChemElectroChem. 5 (2018) 968–978.

https://doi.org/10.1002/celc.201701191.

[107] M. Toybenshlak, R. Carmieli, A New and Robust Method for In-situ EPR Electrochemistry, Isr. J. Chem. 59 (2019) 1020–1026. https://doi.org/10.1002/ijch.201900074.

[108] K. Kholin, M. Valitov, V. Burilov, E. Tselischeva, S. Strekalova, A. Mustafina, Y. Budnikova, M. Kadirov, Spectroelectrochemistry: ESR of Paramagnetic Intermediates in the Electron Transfer Series [Cr(bpy)3]n (n = 3+, 2+, 1+, 0, 1-), Electrochim. Acta. 182 (2015) 212–216. https://doi.org/10.1016/j.electacta.2015.09.073.

[109] T. Niu, J. Cai, P. Shi, G. Zhao, Unique electrochemical system for in situ SO4[rad]− generation and pollutants degradation, Chem. Eng. J. 386 (2020) 123971. https://doi.org/10.1016/j.cej.2019.123971.

[110] A. Petr, V. Kataev, B. Büchner, First direct in situ EPR spectroelectrochemical evidence of the superoxide anion radical, J. Phys. Chem. B. 115 (2011) 12036–12039. https://doi.org/10.1021/jp206540c.

[111] Q. Wang, J. Zheng, E. Walter, H. Pan, D. Lv, P. Zuo, H. Chen, Z.D. Deng, B.Y. Liaw, X. Yu, X. Yang, J.-G. Zhang, J. Liu, J. Xiao, Direct Observation of Sulfur Radicals as Reaction Media in Lithium Sulfur Batteries, J. Electrochem. Soc. 162 (2015) A474–A478. https://doi.org/10.1149/2.0851503jes.

[112] J. Wandt, P. Jakes, J. Granwehr, H.A. Gasteiger, R.-A. Eichel, Singlet Oxygen Formation during the Charging Process of an Aprotic Lithium-Oxygen Battery, Angew. Chemie. 128 (2016) 7006–7009. https://doi.org/10.1002/ange.201602142.

[113] M. Sathiya, J.B. Leriche, E. Salager, D. Gourier, J.M. Tarascon, H. Vezin, Electron paramagnetic resonance imaging for real-time monitoring of Li-ion batteries, Nat. Commun. 6 (2015) 1–7. https://doi.org/10.1038/ncomms7276.

[114] E. Bulak, T. Varnali, B. Schwederski, D. Bubrin, J. Fiedler, W. Kaim, Separation of metal binding and electron transfer sites as a strategy to stabilize the ligand-reduced and metal-oxidized form of [Mo(CO)4L], Organometallics. 30 (2011) 6441–6445. https://doi.org/10.1021/om2007858.

[115] M. Dürr, J. Klein, A. Kahnt, S. Becker, R. Puchta, B. Sarkar, I. Ivanović-Burmazović, Redox Behavior of a Dinuclear Ruthenium(II) Complex

Bearing an Uncommon Bridging Ligand: Insights from High-Pressure Electrochemistry, Inorg. Chem. 56 (2017) 14912–14925. https://doi.org/10.1021/acs.inorgchem.7b02192.

[116] P.A. Abramov, A.A. Dmitriev, K. V. Kholin, N.P. Gritsan, M.K. Kadirov, A.L. Gushchin, M.N. Sokolov, Mechanistic study of the [(dpp-bian)Re(CO)3Br] electrochemical reduction using in situ EPR spectroscopy and computational chemistry, Electrochim. Acta. 270 (2018) 526–534. https://doi.org/10.1016/j.electacta.2018.03.111.

[117] M. Khrizanforov, S. Strekalova, K. Kholin, V. Khrizanforova, V. Grinenko, T. Gryaznova, Y. Budnikova, One-stage synthesis of FcP(O)(OC2H5)2 from ferrocene and α-hydroxyethylphosphonate, RSC Adv. 6 (2016) 42701–42707. https://doi.org/10.1039/c6ra04480h.

[118] M.K. Kadirov, K. V. Kholin, E.Y. Tselishcheva, V.A. Burilov, A.R. Mustafina, Cyclic voltammetry of tris (2 , 2 ´ bipyridine) zinc (II) diperchlorate, Russ. Chem. Bull. 62 (2013) 1327–1331. https://doi.org/10.1007/s11172-013-0187-x.

[119] P. Machata, P. Herich, K. Lušpai, L. Bucinsky, S. Šoralová, M. Breza, J. Kozisek, P. Rapta, Redox reactions of nickel, copper, and cobalt complexes with “noninnocent” dithiolate ligands: Combined in situ spectroelectrochemical and theoretical study, Organometallics. 33 (2014) 4846–4859. https://doi.org/10.1021/om5000584.

[120] M. Sterby, R. Emanuelsson, F. Mamedov, M. Strømme, M. Sjödin, Investigating electron transport in a PEDOT/Quinone conducting redox polymer with in situ methods, Electrochim. Acta. 308 (2019) 277–284. https://doi.org/10.1016/j.electacta.2019.03.207.

[121] H. Wang, R. Emanuelsson, H. Liu, K. Edström, F. Mamedov, M. Strømme, M. Sjödin, Redox-state-dependent interplay between pendant group and conducting polymer backbone in quinone-based conducting redox polymers for lithium ion batteries, ACS Appl. Energy Mater. (2019). https://doi.org/10.1021/acsaem.9b01130.

[122] E. Dmitrieva, M. Rosenkranz, J.S. Danilova, E.A. Smirnova, M.P. Karushev, I.A. Chepurnaya, A.M. Timonov, Radical formation in polymeric nickel complexes with N2O2 Schiff base ligands: An in situ ESR and UV–vis–NIR spectroelectrochemical study, Electrochim. Acta. 283 (2018) 1742–1752. https://doi.org/10.1016/j.electacta.2018.07.131.

[123] E.A. Dmitrieva, I.A. Chepurnaya, M.P. Karushev, A.M. Timonov, The Nature of Charge Carriers in Polymeric Complexes of Nickel with Schiff Bases Containing Electron-Withdrawing Substituents, Russ. J. Electrochem. 55 (2019) 1039–1046. https://doi.org/10.1134/S1023193519110041.

[124] F. Zhang, S. Mu, Influence of potential and temperature on the ESR spectra of polyaniline synthesized using the interface polymerization, J. Phys. Chem. B. 114 (2010) 16687–16693. https://doi.org/10.1021/jp107041m.

[125] M. Lapkowski, J. Zak, K. Karon, B. Marciniec, W. Prukala, The mixed carbon-nitrogen conjugation in the carbazole based polymer; The electrochemical, UVVis, EPR, and IR studies on 1,4 bis[(E)2-(9H-carbazol-9-yl) vinyl]benzene, Electrochim. Acta. 56 (2011) 4105–4111. https://doi.org/10.1016/j.electacta.2011.01.114.

[126] Y. Yang, S. Mu, Poly(aniline-co-o-aminophenol): In situ electrochemical-ESR measurements in aqueous solutions and as a probe of radical scavengers, J. Phys. Chem. C. 115 (2011) 18721–18728. https://doi.org/10.1021/jp205485z.

[127] A.F. Khusnuriyalova, A. Petr, A.T. Gubaidullin, A. V. Sukhov, V.I. Morozov, B. Büchner, V. Kataev, O.G. Sinyashin, D.G. Yakhvarov, Electrochemical generation and observation by magnetic resonance of superparamagnetic cobalt nanoparticles, Electrochim. Acta. 260 (2018) 324–329. https://doi.org/10.1016/j.electacta.2017.12.050.

[128] A. Ruff, P. Schuler, B. Speiser, Redox-active silica nanoparticles. Part 6. Synthesis and spectroscopic and electrochemical characterization of viologen-modified Stöber silica particles with diameters of approximately 125 nm, J. Solid State Electrochem. 17 (2013) 79–97. https://doi.org/10.1007/s10008-012-1834-0.

[129] K. Abdiaziz, E. Salvadori, K.P. Sokol, E. Reisner, M.M. Roessler, Protein film electrochemical EPR spectroscopy as a technique to investigate redox reactions in biomolecules, Chem. Commun. 55 (2019) 8840–8843. https://doi.org/10.1039/c9cc03212f.

[130] D. Hollmann, N. Rockstroh, K. Grabow, U. Bentrup, J. Rabeah, M. Polyakov, A.E. Surkus, W. Schuhmann, S. Hoch, A. Brückner, From the Precursor to the Active State: Monitoring Metamorphosis of Electrocatalysts During Water Oxidation by In Situ Spectroscopy,

ChemElectroChem. 4 (2017) 2117–2122. https://doi.org/10.1002/celc.201700142.

[131] B. Wang, A.J. Fielding, R.A.W. Dryfe, In situ electrochemical electron paramagnetic resonance spectroscopy as a tool to probe electrical double layer capacitance, Chem. Commun. 54 (2018) 3827–3830. https://doi.org/10.1039/c8cc00450a.

[132] B. Wang, V. Likodimos, A.J. Fielding, R.A.W. Dryfe, In situ Electron paramagnetic resonance spectroelectrochemical study of graphene-based supercapacitors: Comparison between chemically reduced graphene oxide and nitrogen-doped reduced graphene oxide, Carbon N. Y. 160 (2020) 236–246. https://doi.org/10.1016/j.carbon.2019.12.045.

[133] J. Cao, B. Wang, P. He, C. Valles, Y. Peng, B. Derby, R.A.W. Dryfe, I.A. Kinloch, High-power energy storage from carbon electrodes using highly acidic electrolytes, J. Phys. Chem. C. 124 (2020) 20701–20711. https://doi.org/10.1021/acs.jpcc.0c04930.

[134] Science Products GmbH, Wires, (2021). https://science-products.com/en/shop/82/electrodes-etc/wire (accessed March 22, 2021).

[135] P. Dutheil, A.L. Thomann, T. Lecas, P. Brault, M. Vayer, Sputtered Ag thin films with modified morphologies: Influence on wetting property, Appl. Surf. Sci. 347 (2015) 101–108. https://doi.org/10.1016/j.apsusc.2015.04.052.

[136] R. Heu, S. Shahbazmohamadi, J. Yorston, P. Capeder, Target Material Selection for Sputter Coating of SEM Samples, Micros. Today. 27 (2019) 32–36. https://doi.org/10.1017/s1551929519000610.

[137] B. Vanrenterghem, B. Geboes, S. Bals, J. Ustarroz, A. Hubin, T. Breugelmans, Influence of the support material and the resulting particle distribution on the deposition of Ag nanoparticles for the electrocatalytic activity of benzyl bromide reduction, Appl. Catal. B Environ. 181 (2016) 542–549. https://doi.org/10.1016/j.apcatb.2015.08.026.

[138] J. Wang, N. Liu, X. Liu, Y. Wang, L. Sun, X. Xu, Z. Zhu, The Impact of “Effective pH” on the Voltammetric Behavior of *p* -Benzoquinone and Hydroquinone in Acetonitrile, J. Electrochem. Soc. 163 (2016) H201–H204. https://doi.org/10.1149/2.0921603jes.

[139] M. Quan, D. Sanchez, M.F. Wasylkiw, D.K. Smith, Voltammetry of

Quinones in Unbuffered Aqueous Solution : Reassessing the Roles of Proton Transfer and Hydrogen Bonding in the Aqueous Electrochemistry of Quinones, 9 (2007) 12847–12856.

[140] Y. Tang, Y. Wu, Z. Wang, Spectroelectrochemistry for Electroreduction of p -Benzoquinone in Unbuffered Aqueous Solution, (2001) 4–9. https://doi.org/10.1149/1.1353575.

[141] S. Klod, L. Dunsch, A combination of in situ ESR and in situ NMR spectroelectrochemistry for mechanistic studies of electrode reactions: The case of p-benzoquinone, Magn. Reson. Chem. 49 (2011) 725–729. https://doi.org/10.1002/mrc.2819.

[142] H. Park, M.S. Won, C. Cheong, Y.B. Shim, In-situ ESR detection of radical species of p-benzoquinone in aqueous media, Electroanalysis. 14 (2002) 1501–1507. https://doi.org/10.1002/1521-4109(200211)14:21<1501::AID-ELAN1501>3.0.CO;2-B.

[143] O.H. Müller, J.P. Baumberger, Oxidation - Reduction Potentials Measured with the Dropping Mercury Electrode : Part I . Studies with Quinhydrone and Estimation of Limits of Measurement, Trans. Electrochem. Soc. 71 (1937) 169–180.

[144] J.O. Howell, R.M. Wightman, Ultrafast Voltammetry and Voltammetry in Highly Resistive Solutions with Microvoltammetric Electrodes, Anal. Chem. 56 (1984) 524–529. https://doi.org/10.1021/ac00267a050.

[145] J. Volke, The relationship between herbicidal activity and electrochemical properties of quaternary bipyridylium salts, Collect. Czechoslov. Chem. Commun. 33 (1968) 3044–3048. https://doi.org/10.1135/cccc19683044.

[146] L. Michaelis, E.S. Hill, The viologen indicators, J. Gen. Physiol. 16 (1933) 859–873. https://doi.org/10.1085/jgp.16.6.859.

[147] L. Xiao, G.G. Wildgoose, R.G. Compton, Investigating the voltammetric reduction of methylviologen at gold and carbon based electrode materials. Evidence for a surface bound adsorption mechanism leading to electrode “protection” using multi-walled carbon nanotubes, New J. Chem. 32 (2008) 1628–1633. https://doi.org/10.1039/b804842h.

[148] I. Shpilevaya, J.S. Foord, Electrochemistry of methyl viologen and anthraquinonedisulfonate at diamond and diamond powder electrodes: The influence of surface chemistry, Electroanalysis. 26 (2014) 2088–

2099. https://doi.org/10.1002/elan.201400310.

[149] N. Gamboa-Valero, P.D. Astudillo, M.A. González-Fuentes, M.A. Leyva, M.D.J. Rosales-Hoz, F.J. González, Hydrogen bonding complexes in the quinone-hydroquinone system and the transition to a reversible two-electron transfer mechanism, Electrochim. Acta. 188 (2016) 602–610. https://doi.org/10.1016/j.electacta.2015.12.060.

[150] P.S. Jain, S. Lal, Electrolytic reduction of oxygen at solid electrodes in aprotic solvents-the superoxide ion, Electrochim. Acta. 27 (1982) 759–763. https://doi.org/10.1016/0013-4686(82)85071-8.

[151] F.J. Millero, F. Huang, T.B. Graham, Solubility of Oxygen in Some 1-1 , 2-1 , 1-2 , and 2-2 Electrolytes as a Function of Concentration at 25 ◦ C, J. Solution Chem. 32 (2003) 473–487.

[152] Z. Wang, C. Cao, Y. Zheng, S. Chen, F. Zhao, Abiotic Oxygen Reduction Reaction Catalysts Used in Microbial Fuel Cells, ChemElectroChem. 1 (2014) 1813–1821. https://doi.org/10.1002/celc.201402093.

[153] J.A. Farrington, M. Ebert, E.J. Land, K. Fletcher, Bipyridylium quaternary salts and related compounds. V. Pulse radiolysis studies of the reaction of paraquat radical with oxygen. Implications for the mode of action of bipyridyl herbicides, Biochim. Biophys. Acta. 314 (1973) 372–381. https://doi.org/10.1016/0005-2728(73)90121-7.

[154] COMSOL, Electrochemistry Module: User's Guide, 2018.

[155] A.W. Colburn, K.J. Levey, D.O. Hare, J. V Macpherson, Lifting the lid on the potentiostat : a beginner ' s guide to understanding electrochemical circuitry and practical operation †, Phys. Chem. Chem. Phys. 23 (2021) 8100–8117. https://doi.org/10.1039/d1cp00661d.

[156] H. Saiki, K. Takami, T. Tominaga, Diffusion of porphyrins and quinones in organic solvents, Phys. Chem. Chem. Phys. 1 (1999) 303–306. https://doi.org/10.1039/a807920j.

[157] R.A. Mackay, S.A. Myers, A. Brajter-Toth, Interpreting Diffusion Coefficients of Electrochemical Probes in Oil-in-Water Microemulsions, Electroanalysis. 8 (1996) 759–764. https://doi.org/10.1002/elan.1140080810.

[158] R.R. Mett, S.S. Hyde, J.W. Sidabras, Aqueous sample holder for EPR and MR spectroscopy, 0017720 A1, 2005.

[159] D. Pauwels, H.Y.V. Ching, M. Samanipour, S. Neukermans, J. Hereijgers, S. Van Doorslaer, K. De Wael, T. Breugelmans, Electrochimica Acta Identifying intermediates in the reductive intramolecular cyclisation of allyl 2-bromobenzyl ether by an improved electron paramagnetic resonance spectroelectrochemical electrode design combined with density functional theory calculati, Electrochim. Acta. 271 (2018) 10–18. https://doi.org/10.1016/j.electacta.2018.03.093.

[160] A.A. Shah, R. Holze, Spectroelectrochemistry of aniline-o-aminophenol copolymers, Electrochim. Acta. 52 (2006) 1374–1382. https://doi.org/10.1016/j.electacta.2006.07.040.

[161] S. Bilal, R. Holze, In situ UV-vis spectroelectrochemistry of poly(o-phenylenediamine-co-m-toluidine), Electrochim. Acta. 52 (2007) 5346–5356. https://doi.org/10.1016/j.electacta.2007.02.034.

[162] G. Sandmann, H. Dietz, W. Plieth, Preparation of silver nanoparticles on ITO surfaces by a double-pulse method, J. Electroanal. Chem. 491 (2000) 78–86. https://doi.org/10.1016/S0022-0728(00)00301-6.

[163] K. Zhang, J. Wei, H. Zhu, F. Ma, S. Wang, Electrodeposition of gold nanoparticle arrays on ITO glass as electrode with high electrocatalytic activity, Mater. Res. Bull. 48 (2013) 1338–1341. https://doi.org/10.1016/j.materresbull.2012.12.029.

[164] A. Schnegg, J. Behrends, M. Fehr, K. Lips, Pulsed electrically detected magnetic resonance for thin film silicon and organic solar cells, Phys. Chem. Chem. Phys. 14 (2012) 14492–14494. https://doi.org/10.1039/c2cp41258f.

[165] A. Petr, L. Dunsch, A. Neudeck, In situ UV-vis ESR spectroelectrochemistry, J. Electroanal. Chem. 412 (1996) 153–158. https://doi.org/10.1016/0022-0728(96)04582-2.

[166] A. Neudeck, L. Kress, Laminated micro-meshes - A new kind of optically transparent electrode, J. Electroanal. Chem. 437 (1997) 141–156.

[167] A. Goux, D. Pratt, L. Dunsch, The reaction mechanism of p-toluenediamine anodic oxidation: An in situ ESR-UV/Vis/NIR spectroelectrochemical study, ChemPhysChem. 8 (2007) 2101–2106. https://doi.org/10.1002/cphc.200700235.

[168] L. Dunsch, A. Neudeck, P. Rapta, LIGA-electrodes in voltammetric and spectroelectrochemical studies, Fresenius. J. Anal. Chem. 367 (2000)

314–319. https://doi.org/10.1007/s002160000418.

[169] P. Rapta, A. Neudeck, A. Petr, L. Dunsch, In situ EPR/UV-VIS spectroelectrochemistry of polypyrrole redox cycling, J. Chem. Soc. - Faraday Trans. 94 (1998) 3625–3630. https://doi.org/10.1039/a806423g.

[170] P. Rapta, R. Fáber, L. Dunsch, A. Neudeck, O. Nuyken, In situ EPR and UV-vis spectroelectrochemistry of hole-transporting organic substrates, Spectrochim. Acta - Part A Mol. Biomol. Spectrosc. 56 (2000) 357–362. https://doi.org/10.1016/S1386-1425(99)00246-2.

[171] P.G. Hoertz, Z. Chen, C.A. Kent, T.J. Meyer, Application of high surface area tin-doped indium oxide nanoparticle films as transparent conducting electrodes, Inorg. Chem. 49 (2010) 8179–8181. https://doi.org/10.1021/ic100719r.

[172] M. Kato, T. Cardona, A.W. Rutherford, E. Reisner, J. Am. Chem. Soc. 2012, 134, 8332−8335.pdf, J. Am. Chem. Soc. 134 (2012) 8332–8335.

[173] M.A. Bajada, S. Roy, J. Warnan, K. Abdiaziz, A. Wagner, M.M. Roessler, E. Reisner, A Precious-Metal-Free Hybrid Electrolyzer for Alcohol Oxidation Coupled to CO 2 -to-Syngas Conversion, Angew. Chemie. 132 (2020) 2–11. https://doi.org/10.1002/ange.202002680.

[174] T. Minami, Transparent conducting oxide semiconductors for transparent electrodes, Semicond. Sci. Technol. 20 (2005) S35–S44. https://doi.org/10.1088/0268-1242/20/4/004.

[175] A. El Amrani, F. Hijazi, B. Lucas, J. Bouclé, M. Aldissi, Electronic transport and optical properties of thin oxide films, Thin Solid Films. 518 (2010) 4582–4585. https://doi.org/10.1016/j.tsf.2009.12.036.

[176] D.H. Kim, H.K. Yoon, D.H. Shin, R.I. Murakami, Electromagnetic wave shielding properties of ITO/PET thin film by film thickness, Key Eng. Mater. 345-346 II (2007) 1585–1588.

[177] S. Neukermans, F. Vorobjov, T. Kenis, R. De Wolf, J. Hereijgers, T. Breugelmans, Electrochemical reduction of halogenated aromatic compounds at metal cathodes in acetonitrile, Electrochim. Acta. 332 (2020) 135484. https://doi.org/10.1016/j.electacta.2019.135484.

[178] B. Vanrenterghem, T. Breugelmans, An activity scale of cathode materials for the electrochemical cyclisation of allyl 2-bromobenzyl ether, Electrochim. Acta. 234 (2017) 28–36.

https://doi.org/10.1016/j.electacta.2017.03.016.

[179] H. Quan, S.U. Park, J. Park, Electrochemical oxidation of glucose on silver nanoparticle-modified composite electrodes, Electrochim. Acta. 55 (2010) 2232–2237. https://doi.org/10.1016/j.electacta.2009.11.074.

[180] A.M. Ghonim, B.E. El-Anadouli, M.M. Saleh, Electrocatalytic glucose oxidation on electrochemically oxidized glassy carbon modified with nickel oxide nanoparticles, Electrochim. Acta. 114 (2013) 713–719. https://doi.org/10.1016/j.electacta.2013.10.115.

[181] M. Fleischmann, K. Korinek, D. Pletcher, The oxidation of organic compounds at a nickel anode in alkaline solution, J. Electroanal. Chem. 31 (1971) 39–49. https://doi.org/10.1016/S0022-0728(71)80040-2.

[182] Z. Li, X. Lu, B. Li, L. Bai, Q. Wang, Research on electrochemical oxidation of formaldehyde on the nanoporous silver electrode in alkaline solution, ECS Electrochem. Lett. 4 (2015) H24–H27. https://doi.org/10.1149/2.0091506eel.

[183] B. Geboes, B. Vanrenterghem, J. Ustarroz, D. Pauwels, S. Sotiropoulos, A. Hubin, T. Breugelmans, Influence of the morphology of electrodeposited nanoparticles on the activity of organic halide reduction, Chem. Eng. Trans. 41 (2014) 73–78. https://doi.org/10.3303/CET1441013.

[184] S. Stoll, A. Schweiger, EasySpin, a comprehensive software package for spectral simulation and analysis in EPR, J. Magn. Reson. 178 (2006) 42–55. https://doi.org/10.1016/j.jmr.2005.08.013.

[185] W. Dunham, J. Fee, L. Harding, H. Grande, Application of fast Fourier transforms to EPR spectra of free radicals in solution, J. Magn. Reson. 40 (1980) 351–359. https://doi.org/10.1016/0022-2364(80)90258-9.

[186] E. Reijerse, A. Savitsky, Electron Paramagnetic Resonance Instrumentation, 6 (2017) 187–206. https://doi.org/10.1002/9780470034590.emrstm1511.

[187] E. Labbe, O. Buriez, J.Y. Ne, Activation of 1-halonaphthalenes by electrogenerated [Co I -salen] À, 600 (2007) 359–363. https://doi.org/10.1016/j.jelechem.2006.10.004.

[188] B.L. Chen, H.W. Zhu, Y. Xiao, Q.L. Sun, H. Wang, J.X. Lu, Asymmetric electrocarboxylation of 1-phenylethyl chloride catalyzed by electrogenerated chiral [CoI(salen)]- complex, Electrochem. Commun.

(2014). https://doi.org/10.1016/j.elecom.2014.02.009.

[189] V. Ramírez-delgado, G. Osorio-monreal, L.F. Hernández-ayala, Y. Reyes-vidal, J.C. García-ramos, L. Ruiz-azuara, L. Ortiz-frade, Electrochemical Behavior of Ni(II) Complexes with N2S2 and N6 Ligands as Potential Catalysts in Hydrogen Evolution Reaction, J. Mex. Chem. Soc. 59 (2015) 294–301. https://doi.org/10.29356/jmcs.v59i4.86.

[190] A. Ahmed, S. Arnaboldi, C. Durante, A. Gennaro, Electrochemical reduction of organic bromides in 1-butyl-3- methylimidazolium tetra fl uoroborate, J. Electroanal. Chem. 804 (2017) 240–247. https://doi.org/10.1016/j.jelechem.2017.09.023.

[191] K. Schulten, Einstein Diffusion Equation, in: Lect. Notes Non-Equilibrium Stat. Mech., University of Illinois, Urbana, 1999: pp. 37–62. https://doi.org/10.1002/0471743984.vse2555.

[192] DexMat, Galvorn CNT Yarn/Wire/Rope, (2018). https://dexmat.com/cnt-products/cnt-yarn-wire-rope/ (accessed April 2, 2021).

[193] D.C. Giancoli, Physics: Principles with Applications Global Edition, 2015.

[194] A. Mouchfiq, T.K. Todorova, S. Dey, M. Fontecave, V. Mougel, A bioinspired molybdenum-copper molecular catalyst for CO2electroreduction, Chem. Sci. 11 (2020) 5503–5510. https://doi.org/10.1039/d0sc01045f.

[195] M. Knüpling, J.T. Törring, S. Un, The relationship between the molecular structure of semiquinone radicals and their g-values, Chem. Phys. 219 (1997) 291–304. https://doi.org/10.1016/S0301-0104(97)00104-3.

[196] F. MacMillan, F. Lendzian, W. Lubitz, EPR and ENDOR characterization of semiquinone anion radicals related to photosynthesis, Magn. Reson. Chem. 33 (1995) S81–S93. https://doi.org/10.1002/mrc.1260331314.

[197] J. R. Welty, C. E. Wicks, R. E. Wilson, G. Rorrer, Fundamentals of momentum, heat and mass transfer, 1970. https://doi.org/10.1016/0017-9310(70)90063-3.

[198] M.M. Britton, Nuclear Magnetic Resonance Studies of the 1 , 4-Cyclohexanedione - Bromate - Acid Oscillatory System, (2003) 5033–5041.

[199] R.W. French, F. Marken, Growth and characterisation of diffusion junctions between paired gold electrodes : diffusion effects in generator

– collector mode, (2009) 609–617. https://doi.org/10.1007/s10008-008-0698-9.

[200] L.R. Sharma, R.K. Kalia, Hydrodynamic Voltammetry at the Tubular Graphite Electrode . Determination of Diffusion Coefficients of Aromatic Amino and Phenolic Compounds, 22 (1977) 39–41.

[201] G.S. Salvapati, K. V. Ramanamurty, M. Janardanarao, Selective catalytic self-condensation of acetone, J. Mol. Catal. 54 (1989) 9–30. https://doi.org/10.1016/0304-5102(89)80134-8.

[202] K. V. Ramanamurty, G.S. Salvapati, New dimensions on value added aldol chemicals of acetone, J. Sci. Ind. Res. (India). 59 (2000) 339–349.

[203] M.J. Darabi Mahboub, J.L. Dubois, F. Cavani, M. Rostamizadeh, G.S. Patience, Catalysis for the synthesis of methacrylic acid and methyl methacrylate, Chem. Soc. Rev. 47 (2018) 7703–7738. https://doi.org/10.1039/c8cs00117k.

[204] H. Li, A. Riisager, S. Saravanamurugan, A. Pandey, R.S. Sangwan, S. Yang, R. Luque, Carbon-Increasing Catalytic Strategies for Upgrading Biomass into Energy-Intensive Fuels and Chemicals, ACS Catal. 8 (2018) 148–187. https://doi.org/10.1021/acscatal.7b02577.

[205] G.G. Podrebarac, F.T.T. Ng, G.L. Rempel, A kinetic study of the aldol condensation of acetone using an anion exchange resin catalyst, Chem. Eng. Sci. 52 (1997) 2991–3002. https://doi.org/10.1016/S0009-2509(97)00098-5.

[206] H. Siegel, M. Eggersdorfer, Ketones, in: Ullmann's Encycl. Ind. Chem., Wiley-VHC, Weinheim, 2000. https://doi.org/10.1246/nikkashi1921.51.560.

[207] K. Weissermel, H.-J. Arpe, Industrial Organic Chemistry, Fourth edi, Wiley-VHC, Weinheim, 2003.

[208] R. Mahrwald, Modern Aldol Reactions, Wiley-VCH, 2004. https://doi.org/10.1055/s-2007-970123.

[209] L. Baigrie, R. Cox, H. Slebockatilk, M. Tencer, T. Tidwell, Acid-Catalyzed Enolization and Aldol Condensation of Acetaldehyde, J. Am. Chem. Soc. 107 (1985) 3640–3645.

[210] G. Zhang, H. Hattori, K. Tanabe, Aldol Addition of Acetone, Catalyzed by Solid Base Catalysts: Magnesium Oxide, Calcium Oxide, Strontium Oxide,

Barium Oxide, Lanthanum (III) Oxide and Zirconium Oxide, Appl. Catal. 36 (1988) 189–197. https://doi.org/10.1016/S0166-9834(00)80114-1.

[211] S. Lippert, W. Baumann, K. Thomke, Secondary reactions of the base-catalyzed aldol condensation of acetone, J. Mol. Catal. 69 (1991) 199–214. https://doi.org/10.1016/0304-5102(91)80145-S.

[212] P. Kuśtrowski, D. Sułkowska, R. Pytlowany, R. Dziembaj, Kinetics of self-condensation of acetone over heterogeneous Ba(OH) 2 and Sr(OH)2 catalysts, React. Kinet. Catal. Lett. 81 (2004) 3–11. https://doi.org/10.1023/B:REAC.0000016510.02042.8d.

[213] F.A. Carey, R.J. Sundberg, Advanced Organic Chemistry Part A: Structure and Mechanisms, 2007.

[214] S. Ordóñez, E. Díaz, M. León, L. Faba, Hydrotalcite-derived mixed oxides as catalysts for different C-C bond formation reactions from bioorganic materials, Catal. Today. 167 (2011) 71–76. https://doi.org/10.1016/j.cattod.2010.11.056.

[215] G. Zhang, H. Hattori, K. Tanabe, Aldol condensation of acetone/acetone d6 over magnesium oxide and lanthanum oxide, Appl. Catal. 40 (1988) 183–190. https://doi.org/10.1016/S0166-9834(00)80436-4.

[216] C. Du, Y. Shen, L. Sun, X. Meng, Condensation of acetone to diacetone alcohol over structured MgO/Al2O3-Al catalyst packing, Adv. Mater. Res. 347–353 (2012) 3050–3053.

[217] K. Tanabe, G. Zhang, H. Hattori, Addition of metal cations to magnesium oxide catalyst for the aldol condensation of acetone, Appl. Catal. 48 (1989) 63–69. https://doi.org/10.1016/S0166-9834(00)80266-3.

[218] M. Paulis, M. Martin, D.. Sirua, A. Diaz, J.. Odriozola, M. Montes, Preparation and characterization of niobium oxide for the catalytic aldol condensation of acetone, Appl. Catal. A Gen. 180 (1999) 411–420.

[219] P.J. Elving, J.T. Leone, Mechanism of the Electrochemical Reduction of Phenyl Ketones, J. Am. Chem. Soc. 80 (1958) 5284–5285. https://doi.org/10.1021/ja01552a068.

[220] X. de Hemptinne, K. Schunck, Electrochemical Reduction of Acetone, Trans. Faraday Soc. 65 (1969) 591–597.

[221] G.A. Noubi, M.F. El-Shahed, F. El-Cheikh, H. Mansour, Electrochemical Reduction of Acetaldehyde, Benzaldehyde in Ethanol-Water Mixture,

Indian J. Chem. 17A (1979) 564–566.

[222] B. Bänsch, T. Härtung, H. Baltruschat, J. Heitbaum, Reduction and oxidation of adsorbed acetone at platinum electrodes studied by DEMS, J. Electroanal. Chem. 259 (1989) 207–215. https://doi.org/10.1016/0022-0728(89)80048-8.

[223] M.L. Tsai, T.C. Chou, Aldol condensation of acetone in an undivided cell via electrochemical catalyzed reaction, J. Chinese Inst. Chem. Eng. 28 (1997).

[224] C.J. Bondue, F. Calle-Vallejo, M.C. Figueiredo, M.T.M. Koper, Structural principles to steer the selectivity of the electrocatalytic reduction of aliphatic ketones on platinum, Nat. Catal. 2 (2019) 243–250. https://doi.org/10.1038/s41929-019-0229-3.

[225] N.R. Armstrong, N.E. Vanderborgh, R.K. Quinn, Rotating Ring-Disk Electrode Studies of the Electrochemistry of Aromatic Carbonyl Compounds in the Solvent Sulfolane, J. Electrochem. Soc. 122 (1975) 615–619. https://doi.org/10.1149/1.2134275.

[226] W.R. Fawcett, A. Lasia, The electroreduction of aromatic aldehydes in aprotic solvents, Can. J. Chem. 59 (1981) 3256–3260. https://doi.org/10.1139/v81-480.

[227] T. Shono, S. Kashimura, M. Sawamura, T. Soejima, Selective C-alkylation of β-diketones, J. Org. Chem. 53 (1988) 907–910. https://doi.org/10.1021/jo00239a052.

[228] T. Shono, M. Ishifune, T. Okada, S. Kashimura, A Novel Trifluoromethylation of Aldehydes and Ketones Promoted by an Electrogenerated Base, J. Org. Chem. 56 (1991) 2–4. https://doi.org/10.1021/jo00001a002.

[229] S.F. Zhao, M. Horne, A.M. Bond, J. Zhang, Electrochemical reduction of aromatic ketones in 1-butyl-3-methylimidazolium-based ionic liquids in the presence of carbon dioxide: the influence of the ketone substituent and the ionic liquid anion on bulk electrolysis product distribution, Phys. Chem. Chem. Phys. 17 (2015) 19247–19254. https://doi.org/10.1039/c5cp00095e.

[230] D. Pauwels, J. Hereijgers, K. Verhulst, K. De Wael, T. Breugelmans, Investigation of the electrosynthetic pathway of the aldol condensation of acetone, Chem. Eng. J. 289 (2016) 554–561.

https://doi.org/10.1016/j.cej.2016.01.018.

[231] D. Pauwels, B. Geboes, J. Hereijgers, D. Choukroun, K. De Wael, T. Breugelmans, The application of an electrochemical microflow reactor for the electrosynthetic aldol reaction of acetone to diacetone alcohol, Chem. Eng. Res. Des. 128 (2017) 205–213. https://doi.org/10.1016/j.cherd.2017.10.014.

[232] T. Shono, S. Kashimura, K. Ishizaki, Electroinduced aldol condensation, Electrochim. Acta. 29 (1984) 603–605. https://doi.org/10.1016/0013-4686(84)87117-0.

[233] S. Kumar, L.X. Sharma, R.K.P. Singh, Electroinduced aldol condenstation at platinum electrode, J. Indian Chem. Soc. 83 (2006) 1160–1162.

[234] M.L. Tsai, The production of diacetone alcohol via paired electrolysis in an undivided cell, J. Chinese Inst. Chem. Eng. 36 (2005) 263–269.

[235] A.T. Nielsen, W.J. Houlihan, The Aldol Condensation, in: Org. React., 1968: pp. 1–438.

[236] D. Pauwels, Electrosynthesis as an environmentally friendly production method: screening methodology towards upscaling, University of Antwerp, 2018.

[237] L. Ebersen, Formation of Hydroxyl Spin Adducts via Nucleophilic Adittion-Oxidation to 5,5-Dimethyl-1-pyrroline N-Oxide, Achta Chem. Scand. 53 (1999) 584–593.

[238] R. Borghi, L. Lunazzi, G. Placucci, G. Cerioni, A. Plumitallo, Photolysis of dialkoxy disulfides: A convenient source of alkoxy radicals for addition to the sphere of fullerene C60, J. Org. Chem. 61 (1996) 3327–3331. https://doi.org/10.1021/jo952169e.

[239] E.G. Janzen, J.I.P. Liu, Radical addition reactions of 5,5-Dimethyl-1-pyrroline-1-oxide. ESR spin trapping with a cyclic nitrone, J. Magn. Reson. 9 (1973) 510–512. https://doi.org/10.1016/0022-2364(73)90194-7.

[240] S. Tero-Kubota, Y. Ikegami, T. Kurokawak, S. Rikuro, K. Sugioka, M. Nakano, Generation of free radicals and initiation of radical reactions in nitrones - Fe2+ - phosphate buffer systems, 8lOCHEMlCAL Biophys. Res. Commun. 108 (1989) 1025–1031.

[241] M. Faraggi, A. Carmichael, P. Riesz, OH radical formation by photolysis of

aqueous porphyrin solutions. A spin trapping and E.S.R. Study, Int. J. Radiat. Biol. 46 (1984) 703–713. https://doi.org/10.1080/09553008414551941.

[242] H. Taniguchi, K.P. Madden, DMPO-alkyl radical spin trapping: An in situ radiolysis steady-state ESR study, Radiat. Res. 153 (2000) 447–453. https://doi.org/10.1667/0033-7587(2000)153[0447:DARSTA]2.0.CO;2.

[243] B.C. Gilbert, G.R. Hodges, J.R.L. Smith, P. Macfaul, P. Taylor, Photo-decarboxylation of substituted alkylcarboxylic acids brought about by visible light and iron(III) tetra(2-N-methylpyridy)-porphyrin in aqueous solution, J. Chem. Soc. Perkin Trans. 2. (1996) 519–524.

[244] J.R. Harbour, M.L. Hair, Detection of Superoxide Ions in Nonaqueous Media. Generation by Photolysis of Pigment Dispersions, J. Phys. Chem. 82 (1978) 1397–1399.

[245] K. Reszka, P. Bilski, R.H. Sik, F. Chignell, Photosensitized generation of superoxide radical in aprotic solvents: An EPR and spin trapping study, Free Rad. Res. Comms. 19(s1) (1993) S33–S44.

[246] M. Yamada, K.D. Karlin, S. Fukuzumi, One-step selective hydroxylation of benzene to phenol with hydrogen peroxide catalysed by copper complexes incorporated into mesoporous silica-alumina, Chem. Sci. 7 (2016) 2856–2863. https://doi.org/10.1039/c5sc04312c.

[247] R. Koppe, P.H. Kasai, Aliphatic ketone anion-radicals: A matrix isolation ESR study, J. Phys. Chem. 98 (1994) 12904–12910. https://doi.org/10.1021/j100100a016.

[248] P. Toffel, A. Henglein, Temperature Dependence of the Electrolytic Dissociation of Some 1-Hydroxy-Alkyl Radicals in Aqueous Solution (a Pulse Radiolysis Study)., Berichte Der Bunsengesellschaft/Physical Chem. Chem. Phys. 80 (1976) 525–528. https://doi.org/10.1002/bbpc.19760800613.

[249] G.P. Laroff, R.W. Fessenden, Equilibrium and kinetics of the acid dissociation of several hydroxyalkyl radicals, J. Phys. Chem. 77 (1973) 1283–1288. https://doi.org/10.1021/j100629a021.

[250] B. Demir, T. Kropp, K.R. Rivera-Dones, E.B. Gilcher, G.W. Huber, M. Mavrikakis, J.A. Dumesic, A self-adjusting platinum surface for acetone hydrogenation, Proc. Natl. Acad. Sci. U. S. A. 117 (2020) 3446–3450. https://doi.org/10.1073/pnas.1917110117.

[251] M.E. Peover, B.S. White, The formation of the superoxide ion by electrolysis of oxygen in aprotic solvents, Chem. Commun. 11 (1965) 183–184. https://doi.org/10.1039/C19650000183.

[252] M. Mohammad, A.Y. Khan, M.S. Subhani, N. Bibi, S. Ahmad, S. Saleemi, Kinetics and electrochemical studies on superoxide, Res. Chem. Intermed. 27 (2001) 259–267. https://doi.org/10.1163/156856701300356473.

[253] J.M. Noël, A. Latus, C. Lagrost, E. Volanschi, P. Hapiot, Evidence for OH radical production during electrocatalysis of oxygen reduction on pt surfaces: Consequences and application, J. Am. Chem. Soc. 134 (2012) 2835–2841. https://doi.org/10.1021/ja211663t.

[254] R.K. Talukdar, T. Gierczak, D.C. McCabe, A.R. Ravishankara, Reaction of hydroxyl radical with acetone. 1. Kinetics of the reactions of OH, OD, and 18OH with acetone and acetone-d6, J. Phys. Chem. A. 107 (2003) 5014–5020. https://doi.org/10.1021/jp027301a.

[255] G.S. Tyndall, J.J. Orlando, T.J. Wallington, M.D. Hurley, M. Goto, M. Kawasaki, Mechanism of the reaction of OH radicals with acetone and acetaldehyde at 251 and 296 K, Phys. Chem. Chem. Phys. 4 (2002) 2189–2193. https://doi.org/10.1039/b111195g.

[256] Y. Zhang, S. Yu, P. Luo, S. Xu, X. Zhang, H. Zhou, J. Du, J. Yang, N. Xin, Y. Kong, J. Liu, B. Chen, J. Lu, Fixation of CO 2 along with bromopyridines on a silver electrode, R. Soc. Open Sci. 5 (2018). https://doi.org/10.1098/rsos.180897.

[257] G.J. Rowlands, Radicals in organic synthesis: part 2, Tetrahedron. 66 (2010) 1593–1636. https://doi.org/10.1016/j.tet.2009.12.023.

[258] M.S. Mubarak, D.G. Peters, Using silver cathodes for organic electrosynthesis and mechanistic studies, Curr. Opin. Electrochem. 2 (2017) 60–66. https://doi.org/10.1016/j.coelec.2017.03.001.

[259] E. Du?ach, M. Jos? Medeiros, S. Olivero, Intramolecular reductive cyclisations using electrochemistry: development of environmentally friendly synthetic methodologies, New J. Chem. 30 (2006) 1534. https://doi.org/10.1039/b608228a.

[260] Y. Wang, X. Lu, Study on the effect of electrochemical dechlorination reduction of hexachlorobenzene using different cathodes, J. Anal. Methods Chem. 2014 (2014). https://doi.org/10.1155/2014/371510.

[261] A.A. Isse, S. Gottardello, C. Durante, A. Gennaro, Dissociative electron transfer to organic chlorides : Electrocatalysis at metal cathodes, (2008) 2409–2416. https://doi.org/10.1039/b719936h.

[262] E. Duñach, A.P. Esteves, M.J. Medeiros, D. Pletcher, S. Olivero, The study of nickel(II) and cobalt(II) complexes with a chiral salen derivative as catalysts for the electrochemical cyclisation of unsaturated 2-bromophenyl ethers, J. Electroanal. Chem. 566 (2004) 39–45. https://doi.org/10.1016/j.jelechem.2003.10.045.

[263] S.B. Rondinini, P.R. Mussini, F. Crippa, G. Sello, Electrocatalytic potentialities of silver as a cathode for organic halide reductions, Electrochem. Commun. 2 (2000) 491–496. https://doi.org/10.1016/S1388-2481(00)00065-5.

[264] C. Durante, A.A. Isse, F. Todesco, A. Gennaro, Electrocatalytic Activation of Aromatic Carbon-Bromine Bonds toward Carboxylation at Silver and Copper Cathodes, J. Electrochem. Soc. 160 (2013) G3073–G3079. https://doi.org/10.1149/2.008307jes.

[265] Y.F. Huang, D.Y. Wu, A. Wang, B. Ren, S. Rondinini, Z.Q. Tian, C. Amatore, Bridging the gap between electrochemical and organometallic activation: Benzyl chloride reduction at silver cathodes, J. Am. Chem. Soc. 132 (2010) 17199–17210. https://doi.org/10.1021/ja106049c.

[266] C. Bellomunno, D. Bonanomi, L. Falciola, M. Longhi, P.R. Mussini, L.M. Doubova, G. Di Silvestro, Building up an electrocatalytic activity scale of cathode materials for organic halide reductions, 50 (2005) 2331–2341. https://doi.org/10.1016/j.electacta.2004.10.047.

[267] L. Perini, C. Durante, M. Favaro, S. Agnoli, G. Granozzi, A. Gennaro, Applied Catalysis B : Environmental Electrocatalysis at palladium nanoparticles : Effect of the support nitrogen doping on the catalytic activation of carbon halogen bond, "Applied Catal. B, Environ. 144 (2014) 300–307. https://doi.org/10.1016/j.apcatb.2013.07.023.

[268] B. Vanrenterghem, P. Jovanovič, M. Šala, M. Bele, V.S. Šelih, N. Hodnik, T. Breugelmans, Stability study of silver nanoparticles towards the halide electroreduction, Electrochim. Acta. 286 (2018) 123–130. https://doi.org/10.1016/j.electacta.2018.08.037.

[269] B. Vanrenterghem, N. Hodnik, M. Bele, M. Šala, G. Amelinckx, S. Neukermans, R. Zaplotnik, G. Primc, M. Mozetič, T. Breugelmans,

Increase of electrodeposited catalyst stability via plasma grown vertically oriented graphene nanoparticle movement restriction, Chem. Commun. 53 (2017) 9340–9343. https://doi.org/10.1039/c7cc05828d.

[270] B. Vanrenterghem, A. Papaderakis, S. Sotiropoulos, D. Tsiplakides, S. Balomenou, S. Bals, T. Breugelmans, The reduction of benzylbromide at Ag-Ni deposits prepared by galvanic replacement, Electrochim. Acta. 196 (2016) 756–768. https://doi.org/10.1016/j.electacta.2016.02.135.

[271] C.P. Andrieux, G. Delgado, J.M. Savéant, Improvement and estimation of precision in the cyclic voltammetric determination of rate constants and activation parameters of coupled homogeneous first order reactions. Halide cleavage in anion radicals of chloroanthracenes, J. Electroanal. Chem. 348 (1993) 123–139. https://doi.org/10.1016/0022-0728(93)80127-4.

[272] C.P. Andrieux, I. Gallardo, J. Saveant, Outer-sphere electron-transfer reduction of alkyl halides. A source of alkyl radicals or carbanions? Reduction of alkyl radicals., J. Am. Chem. Soc. 111 (1989) 1620–1626.

[273] A.A. Isse, P.R. Mussini, A. Gennaro, New Insights into Electrocatalysis and Dissociative Electron Transfer Mechanisms : The Case of Aromatic Bromides, J. Phys. Chem. 113 (2009) 14983–14992.

[274] S. Ardizzone, G. Cappelletti, P.R. Mussini, S. Rondinini, L.M. Doubova, Adsorption competition effects in the electrocatalytic reduction of organic halides on silver, J. Electroanal. Chem. 532 (2002) 285–293. https://doi.org/10.1016/S0022-0728(02)00950-6.

[275] A. Gennaro, A. Ahmed, E. Giussani, P. Romana, I. Primerano, M. Rossi, Electrochimica Acta Relationship between supporting electrolyte bulkiness and dissociative electron transfer at catalytic and non-catalytic electrodes, Electrochim. Acta. 89 (2013) 52–62. https://doi.org/10.1016/j.electacta.2012.11.013.

[276] A.A. Isse, A. De Giusti, A. Gennaro, L. Falciola, P.R. Mussini, Electrochemical reduction of benzyl halides at a silver electrode, Electrochim. Acta. 51 (2006) 4956–4964. https://doi.org/10.1016/j.electacta.2006.01.039.

[277] F. M'Halla, J. Pinson, J.M. Savéant, The Solvent as H-Atom Donor in Organic Electrochemical Reactions. Reduction of Aromatic Halides, J. Am. Chem. Soc. 102 (1980) 4120–4127.

[278] A. Wang, Y.F. Huang, U.K. Sur, D.Y. Wu, B. Ren, S. Rondinini, C. Amatore, Z.Q. Tian, In situ identification of intermediates of benzyl chloride reduction at a silver electrode by SERS coupled with DFT calculations, J. Am. Chem. Soc. 132 (2010) 9534–9536. https://doi.org/10.1021/ja1024639.

[279] W. Oelßner, F. Berthold, U. Guth, The iR drop – well-known but often underestimated in electrochemical polarization measurements and corrosion testing, Mater. Corros. 57 (2006) 455–466. https://doi.org/10.1002/maco.200603982.

[280] D.O. Wipf, Ohmic Drop Compensation in Voltammetry : Iterative Correction of the Applied Potential, Anal. Chem. 68 (1996) 1871–1876.

[281] L. Nadjo, J.M. Savéant, Linear sweep voltammetry: Kinetic control by charge transfer and/or secondary chemical reactions. I. Formal kinetics, J. Electroanal. Chem. 48 (1973) 113–145. https://doi.org/10.1016/S0022-0728(73)80300-6.

[282] L. Falciola, A. Gennaro, A.A. Isse, P.R. Mussini, M. Rossi, The solvent effect in the electrocatalytic reduction of organic bromides on silver, J. Electroanal. Chem. 593 (2006) 47–56. https://doi.org/10.1016/j.jelechem.2006.02.003.

[283] A.A. Isse, G. Berzi, L. Falciola, M. Rossi, P.R. Mussini, A. Gennaro, Electrocatalysis and electron transfer mechanisms in the reduction of organic halides at Ag, J. Appl. Electrochem. 39 (2009) 2217–2225. https://doi.org/10.1007/s10800-008-9768-z.

[284] E.T. Martin, L.M. Strawsine, M.S. Mubarak, D.G. Peters, Electrochimica Acta Direct Reduction of 1 , 2- and 1 , 6-Dibromohexane at Silver Cathodes in Dimethylformamide, Electrochim. Acta. 186 (2015) 369–376. https://doi.org/10.1016/j.electacta.2015.10.164.

[285] D.A. Koch, B.J. Henne, D.E. Bartak, Carbanion and Radical Intermediacy in the Electrochemical Reduction of Benzyl Halides in Acetonitrile, J. Electrochem. Soc. 134 (1987) 3062. https://doi.org/10.1149/1.2100340.

[286] V. Jouikov, J. Simonet, Reduction of aryl halides at transition metal cathodes. Conditions for aryl-aryl bond formation: The Ullmann's reaction revisited, Electrochem. Commun. 12 (2010) 781–783. https://doi.org/10.1016/j.elecom.2010.03.032.

[287] A.A. Isse, A. De Giusti, A. Gennaro, One- versus two-electron reaction

pathways in the electrocatalytic reduction of benzyl bromide at silver cathodes, Tetrahedron Lett. 47 (2006) 7735–7739. https://doi.org/10.1016/j.tetlet.2006.08.123.

[288] R. Sokolová, M. Hromadová, J. Fiedler, L. Pospíšil, S. Giannarelli, M. Valášek, Reduction of substituted benzonitrile pesticides, J. Electroanal. Chem. 622 (2008) 211–218. https://doi.org/10.1016/j.jelechem.2008.06.008.

[289] J.R. Bolton, G.K. Fraenkel, Electron spin resonance study of the pairing theorem for alternant hydrocarbons:13C splittings in the anthracene positive and negative ions, J. Chem. Phys. 40 (1964) 3307–3320. https://doi.org/10.1063/1.1724999.

[290] C. Karunakaran, M. Balamurugan, Electron Paramagnetic Resonance Spectroscopy, Elsevier Inc., 2018. https://doi.org/10.1016/B978-0-12-813608-9.00004-6.

Personal information

Publications in international peer-reviewed journals included in the Web of Science

1. B. Vanrenterghem, N. Hodnik, M. Bele, M. Sala, G. Amelinckx, **S. Neukermans**, Zaplotnik, G. Primc, M. Mozetic and T. Breugelmans, Increase of electrodeposited catalyst stability via plasma grown vertically oriented graphene nanoparticle movement restriction, *Chemical communications*, 26 (2017) 9340-9343.

2. D. Pauwels, H.Y.V. Ching, M. Samanipour, **S. Neukermans**, J. Hereijgers, S. Van Doorslaer, K. De Wael, T. Breugelmans, Identifying intermediates in the reductive intramolecular cyclisation of allyl 2-bromobenzyl ether by an improved electron paramagnetic resonance spectro-electrochemical electrode design combined with density functional theory calculations, *Electrochimica Acta*, 271 (2018) 10-18

3. **S. Neukermans**, J. Hereijgers, H.Y.V. Ching, M. Samanipour, S. Van Doorslaer, A. Hubin, T. Breugelmans, A continuous *in-situ* EPR-electrochemical reactor as a rapid in-depth mechanistic screening tool for electrocatalysis, *Electrochemistry Communications*, 97 (2018) 42-45

4. **S. Neukermans**, F. Vorobjov, T. Kenis, R. De Wolf, J. Hereijgers, T. Breugelmans, Electrochemical reduction of halogenated aromatic compounds at metal cathodes in acetonitrile, *Electrochimica Acta,* 332 (2020) 135484

5. L. Pacquets, E. Irtem, **S. Neukermans**, N. Daems, S. Bals, T. Breugelmans, Size-controlled electrodeposition of Cu nanoparticles on gas diffusion electrodes in methanesulfonic acid solution, *Journal of applied electrochemistry*, 51 (2020) 317-330

6. **S. Neukermans**, M. Samanipour, H.Y.V. Ching, J. Hereijgers, S. Van Doorslaer, A. Hubin, T. Breugelmans, A versatile *in-situ* EPR-spectroelectrochemical approach for electrocatalyst research, *ChemElectroChem,* 7 (2020) 4578-4586

Oral Presentations at international conferences

1. **S. Neukermans**, D. Pauwels, B. Vanrenterghem, H.Y.V. Ching, M. Samanipour, J. Hereijgers, S. Van Doorslaer, T. Breugelmans, Electrocatalytic reduction of 1-bromonaphthalene at nanostructured electrodes combined with EPR techniques to provide an in-depth understanding of the reaction mechanism, *Chemcys,* 21-23 February 2018, Blankenberge, Belgium.

2. **S. Neukermans**, J. Hereijgers, M. Samanipour, H.Y.V. Ching, S. Van Doorslaer, A. Hubin, T. Breugelmans, *In-situ* EPR measurements of electrocatalytically formed radicals as a spectro-electrochemical technique to investigate reaction mechanisms, *ISE Annual Meeting,* 2018, Bologna, Italy

3. **S. Neukermans**, C. De Jongh, T. Altantzis, T. Breugelmans, Electrocatalytic reduction of aromatic bromides at silver nanoparticles: size matters?, *24th ISE Topical meeting*, 2019, Merida, Mexico